Copyright Statement

This copy of this thesis has been supplied on condition that anyone who consults it is understood to recognize that its copyright rests with its author and due acknowledgement must always be made to the use of any material contained in, or derived from, this thesis.

DISTINCT ELEMENT NUMERICAL MODELLING OF VOLCANIC DEBRIS AVALANCHE EMPLACEMENT GEOMECHANICS

NICHOLAS DARRELL THOMPSON

A thesis submitted in partial fulfilment of the requirements of Bournemouth University for the degree of Doctor of Philosophy

October 2009

Abstract

Catastrophic collapse of volcanic edifices is a relatively common phenomenon in the geological record, representing the largest subaerial landsliding events on Earth. Subsequent volcanic debris avalanche (VDA) runout lengths often exceed 50 km and inundated areas may be greater than 1,000 km^2. The geomechanical processes that occur during emplacement, however, remain poorly understood as emplacement processes must generally be inferred from deposit analysis. Summarizing the literature, this thesis first introduces the general factors that control edifice collapse, mechanisms thought to control avalanche mobility and commonly observed deposit features. The mechanisms which have led to the formation of characteristic deposit features specifically are then reviewed; commonly discussed themes are then used to develop a general emplacement model which summarizes the geomechanical evolution of VDAs. This model is then tested by analyzing orthophotographic images of VDA deposits; common deposit morphologies are observed in each case, suggesting a common deformation sequence may occur during emplacement. To better understand emplacement processes, a distinct element numerical model is then created. Initial unbonded particulate avalanche simulations allow spatial/temporal variations in avalanche body stress, energy and deformation to be considered in relation to the development of characteristic deposit features. A more sophisticated bonded particle model is then utilized to allow the consideration of emerging brittle behaviour. Resulting simulations display the development of characteristic VDA deposit features from initial block sliding and horst and graben development. Evolution to a fully-flowing granular avalanche occurs through the initiation and propagation of faults generated due to stresses in the avalanche body, reflective of the proposed common deformation sequence. Features commonly observed in VDA deposits, such as toreva blocks and surface hummocks, are created in the bonded avalanche simulations. Use of this innovative numerical model therefore allows for new insight into the geomechanical evolution of rock and debris avalanches to be developed.

List of contents

List of figures

List of tables

Acknowledgments

I would first like to thank Bournemouth University for the bursary award under which this research conducted and Itasca Consulting Group, Inc. for their generous loan of the *PFC*^{2D} software for the duration of this research.

I would also like to thank Dr. Nick Petford for providing the opportunity and initial ideas for this PhD research and Dr. Matthew Bennett for his steady encouragement, direction and insight throughout this project. Of the many people who have helped guide the me with encouragement and advice at various points throughout this project, special thanks is given to Andrew Ford, Rebecca Dolling, Marie Dunning, Julie Cheshire, Maureen Freeman, Louise Pearson, Kate Welham, Cathy Symonds, Eddie Bromhead, Geoff Wadge, Stefano Utili, Kurt Koenders, Marcel Hürlimann, Martin Schöpfer, John Walsh, Fabian Dedecker, Dave DeGagne, Roger Hart, Michelle Nelson, David Potyondy, Peter Cundall, Ben van Wyk de Vries, Gerald Ernst, Nico Fournier, Colin Thornton, Giovanni Crosta, Catherine O'Sullivan, Chris Wood, Ross Hill, Paul Cheetham and Simon Day (in no particular order).

Lastly, to all my friends and family, my most sincere thanks for all your support during my years in the United Kingdom.

Author's declaration

Portions of this research have been previously presented in peer-reviewed publications:

Thompson, **N**., Bennett, M.R., Petford, N., Analyses on granular mass movement mechanics and deformation with distinct element numerical modeling: implications for large scale rock and debris avalanches. *Acta Geotechnica*, 2009, doi: 10.1007/s11440-009-0093-4.

Thompson, **N**., 2008. Using *PFC*^{2D} to investigate volcanic debris avalanche emplacement processes and deposit features with special consideration to Mexican volcanic collapse deposits. *In*: Hart, R., Detournay, C., Cundall, P, eds. *Continuum and Distinct Element Numerical Modeling in Geo-engineering, Proceedings of the 1*st *International FLAC/DEM Symposium, 25-27 August, Minneapolis, Minnesota*, 189-196.

Two additional publications are currently in preparation. Furthermore, material contained in this thesis has been presented at a number of internationally recognized meetings:

Thompson, **N**., Bennett, M., Petford, N., 2009. Emplacement of volcanic debris avalanche landslide deposits: new insight from distinct element numerical model simulations. *Geophysical Research Abstracts, EGU General Assembly, Vienna, Austria*, 11, EGU2009-198.

Thompson, **N**., Bennett, M., Petford, N., 2009. Emplacement of volcanic debris avalanche landslide deposits: new insight from distinct element numerical simulations. *Volcanic and Magmatic Studies Group annual meeting, Bournemouth, England*, 4-6 January.

Thompson, **N**., Bennett, M., Petford, N., 2008. Emplacement of volcanic debris avalanche landslide deposits: new insight from distinct element numerical model simulations. *EOS Transactions AGU, 89, Fall Meeting Supplement, San Francisco, California*, abstract H51F-0888.

Thompson, **N**., Bennett, M. R., Petford, N., 2008. Using the discrete element method to investigate volcanic debris avalanche emplacement processes and deposit features with special consideration to Mexican volcanic collapse deposits. *Volcanic and Magmatic Studies Group annual meeting, Dublin, Ireland*, 3-5 January.

Thompson, **N**., Bennett, M. R., Petford, N., 2007. Using *PFC*^{2D} to investigate volcanic debris avalanche flow processes and features with special consideration to Mexican volcanic collapse deposits. *In: Earth Sciences in the Service of Society, The Geological Society of London Bicentennial Conference, London, September 2007*, 140 pp.

Chapter 1 - Introduction

Since the 18 May, 1980 collapse of Mount St. Helens in Washington, USA, large-scale catastrophic collapse has been recognized as a relatively common and perhaps inevitable process in the evolution of volcanic edifices. Descriptions of similar events stemmed from the insight developed during the Mount St. Helens failure; important papers such as Schuster and Crandell (1984), Siebert (1984) and Siebert *et al.* (1987) highlight the relatively common occurrence, causes and magnitude of large-scale edifices collapse worldwide. More recent reviews such as McGuire (1996, 2003), Ui *et al.* (2000) and Francis and Oppenheimer (2004) build upon these earlier summaries by detailing our latest understanding of this complex phenomenon and introducing the most recent advancements in computer modelling and digital terrain analysis. What is recognized in all research is the immense scale and relatively common occurrence of edifice collapse. Runout lengths of up to 120 km with inundation areas of hundreds to thousands of square kilometres are not uncommon; submarine and extraterrestrial deposits can be even larger (Siebert 1984; Siebert *et al.*, 1987; McGuire 1996, 2003). Over 1 km^3 of material is commonly involved in such failures, though avalanches with volumes an order of magnitude above this have been recorded (Siebert, 1984). The energy driving these flows is enormous; subaerial failures are thought to reach speeds exceeding 100 km/hr and surmount topographic highs of hundreds of metres (Voight *et al.*, 1983; Francis and Wells, 1988; Glicken, 1998; Sousa and Voight, 1985; Richards and Villeneuve, 2001; Alloway *et al.*, 2005; Kelfoun *et al.*, 2008). 20,000 fatalities are thought to have been caused by volcanic flank failures and their related products in historic time (Siebert *et al.*, 1987). Given that four to five of these large-scale events have been recorded during the past four centuries the hazard potential may be considerable; the threat of associated tsunamis amplifies this potential (Siebert *et al.*, 1987).

Though volcanic collapse occurs relatively frequently, our ability to predict and monitor this phenomenon is limited. Much of what we know about the behaviour of large-scale debris and rock avalanches in any environment is deduced in the field from the deposits which contain structures and morphologies reflective of their mode of emplacement (Glicken, 1991, 1998; Wadge *et al.*, 1995; Schneider and Fisher, 1998; Reubi and Hernandez, 2000; van Wyk de Vries, 2001; Clavero *et al.*, 2002, 2004; Strom, 2006; Bernard *et al.*, 2008; Shea and van Wyk de Vries, 2008; Shea *et al.*, 2008). Avalanche behaviour is also studied with theoretical, analogue, and numerical modelling; each approach allowing varying degrees of experimentation, reproducibility and accuracy in

capturing avalanche behaviours (Crosta *et al.*, 2001; Pudasaini and Hutter, 2007). The objective of this study is to use both deposit analysis and avalanche modelling, innovative numerical modelling in this case, to further our understanding of large-scale volcanic debris avalanche (VDA) emplacement processes.

After a brief introduction into the causes of edifice collapse and the phenomena of long avalanche runout (Chapter 2), this thesis will be presented in two broad sections: deposit characterization and analysis (Chapters 3-5) and numerical investigation (Chapters 6-8). Chapters 2-4 represent the majority of the literature review conducted, though additional reviews concerning numerical modelling will be given in latter sections. The first objective of the deposit characterization section of this paper is to review the principal features of VDA deposits as discussed in the literature (Chapter 3). A detailed description of the most notable deposit features is given, many of which are observed universally. The influence of factors likely to have significant impact on emplacement behaviour, namely the presence of water and topographic controls, are also reviewed. Lastly, as many types of deposits can be found within the sedimentary record in volcanic environments, the factors which distinguish VDAs from other sediment-producing phenomena are briefly discussed. Chapter 4 builds upon this introduction by considering characteristic feature formation and general emplacement mechanisms at a number of notable VDA deposits, as proposed by previous authors. Based on these descriptions, an emplacement model generally applicable to all cases is described, which highlights the fundamental processes occurring as emplacement evolves. This model is meant to describe a brittle deformation sequence which is fundamentally universal to all VDA cases and the geomechanical basis for the development of characteristic deposit features. As discrete stages of the general emplacement model can be recognized, each discernible in the resulting deposit by varying morphological characteristics, a system of identifying the geomechanical conditions most prevalent at a given time or place of emplacement is suggested. This system, as well as the general emplacement model, is then tested by examining several VDA deposits with digital orthophotographic imagery, mapping key surface structures and developing a likely series of emplacement events for each case (Chapter 5). The similarities between each deposit are then discussed with the general model in mind. Each of these exercises is performed in an effort to further identify common themes in VDA emplacement behaviour evolution, which, if they exist, may be universal in large-scale rock and debris avalanches and help to explain the development of characteristic deposit features.

Distinct element numerical modelling (DEM) is then used as a tool to develop further insight into VDA emplacement processes and validate the emplacement hypotheses discussed in previous chapters (Chapters 6-8). This novel numerical approach was chosen for: A) its ability to simulate the large deformations that occur during VDA emplacement; B) its discrete nature which allows internal deformations to be realistically considered, and; C) its bonding capability which allows the emergent behaviour of a fracturing brittle rock mass to be simulated. The governing principles, operation and limitations of this method, as well as the principal findings of a number of relevant previous studies which have used DEM to investigate similar processes, are discussed in Chapter 6. The DEM avalanche simulations conducted for this study are then presented in two parts: using an exclusively unbonded approach which considers the medium as a true granular (i.e., discrete) medium (Chapter 7) and a bonded approach whereby particles in the assemblage are connected to their immediate neighbours and are broken once sufficient stresses are reached, thereby allowing emerging brittle behaviour to be considered (Chapter 8). Model setup methodology is described in each respective section. Unbonded simulations are performed in order to gain an understanding of model controls and basic simulation avalanche behaviour. These simulations are shown to be valuable in developing both quantitative and qualitative insight into avalanche behaviour but are limited in their ability to capture important aspects of avalanche behaviour, such as brittle behaviour (e.g., fault propagation) and irregular topography development. These processes, however, are captured by the bonded emplacement simulations. In addition to a general extensional runout case, other emplacement scenarios are explored, such as the influence runout basin topography and changes in basal surface material properties.

Each chapter in this thesis is designed to answer a series of key question concerning avalanche emplacement mechanics. These questions are presented at the beginning of each chapter and addressed throughout that chapter. A discussion which summarizes the principal findings of each exercise in relation to potential real world processes is also presented at the end of each chapter. These discussions are then reviewed in the final section of this paper (Chapter 9) to summarize the new insight developed from this work. As this study represents one of only a handful which has used DEM to investigate debris avalanche emplacement specifically, the feasibility of this approach in capturing the complex behaviour of actual events is discussed further in the final part of this paper. Lastly, ideas for additional work are presented.

Several definitions may helpful to the reader. First, when discussing the spatial location of features within VDA deposits or sections of the travelling avalanches, the terms *proximal*, *medial*, and *distal* will be used throughout this paper. Proximal generally refers those portions closest to the source edifice (proximal third), medial the central section of the deposit or avalanche (medial third), and distal those sections located furthest away from the source edifice (distal third). The terms *head* and *toe* refer to the most proximal and distal portions of a failure body. Also, VDAs are considered to evolve in three stages: *initiation*, *emplacement*, and *deposition* (after Takarada *et al.* [1999]). Initiation refers to the instant a particular failure separates from its host edifice and begins to accelerate downslope under the force of gravity. The term emplacement is used here to refer to any moment after failure initiation and before deposition, which is considered to be the instant of complete movement cessation. Following Glicken (1991), breakup of the initially intact edifice flank into individual constituents during emplacement is generally considered to be through *fragmentation* or *disaggregation*. *Fracture* is defined as the breaking of individual clasts. *Structure* refers to features that can be observed at any scale and typically implies larger-scale elements such as faults and hummocks. Other definitions will be given as appropriate.

During the course of this work several field sites were visited. The first of these sites was the VDA deposit of Popocatepetl in Central Mexico, where a full reconnaissance of the deposit was performed. This activity took place over four days and included traverses of the full width and length of the deposit as well as analysis of each of the exposures present along the lateral axis of the deposit, which were typically roadcuts (see Figure 8). This experience provided the author with first-hand observations of VDA deposit morphology, characteristic features and internal structure. The author also worked as a volunteer for one month at the Montserrat Volcano Observatory (MVO), which experienced a headwall collapse in the early stages of its current activity. While the deposit of this VDA was not analyzed directly during this time, the products of similar events, such as lahars and pyroclastic flows, were observed. Numerous discussions concerning edifice stability in general and this project specifically were held with both MVO staff and several visiting scientists. The author was also able to observe the morphology of characteristic VDA deposit features during a personal trip to Mount Meru in Tanzania. Photographs from each of these field experiences are included in this thesis. Additionally, the author had previously taken part in a reconnaissance of the Mount Shasta VDA deposit in northern California, USA, prior to beginning this study.

Chapter 2 - Volcanic edifice instability

The objective of this chapter is to provide a clear definition of a volcanic debris avalanche and introduce the major factors that influence edifice instability and avalanche mobility as discussed in the literature. Though it is not the purpose of this study to consider these topics in detail, a general introduction is necessary as they are important in understanding avalanche emplacement mechanics. Further reading on these subjects can be found in the references provided in each respective section.

Key questions:
- What factors influence edifice instability?
- What factors influence debris avalanche mobility?

2.1. Introduction

A number of descriptions in the literature characterize the catastrophic, large-scale failure of volcanic edifices. Schuster and Crandell (1984, p. 567) describe these events as "the sudden and very rapid flowage of an incoherent, unsorted mixture of rock and soil material in response to gravity". The terms *sector collapse* (Siebert *et al.*, 1984), *flank collapse* (Capra *et al.*, 2002), *volcanic dry avalanche* (Nakamura, 1978), *rockslide avalanche* (Voight *et al.*, 1983; Shea and van Wyk de Vries, 2008), *debris avalanche* and *volcanic debris avalanche* (Crandell, 1989; Wadge *et al.*, 1995; Francis and Wells, 1988; Clavero *et al.*, 2002) are commonly used terms used to summarize this phenomenon. The wide range of terminology reflects an ever broader range of failure scenarios, material properties and emplacement conditions. The term *volcanic debris avalanche,* or *VDA,* will be used throughout the remainder of this thesis as it is both a widely used and accepted term and represents the volcanic environment specifically.

2.2. Source edifice composition

The properties of the materials that comprise volcanic edifices are important in both promoting collapse and governing the emplacement of resulting avalanches. Activity related to subduction zone volcanism tends to emit intermediate to felsic lavas relatively rich in silica (> 52% SiO_2) and therefore high in viscosity. Subsequently, lavas build up to form large, steep (upwards of 40°) and mechanically unstable cones (Francis and Self, 1987; Francis and Wells, 1988; Siebe *et al.*, 1992; Francis, 1994; Richards and Villeneuve,

2001). This geometry presents a first-order control on instability and potential failure volume; Francis and Wells (1988) suggest that once a height of 2,000-3,000 m is reached, a threshold may be achieved where large-scale collapse could in fact be inevitable. Indeed, many volcanic edifices around the globe currently stand at these heights (e.g. South America, see Francis and Wells [1988]). Height is not necessarily a determining factor in edifice collapse, however, as failure may occur along bedding or joint planes subparallel to the edifice surface in volcanoes as low as 500-1,000 m (Siebert, 1984). Repeated collapse of particularly unstable edifices is also common: Russia's Shiveluch (Belousov *et al.*, 1999; Ponomareva *et al.*, 1998; Ponomareva *et al.*, 2006), Alaska's Mt. Augustine (Beget and Kienle, 1992), New Zealand's Mt. Egmont (Alloway *et al.*, 2005) and several volcanoes in Mexico (Capra *et al.*, 2002) are particularly good examples of this phenomenon.

It should be noted that subaerial stratovolcanoes and composite cones are not the only volcano type susceptible to collapse. Oceanic island shield volcanoes (Moore *et al.*, 1994; McGuire, 1996, 2003) and dome complexes, such as Mexico's Las Derrumbadas complex (Capra *et al.*, 2002), are also prone to mechanical failure.

Outward dipping layers of competent rock alternating with unconsolidated volcaniclastic layers and local saturation further influences stability (Voight *et al.*, 1981; Schuster and Crandell, 1984; Boudal and Robin, 1989; Crandell, 1989; Francis, 1994; Kerle and van Wyk de Vries, 2001; Capra *et al.*, 2002; Clavero *et al.*, 2002; McGuire, 2003; Carrasco-Núñez *et al.*, 2006; Shea *et al.*, 2008; Vezzoli *et al.*, 2008). Additionally, constituent materials may have been degraded to low strength clay materials, such as kaolinite and montmorillonite, through hydrothermal alteration processes (Schuster and Crandell, 1984; Siebert, 1984; Lopez and Williams, 1993; Reid *et al.*, 2001). The presence of these mechanically unsound layers and weak materials may also influence avalanche emplacement processes. For instance, Ui (1983) suggests that a VDA mass may have a lower rigidity due to the presence of hydrothermally altered and/or pyroclastic layers, fracture development around an intruding cryptodome, and the boiling of supercritical fluids.

Fault structures present in fast-growing and unstable edifices or underlying basements also play an important role in promoting flank and sector failure (van Wyk de Vries *et al.*, 2001; Shea *et al.*, 2008). Structural influences are discussed only briefly below; the reader is directed to McGuire (1996, 2003), van Wyk de Vries *et al.* (2000, 2001), Vidal and

Merle (2000), Kerle and van Wyk de Vries (2001), Tibaldi *et al.* (2006) and Shea *et al.* (2008) for more detailed descriptions on the relationship between edifice structure and instability.

2.3. Triggering mechanisms

The natural instabilities present in volcanic edifices, however, do not necessarily translate into certain flank collapse. A number of authors have suggested that because a large number of volcanoes worldwide meet the general requirements of an unstable slope, such as slope angles of 28-32°, and large-scale collapse is not a relatively common phenomenon, some type of triggering mechanism may be needed to initiate failure (Siebert, 1984; McGuire, 1996, 2003; Belousov *et al.*, 1999; Thompson *et al.*, 2008). Factors that may be involved in triggering edifice failure include magmatic intrusion, phreatic and seismic activity, dike emplacement, regional stress patterns, local water levels, weak underling material, unfavourable topography and/or associated tectonic and structural factors (Voight *et al.*, 1983; Siebert, 1984; Siebert *et al.*, 1987; Francis and Wells, 1988; Elsworth and Voight, 1996; McGuire 1996; Voight and Elsworth, 1997; Day, 1996; Day *et al*., 1999; Kerle and van Wyk de Vries, 2001; van Wyk de Vries *et al.*, 2000, 2001; Vidal and Merle, 2000; Capra *et al.* 2002; Carrasco-Núñez *et al.*, 2006; Ponomareva *et al.*, 2006; Tibaldi *et al.*, 2006; Shea *et al.*, 2008; Vezzoli *et al.*, 2008).

Edifice collapse events are generally divided into three categories based on their proposed failure initiation mechanism, each named after a specific event (Siebert, 1984; Francis and Self, 1987; Siebert *et al.*, 1987; Francis, 1994; Reubi and Hernandez, 2000; Ui *et al.*, 2000). Bezymianny-type collapses are those in which a magmatic component was clearly involved in the collapse. Failure in this case is thought to be influenced by the deformation caused by magma body intrusion, increased fluid pressure and thermal effects (Voight and Elsworth, 1997). Prismatically jointed juvenile material, pyroclastic and airfall tephras and breadcrusted blocks present in a VDA deposit may indicate this type of collapse (Francis *et al.*, 1985; Francis and Self, 1987; Siebe *et al.*, 1992; McGuire, 1996; Glicken, 1998; Richards and Villeneuve, 2001; Vezzoli *et al.*, 2008). The second category of failure is Bandai-type events, which are exclusively phreatic explosion induced. The final category are Unzen-type failures; those considered as ‘cold collapses’ where no magmatic or phreatic influence is suspected. Such a collapse could occur in a strongly hydrothermally altered edifice or those with influential structural weaknesses (Schuster and Crandell, 1984). Unzen-type failure may also be induced by seismic activity, which may indeed play

a part in each type of event (Siebert, 1984; Endo *et al.*, 1989; Voight and Sousa, 1994; Voight and Elsworth, 1997).

In reality, large-scale collapse is presumably triggered by a complex combination of the aforementioned mechanisms and no simple, singular explanation likely exists (Voight and Elsworth, 1997).

2.4. Avalanche mobility

Due to the importance of hazard prediction, one of the most important topics in landslide research concerns the distance travelled by large-scale catastrophic flows, which are often observed to cover great distances. This phenomenon appears to increase with increasing avalanche volume, and as large-scale VDAs are amongst the largest mass failures known, considerable attention has been given to determining their mobility mechanisms (Ui, 1983; Siebert, 1984; Hayashi and Self, 1992; Takarada *et al.*, 1999; Hürlimann *et al.*, 2000; Legros, 2002; Shea and van Wyk de Vries, 2008). As this is a complex and much debated topic, only a brief introduction of the main themes will be presented here that focus on basic understanding of the likely mechanisms occurring during emplacement. More thorough reviews can be found in Shaller and Smith-Shaller (1996), Takarada *et al.* (1999), Legros (2002) and Francis and Oppenheimer (2004).

If the centre of mass of a given failure slides down a slope through an elevation difference, H, the length to which it will travel along the runout path, L (runout length) is related by Coulomb's law of sliding friction:

$$H = \tan\alpha L \qquad (1)$$

where $\tan\alpha$ represents the friction of the sliding surface, commonly assumed to be ≈ 0.6 (Figure 1; Hsü, 1975). Therefore, normal circumstances predict $H/L = 0.6$. As the location of a failure's centre of mass is difficult to estimate, H is typically taken as the highest vertical point of the failure surface while L is taken as the most distal point of the subsequent deposit. In large-scale rock slides and avalanches, however, H/L is observed to be much lower than 0.6, typically < 0.25. H/L ratios for large-scale VDAs, for instance, are on the order of 0.06-0.13 though even lower values are recorded, particularly for volumes greater than 1 km^3 (Ui, 1983; Schuster and Crandell, 1984; Crandell, 1989). Submarine and extraterrestrial avalanche deposits possess even lower values (to 0.004)

(McEwan, 1989; Hampton *et al.*, 1996; Legros, 2002). This *H*/*L* ratio, termed the *fahrböschung* by Heim (1932) and now referred to as the *Heim coefficient*, *apparent friction coefficient* or *friction ratio*, is commonly used as a measure of avalanche mobility and is observed to systematically decrease with increasing *H* (Hsü, 1975; Legros, 2002). Numerous authors, however, claim that it is not *H* which affects *L*, but the failure volume, *V*, on which runout is most dependent (Scheidegger, 1973; Ui, 1983; McEwan, 1989; Legros, 2002; Shea and van Wyk de Vries, 2008). Shea and van Wyk de Vries (2008) note that whatever their size, empirical studies show smaller nonvolcanic rockslides and large-scale VDAs possess essentially similar behaviour and can therefore be assumed to be governed by the same processes.

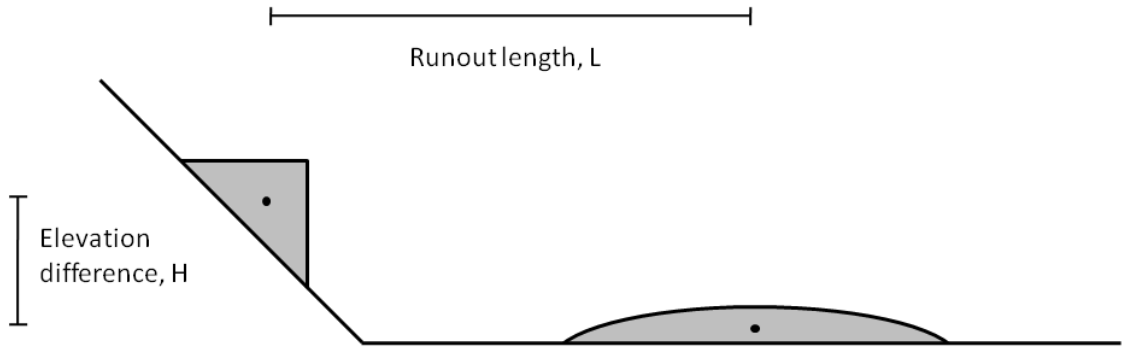

Figure 1 – Elevation difference (H) to runout length (L) relationship (H/L). Centres of mass of pre-failure and deposit bodies denoted by black dot.

The long avalanche runouts observed have brought significant speculation as to the possible mechanisms driving this phenomenon. The inclusion of a fluidising medium, be it water (Johnson, 1978; Voight and Sousa, 1994; Legros, 2002), air (Kent, 1966; Shreve, 1968a, 1968b; Fahnestock, 1978), interstitial dust (Hsü, 1975), basal frictional melt (Erismann, 1979), steam (Habib, 1975; Goguel, 1978) or volcanic gases (Voight *et al.*, 1983) has been suggested as likely catalysts. However, a number of fluid absent, granular (i.e., mechanical) models have also been proposed (MacSaveney, 1978; Melosh, 1979, 1986; Davies, 1982; Campbell, 1989, 1990; Cleary and Campbell, 1993; Campbell *et al.*, 1995; Straub, 1996; Collins and Melosh, 2003; Davies *et al.*, 2006; Davies and MacSaveney, 2002, 2008), as have viscosity and yield strength based continuum (McEwan and Malin, 1989; Dade and Huppert, 1998) and mass change models (Van Gassen and Cruden, 1989; Hungr and Evans, 1997). Seismic energy may also play a role in promoting mobility and subsequent long runout (Voight *et al.*, 1983; Francis and Self, 1987; Siebe *et al.*, 1992; Glicken, 1998). It should be noted that, while many of these hypotheses may explain certain aspects of long runout avalanches, no one mechanism has been found to universally explain long runout (Legros, 2002).

Though early researchers often attributed increased avalanche mobility to unique mechanisms such as fluid/gas pressures and other fluidising mediums, mechanical explanations have since been accepted as the most likely factors (MacSaveney, 1978; Melosh, 1979, 1986; Davies, 1982; Voight *et al.*, 1983; Schneider and Fisher, 1998). Previous researchers often agree that avalanche motion can best be explained as some form of *plug flow*; a term that implies neither continuum or discontinuum mechanics but simply indicates the basal section of the moving avalanche experiences a different deformational regime than the upper majority of the failure mass (Shreve, 1968a; Johnson, 1978; Erismann, 1979; Davies, 1982; Campbell, 1989; Straub, 1996; Belousov *et al.*, 1999; Reubi and Hernandez, 2002; van Wyk de Vries *et al.*, 2001; Clavero *et al.*, 2002; Davies and MacSaveney, 2002, 2008; Kelfoun and Druitt, 2005; Davies *et al.*, 2006; Kelfoun *et al.*, 2008; Shea and van Wyk de Vries, 2008; Shea *et al.*, 2008). Due to the avalanches' interaction with the basal surface and overburden from the large failure, intense shear develops in a thin basal layer while the 'plug' above remains relatively undisturbed and is free to spread in translation without suffering intense shearing (Strom, 2006; Shea and van Wyk de Vries, 2008). For instance, Francis and Oppenheimer (2004) suggest upwards of 50% of the shear experienced by a moving VDA is concentrated in the bottom 8% of the flow depth. Bulk flow is essentially laminar which may allow retention of original stratigraphic relationships and fragile materials such as jigsaw fractured blocks; common VDA deposit characteristics described in detail below (Reubi and Hernandez, 2000). The upper plug may retain the properties of a brittle material, allowing faulting to develop (Kelfoun *et al.*, 2008; Shea *et al.*, 2008; Shea and van Wyk de Vries, 2008). Bingham plastic rheology is often invoked to describe the plug flow behaviour (Voight *et al.*, 1983; Mimura *et al.*, 1988; Sousa and Voight, 1995; Takarada *et al.*, 1999). Bingham materials are defined by yield strength: they behave as viscoplastic materials below their apparent yield strength and viscous Newtonian fluids above. If shear stress exceeds material strength, the material flows. As avalanche velocity is reduced, the shear stress in this layer falls below the yield strength value and deposition ensues *en masse*. Indeed, yield strength controlled materials have been suggested by several VDA researchers based on field observations of steep lateral and distal margins (see Section 3.3.4).

As avalanche material can generally be represented as a granular material, granular flow theories are also used to explain avalanche motion (Voight *et al.*, 1983; Komorowski *et al.*, 1991; Glicken, 1998; Schneider and Fisher, 1998; Legros *et al.*, 2000; van Wyk de Vries *et al.*, 2001; Legros, 2002; Francis and Oppenheimer, 2004; Pudasaini and Hutter, 2007; Shea and van Wyk de Vries, 2008). For flow to occur in a granular material, interparticle

friction must be reduced through some mechanism. When shear is introduced to a granular medium, in this case by downslope movement, the result is dilation, a defining characteristic of granular materials (Bagnold, 1954; Iverson, 1997; Schneider and Fisher, 1999; Crosta *et al.*, 2001; Pudasaini and Hutter, 2007). Dilation in turn reduces interparticle friction through volume expansion and allows the material to flow. Once flow has been initiated, constituent clasts collide through brief, high energy contacts which expend little energy and create further dispersive normal pressures, thus preserving dilatancy. Though particles frequently lose contact with one another, the material does not completely lose strength, coherence, or its ability to form features such as steep flow fronts and margins (Glicken, 1998). An additional characteristic of granular flows is segregation and reverse grading based on particle size, a phenomenon often observed in VDA deposits (Schneider and Fisher, 1998; Takarada *et al.*, 1999; Reubi and Hernandez, 2000; Bernard *et al.*, 2008; Shea *et al.*, 2008).

Plug flow may develop in a granular material through a *granular temperature* mechanism, a term adopted from the field of chemistry. In granular avalanches, the phenomenon of granular temperature occurs when basal asperities cause increased agitation along the assembly boundary, in this case the basal surface, and, in turn, dispersive normal pressures normal to the direction of movement (downslope) (Campbell, 1989; Iverson 1997). The increased dispersive normal pressures reduce the frictional contact force between constituent particles, thus increasing the ability of the material to flow. Due to overburden pressure, however, the influence of the dispersive normal stresses is increasingly limited vertically upwards from the basal surface; the region of reduced frictional contact force is thus restricted to the basal area of a moving failure body. In this sense two flow regimes are defined; the lower agitated layer by collision particle contacts and an upper layer by Coulomb frictional relationships (Legros, 2002). Deposition occurs as energy is expended through the increasing influence of frictional contacts as the avalanche loses momentum and overburden reduces the influence of dispersive normal pressures (Schneider and Fisher, 1998; Legros, 2002).

Granular flows, particularly those with large grain size distributions such as VDAs, are ultimately very poorly understood. Legros (2002) notes that even simple granular flows, such as small-scale laboratory experiments present inexplicable complexities. For instance Legros (2002) describes the presence of the basal shearing layer and plug flow type mechanisms in some numerical simulations (Cleary and Campbell, 1993; Straub, 1996, 1997) while shearing throughout the avalanche depth and an upwards decreasing density

occurs in others (Drake, 1990; Campbell *et al.*, 1995). This discrepancy is also revealed in VDA literature: Clavero *et al.* (2002) describe a large number of percussion marks on blocks found in the upper layers of the deposit, claiming these features indicate repeated collision, and thus a pervasively sheared granular flow must be ruled out though there is no discussion of a potential collisional granular flow regime (Legros, 2002).

Therefore, and perhaps expectedly, significant debate of avalanche motion mechanisms can thus be found in the literature. For instance, Takarada *et al.* (1999) claim that granular flow mechanisms are inappropriate as many of the brecciated blocks they observed in two Japanese VDA deposits are particularly fragile and would likely be destroyed by associated dispersive normal pressures. These authors subsequently suggest Bingham-type plug flow as the principal VDA flow type. Legros *et al.* (2000), on the other hand, suggest that plug flow models might also be inappropriate as calculations they performed to determine whether all avalanche motion might be expended through basal friction indicate it could not, and therefore energy dissipation throughout the entire depth of the avalanche body may be required for deposition. Clavero *et al.* (2002) note that deformation in the basal layer alone cannot explain the overall spreading of the avalanche body, which does indeed occur. These authors suggest that spreading between material 'domains' with little frictional resistance between them best explains the deposit features observed. On the other hand, reverse grading observed throughout the depth of some large-scale avalanche deposits does suggest shearing throughout the avalanche mass and granular flow similar to that of Campbell *et al.* (1995).

In any case, the generally accepted model for VDA motion is that of a generally undisturbed competent sheet over a highly stressed and potentially mechanically fluidized basal layer, though significant departures from any ideal model should be expected (Kelfoun *et al.*, 2008). What may be laminar plug flow in one area may take on a completely different mechanical character in another due to material heterogeneity and topography, among other complicating influences. Glicken (1998) regards the plug flow model as more of a local phenomenon as a basal shearing layer is not observed continuously throughout the Mount St. Helens VDA deposit. In fact, this observation leads Glicken (1998) to suggest that a basal shearing layer is therefore not necessarily needed to explain the characteristic VDA deposit features described below. Several authors (Drake, 1990; Schneider and Fisher, 1998; Legros, 2002) suggest that the influential mechanisms are likely based on time of emplacement: frictional contacts control the beginning and end of the emplacement while collisional contacts control the main emplacement phase.

Deposition in this case is controlled by plug flow mechanisms which preserves the deposit features subsequently observed.

2.5. Discussion

The current terminology that describes large-scale, catastrophic volcanic edifice collapse has been reviewed in this chapter. Additionally, the many factors that may influence or promote edifice instability have been introduced. The properties of the materials that comprise a volcanic edifice, such as unconsolidated volcaniclastic sediments and hydrothermally altered or weathered rock masses, play a key role in determining the initial stability of a volcanic edifice. These materials also influence how an avalanche might evolve during emplacement and the characteristics of the subsequent deposit; this fact will become clear as the characteristics of specific deposits are discussed in Chapter 4 and material property influences are discussed throughout this thesis (e.g., Chapters 8 and 9). The potential triggering mechanisms introduced here are important for understating why edifices collapse but for the most part are not considered further in this study, which is primarily focused on the events that occur after the onset of instability. However, the potential impacts of triggering mechanisms on emplacement, such as material brecciation and blast effects, will be considered when developing a model to generally describe VDA emplacement behaviour (Section 4.3).

The most common mechanisms typically invoked as agents of avalanche mobility have been introduced, including plug and granular flow theories. It is most likely that true avalanche behaviour is a complex combination of many of these factors that vary spatially and temporally throughout emplacement. While it is beyond the scope of this study to detail and debate the validity of proposed mobility mechanisms, observations relevant to this topic developed here from numerical avalanche simulations will be discussed in later chapters (Chapters 6-9).

Chapter 3 - Major features of volcanic debris avalanche deposits

The objective of this chapter is to introduce and define the principal sedimentary facies and features commonly observed in VDA deposits, as discussed in the literature and review several key factors affecting deposit morphology. The morphology and spatial orientation of these features is important for understanding emplacement mechanics. The characteristics that help to distinguish VDA deposits from similar sedimentary products observed in volcanic settings are also considered.

Key questions:

- What features are commonly observed in VDA deposits?
- What factors might affect emplacement and subsequent deposit morphology?
- How are VDA deposits distinguished from other sedimentary deposits found in volcanic environments?

3.1. Introduction

VDAs are commonly recognised and classified by a general suite of characteristics, including: (1) distinctive sedimentary facies; (2) hummocky topography; (3) longitudinal/transverse ridges (toreva blocks), (4) closed surface depressions, (5) steep marginal and lateral levees, (6) distinct sediment deformation structures, and; (7) source amphitheatres (Siebert, 1984; Francis and Self, 1987; Siebert *et al.*, 1987; Ui, 1989; Ui *et al.*, 2000; Capra *et al.*, 2002). Lobate or fan-like map-scale flow morphologies and the retention of original stratigraphic relationships are also commonly observed (Francis and Wells, 1988; Siebe *et al.*, 1992; Schneider and Fisher, 1998; Clavero *et al.*, 2002). While each of these features are not found at *every* deposit, they are in one form or another recognized at the majority of VDA deposits and give important clues concerning avalanche emplacement mechanics. With the exception of source area characteristics, these features are described here.

VDA deposits are most generally defined as unconsolidated and/or poorly sorted mixtures of brecciated volcaniclastic debris (Voight *et al.*, 1983; Siebert, 1984; Siebert, 1987). The Mount St. Helens deposit, for instance, is described by Voight *et al.* (1983) as heterogeneous with components ranging in size from clay sized particles to blocks over 100 m in maximum dimension. Representative sampling is therefore impractical though

Voight *et al.* (1983) were able to conduct grain size analyses, which showed clay (4%), silt (11%) and sand (42%) with the remainder being pebbles, cobbles and organics though larger-scale material is unrepresented. Similar results are shown by Voight *et al.* (1981), Siebert *et al.* (1987), Glicken (1998) and Belousov *et al.* (1999). Grain size distributions are typically normally distributed and mostly bimodal, indicating derivation from a single source (Glicken, 1998). Each of these descriptions conveys the general suggestion that VDA deposits consist of a large variation of materials with a wide range of mechanical properties.

In order to interpret the chaotic mixture of material observed in VDA deposits, previous authors have simplified their descriptions by recording the debris elements observed into either sedimentary facies or descriptive classification schemes (Schneider and Fisher, 1998). The former approach generally distinguishes between end-member block and matrix facies and was developed by Crandell *et al.* (1984), Ui and Glicken (1986), Ui (1989) and Glicken (1991) following the ideas of Mimura *et al.* (1971). This approach has become the generally accepted terminology in the literature. Palmer *et al.* (1991), however, use a slightly different scheme which is based upon the major components observed in a particular outcrop, an approach also used by several later authors (Endo *et al.* [1989], Schneider and Fisher [1998], Richards and Villeneuve [2001] and Alloway *et al.* [2005], for instance). An advantage of the Palmer (1991) scheme is that lithofacies are generally mappable on an outcrop scale whereas in the sedimentary description scheme of Crandell *et al.* (1984) outcrops may contain both the block and matrix facies (Glicken, 1991). In keeping with the most common descriptions used the literature, the sedimentary facies description scheme will be used for the remainder of this paper and is described in further detail below.

3.2. Sedimentary facies descriptions

3.2.1. Block facies

The block facies is described as consisting entirely of debris avalanche blocks tens to hundreds of metres in maximum dimension, often brecciated, slightly deformed or elongated and/or preserving original stratigraphy or volcanic structures (Glicken, 1982, 1991, 1998; Ui, 1983; Crandell *et al.*, 1984; Ui *et al.*, 1986; Ui, 1989; Siebe *et al.*, 1992; Belousov *et al.*, 1999; Takarada *et al.*, 1999; Reubi and Hernandez, 2000; Alloway *et al.*, 2005). A *debris avalanche block* itself, or simply *block*, is defined as a coherent, poorly

consolidated, or possibly shattered piece of the volcano that was transported to its place of deposition relatively intact (Glicken, 1991). The terms *megablock* or *megaclast* may also be used to refer to blocks of extraordinarily large dimension (Ui, 1983; Palmer *et al.*, 1991). Individual block fragments are typically subangular to angular, indicating a lack of abrasion, though roundness tends to increase with distance (Ui and Glicken, 1986; Ui *et al.*, 1986; Ui, 1989; Glicken, 1991, 1998; Schneider and Fisher, 1998). In general, the size and relative percentage of blocks decreases distally and laterally in a deposit and blocks of entrained material are commonly observed in distal sections (Ui, 1983; Siebert, 1984; Ui and Glicken, 1986; Ui *et al.*, 1986; Glicken, 1998; Palmer *et al.*, 1991; McGuire, 1996; Schneider and Fisher, 1998; Takarada *et al.*, 1999; Clavero *et al.*, 2002). Blocks are commonly more prevalent on the deposit surface, creating a reverse grading characteristic of granular flows (Reubi and Hernandez, 2000; Pudasaini and Hutter, 2007; Shea *et al.*, 2008; Bernard *et al.*, 2008). Tilting, faulting and rotation of large blocks may occur though they are generally thought to remain right side up during emplacement (Glicken, 1982, 1989; Siebert, 1984; Ui and Glicken, 1986; Crandell, 1989; Reubi and Hernandez, 2000).

It is often possible to visually reconstruct shattered blocks across fractures, termed the *three-dimensional jigsaw puzzle effect* by Shreve (1968a) (Figure 2; Ui, 1983; Siebert, 1984). Though shattering may be prevalent, full dispersion from the parent block does not necessarily have to occur (Siebe *et al.*, 1992; Glicken, 1998). Fractures are distinctive from those created by cooling (lava flow, chilled margins, dikes) in that they are not smooth in texture, typically remaining closed but possibly expanded (Ui, 1989; Ui *et al.*, 2000). Macroscopic jigsaw fracture patterns are also mimicked in constituent crystals observed at the microscopic level (Glicken, 1991; Komorowski *et al.*, 1991; Schneider and Fisher, 1998; Belousov *et al.*1999; Reubi and Hernandez, 2000).

Figure 2 – Small-scale jigsaw fractured block showing an evolved state of disaggregation as matrix material has been injected into the fractures. Photo taken at the Popocatepetl VDA deposit, central Mexico. Pencil for scale (14 cm in length).

Fragmentation is generally thought to occur along pre-existing discontinuities. A high density of fractures could be the result of pre-eruption deformation and/or brecciation; pre-deposition in any case (Glicken, 1991, 1998; Schneider and Fisher, 1998). An additional mechanism suggested for the formation of jigsaw fractures is *rarefaction*, a phenomenon where rough topography results in the repeated propagation of waves of compressional stress where fracture occurs in the instant after brief but intense collisions (Glicken, 1991; Komorowski *et al.*, 1991; Reubi and Hernandez, 2000). Neighbouring constituents remain in contact and preserve their relative position, including stratigraphic relationships (Glicken, 1991). Fracture formation could also be caused by locally dominant compressional stresses or intense shear during the initial stages of emplacement (Ui, 1989; Reubi and Hernandez, 2000).

Early VDA literature often notes that blocks are progressively more fragmented with distance, suggesting that intense shearing breaks smaller blocks into fragments (Crandell *et al.*, 1984; Siebert, 1984). Several later studies, however, indicate that there is no correlation between the degree of jigsaw fracturing with distance, suggesting they are *not* a

result of emplacement processes (Ui *et al.*, 1983; Reubi and Hernandez, 2000). An increase in joint *width* with distance, however, is seen with distance at both Mount Shasta and Mt. Egmont deposits by Ui and Glicken (1986) and Ui *et al.* (1986), indicating a gradual loosening of the blocks and expansion of the joints during emplacement, perhaps what early authors referred have to as 'fragmentation' (Ui *et al.*, 1986). Similarly, Takarada *et al.* (1999) observe that while numerous jigsaw fractures are observed in proximal blocks at Japan's Iwasegawa VDA deposit, few are found distally, indicating progressive separation and dispersion.

3.2.2. Matrix facies

The second component of the sedimentary facies description is the matrix facies which is best described as an unconsolidated, unstratified, and unsorted mixture of all rock types with components ranging in size from microns to metres (Figure 3; Crandell *et al.*, 1984; Crandell, 1989; Ui, 1989; Glicken, 1998). For instance, grain size analyses of the matrix facies at Mount Shasta resulted in 54% sand, 20% silt, and 12% clay with the remainder being material coarser than sand (Crandell, 1989). Textural studies performed by Glicken (1998) on the Mount St. Helens VDA deposit indicate that mixing of disaggregated blocks during emplacement creates the matrix facies, though it is likely not the only process. The fine grained portion of the matrix facies can be derived from a number several sources: pre-failure volcaniclastic material, basement sediments, pulverized rock, silt, and sand from larger source material, and basin sediments entrained during emplacement (Crandell *et al.,* 1984; Crandell, 1989; Palmer *et al.*, 1991). Soil, stream gravels and wood are also commonly found (Ui, 1989). These entrained materials typically increase in proportion with distance while the percentage of source-derived clasts decreases (Crandell, 1989). In some cases, entrained materials make up a significant proportion of VDA deposits, up to 70% of the matrix material (e.g., Chimborazo, Bernard *et al*. [2008]). Matrix materials are typically better mixed and more well-sorted with distance (Takarada *et al.*, 1999). Source-derived clasts are generally slightly abraded and angular to subangular while those entrained are of a variable roundness (Ui and Glicken, 1986; Crandell, 1989; Ui, 1989).

Figure 3 – Matrix material of the Popocatepetl VDA deposit displaying a generally fine-grained texture with chaotic assortment of angular blocks of various sizes. Pencil for scale (14 cm in length).

The matrix facies is not present at all VDA deposits. Siebe *et al.* (1992), for instance, note there is very little matrix facies present in the Jocotitlan VDA deposit, what little there is being sand-size (Siebe *et al.*, 1992). This observation leads Siebe *et al.* (1992) to suggest the term matrix facies does not even apply to this particular deposit. Additionally, no entrained material is observed in this deposit (Siebe *et al.*, 1992). Clavero *et al.* (2002) describe a similar lack of fine grained matrix material at the Parinacota VDA deposit.

3.2.3. Relationships between block and matrix facies

Important indications of emplacement kinematics can be observed by considering the spatial relationship of the block and matrix facies. The matrix facies is typically found in distal lobes and surrounding and/or penetrating open joints in the block facies, indicating its relatively fluid and mobile nature (Crandell *et al.*, 1984; Crandell, 1989; Belousov *et al.*, 1999). Crandell (1989) suggests some blocks are carried completely submerged in the matrix while others may partially 'float' on top. Matrix facies veneers found on some hummocks and blocks are suggested to have been left as a lag deposit as the remainder of the matrix drained away (Crandell *et al.*, 1984; Ui and Glicken, 1986; Ui *et al.*, 1986;

Crandell, 1989; Palmer *et al.*, 1991). As the size and number of blocks in a deposit tends to decrease marginally and distally, the matrix proportion increases, indicating progressive block disaggregation and finer-grained debris entrainment (Ui, 1983; Siebert, 1984; Ui and Glicken, 1986; Glicken, 1998; Palmer *et al.*, 1991; McGuire, 1996; Schneider and Fisher, 1998; Takarada *et al.*, 1999; Clavero *et al.*, 2002; Alloway *et al.*, 2005).

3.3. Additional common features

3.3.1. Hummocks

Hummocks are described as mounds or hills scattered on the surface of a deposit, often extraordinarily symmetrical and/or conical in form and circular in map view (Figure 4). Shapes may also be varied and irregular, elliptical, oval or linear (Clavero et al, 2002; Alloway *et al.*, 2005). Hummock size may be hundreds of metres high and kilometres in maximum dimension. Steep normal faulting of hummock margins is commonly observed and suggested to have occurred as the mass settled after emplacement (Voight *et al.*, 1983; Crandell *et al.*, 1984; Ui and Glicken, 1986; Crandell, 1989). The number of hummocks in a particular deposit may range into the thousands: Siebert (1984) notes 3,648 hummocks at Indonesia's Galunggung deposit, over 2,000 hummocks at Indonesia's Raung deposit, and 3,000 mounds at New Zealand's Mt. Egmont Pungarahu deposit. Over 2,900 hummocks were mapped at Mombacho's El Crater deposit by Shea *et al.* (2008).

A B

Figure 4 – (A) Hummocks scattered over the surface of the Tata Sabaya VDA deposit, Bolivia. Image generated via Google Earth©; (B) Conical hummock located in the proximal section of the Mount Meru VDA deposit, Tanzania, height approximately 75 m.

Internally, hummocks may be structurally complex (Siebert, 1984). They can be composed of unconsolidated or poorly consolidated material with enough cohesion to

produce the conical morphology upon deposition, clast supported or cored by one or more blocks, which may be the controlling factor on overall morphology (Crandell *et al.*, 1984; Siebert, 1984; Crandell, 1989; Ui, 1989; Glicken, 1991). Simple conical hummocks are generally composed of one rock type and symmetric in form whereas compound hummocks may be formed of several rock types and can form ridges or hummock 'trains' hundreds of metres long. Hummocks may also be composed of unconsolidated volcaniclastic deposits often found in their original stratigraphic succession or with volcaniclastic deposits carried intact (Crandell *et al.* 1984; Crandell, 1989).

Hummocks are often found in clusters and tend to be concentrated near the axis of a deposit with density decreasing towards the margins (Siebert, 1984; Siebe *et al.*, 1992). Hummocks are generally observed to decrease in number and size with distance (Crandell *et al.*, 1984; Siebert, 1984; Ui and Glicken, 1986; Crandell, 1989; Ui, 1989; Siebe *et al.*, 1992; Clavero *et al.*, 2004; Alloway *et al.*, 2005; Shea *et al.*, 2008). Overall, smaller hummocks are more common than larger ones, suggesting only a relatively small volume of homogeneous material may be present in the original failure (Glicken, 1998). No *overall* hummock alignment trend is observed, though the long axis of linear hummocks or hummock trains often points in the direction of flow, radially away from the source (Glicken, 1982; Siebert, 1984; Ui, 1989; Glicken, 1998; Ui *et al.*, 2000; Shea *et al.*, 2008). At the Popocatepetl VDA deposit, for instance, hummocks are elongate parallel to flow direction except for the largest proximal ones, which are aligned perpendicular to flow direction (see toreva block description below; Robin and Boudal, 1987).

Based upon observation of the Mount St. Helens VDA deposit, three types of hummocks are proposed by Glicken (1991, 1998). The first type (A-type) is composed exclusively of block facies with no matrix. This type of hummock is located in proximal sections and likely represents toreva block structures described below. The second type of hummock (B-type) is predominantly composed of matrix facies but contains small blocks; overall size is much smaller than A-type hummocks. The third type (C-type) consists of isolated blocks completely surrounded by matrix facies.

The mechanisms whereby hummocks develop are debated in the literature. In general, hummocks are believed to form due to the heterogeneity of VDA materials; some material lends itself to early deposition (e.g., large blocks) while other material continues to flow (saturated matrix material) (Siebert, 1984; Glicken, 1991; Shea *et al.*, 2008). At Nicaragua's Mombacho VDA deposit, for instance, hummock forms are clearly a function

of the materials they are composed of: steep hummocks being formed by coherent lava blocks and low, broad hummocks of matrix-rich units (Shea *et al.*, 2008). Hummocks of matrix material are generally smaller in overall dimension. Glicken (1991, 1998) suggests three common hummock forming mechanisms. The first mechanism is a horst and graben process where original stratigraphies are preserved intact but faulted during extension (Glicken, 1998). Glicken's A-type hummocks are likely formed in this fashion. The second mechanism is a simple preservation of source edifice topography with stratigraphy parallel to the hummock surface (Glicken, 1991, 1998). In the more distal deposit sections this mechanism forms more C-type hummocks cored by a single block (Glicken, 1991, 1998). The third mechanism involves the deposition of material through increased basal/lateral shear and is divided into two categories, the first being hummocks composed of material piled-up due to increased basal shear as more mobile material moves around it. The second category consists of a pile-up of material in the distal regions as an avalanche decelerates, often with random orientations (Glicken, 1991, 1998). A-type hummocks generally consist of one or two blocks formed through the first or third mechanism; as blocks break, increasingly smaller hummocks are formed. In the case of the Mount St. Helens VDA deposit from which these distinctions were derived, B-type hummocks are found only in the distal section of the deposit.

Strom (2006) suggests the presence of hummocks indicates intense tensile strain in the upper, central section of the avalanche body. The general hummock formation process is envisioned by Strom (2006) as follows: overthrusting creates increased thickness and subsequent crushing and shattering of the lower sections of the avalanche, which develops a more fluid-like behaviour and thins due to the weight of the overburden. An abrupt change in mechanical properties subsequently occurs between the lower (shattered) and upper (blocky) sections. Thinning and stretching of the lower zones creates tension in the upper part of the failure and hummocks are subsequently formed.

An additional hummock-forming mechanism is suggested by Ponomareva *et al.* (1998) and Belousov *et al.* (1999) who suggest post-emplacement breakdown of frozen or unstable superficial blocks as the reason for extraordinarily conical shape. Each of these authors cites time-series observations after the 1964 Shiveluch VDA as evidence of this process.

Elongate hummock ridges parallel to the direction of flow are observed at a number of VDA deposits: Socompa (Francis and Wells, 1988; Kelfoun *et al.*, 2008), Ontake (Endo *et al.*, 1989), Shiveluch (Ponomareva *et al.*, 1998; Belousov *et al.*, 1999). These features may

take the place of hummocky topography completely in some cases, representing a situation where hummocks do not develop due to inherently weak avalanche material strengths or high emplacement velocities, such as at the Aucanquilcha, Llullaillaco, San Pedro and Lastarria VDA deposits (Naranjo and Francis, 1987; Francis and Wells, 1988).

3.3.2. Toreva blocks

Reiche (1938) first defined *toreva* block structures when describing the collapse and emplacement of large sections of mesa structures which remained relatively intact but tilted after deposition, typically backwards towards the source. Only the extreme lowest sections of the block are deformed in any way, if at all (Reiche, 1938; Anders *et al.*, 2000). This term has subsequently been adopted to describe the emplacement of large block structures in VDA deposits (see Francis and Wells [1988], for instance). These blocks are typically of very large dimension, retain original stratigraphic relationships and volcanic structures with little or no deformation and are often found back rotated in proximal sections of VDA deposits (Figure 5; Francis *et al.*, 1985; Belousov *et al.*, 1999; Ui *et al.*, 2000; Clavero *et al.*, 2002). These features can be so large, in fact, that they may have on occasion been misinterpreted as small volcanoes themselves (Crandell, 1984; Ponomareva *et al.*, 2006).

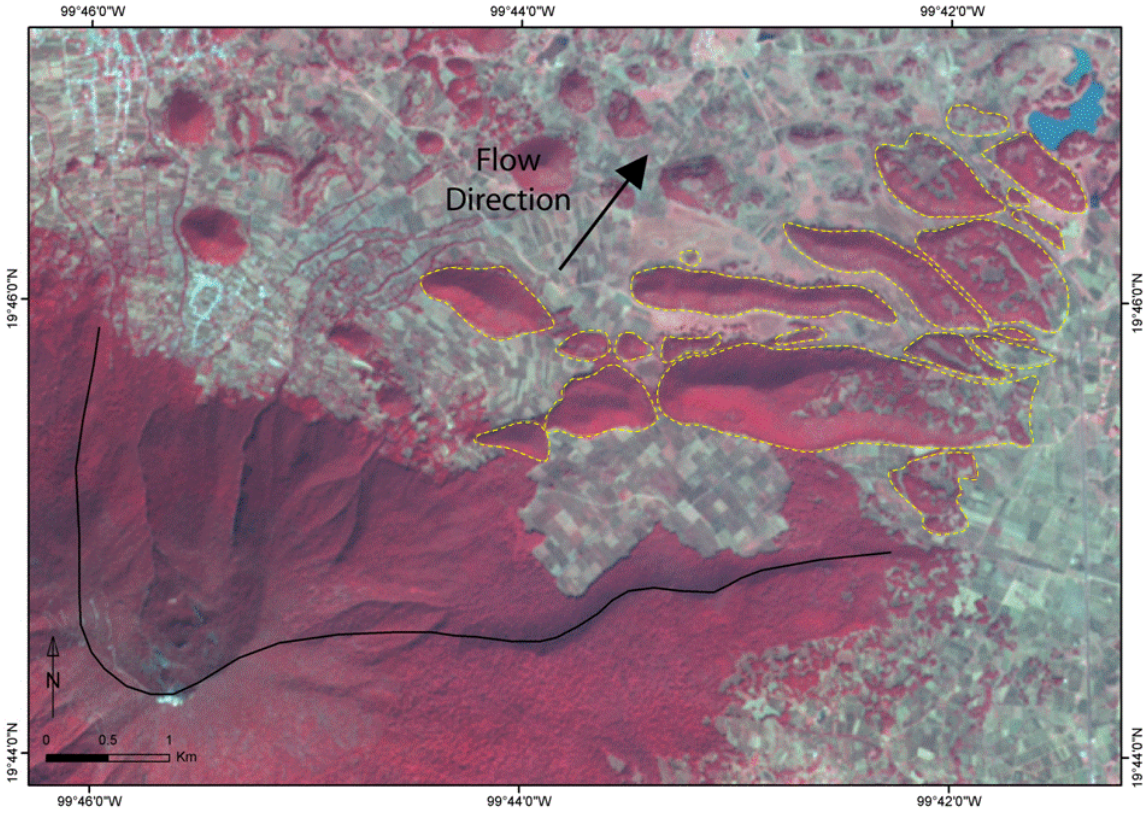

Figure 5 – Toreva block structures at the Jocotitlan VDA deposit, central Mexico (yellow outline). Black line denotes the likely rim of collapse scar.

In general, there is no clear distinction between torevas or hummocks; torevas may be considered to be hummocks. However, torevas usually indicate an extraordinarily large scale and are clearly intact blocks of the original edifice which have slid into place relatively undisturbed at the foot of the source edifice. In this respect, A-type hummocks defined by Glicken (1991, 1998) can be considered toreva blocks. They are typically orientated with their long axes perpendicular to the principal direction of avalanche flow and emplacement is clearly characterized by horst and graben extensional mechanics. On the other hand, hummocks may be composed of a range of materials covering a large size range and the entire surface a given deposit and may be formed by a number of processes.

Torevas can travel a considerable distance while remaining relatively intact. At Mount Shasta, for instance, toreva blocks have moved further than 20 km without being severely disrupted; a phenomenon that Crandell *et al.* (1984) and Crandell (1989) suggests is a result of their high kinetic energy. The relative proximity of many of these blocks to the source edifice in most cases, however, suggests they had *less* kinetic energy than the remainder of the failure (Crandell, 1989). The precise timing of toreva emplacement is debated: during the early (Francis and Self, 1987), main (van Wyk de Vries *et al.*, 2001) or latter stages of emplacement (Wadge *et al.*, 1995).

van Wyk de Vries *et al*. (2001) suggest the toreva blocks at Socompa have three basic morphologies. The first consists of intact blocks formed with minimal disruption formed through short, simple sliding, equivalent to the A-type hummocks of Glicken (1991, 1998). The second morphology consists of blocks that have been progressively more faulted away from the volcano and broken into smaller pieces, which implies the blocks were emplaced *during* the development of the avalanche, rather than before or afterwards (van Wyk de Vries *et al.*, 2001). The third morphology is composed of blocks with sharp, arcuate and eroded margins and does not display progressive faulting but a simple geometry with smooth, curved margin slopes (van Wyk de Vries *et al.*, 2001). This morphology is suggested to have formed from deflation of the proximal avalanche as substrata material was ejected out from under the blocks as they slid into place (van Wyk de Vries *et al.*, 2001).

3.3.3. Closed Depressions

Closed depressions, often remarkably circular in plan, are observed at a number of VDA deposits: Mount St. Helens (Voight *et al.*, 1983; Glicken, 1998), Mount Shasta (Crandell, 1989), Jocotitlan (Siebe *et al.*, 1992), Shiveluch (Belousov *et al.* 1999), Parinacota (Clavero *et al.*, 2002), and Mombacho (Shea *et al.*, 2008). They are typically found in inter-hummock areas and can be hundreds of metres across and tens of metres deep (Voight *et al.*, 1983; Glicken, 1998). Several mechanisms are suggested to have formed these features. Voight *et al.* (1983) originally proposed that graben formation, melting ice, or high velocity releases of steam caused these features. Crandell (1989) suggests formation through differential compaction, ice kettles, or the shifting of blocks. Glicken (1998) hypothesizes that the depression features were formed within hours or days of emplacement by loose or block material collapsing into void space, suggesting the voids were likely not created by melting ice but mostly from dilation and break-up of the avalanche material.

3.3.4. Levees and margins

Steep distal (terminal) levees and lateral margins up to tens of metres high are additional distinguishing features of VDA deposits (Figure 6; Ui, 1983; Voight *et al.*, 1983; Francis *et al.*, 1985; Robin and Boudal, 1987; Ui, 1989; Siebe *et al.*, 1992; McGuire, 1996). The steep morphology observed suggests an *en masse* freezing of high yield strength material upon deposition (Robin and Boudal, 1987; Belousov *et al.*, 1999; Richards and Villeneuve,

2001). Ui (1983) notes that lateral levee interiors are a mixture of matrix material though imbricate structures of debris separated by thrust faults have been recorded, a pattern likely the result of deposition of material with enough shear strength to remain intact along narrow zones (Siebe *et al.*, 1992; Glicken, 1998). This pattern may also reflect lateral compressive deformation from pulses of the moving avalanche (Voight *et al.*, 1983).

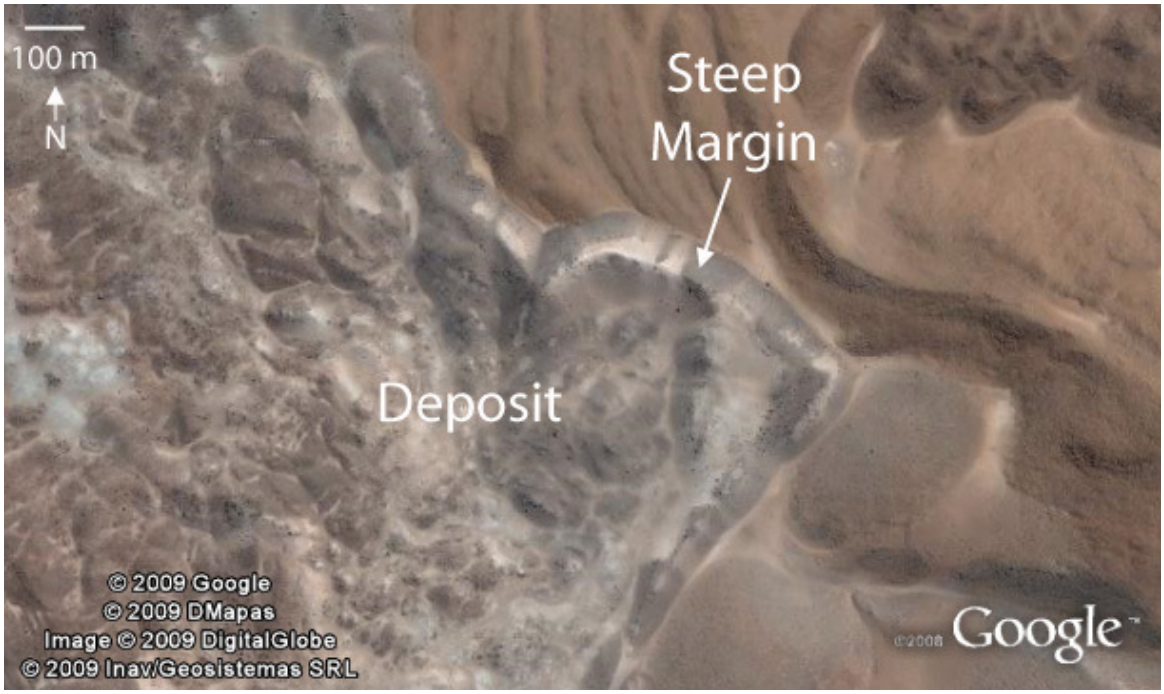

Figure 6 – Steep lateral margin of the Socompa VDA deposit. Figure generated via Google Earth©. Approximate location of the margin pictured here noted in Figure 18.

3.3.5. Deformation structures

An array of deformation structures are observed at VDA deposits including boudinage, folding, normal and thrust faulting, layer mixing, and injection structures such as clastic dikes. Many of these structures indicate dynamic conditions occurring during emplacement and/or the moments immediately preceding deposition. While the geometry and dimensions of these features are highly variable, similar derivations of particular structures can be collectively observed in VDA deposits, indicating a similarity in emplacement kinematics. For instance, a significant proportion of deformation structures are found in the basal region of VDA deposits or adjacent to pre-existing topographic features in the deposition basin (e.g., Takarada *et al.*, 1999; Legros *et al.*, 2000; Bernard *et al.*, 2008). As an example, lateral fault displacement and conjugate thrust structures observed in the Kaida VDA deposit in Japan suggest the avalanche acted as a rigid body where structure was created through impact of the avalanche with curved valleys it

encountered (Takarada *et al.*, 1999). Flame structures and clastic dikes, where typically finer-grained, fluidized material has penetrated upwards into more competent material are also commonly observed, indicating a distinct contrast in material behaviour between the upper and lower layers (Figure 7; Belousov *et al.*, 1999; Schneider and Fisher, 1999; Legros *et al.*, 2000; Clavero *et al.*, 2002; Bernard *et al.*, 2008). Intense deformation of underlying basin sediments is also noted by numerous authors (Siebe *et al.*, 1992; Belousov *et al.*, 1999; van Wyk de Vries *et al.*, 2001; Ponomareva *et al.*, 2006).

Figure 7 – Flame injection structure at a roadcut within the Popocatepetl VDA deposit. Texture of the flame structure is finer grained as compared to the coarse material above and adjacent. Scale of structure approximately 10 m.

Thin (≈ 1 m), typically fine-grained and featureless basal layers are also commonly observed in VDA deposits (Siebert, 1984; Francis and Self, 1987; Robin and Boudal, 1987; Crandell, 1989; Sousa and Voight, 1995; McGuire, 1996; Schneider and Fisher, 1998; Belousov *et al.*, 1999; Takarada *et al.*, 1999; Ui *et al.*, 2000; van Wyk de Vries *et al.*, 2001; Clavero *et al.*, 2002; Strom, 2006; Bernard *et al.*, 2008; Kelfoun *et al.*, 2008; Shea *et al.*, 2008). The fabric of these basal layers suggests high shear and a potentially turbulent behaviour and support the plug flow hypotheses introduced in Section 2.4. Clastic dikes

derived from this material are often seen injecting upwards into fractures in the more competent plug material above (Legros *et al.*, 2000; Bernard *et al.*, 2008). Furthermore, inverse grading of clasts in this layer has also been described, again suggesting turbulent conditions (Schneider and Fisher, 1998; Anders *et al.*, 2000; Takarada *et al.,* 1999). While intense shearing is often assumed to be the cause of the basal layer, Strom (2006) suggests intense crushing from overburden may help facilitate formation.

3.4. Major factors affecting emplacement and deposit morphology

As discussed in Section 2.2, Ui (1983) introduced the idea that material properties may have a significant influence on emplacement behaviour and resulting deposit morphology. This idea will be explored throughout later chapters, but there are a number of other factors which can be considered important influences on emplacement behaviour; namely the presence of significant volumes of water and topographic influences. These factors are discussed here.

3.4.1. The role of water

In general, VDAs are considered to be relatively dry during formation but can assume fluid flow properties through water acquisition and the separation of avalanche materials into fluid-saturated and unsaturated portions (Siebert, 1984; Legros, 2006). There are many sources from which a VDA can obtain water including meteoric or surface water, snow and ice (glaciers), subsurface aquifer water and water present within a hydrothermal system (Crandell, 1989; Palmer *et al.*, 1991). Additionally, saturated surface sediments, which may be present in the original failure or entrained during emplacement, may contain significant amounts of water (Endo *et al.*, 1989).

VDAs are mostly considered to be granular flows with associated dispersive forces; a small part of this lift force is credited to fluids and gases (Voight *et al.*, 1983). Though water and gas may play an important role in emplacement dynamics, pervasive fluidisation is not possible in materials with large grain size distributions (poor sorting) such as VDAs and therefore the mechanical role of water may be limited (Voight *et al.*, 1983; Crandell, 1989; Glicken, 1998; Clavero *et al.*, 2002; Kelfoun and Druitt, 2005). Preservation of delicate surface features and original stratigraphy is proof of this incomplete fluidisation. Also, if VDAs behave as granular mass flows, then inertial collisions of particles are much more important than surface tension created by interstitial water (Schneider and Fisher,

1998). Accordingly, a 'wet' avalanche may be no more mobile than a 'dry' avalanche. For instance, the role of water is not particularly evident in most of the VDAs located in the arid central Andes though they typically possess runouts to great distances (Francis and Wells, 1988; Francis, 1994). A wet VDA, however, may have a much greater potential of developing into a lahar which could extend to great distances instead of stopping abruptly (Crandell, 1989; Kerle and van Wyk de Vries, 2001). Thus, the true influence of water on VDA emplacement dynamics and mobility is debated.

The avalanche material at the most recent VDA example, Mount St. Helens, is not thought to have been entirely saturated during emplacement though the pre-failure edifice contained water (Voight *et al.*, 1983). This failure volume is thought to have contained 15% water by volume, 20% of this was removed by subsequent lahars, which were themselves 35-50% water (Glicken, 1998). The temperature of the water in the VDA was approximately near its boiling point due to its origin deep within the edifice and therefore steam most likely occupied a significant volume of the pore space (Voight *et al.*, 1981; Voight *et al.*, 1983).

3.4.2. Topographic influence

Many observations suggest VDA deposit morphology and internal features are heavily influenced by the topography the avalanche may encounter during emplacement, which may include isolated hills or ridges within the runout basin or topographic highs surrounding the emplacement basin or one or more sides. For instance, Francis and Wells (1988) describe a relative lack of hummocky topography at a number of highly confined or channelled deposits in South America as the matrix facies is not able to easily drain away from grounded hummock features to leave them exposed. The term *confined* herby refers to scenarios where the emplacement basin is surrounded on all sides by relatively high topography which may be parallel or possibly converging, particularly in the distal reaches of the basin relative to the source edifice.

The influence of topographic confinement was closely considered by Palmer *et al.* (1991). In the New Zealand VDA deposits studied by these authors, large failures appear to be less affected by topography than smaller events and tend to spread out in fan-shaped sheets on relatively flat coastal plains (Palmer *et al.*, 1991). Concentric, multidirectional lithofacies are commonly observed in these deposits where distinct lobes of coarser block material are surrounded both laterally and distally by finer-grained deposits. This type of lithologic

separation is also observed at Mount Shasta though the clast-rich (i.e., block) facies is not large enough to completely fill the valley, allowing the matrix material to drain away (Palmer *et al.*, 1991). Distal channelization of matrix dominated material occurs in each of these cases. Palmer *et al.* (1991) suggest that this radial type of spreading produces distinctly different deposits than do VDAs which have been confined to valleys. Additionally, hummock density decreases towards deposit margins in unconfined VDAs (Siebert, 1984).

Joint spacing measurements by Ui and Glicken (1986) show that gradual loosening of blocks with distance is not as apparent at Mount Shasta, which was deposited in a relatively confined basin as compared to New Zealand's Pungarehu deposit, deposited onto an unconfined and relatively flat coastal plain. This fact suggests the basin into which the Mount Shasta VDA was emplaced may have limited the opening of jigsaw fractured blocks to some degree (Ui and Glicken, 1986). Additionally, highly deformed or elongated blocks are commonly observed in the distal parts of the Pungarehu deposit but rare at Mount Shasta, likely reflecting the lateral spreading capability of the Pungarehu VDA (Ui and Glicken, 1986). Also, hummocks are also relatively spread out at Mt. Egmont but closely spaced at Mount Shasta (Ui and Glicken, 1986).

Thus, block collisions and deformation can be considered to be a function of topographic confinement. In general, confined VDAs tend to have smaller blocks and more matrix facies than do unconfined VDAs (Takarada *et al.*, 1999). For instance, at Japan's unconfined Zenkoji VDA, matrix proportions are 0-5% proximally and maximum 20% distally but 35-70% proximally and 80-95% distally at the confined Iwasegawa and Kaida VDA deposits (Takarada *et al.*, 1999). A similar observation is made by Shea *et al.* (2008) at the Mombacho VDA deposits in Nicaragua where a lack of jigsaw fractured blocks in the each of the deposits emplaced on smooth topography suggests blocks were not in violent contact as they would have been if confined by topography. In considering the Mombacho deposits further, structures typically created in compressional stress regimes, such as thrust faults and clastic dikes, are not observed in either deposit as pure extension is envisioned for these cases (Shea *et al.*, 2008). Bernard *et al*. (2008) note that deformation structures, particularly near the deposit base, increase near topographic features at Ecuador's Chimborazo VDA deposit. Bernard *et al.* (2008) also note that the shape, aerial distribution and orientation of hummocks at Chimborazo correlates with confinement imposed by topography, the deposit topography being smoother on more uniform terrain. These observations lead Bernard *et al.* (2008) to suggest hummocks are

mainly produced as the avalanche mass passes over or next to a topographic irregularity; deposit structures are lost or diminish as flow progresses away from the points.

3.5. Distinction from similar deposits

As edifice collapse often occurs in conjunction with complex magmatic or phreatic activity, VDA deposits may often be found closely associated with lahar, pyroclastic flow and surge, ashfall, or pumiceous airfall deposits (Figure 8). This is particularly true if flank failure has triggered decompression of a magma body (Bezymianny-type) (McGuire, 1996). Therefore, VDA deposits are not typically straightforward mixtures of source blocks and matrix and can be complex records of a series of interrelated events. Additionally, the association of materials with varying properties may influence the emplacement rheology of an avalanche (Ui, 1983; Reubi and Hernandez, 2000).

Figure 8 – View of roadcut through the Popocatepetl VDA deposit highlighting the close relationship between the principal collapse and latter events, which may or may not be related to the initial failure. Road running perpendicular to the principal direction of emplacement, which is right to left. Notice lorry for scale.

Lahar generally refers to a flowing mixture of rock debris and water, similar to a debris flow, but specific to volcanic settings (Palmer *et al.*, 1991). A large volume of water is not

necessary for the lahar formation, which may develop from the transformation of local water soaked portions of the failure, slumping and flowing of saturated portions soon after emplacement and/or through breakout of dammed fluids (Voight *et al.*, 1983; Schuster and Crandell, 1984; Siebert *et al.*, 1987; Glicken, 1991; McGuire, 1996, 2003; Kerle and van Wyk de Vries, 2001). Capra *et al.* (2002) adds failure within soil, liquefaction, and internal vibrational energy as additional lahar generating mechanisms. The texture of lahar deposits is similar to that of the VDA matrix facies but typically does not possess a block facies (Ui, 1989). Topography is generally flatter than VDA deposit topography, though discrete large boulders may be present on the surface (Figure 9; Ui, 1989). Steep lateral margins or internal structure are generally not observed and percussion marks and scratches may be present on some clasts (Ui, 1989). Additionally, the amount of entrained material is typically larger and mixing more complete in lahar deposits; VDA deposits are much better sorted and finer-grained than lahar deposits (Siebert, 1984; Ui, 1989; Glicken, 1998).

Figure 9 – Flat, generally featureless morphology of the recent lahar deposit in the Belham Valley, Montserrat. Notice small-scale, rounded blocks found on the surface of the deposits. Emplacement direction is left to right.

In relation to pyroclastic flow deposits, VDA deposits are generally more poorly sorted and coarser grained (Siebert, 1984; Glicken, 1998; Belousov *et al.*, 1999). Pyroclastic flow

deposits typically undulate topographically in a more regular fashion than VDA deposits and steep lateral or distal slopes are uncommon (Ui, 1989). Channelled surface patterns may also be present (Ui, 1989). An abundance of juvenile material is typically associated with pyroclastic flows and they normally do not contain internal grading structures (Ui, 1989). Surface blocks may show frictional features such as abrasion marks as a result of tumbling and sliding (Clavero *et al.*, 2002).

Glacial moraines are additional sedimentary deposits which may often be difficult to distinguish from VDA deposits as topographically they may be very similar (Ui, 1989). In fact, the VDA deposit at Mount Shasta was originally interpreted as glacial moraine sediments (Crandell, 1989). Both topographies possess hummocky topography but fractured blocks are not present in glacial deposits (Ui, 1989). Furthermore, striations and grooves are typically present on the surface of larger clasts in glacial moraine deposits, which may also be faceted and/or polished. No internal structure is generally present in glacial moraine deposits (Ui, 1989).

3.6. Discussion

The sedimentary facies and macroscopic features that are most commonly observed in VDA deposits have been identified and discussed above. These features give important clues on the general behaviour of VDAs during emplacement. The block and matrix facies are the most commonly observed sedimentary facies; the spatial relationship of these facies to each other throughout the deposit is a key indicator of emplacement mechanics. For instance, the simultaneous decrease in the block component and increase in matrix material with distance suggests a progressive deposition, breakdown of original failure material and increased basal sediment entrainment. Entrained materials, which may potentially be saturated and relatively fine-grained, often make up a significant proportion of the matrix material. The incorporation of this type of material may have a significant effect on the emplacement behaviour of a VDA. For instance, large amounts of relatively ductile basement sediments included in the VDA at Socompa are thought to have substantially increased the mobility of this avalanche, leading to a relatively fluid-like spreading behaviour over the full area of its emplacement basin (see Section 4.2.3). Additionally, incorporation of highly saturated basin materials or large proportion of water bodies may lead to the development of highly mobile downstream lahars, such as that which occurred at Mount St. Helens in 1980 (see Section 4.2.1). Analysis of the block facies shows distinct fracture patterns (jigsaw) that suggest the majority of block fracture occurs upon

failure or early in the emplacement process; relatively little fragmentation and fracture takes place as the blocks are transported though disaggregation of fractured blocks occurs. The preservation of these blocks also implies that VDA motion is relatively gentle and organized after an initial stage of disorder. Commonly observed deposit features include hummocks and toreva blocks, closed depressions, steep distal and lateral margins and deformation features. Hummocks can be formed by a number of processes but generally result from heterogeneity in the properties of the failure material. The timing of hummock formation is debated (i.e., upon deposition or by post-emplacement erosion) (Palmer *et al.*, 1991; Siebe *et al.*, 1992; Belousov *et al.*, 1999; Clavero *et al.*, 2002). Alternatively, Voight *et al.* (1983) suggest that hummock forms develop early in emplacement with only relatively minor morphological changes occurring subsequently. Toreva blocks are large blocks derived from the source edifice, which have often travelled great distances relatively undisturbed, indicating ordered extensional motion and high kinetic energies. Steep lateral and distal margins are indicators of the generally high yield strength of a given avalanche mass; once stress fall below the level at which motion occurs, the failure stops abruptly. Lack of these features indicates low material yield strength or a high degree of saturation and possible transition to lahar conditions. The commonly observed deformation structures such as clastic dikes and flame structures indicate contrasting material properties and dynamic, possibly turbulent behaviour in some parts of the avalanche. These features also support avalanche mobility models such as plug flow. On the other hand, reverse grading from deposit bottom to surface may indicate shear over the entire thickness of the avalanche.

The major factors identified as having a significant effect on emplacement behaviour and deposit morphology are initial material properties, the presence of significant volumes of water and the topographic environment into which an avalanche is deposited. Further influence of these factors will be discussed throughout the remainder of this thesis. Additionally, the major characteristics which distinguish VDA deposits from the deposits of similar mass wasting processes occurring in volcanic environments have been identified.

Chapter 4 - Emplacement processes

As established in the preceding chapter, characteristic VDA deposit features are key indicators of the geomechanical processes occurring during avalanche emplacement. The fact that these features possess common morphologic characteristics, spatial relationships and locations within VDA deposits may suggest that the processes leading to their formation are generally similar, which in turn may make it possible to develop a universal model for the emplacement behaviour of VDAs. To reinforce this notion, the first objective of this chapter is to discuss specific volcanic debris avalanche events and their resulting deposits, highlighting likely emplacement behaviour as hypothesized by previous authors. The characteristics and formation mechanisms of the deposit features introduced in the preceding chapter are discussed where appropriate. Based on these descriptions, the next objective of this chapter is to develop a general model that captures the most basic processes occurring during avalanche emplacement. In this manner, the presence, morphology and formation mechanisms of commonly observed deposit features can be straightforwardly explained for all cases. As these features are indicative of emplacement processes, the final objective of this chapter is to outline a general classification system whereby the presence and morphology of characteristic deposit features might be used to determine the likely geomechanical conditions occurring at a given time or point of emplacement.

Key questions:

- What processes occur in specific VDA emplacement scenarios?
- What processes are thought to have developed the deposit features observed?
- Can a common emplacement process model, generally applicable to all cases, be established based on common observations discussed in the literature?
- How might spatially and temporally variable emplacement processes be inferred from observed deposit features?

4.1. Introduction

The materials involved in the collapse of volcanic edifices are highly variable both within an individual event and between cases, involving different proportions and types of rock (some possibly molten), soil, clays, water, ice, gases, and organic materials. Depositional

environment also varies from case to case. However, as introduced in Chapter 3, VDA deposits are often very similar to one another in terms of morphologic characteristics. Because initial failure geometries are also generally similar, as determined by collapse scar observations, it is reasonable to assume that avalanche deformational evolution, and therefore emplacement mechanics, might also be similar, to some degree, in all large-scale volcanic edifice failure events (Siebert, 1984; Schuster and Crandell, 1984; Reubi and Hernandez, 2000; Strom, 2006). This idea suggests that a common sequence of geomechanical processes likely determines the characteristics and morphology of the resultant deposit. Equifinality, however, where multiple processes may result in similar end-products, is not ruled out. For instance, various processes may still be at work in creating different types of hummock forms (see discussion in Section 3.3.1). However, these mechanisms can be considered as lower-order processes controlled by the overall deformational evolution of the failure body. General deformational evolution may thus be considered as the main influence in avalanche emplacement mechanics and deposit character though saturation levels, topographic influence and material properties remain influential factors in determining emplacement behaviour and resulting deposit characteristics.

This hypothesis makes it possible to develop an emplacement model generally applicable to all cases. The first step in conceiving this model is to identify features universally observed in large-scale avalanche deposits, performed in Chapter 3. The next step is to scrutinize the emplacement of a number of VDA events in terms of their evolving geomechanical behaviour. Subsequently, it may be possible to identify general emplacement process themes common to all cases. This exercise is presented below in the form of summaries of VDA events discussed in the literature with specific focus on emplacement mechanics and deposit feature formation. Common emplacement process themes are then combined to develop a picture of the most fundamental and universal processes occurring during avalanche emplacement; the general emplacement model. Aspects of similar models hypothesized by previous authors are also included in this exercise.

As recognized in Chapter 3, avalanche behaviour may be represented by the deposit features they left behind. For instance, toreva blocks are a product of normal faulting in extensional stress regimes whereas steep, raised levees represent compressional stresses as an avalanche encounters topographic barriers or experiences increased influence of yield strength materials. Thus, spatially and temporally variable avalanche behaviour may be

tentatively recognized by identifying key features in a VDA deposit. The final section of this chapter applies this concept by introducing a general classification system by which the major avalanche behaviours and/or feature formation processes occurring during emplacement might be recognized by the spatially distinct deposit features observed. In this manner, distinct areas of varying emplacement behaviours within a deposit can be readily recognized and mapped, allowing for valuable comparisons between events.

4.2. Deposit descriptions

In order to recognize key morphologic features used to infer likely emplacement processes, a number of VDA cases are reviewed below. The major features of each event are first described, followed by the likely sequence of emplacement events, as hypothesized by previous authors. The examples discussed in detail below have been selected because they represent the world's best preserved and most well-studied subaerial VDA events, and therefore, a large body of research exists concerning their failure and emplacement mechanisms. In most cases the literature results from years of concentrated field study (e.g., Mount St. Helens and Socompa). Where only limited literature exists for less recognized VDA events, relevant summaries are still provided here in order to further highlight common emplacement mechanics themes. The review provided in this chapter generally represents the current body of literature concerning large-scale VDA emplacement mechanics, i.e. no literature discussing this topic has been overlooked. Most cases discussed represent generally similar initial conditions (large-scale, Bezymianny-type collapse of intermediate-felsic composite cones); variations from this model are discussed where appropriate.

4.2.1. Mount St. Helens, USA

Owing to its recent occurrence, in daylight hours on a clear day, the collapse of Mount St. Helens on 18 May, 1980 is undoubtedly the world's best documented VDA event. Months of precursor activity meant the volcano was carefully observed and monitored with then state-of-the-art equipment. Though it had been hypothesized previously (Gorshkov, 1959; Nakamura, 1978, for example), it was unquestionably established here that volcanic edifices are unstable entities prone to large-scale collapse, allowing evidence of similar events to be recognized around the globe. Most importantly for this study, numerous publications have been devoted to the pre-failure circumstances, collapse, and emplacement of the subsequent avalanche and associated deposit features (Lipman and

Mullineaux, 1981; Voight *et al.*, 1981; Voight *et al.*, 1983; Sousa and Voight, 1995; Glicken, 1998; Ward and Day, 2005). It is through these studies that our understanding of volcanic edifice instability and collapse was established.

The pre-failure Mount St. Helens edifice consisted of various units of fresh, brecciated and hydrothermally altered dacites, andesites and basalts and the newly intruded cryptodome (Glicken, 1998; Ward and Day, 2005). The cryptodome material was near molten. Before collapse, the north slope of the edifice bulged steadily northwards at 1.5-2.5 m/day with a significant downward component; deformation was as high as 5 m/day in the early stages of cryptodome intrusion (Voight *et al.*, 1983; Glicken, 1998). Intrusion of the bulbous or possibly sheet-like cryptodome increased the volume of the edifice by 0.11-0.23 km^3 (Voight *et al.*, 1983; Glicken, 1998). The intrusion of this material increased shear stress within the edifice while reducing rock mass strength by deforming and fracturing the host rock (Voight *et al.*, 1983; Schuster and Crandell, 1984). Major shear surfaces which progressively developed through cryptodome intrusion and subsequent gravitational adjustments eventually became the slide detachment surfaces (Voight *et al.*, 1983; Schuster and Crandell, 1984).

Large-scale fractures eventually developed in the summit area and spread across 1.5 km along the north slope along the apex of the bulge created by the cryptodome intrusion (Voight *et al.*, 1983). Initiation of the avalanche itself was the triggered by a 5.2 magnitude seismic event (Voight *et al.*, 1983; Glicken, 1998). The bulge pulsated for several seconds and the slide began within 10 seconds of the seismic event; detachment then occurred retrogressively in three distinct slide blocks. Failure of the first slide block occurred along back wall fractures dipping at 50-60°; acceleration of the slide mass was approximately 1.9 m/s^2 (Voight *et al.*, 1983; Glicken, 1998). An immense lateral blast created by decompression of the cryptodome overran the initial slide block as it spread out along the base of the cone. This blast likely had little effect on the first slide block but significant influence on the mobility of subsequent slide blocks, taking place directly through the second block (Voight *et al.*, 1983; Siebert, 1984). The second block was created as the edifice crown collapsed. The distal portion of this block connected to the proximal section of the first detachment as they essentially began to travel together (Voight *et al.*, 1983). The third slide block was composed of numerous discrete but sequential failures (Voight *et al.*, 1983). In addition to the initial blast, continuing pyroclastic flows likely influenced the emplacement of this block (Glicken, 1998). The three slide blocks eventually coalesced into an avalanche of fragmented debris travelling downslope in pulses

(Voight *et al.*, 1981; Voight *et al.*, 1983; Sousa and Voight, 1995). Based on seismic records, emplacement of the entire VDA took about 10 minutes (Glicken, 1998). The final VDA deposit covered an area (*A*) of roughly 60 km^2, had a volume (*V*) of 2.5 km^3 and runout distance (*L*) of approximately 24 km (McGuire, 2003). Lahars extended the debris to 95 km; the crest of these lahars left the terminus of the VDA deposit approximately 5 hours after general emplacement and travelled at 30-40 m/s down-valley (Voight *et al.*, 1983; Siebert, 1984; Siebert *et al.*, 1987). Moving surface water further altered the morphology of the deposit by oversteepening hummock walls and causing slumping; reworking of inter-hummock areas by post-emplacement lahar activity is common (Glicken, 1982; Voight *et al.*, 1983; Siebert, 1984).

In an immense effort to fully characterize the Mount St. Helens VDA and its deposit, Glicken (1998) produced two types of maps, morphologic and lithologic. The morphologic maps consisted of six units observed in the deposit; North Fork, Johnston Ridge, Spirit Lake, marginal, proximal, and distal units (note this use of spatial terminology slightly differs from that used throughout this thesis [i.e. proximal, medial, distal]). The North Fork unit makes up most of the deposit and has up to 75 m of relief and distinct levees. The Johnston Ridge and Spirit Lake units are located in those specific areas and reflect the degree to which the deposit travelled out of the main emplacement channel and up topography. The marginal unit forms lobate deposits and is thought to have been pushed aside by the main mass of moving material (Glicken, 1998). The proximal unit is located in the crater and on the slope adjacent to the edifice and is where the largest hummocks are located, up to 100 m high and 1 km wide, representing toreva block structures. The distal unit is composed of chaotic mounds of broken trees and wood debris, entrained material and clasts from the original edifice. Entrained material makes up as much as 30% of this unit. A flow front of up to 8 m is present though this unit grades into lahars locally (Glicken, 1998). The lithologic map details the location of the pre-failure edifice material in the present deposit and describes how these units are chaotically mixed distally from a prominent valley constriction. Sharp contacts between units indicate they were generally transported with little deformation. Blast deposits caused by cryptodome unroofing overran the VDA and devastated an area of 600 km^2.

Glicken (1998) describes two main divisions of the Mount St. Helens VDA deposit, distal and proximal, separated by a prominent valley constriction and break in slope approximately 17 km from source. In the proximal section, a significant majority of the debris is block facies. Each lithologic unit tends to be composed of one or more blocks. A

single contact extends across five hummocks in one section, indicating it travelled relatively intact. It is also possible that large areas of this section are made up of one toreva block which has been internally faulted. Distally from the break in slope only isolated block facies are found, the majority being mixed block and matrix facies. This material is thought to have travelled over the proximal block facies and therefore is suggested to have been deposited after the proximal block facies section, a view shared by Sousa and Voight (1995). The marginal areas have a more chaotic lithologic pattern. The above observations suggest two types of flow: an initial flow of blocks and unconsolidated pieces of all three slide blocks, which stopped at the valley constriction, and a latter flow of matrix material that contained isolated source blocks and juvenile material (Glicken, 1998). Further studies performed by Glicken (1998) on the Mount St. Helens deposit reveal a range of deposit textures from mostly undisturbed blocks to completely mixed material, providing evidence for an increasing degree of clast fracture, disaggregation and mixing of material during emplacement.

4.2.2. Mount Shasta, USA

The Mount Shasta VDA (300,000 – 380,000 ybp, L = 55 km, V = 45 km^3, A = 675 km^2) is the largest known subaerial Quaternary landslide on Earth (Crandell *et al.*, 1984; Crandell, 1989; Ui and Glicken, 1986). Surprisingly, little research has been conducted into the origin of this event. No evidence of juvenile material was found in the deposit, indicating collapse may have been caused by a steam explosion, seismic activity, or glacial erosion (Bandai- or Unzen-type) (Crandell, *et al.*, 1984; Crandell, 1989). The most significant feature of this deposit is the series of large ridges along the axis of the avalanche path, generally evenly-spaced, trending perpendicular to principal avalanche flow direction and separated by flat areas. These ridges likely represent intact toreva block structures which travelled coherently, the largest of which is 8-9 km long, 1.5 km wide, and 210 m high (Crandell *et al.*, 1984). This particular ridge travelled over 20 km from its source and possesses a sinuous trend which represents either emplacement deformation or original structure (Crandell, 1989). Crandell (1989) suggests this block could represent the intact head wall of a retrogressive slide sequence. The ridges are composed of individual blocks or volcaniclastic sequences, many of them showing retaining original stratigraphy (Crandell, 1989). Additionally, extraordinary conical hummocks are scattered throughout the deposit, decreasing in number, height and area with distance (Crandell *et al.*, 1984). Many of the hummocks and ridges are draped with veneers of matrix material, indicating at least partial transport within the matrix.

Crandell *et al.* (1984), Ui and Glicken (1986) and Crandell (1989) each describe a clear recognition of block and matrix facies in this deposit. Ui and Glicken (1986) observe that the percentage of block facies is nearly 100% within hummocks for the entire length of the deposit. The mean maximum dimension of blocks in layered volcaniclastic material was 220 m and in lava blocks just 110 m, suggesting plastic deformation of the volcaniclastic blocks and brittle fracturing of the competent lava blocks (Ui and Glicken, 1986). Accordingly, numerous jigsaw fractures were found in the brittle lava blocks while volcaniclastic blocks are faulted and deformed plastically (Ui and Glicken, 1986).

Exposures in the flat areas between hummocks predominantly consist of matrix facies with less than 20% block facies (Ui and Glicken, 1986). The matrix facies also contains significant aquatic fossils indicating possible emplacement into a lacustrine or fluvial environment (Crandell *et al.*, 1984).

It is suggested that the avalanche began as a series of large slide blocks, possibly originating retrogressively, that became progressively more fragmented as they travelled, representing a gradual transition from rockslide to debris avalanche to mudflow (Crandell *et al.*, 1984; Crandell, 1989). The avalanche is thought to have travelled and been deposited as a single unit with mobility being enhanced by the incorporation of potentially saturated basin sediments (Crandell *et al.*, 1984). Accordingly, the matrix is thought to have been rather fluid, enough to drain away from the decelerating block facies to some degree. Blocks from the initial part of the slide are thought to have come to rest at the south western margin of the deposit while latter blocks form prominent torevas, some of which are tilted backwards (Crandell *et al.*, 1984). In general, blocks from the northernmost part of the original edifice are thought to have travelled the furthest and those from deeper within the edifice (south) the shortest distance, suggesting the more proximal toreva ridges observed today likely originated higher up and within the initial edifice. The Mount Shasta VDA is discussed in further detail in Section 5.3.1.

4.2.3. Socompa, Chile

The Socompa VDA (6,000 – 7,000 ybp, L = 40 km, V = 36 km^3, A = 500 km^2) is located in an arid climate and is therefore one of best preserved deposits in the world and an ideal location to study emplacement processes (Francis *et al.*, 1985; Francis and Self, 1987; Francis and Wells, 1988; Francis, 1994; Wadge *et al.*, 1995; Ui *et al.*, 2000; van Wyk de Vries *et al.*, 2001; Kelfoun and Druitt, 2005; Kelfoun *et al.*, 2008). The avalanche was

mostly comprised of two lithologies that differ significantly in material properties, and thus, in emplacement behaviour: brecciated edifice lavas and ductile basement materials (gravel, sand and ignimbrite mix) originally underlying the edifice. Collapse was likely triggered by failure of active thrusts that extended into weak underlying materials as a result of gravitational spreading promoted by edifice load and the resultant extrusion of the basement material (van Wyk de Vries *et al.*, 2001). It is debated whether or not liquefaction of these substrate materials caused the collapse, or vice versa (van Wyk de Vries *et al.*, 2001). Due to its lower position, this material possessed a lower potential energy but is observed to have travelled the furthest while material from higher in the edifice travelled the shortest distance. This phenomenon is thought to be the result of the high stresses present from gravitational spreading and efficient mobilization of this material (van Wyk de Vries *et al.*, 2001). A magmatic component may also have been involved (van Wyk de Vries *et al.*, 2001). The original relative position of each lithology is retained in the deposit, though layers that were originally tens to hundreds of metres thick are now stretched to only a few metres thick (Francis and Self, 1987). The deposit has a flow front of greater than 40 metres high with a curved trajectory, suggesting a high emplacement velocity (Francis and Self, 1987).

Deposit topography is separated into distinct regions where the avalanche first travelled and stretched away from the source edifice, encountered an elevated topographic margin, compressed, then reflected back onto itself to completely change direction (van Wyk de Vries *et al.*, 2001; Kelfoun and Druitt, 2005). A large, prominent escarpment is thus preserved across the deposit, which possesses a complicated series of compressional faults and represents the essentially frozen wave of rock and debris that reflected back onto itself (van Wyk de Vries *et al.*, 2001; Kelfoun and Druitt, 2005). This type of topographic reflection is a genuine indicator of the high mobility (Kelfoun *et al.*, 2008). Between the source edifice and the escarpment, normal faults scarps all dip consistently away from the volcano and block rotation indicates the lower materials must have been travelling faster than those above (van Wyk de Vries *et al.*, 2001). Faulting occurred at a wide range of scales but significant flow-perpendicular horst and graben structures located throughout the deposit indicate predominant extension.

In total, the avalanche is thought to have slid into place as a fast moving sheet of fragmented rock debris with a leading edge and crust with near normal friction and an almost frictionless interior and thin basal layer (Kelfoun *et al.*, 2008). Spreading occurred mainly in the ductile basal shearing layer of basement and substratum material which

drained out from underneath the more competent slabs above (Kelfoun and Druitt, 2005). A significant portion of the deposit, up to 80%, is comprised of the weak basement material (Francis *et al.*, 1985; Francis and Self, 1987; Francis, 1994; van Wyk de Vries *et al.*, 2001). This unit rarely contains intact blocks whereas the more brittle lavas show clear signs of shear, mainly faulting and block rotation (van Wyk de Vries *et al.*, 2001). Blocky surface lithologies rifted in a brittle manner as large slabs of lava were sheared and interacted with topographic features (Kelfoun *et al.*, 2008). Large-scale jigsaw fracture patters are observed in the rafted slabs, many of which pulled apart and left gaps of the underlying fluidized material in between (Kelfoun *et al.*, 2008). Some of this material was so fluid it extruded vertically, leaving high-standing ridges.

The primary (pre-reflection) and secondary (reflected) avalanche waves are suggested to have occurred simultaneously (Francis *et al.*, 1985; Kelfoun *et al.*, 2008). Emplacement was considered to be a short-lived event with minor slumping after deposition (Kelfoun *et al.*, 2008). Primary flow was extensional with pervasive thinning at high speeds where flow-parallel ridges and furrows were formed. Secondary flow occurred at low speeds and was controlled by local slope with rifting and extension into horst and graben structures; secondary terrain is accordingly much rougher in texture. Most evidence suggests the avalanche was not saturated as there is no evidence of post-emplacement lahars. Possible basal saturation, however, cannot be ruled out (Kelfoun *et al.*, 2008).

At the mouth of the collapse amphitheatre, prominent toreva block structures are observed, which are internally coherent though slumped and back-tilted without internal disruption (Crandell, 1989). These blocks have dimensions of up to 2.5 km, have slid 5-10 km from their source area and occupy a volume of 11 km^3 (> 30% of the 36 km^3 total deposit volume) (van Wyk de Vries *et al.*, 2001; Kelfoun and Druitt, 2005; Kelfoun *et al.*, 2008). Kelfoun *et al.* (2008) note a further 23 km^3 of blocks that toppled into the amphitheatre, which are not included in the main toreva area. Distinct shear zones are observed at the base of the toreva blocks, evidence of interaction between the blocks and a proposed mobilised substratum, which is thought to have 'dragged' the large edifice blocks with it as it liquefied (van Wyk de Vries *et al.*, 2001). However, as there is no evidence of avalanche material overlying these features, Wadge *et al.* (1995) suggest these torevas slid into place after the emplacement of the main mass of the avalanche, likely from a position high on the northern flank of the source edifice (Wadge *et al.*, 1995). The Socompa VDA is discussed further in Section 5.3.2.

4.2.4. Jocotitlan, Mexico

The Jocotitlan VDA of central Mexico (≈ 10,000 ybp, L = 12 km, V = 2.8 km^3, A = 80 km^2) displays a unique morphology which is attributed to the competency of its constituent materials (Siebe *et al.*, 1992; Capra *et al.*, 2002). Large toreva ridges located in the proximal section of the deposit, transverse or oblique to emplacement direction, are the most noticeable feature. The largest of these ridges, Loma Alta, stretches 2.7 km at a height of 205 m. These ridges are subparallel, separated by closed depressions, can be visually re-fit back together back into a single large block and are within 5 km of the source (proximal 40%) (Siebe *et al.*, 1992). Steep (29-32°) and extraordinarily conical hummocks to 165 m in height are observed adjacent to the toreva structures, representing two morphologically distinct sections of the deposit (Siebe *et al.*, 1992). Both the toreva ridges and conical hummocks decrease in size distally. Smaller distal hummocks are less conical, have diffuse outlines and tend to cluster into complex shapes, some of which are elongated in the direction of flow.

The deposit itself consists of a very poorly sorted mixture of angular to subangular clasts, the majority of which are 1-5 m in maximum dimension. Very little matrix material is present; the deposit is therefore clast supported, even at its distal reaches and margins, with a homogeneous composition and coarse internal texture (Siebe *et al.*, 1992). Steep hummock slopes are attributed to the accumulation of this coarse material at its angle of repose around large core blocks. Jigsaw fractures are observed in many of the clasts.

Siebe *et al.* (1992) suggest the intrusion of a magma body into the source edifice created an oversteepening of the flanks and failure may have subsequently been triggered by a seismic event (Bezymianny-type). Juvenile material and pyroclastic surge layers found in nearby stratigraphic sequences support this claim. Regional tectonics may have also played an influential role in collapse (Siebe *et al.*, 1992).

Due to the fit of the large toreva ridges and hummocks, Siebe *et al.* (1992) suggest that the initial failure occurred as a single large block which progressively disaggregated into smaller parallel ridges and conical hummocks. Sliding was maintained to great distances due to the competency of the material involved and a transition from inertial rockslide to fluid-like spreading at the base of the volcano is envisioned (Siebe *et al.*, 1992). The conical form of many of the hummocks is thought to be the result of strong shaking of the coarse material to its angle of repose during disaggregation, and therefore, not a result of

post-emplacement erosion (Siebe *et al.*, 1992). Steep marginal scarps indicate *en masse* deposition as shear stress fell below the material yield strength (Siebe *et al.*, 1992). This idea is supported by deformation in distal lacustrine sediments which were disturbed by individual blocks projecting away from main avalanche as it stopped suddenly (Siebe *et al.*, 1992). Bulldozing, folding and thrust-faulting are also observed in the distal basin sediments. The Jocotitlan VDA is discussed in further detail in Section 5.3.3.

4.2.5. Shiveluch, Russia

Numerous VDA deposits are summarized by Melekestsev (2006) and Ponomareva *et al.* (2006) in Russia's Kamchatka region. In fact, these authors note that 60% of the 30 major edifices in this region show evidence of collapse. The Bezymianny VDA, whose name is synonymous with magmatic activity related instability, is located here (Belousov, 1996). However, little literature specifically concerning the emplacement mechanics of this VDA exists, and it is therefore not discussed further in this thesis. A notable aspect of the Kamchatka region summary of Ponomareva *et al.* (2006) their description of large-scale toreva structures located in the proximal sections many of the Kamchatka deposits. These structures are up to 2 km^3 in volume and have moved several kilometres from their source.

Arguably the most significant Kamchatka phenomenon is the repeated collapse of Shiveluch. This edifice is thought to have failed originally in pre-Holocene (≈ 30,000 ybp) times to produce a deposit of L = 32 km, V = 30 km^3 and A = 400 km^2 (Ponomareva *et al.*, 2006). Since this event, it is argued that collapse has occurred upwards of 15 times, most recently in 1964 AD, to produce a deposit reaching to 16 km covering an area of 98 km^2 (Ponomareva *et al.*, 1998; Belousov *et al.* 1999; Melekestsev, 2006; Ponomareva *et al.*, 2006). Repeated collapse of this nature represents the recurring failure of unstable extrusive dome material with various amounts of flank and headwall material involved. In the case of the 1964 VDA, much of the failed dome material travelled downslope while the initial flank material became large toreva structures deposited in the proximal area of the deposit. The high rate of instability at Shiveluch is attributed to an increased production of highly viscous magmas beginning approximately 10,000 ybp (Belousov *et al.*, 1999). Each deposit is generally associated with post-collapse explosive products and differs in colour from other events, thus indicating origin from a separate area of the source edifice. In any case, the exposed deposits display hummocky topography with a composition of predominantly block facies material underlain by matrix facies. Backwards rotation is observed in the larger slide blocks, which generally remain intact, while more distal

material is fragmented (Belousov *et al.*, 1999). Blocks are often observed to be stretched and deformed in the direction of avalanche flow (Belousov *et al.*, 1999). Matrix facies material is present in significant proportions at the margins and basal regions of the deposit; in some cases injected upwards into the block facies, an indication of its relative mobility (Belousov *et al.*, 1999). Though there are no clear grain size trends in studies by Belousov *et al*. (1999), distal increases in sand content suggest either increased initial fragmentation of the toe material or progressive fragmentation with emplacement distance. Steep terminal margins indicate high yield strength and *en masse* deposition.
Orthoimagery source explained in Section 5.2.

Belousov *et al.* (1999) suggest the 1964 VDA deposit is the most significant in terms of emplacement process interpretation. These authors divide deposit features into three categories: features created by incomplete edifice material disintegration, features resulting from emplacement, and deceleration features. Incomplete disintegration features include the large proximal toreva 'steps', conical hummocks and closed depressions. Hummock density in this case is not correlated to distance from source or deposit axis and is thought to be the result of brecciated pieces of the edifice material which did not fully disintegrate during emplacement. Features resulting from emplacement include marginal levees and medial/distal 'furrows' aligned with flow direction, produced by extensional strain existing in the travelling avalanche body. Lastly, features resulting from deposition include distal graben-like trenches and undulating ridges, thought to be the surface expression of compressional folds and faults (Belousov *et al.*, 1999). Previous authors have suggested the likelihood of two separate failure events for the 1964 avalanche, perhaps in retrogressive fashion (Ponomareva *et al.*, 1998; Belousov *et al.*, 1999; Melekestsev, 2006). The 1964 Shiveluch VDA is discussed in further detail in Section 5.3.4.

4.2.6. Parinacota, Chile

Chile's Parinacota VDA (8,000 ybp, L = 22 km, V = 6 km^3, A = 140 km^2) is another example of a well preserved deposit in the arid central Andes (Francis and Self, 1987; Francis and Wells, 1988; Clavero *et al.*, 2002; Shea and van Wyk de Vries, 2008). Though the collapse scar has been completely filled in with post-failure eruption materials, the deposit is clearly visible. The path of the deposit appears to have been channelled by topographic highs in the distal reaches of emplacement. Hummocky topography is clearly visible throughout the deposit, particularly in the medial area where topographic lows between hummocks now hold a series of large lakes. In the proximal section, torevas are

400-500 m in maximum dimension and up to 120 m high (Francis and Wells, 1988; Clavero *et al.*, 2002). These structures represent slumped edifice blocks that slid into place coherently, preserving original volcanic stratigraphy and showing backwards tilting (Francis and Wells, 1988; Clavero *et al.*, 2002). Similar to the collapse of Socompa, Clavero *et al.* (2002) suggest collapse at Parinacota may be due to loading of basement sediments.

The Parinacota deposit is composed of two units, an upper coarse-grained breccia with little matrix and a majority of large, coherent and angular blocks and a lower brecciated unit of block and ash flow deposits and entrained basin materials (Clavero *et al.*, 2002). The edifice is thought to have failed sequentially to produce the lower unit from rhyodacite domes originally found low in the edifice and the upper unit from the upper andesitic sections of the cone. The surfaces of many of the blocks contained in the upper units show thousands of small impact marks, indicating repeated vibration and collision without significant shear. These impact marks are often aligned in narrow zones which imply some differential motion between blocks. Most of the avalanches' deformation was confined to the lower layer; now observed as a wet, structureless basal material composed of pebbly sand composed and entrained basin materials (Clavero *et al.*, 2002).

Similar to Jocotitlan, individual hummocks consist of coarse grained, clast supported lava breccias with little fine grained matrix. Individual clasts show little abrasion or mixing except near the base. Fresh distal fracturing indicates a limited amount of fracturing occurred during emplacement (Clavero *et al.*, 2002). Larger proximal hummocks typically have higher slope angles (26-35°) where as smaller, more distal hummocks are broad with little internal structure preserved.

Clavero *et al.* (2002) recognize two types of lateral margin at Parinacota. The first type is sharp and steep and commonly found in proximal and medial areas. The second type of margin is typically found distally and consists of a thinning wedge merging into small hummocks and isolated blocks. A distal 'bulldozer' effect, which creates folds and faults may also be observed and is even considered to be an additional sedimentary facies by Belousov *et al.* (1999).

Clavero *et al.* (2002) suspect that the toreva and hummocks observed here result from the separation of the collapsing edifice along pre-existing fractures into distinct domains which were subsequently transported with little internal deformation, modest internal shear and

some dilation (Clavero *et al.*, 2002). Similar pre-existing fractures are observed in a current dome that was not involved in the collapse. Domains subsequently fragment into smaller brecciated blocks with distance, and accordingly, hummock volume, amplitude, and maximum block size decrease both distally and laterally (Francis and Self, 1987; Clavero *et al.*, 2002). The break up into domains likely occurred during an early stage when the avalanche impacted the ground with only minor disaggregation occurring during emplacement (Clavero *et al.*, 2002). Spreading of the Parinacota VDA is thought to have occurred in a fluid-like manner accompanied by dislocation of the individual domains and intense shear at the base of the avalanche. This basal shear surface may be related to the original décollement surface. Lower spreading caused the upper layers to spread themselves. Near source domains were large and had a low energy resulting in the formation of toreva blocks near source whereas small-scale domains had a high kinetic energy and spread to form smaller distal hummocks of low relief. The Parinacota VDA is discussed further in Section 5.3.5.

4.2.7. Mombacho, Nicaragua

Shea *et al.* (2008) detail two VDA deposits at Nicaragua's Mombacho volcano. The Las Isletas VDA (pre-Columbian, L = 11.9 km, V = 1.2 km^3, A = 56.8 km^2) failed to the northeast and is partially exposed as a collection of small islands in present-day Lake Nicaragua; the El Crater VDA (Historic?, L = 12.4 km, V = 1.75 km^3, A = 49.5 km^2) failed directly south (Shea *et al.*, 2008). Each of these deposits possesses a lobate plan-view shape and was emplaced on relatively flat slopes with no topographic confinement and relatively little entrainment of basin materials. The materials involved in each collapse were generally similar, though the initial amount of substrate material and degree of alteration varies. Though two separate collapse mechanisms are proposed for each event, similar deposit stratigraphy of a coarse-grained upper layer over a fine-grained layer is produced. The lower layer is suspected to have provided a low friction basal shear layer on which pervasive spreading would have occurred (Shea *et al.*, 2008). Extensional structures such as normal faulting and boudinage features predominate in each deposit as the upper layers experienced distal and lateral extension. No evidence of thrust faulting or imbricate structure formation is observed (Shea *et al.*, 2008). Large blocks are preserved in the upper sections of both deposits in a reversely-graded manner; little block-to-block interaction is suggested (Shea *et al.*, 2008).

The Las Isletas deposit is composed of a significant degree of weak substrate material thought to have been derived from beneath the flank of the failed edifice and thus a potential collapse initiating mechanism (Shea *et al.*, 2008). The deposit morphology is representative of a spreading related failure as compressional features are not observed (Shea *et al.*, 2008). Prominent proximal normal faults, striking perpendicular to flow direction, are replaced distally with inter-hummock depressions. Some strike-slip faults are also observed. Hummocks are generally absent in the proximal sections of the deposit though significant hummock 'trains' are noticeable in distal sections, typically aligned parallel to flow direction. A block-rich unit forms steep-sloped hummocks in which the blocks possess sharp angular edges and show little evidence of collision. Some blocks increase in roundness with increasing hydrothermal alteration. Few jigsaw fractured blocks are present indicating violent block interaction was limited. A prominent basal shearing layer is present, composed mainly of original substrate materials and is always found at the base of a coarsening upwards sequence (reverse grading throughout depth of deposit). No stratigraphic rollover is observed and the units above the basal layer preserve original structures and stratigraphies, indicating translational and non-turbulent motion (Shea *et al.*, 2008).

The El Crater deposit shows a high degree of hydrothermal alteration of the original materials and no entrained or original substrate materials are recognized. The increased alteration may represent a source near the edifice core and a potential collapse factor. This soft material may also have cushioned fractured blocks and acted as a ductile lubricating or shearing layer (Shea *et al.*, 2008). Faulting is observed throughout the deposit as hummocks cover the entire surface. Blocks are sharp and angular and lack signs of collision. Reverse grading is again observed throughout the depth of the deposit as the block facies is generally found in the upper sections of the deposit and the matrix proportion increases towards the deposit base. Hummocks are generally aligned with flow direction near flow axes while those at the margins are aligned obliquely, a morphology thought to have occurred just before deposition as the avalanche decelerated (Shea *et al.*, 2008). Hummock alignment thus represents extension as compression would likely result in hummock trains aligning perpendicular to flow. A scarcity of jigsaw fractured blocks and predominant normal faulting signifies extensional conditions were dominant, particularly in the proximal and medial sections of the flow. The nearly constant dip of the normal faults (≈ 50°) leads Shea *et al.* (2008) to suggest the horst and graben model of Voight *et al.* (1981) is appropriate. As at Las Isletas, original stratigraphy is preserved as no rollover is observed, indicating a global sliding and or translational motion.

Shea *et al.* (2008) note that while general absence of compressional regime features (clastic dikes, jigsaw fractures, impact marks) is indicative of purely extensional emplacement conditions, compression and violent block-to-block interaction during the initial stages of collapse should not ruled out.

4.2.8. Chimborazo, Ecuador

Bernard *et al.* (2008) recently detailed the Riobamba VDA ($L > 35$ km, $V = 11$ km^3, $A = 280$ km^2) deposit from Ecuador's Chimborazo volcano. The most significant aspect of this study is the clear spatial distinctions of the sedimentary facies and their relation to emplacement sequences. The block facies of this deposit is highly brecciated and coarse grained with many jigsaw fractures, few interblock structures (representing incomplete mixing) and no blocks greater than 5 m^2. The lack of relatively large blocks may indicate the collapsed edifice was highly brecciated prior to or during the initial stages of failure. The matrix facies is a sandy silt with few blocks which are often rounded with dispersed boundaries. The amount of entrained material is high, estimated at 50-70% for the entire matrix facies of the deposit (Bernard *et al.*, 2008).

The block facies, created through initial disaggregation of the collapsed edifice, is the main component of the proximal section of the deposit. The matrix facies represents less than 10% of this section and is present only in sporadic dikes found on top of the deposit. The block facies is also predominant in the medial section, approximately 75% by volume, but outcrops observed have significantly more mixing features and dike injections (Bernard *et al.*, 2008). The proportions of block and matrix facies are occasionally almost equal at some outcrops in the medial section. In distal sections, matrix facies dominates (> 50% by volume) though large matrix supported blocks are common. In total, the block facies comprises 80-85% of the deposit volume with the remainder being matrix facies created through mixing of brecciated edifice rock with entrained basin materials. A fine-grained basal layer with significant proportions of entrained material is common throughout, as is large-scale reverse grading.

Near the basal contact, shattered block fragments are progressively more dispersed. This area also possesses significant structure including laminations, entrainment along shear zones, stretched blocks, and faulting and erosion of the substrata. Additionally, structures observed in the matrix facies are commonly found near block boundaries, indicting differential movement. Stretched blocks are observed along the contact between the fine-

grained basal layer and blocky upper avalanche, suggesting high shear in this area and the possibility of differing flow regimes. Banding and jigsaw fractured blocks seen in the upper layers indicate laminar flow above while the lower region could have been turbulent, as suggested by the presence of some fully eroded and fluidized ignimbrites (Bernard *et al.* 2008).

Injections of fluidized material are common throughout the deposit, though mainly found in the more distal sections. Some of the more fluid dikes extend through the entire depth of the deposit and are thought to have occurred late in the emplacement process (Bernard *et al.*, 2008). Injected matrix material can also extend into jigsaw fractures, causing clast separation. The formation of these types of structures is likely influenced by stress conditions caused from pre-avalanche basin topography and confinement, in contrast to the purely extensional conditions seen in the VDAs at Mombacho.

Hummocky topography is also observed. Proximal hummocks are mainly ridges composed of block facies while distal hummocks are matrix facies and commonly circular in plan view. Rather than being aligned perpendicular to flow as typically observed in ridges and toreva structures at other VDA deposits, proximal ridges at Chimborazo are predominantly aligned parallel to flow direction as emplacement in this section is thought to have been heavily influenced by confinement from adjacent topographic highs (Bernard *et al.*, 2008). In distal areas of the deposit, hummock ridges are more commonly aligned transverse to flow direction as the avalanche spread laterally into a broad pre-emplacement topographic low.

The emplacement sequence of the Riobamba VDA is envisioned by Bernard *et al.* (2008) as follows. A block dominated avalanche, strongly shattered before and/or during failure initiation, mobilised into a cohesive avalanche and experienced strong disaggregation. The failure is thought to have entrained a significant amount of basin material, developing a fine-grained, lubricated basal layer as flow progressed. Progressively more basin sediments were entrained as emplacement advanced and the proportion of matrix facies increased along the flow path without significant rock fracturing to produce additional fine-grained material while increased mixing of the block and matrix facies occurred up to the time of deposition (Bernard *et al.*, 2008). The incorporation of fine-grained and potentially saturated basin sediments worked to increase the downstream mobility of the VDA, likely resulting in the fluid-like behaviour structures such as upwards-propagating clastic dikes and the basal shearing layer.

4.2.9. Additional examples

In addition to the descriptions above, a number of other studies have described VDA deposits with regard to the commonly observed structures discussed in Chapter 3 and emplacement mechanics. As these additional studies are generally not as comprehensive as those presented above only the significant observations presented therein are consolidated here for brevity.

The collapse of Ollagüe on the Chile-Bolivia border has been addressed in both in terms of likely failure mechanism (tectonics) (Tibaldi *et al.*, 2006; Vezzoli *et al.*, 2008) and subsequent emplacement products and processes (Clavero *et al.*, 2004). The deposit (400,000 – 600,000 ybp, $L > 12$ km, $V = 1$ km^3, $A = 50$ km^2) is composed of 75% original edifice material and 25% entrained basin sediments and can be divided into distinct units based on hummock morphology, composition and internal structures (Clavero *et al.*, 2004). Two large toreva blocks showing original layering are observed in the proximal section of the deposit. The largest of these blocks is back-tilted 6-8°. The main body of the deposit is composed of the central andesite facies, which is derived mainly from brecciated edifice material and shows distinct hummocks with a range of geometries, conical to compound. Many hummocks form ridges subparallel to flow direction. Hummocks decrease in size with distance and generally have steep slopes (20-39°) which are typically steeper on their proximal side. The size of largest block contained within the hummocks also shows the tendency to decrease distally. The remainder of the deposit is composed mainly of mixtures of initial volcanic and entrained basin materials, forming hummocks of relatively low relief. Jigsaw fractured blocks, many with impact marks similar to those observed at Parinacota, are observed on the surface of the deposit. Deformation structures such as upwardly injected ductile material, folds and imbricate thrust faults are also observed, particularly in the entrained basin materials, which increase distally due to pre-deposition compression. Clavero *et al.* (2004) speculate that the initial collapse material slid on unconsolidated basin materials which reduced basal friction and enhanced mobility. The large volume of ductile basin sediments entrained during subsequent emplacement is thought to have ultimately decreased avalanche mobility and promoted deposition (Clavero *et al.*, 2004).

In addition to the deposit described at Jocotitlan, numerous additional edifice failures have occurred in Mexico, as summarized by Capra *et al.* (2002). Though little additional work has been done to characterize the deposits of these failures, it is arguably the most

significant event, in terms of volume and deposit morphology, is the Popocatepetl VDA. The main body of this deposit is clearly identifiable in plan view due its lobate form and exceptionally large toreva structures. Robin and Boudal (1987) originally described the morphology of this deposit (< 50,000 ybp, L = 30 km, V = 28-30 km^3, A = 300 km^2) though subsequent description by Siebe *et al.* (1995) increases the size of the deposit considerably. It should be noted that in this case there is evidence of the deposit possibly being constructed from several distinct events (Siebe *et al.*, 1995). Robin and Boudal (1987) describe a distal decrease in hummock size from the proximal torevas which are upwards of 450 m high and 2 km in their largest dimension. The largest, most proximal torevas and/or hummocks are orientated with their long axis perpendicular to flow direction while smaller, more distal hummocks tend to be parallel to flow. As compared to the Mt. Shasta deposit, the number of hummocks is small (≈ 150) though their general dimensions are greater. Additionally, topographic relief is 'levelled' by the accumulation of infill products adjacent to the toreva block areas, rather than this material spreading freely across the emplacement basin. Accordingly, this deposit has a more compact morphology then other VDA deposits (Mt. Shasta and Colima, for instance) and has the appearance of having had stopped suddenly, *en masse* (Robin and Boudal, 1987). Furthermore, Robin and Boudal (1987) describe the occurrence of large 'slabs' of original edifice material now preserved as rafted material in the deposit matrix. Many of these slabs contain original edifice structure and stratigraphy and are brecciated into angular blocks by radial fracture patterns (Robin and Boudal, 1987).

Though the edifice itself has long since eroded, two distinct Miocene VDA deposits are recognized at France's Cantal volcano: VDA1 and VDA2 (Schneider and Fisher, 1998; Reubi and Hernandez, 2000). While erosion means morphology and spatial dimensions are difficult to interpret, stratigraphic sections containing these deposits allow important observations concerning avalanche emplacement behaviour to be made. An irregular upper contact does, however, suggest an ancient hummocky topography (Schneider and Fisher, 1998; Reubi and Hernandez, 2000).

The lower deposit (VDA1) is poorly sorted and consists primarily of matrix facies at the base with block facies in the middle and upper sections (reverse grading). Jigsaw fractures are rare, though some joints in the block facies are filled with injected matrix material. A progressive dispersion of clasts with distance is also recognized (Reubi and Hernandez, 2000). Entrained material, mixing, and differential movement are generally absent throughout the entire sequence but prevalent in the basal section, which also contains

oblique ramp structures and a preferential alignment of clasts. Reubi and Hernandez (2000) thus interpret the basal shear zone as the principal cause of fracture of blocks present near this region. The basement rock below is highly fractured, which, along with foliated gouge and fold structures in the basal VDA, indicate strong frictional shearing (Schneider and Fisher, 1998).

The upper deposit (VDA2) is also poorly sorted and matrix supported (70-80%) with no discernible internal structure except for near its base. The matrix material composed almost entirely of juvenile volcanic glass, implying this avalanche is the result of a Bezymianny-type event (Reubi and Hernandez, 2000). Large blocks are present in small proportions, decrease in size distally and are often shattered by a dense network of fractures, which commonly radiate out from a central point. These fractures are typically wider near the block edge, leading to an 'inflation' of the block, termed Isotropic Dispersive Inflation (IDI) by Schneider and Fisher (1998). Inverse grading radially away from these blocks is often observed, suggesting differential shear movement between the block and matrix facies with enough energy to cause the necessary dispersive pressures. Reubi and Hernandez (2000) suggest the lower section of this avalanche was a hyperconcentrated flow while the upper was a dilute layer; a magmatic intrusion or decompression event may have contributed a gas component to the flow, allowing it to undergo a transition from turbulent to laminar conditions and vice versa (Reubi and Hernandez, 2000). As the emplacement of VDA2 was most likely heavily affected by the hypothesized fluids and gases present, its emplacement sequence is not considered further.

The mechanism for VDA1 is envisioned by Reubi and Hernandez (2000) as follows. In response to gravity, the edifice is affected by normal faults that delimit 'gigablocks' which start to slide, producing huge scarps. Shear stress is produced which fragments the mass more efficiently at the base, progressively producing a layer of fine particles. This layer reduces stress in the middle and upper parts of the avalanche where blocks are brecciated but not dispersed. The basal layer develops and acquires, at least temporarily, a turbulent behaviour possibly due to dilation induced shear (Reubi and Hernandez, 2000). Entrained material adds further to the matrix facies as the mass remains relatively coherent and moves as a rigid sheet. The block facies is formed with relief acquired during early sliding partially preserved as hummocks. The more fluid matrix facies injects into the more competent block facies but their different material behaviours prevent significant mixing. Deposition occurs *en masse* by 'freezing' of the turbulent basal layer as shear becomes

smaller due to deceleration. Some blocks may have a higher kinetic energy and form shear structures as their momentum briefly keeps them moving in the matrix.

Several VDA deposits are also described in Japan, such as at Ontake (Endo *et al.*, 1989; Voight and Sousa, 1994; Takarada *et al.*, 1999) and Tashirodake (Takarada *et al.*, 1999). The deposit of the 1984 AD Ontake collapse (L = 13 km, V = 0.03 km^3) is separated by Endo *et al.* (1989) into three lithofacies which generally correspond to the descriptive terminology classification scheme of Palmer *et al.* (1991). The main VDA is characterized by large, brecciated (jigsaw) blocks and hummocky topography which is often in the form of ridges perpendicular to flow direction. Flow-parallel elongated furrows are also observed as are 'wrinkles' or 'pressure ridges' formed near topographic obstructions. While there are no systematic grain size patterns observed, a noticeable absence of fine-grained material is seen on the block facies, reflecting the character of the initial failure material (Endo *et al.*, 1989). As much as 40% of the matrix is thought to be derived from materials entrained from the emplacement basin (Endo *et al.*, 1989).

The work of Takarada *et al.* (1999) in describing the sedimentology of the Iwasegawa (Tashirodake volcano) and Kaida (Ontake volcano) VDA deposits in Japan has already been referred to several times throughout this thesis. This study is important as it describes several fundamental observations: a decrease in block size with distance, an increase in matrix facies proportion with distance and vertical location within the deposit (the basal section having a significantly higher percentage of fine-grained material). Specifically, Takarada *et al.* (1999) observe 80-90% matrix facies in the distal, marginal, and basal sections of the deposits, an increase from a mean of roughly 55% in proximal sections. Increased proportions of entrained clasts and deformation structures with distance are also described. Furthermore, Takarada *et al.* (1999) also recognize normal grading of clasts but reverse grading of wood material throughout the depth of the deposit and reverse grading in basal clasts. These observations suggest larger clasts sank as the wood 'floated' upwards. Additionally, the majority of the wood fragments are orientated with the direction of flow.

Several VDA deposits in New Zealand have also been recognized and detailed (Ui *et al.*, 1986; Palmer *et al.*, 1991; Alloway *et al.*, 2005). Though larger deposits exist, particular attention is paid to the Pungarehu VDA deposit from Mt. Egmont (20,000 ybp, L = 26 km, V > 7.5 km^3, A > 250 km^2) (Palmer *et al.*, 1991). The principal observation made at these deposits is that of sedimentary facies evolution. Specifically, the distal and marginal

evolution from coarse block facies to fine-grained, mobile matrix facies through disaggregation and entrainment processes is well documented at the New Zealand deposits. Furthermore, Ui *et al.* (1986) document an increase in jigsaw fracture number and spacing and clast roundness with distance in the Pungarehu deposit. This concept supports the notion of loosening of brecciated blocks with emplacement distance.

Voight *et al.* (2002) describe the relatively small 1997 sector collapse of the Soufrière Hills volcano in Montserrat ($L > 4$ km, $V > 0.05$ km^3, $A > 2.7$ km^2). These authors describe overlapping, rotated toreva structures 50 m high and > 100 m in maximum dimension with pre-failure stratigraphy intact. Voight *et al.* (2002) also describe hummock bounded by normal faults, representing horst and graben structures of and extensional emplacement system. Furthermore, imbricate thrusts and strike slip faults are observed in the distal reaches of the deposit and near channel constrictions as compressional stresses dominated. Deformation structures, such as block deformation, shear textures and clastic dikes, are increasingly recognized in the distal parts of this deposit.

Naranjo and Francis (1987) describe the lobate deposit of Chile's Lastarria VDA ($L = 6.7$ km, $V = 1$ km^3, $A = 9.3$ km^2) a deposit unique because of its noticeable *lack* of the characteristic VDA features described above and in Chapter 3. The Lastarria deposit is composed of small, angular pumice and scoria fragments with little mechanical strength, possessing no large blocks or hummocky topography, which is generally featureless. It is therefore suggested that the mechanical competence of the constituent material is a determining factor in subsequent deposit topography (Naranjo and Francis, 1987; Francis and Wells; 1988; Siebe *et al.*, 1992). The morphology of this deposit therefore stands in stark contrast to deposits such as Jocotitlan, whose mechanical strength held the constituent material together during emplacement, producing the extreme relief observed.

4.3. Emplacement fundamentals

Though the deposits detailed above are unique in terms of scale, material properties, initiation mechanism and deposition basin geometry, they each possess similar morphologic features. The features discussed in Chapter 3 have generally been observed in each of these deposits: block and matrix facies, hummocks, toreva blocks, steep margins and deformation structures. Furthermore, the spatial arrangement of these features is generally consistent in each case. For instance, toreva blocks are most commonly located proximally to medially and separated by closed basins and normal faults, representing

purely extensional behaviour in these areas. Torevas decrease in size distally and give way to conical or irregular hummock forms which are either aligned randomly or parallel to the principal direction of emplacement. As the proportion of block facies decreases, the matrix facies proportion increases as blocks disaggregate and fine-grained basal material is entrained. It is in these distal locations, representing latter stage emplacement behaviour, where observed deformation structures such as basal shearing layers might be most likely to develop. Compressional features such as thrust fault complexes are for the most part observed only near deposit margins or adjacent to topographic highs. Because these themes are observed to be generally common from deposit to deposit, it is likely that the processes that form the morphologic characteristics and their spatial relationship to one another might be similar to some degree. Therefore, a general model of emplacement can be developed, which represents the fundamental processes that occur during VDA emplacement and may help to explain the development of the characteristic deposit features so often observed. In combination with similar ideas described in the literature, this general emplacement model is described below.

4.3.1. General emplacement model

Though magmatic, phreatic and seismic forces may initially be involved, VDA energy is mainly gravitational and for the most part not influenced by its unique environment (Ui, 1983; Francis and Self, 1987; Glicken, 1998; Reubi and Hernandez, 2000; Ui *et al.*, 2000; van Wyk de Vries *et al.*, 2001). Therefore, avalanche development fundamentally involves the transition from initial potential energy to kinetic energy (Ui *et al.*, 2000). A certain degree of energy may, however, be added by the locked-in gravitational stresses maintained in the edifice and any loaded substrata (van Wyk de Vries *et al.*, 2001). Accelerated creep of a failed slope leads to a slide with rapid downward and outward movement along one or several surfaces or narrow zones (Voight *et al.*, 1981; Voight *et al.*, 1983; Crandell, 1989; Siebe *et al.*, 1992; Takarada *et al.*, 1999; Vezzoli *et al.*, 2008). Early motion is characterized as frictional block sliding, perhaps in retrogressive fashion (Voight *et al.*, 1983; Glicken, 1998; Reubi and Hernandez, 2000). Lateral spreading through normal faulting and disaggregation in the upper unsaturated zone of the initial slide block develops into proximal elongate ridges transverse to flow direction (torevas) separated by closed basins, representing an extensional horst and graben system (Voight *et al.*, 1981; Voight *et al.*, 1983; Siebert, 1984; Abele, 1997; Shea *et al.*, 2008). Accordingly, pervasive normal faulting is observed in the proximal area of many deposits (Shea *et al.*, 2008). Further disruption forms progressively smaller blocks, which develop into

hummocks (Siebe *et al.*, 1992). Therefore, emplacement evolves from the slow slip of a relatively strong body over a weak basal surface or zone of limited dimension to the rapid mass flowage and spreading of a deformable body that is relatively weak throughout (Voight *et al.*, 1983; Siebert, 1984). Voight *et al.* (1983) estimate a global rock mass strength loss of 75% during this transition.

Progressive fragmentation and disintegration of the distal material develops into increasingly smaller blocks, leading to a transformation into fully developed flow, likely near the base of the edifice (Siebe *et al*., 1992). Latter stage motion involves spreading of the original rock mass into thin sheets of material where the lower parts of the initial edifice become the forward (i.e., distal) parts of the avalanche; original stratigraphic relationships are retained though highly stretched (Siebe *et al.*, 1992; Schneider and Fisher, 1998; Clavero *et al.*, 2002). Coarser block facies material comes to rest through deceleration; shearing of the block material and substrata progressively produces matrix facies material (Takarada *et al.*, 1999). Disaggregation into smaller components works to reduce the kinetic energy lost by the avalanche and increase mobility as particles interact with each other and any interstitial fluids present (Voight *et al.*, 1983; Schuster and Crandell, 1984; Francis and Self, 1987; Glicken, 1998; Reubi and Hernandez, 2000). Wet or saturated matrix facies is thought to drain away from the block facies as it becomes 'grounded' and deposits though deceleration, thus forming block-facies hummocks (Ui *et al.*, 1986; Crandell, 1989; Palmer *et al.*, 1991). A pulsating or surging type motion of the flowing avalanche has been suggested by Voight *et al.* (1981), Voight *et al.* (1983), Schneider and Fisher (1998) and Legros *et al.* (2000).

It is often suggested that the edifice rock mass is highly fractured before failure through cryptodome-induced deformation, heat discharge, blast effects and hydrothermal alteration processes (Ui, 1983; Siebert, 1984; Ui and Glicken 1986; Ui *et al.*, 1986; Siebe *et al.*, 1992; Glicken, 1998; Takarada *et al.*, 1999; Reubi and Hernandez, 2000; Clavero *et al.*, 2002). Significant fracturing may also occur in the initial chaotic stages of failure through intensive shearing and lithostatic unloading, which likely also produces significant microcracking to facilitate further fragmentation during emplacement (Ui *et al.* 1986; Belousov *et al.*, 1999; Reubi and Hernandez, 2000). Additionally, brittle fracture could result from compression caused by the transfer from vertical to horizontal stresses as the avalanche moves out of the initial failure slope into the runout area (Shea *et al.*, 2008).

In comparison to the fracturing occurring near source, relatively little progressive fragmentation is thought to occur during emplacement, as confirmed by the grain size studies of Ui and Glicken (1986), Endo *et al.* (1989), Glicken (1998) and Belousov *et al.* (1999). Fragmentation, disaggregation and general load stress relief leads to bulking (i.e., dilation) of the failure mass, which has the effect of reducing normal stresses and allowing the transition to avalanche flow to occur. Volumetric increase decreases bulk density and particle separation results in decreases frictional and cohesional resistance (Voight *et al.*, 1983). Internal friction is also lowered through packing rearrangements, rebounds from clast collisions and the increased mobility of pore fluids and juvenile or hydrothermal gases (Glicken, 1998). Dilation of up to 30% of original failure volume has been reported (Glicken, 1998; Voight *et al.*, 1983; Kerle and van Wyk de Vries, 2001; Shea *et al.*, 2008; Bernard *et al.*, 2008). Radial block fracture patterns and IDI as observed at the Popocatepetl and Cantal VDA deposits, respectively, is visual evidence of material bulking (Robin and Boudal, 1987; Schneider and Fisher, 1998; Reubi and Hernandez, 2000). Importantly, however, progressive trends of increasing or decreasing final (at rest) density with distance from the source have not been observed. A decreasing trend would be expected if dilation resulted from transport or shear; lack of this trend suggests the material is likely dilated to its maximum extent through near-source shattering and not dilated further during emplacement (Glicken, 1991, 1998; Siebe *et al.*, 1992). Therefore, maximum dilation is likely achieved near the base of the failed edifice where the avalanche begins to attain its true flowing and mobile character; continued bulking is not thought to be necessary to sustain flow (Glicken, 1991; Sousa and Voight, 1995). No discussion of dynamic (in motion) density was presented by these authors

Deposition results from a loss of kinetic energy. The exact process is debated: progressive upward aggradation may occur through volume reduction caused by deflation or shear stress conditions falling below the material yield strength (i.e., *en masse* 'freezing') (Crandell *et al.*, 1984; Robin and Boudal, 1987; Crandell, 1989; Endo *et al.*, 1989; Siebe *et al.*, 1992; Voight and Sousa, 1994; Schneider and Fisher, 1998; Belousov *et al.*, 1999; Francis and Oppenheimer, 2004; Bernard *et al.*, 2008). During *en masse* deposition, the avalanche comes to rest essentially as a single unit; steep lateral and distal margins are evidence of this (Siebe *et al.*, 1992). Friction related structures such as pseudotachylyte may further support this hypothesis (Schneider and Fisher, 1998; Legros *et al.*, 2000). In any case, thrust and imbricate faulting and other compressional regime structures are formed mostly in distal areas in the moments immediately preceding deposition or as avalanche velocity slows as it encounters elevated topographic features. Emplacement

time of recent VDA examples, Mount St. Helens and Montserrat, was approximately 10-15 minutes (Voight *et al*., 1983; Voight *et al*., 2002).

4.3.2. Emplacement behaviour zonation

Based upon the discussion above, characteristic VDA deposit features can be considered as direct products of the controlling geomechanical processes occurring at a given time of avalanche emplacement. At the very least, deposit features are indicative of the general stress conditions being experienced at a particular instance and/or the relative organization of the avalanche. This idea is similar to that of Bull *et al.* (2008) and Shea and van Wyk de Vries (2008) who used the term *kinematic indicators* to refer to the deposit features which reflect avalanche behaviour. For instance, flow-perpendicular normal faulting and toreva blocks represent extensional conditions and are most prevalent in the proximal areas of VDA deposits (Shea *et al*., 2008). Compressional conditions are represented by complex folding and reverse/thrust faulting complexes in the distal deposit areas as initial momentum is lost and topographic highs are encountered (Kelfoun *et al*., 2008; Shea and van Wyk de Vries, 2008). Furthermore, variations in surface feature (i.e., hummocks and torevas) morphology, from proximal flow-perpendicular linear forms to distal irregular or flow-parallel forms, might indicate a reduction in block sliding and an increase in matrix control (Takarada *et al*., 1999; Shea *et al*., 2008). Thus, it may be possible to use the presence and morphology of characteristic deposit features to determine the likely geomechanical conditions present at a particular space and time during a given avalanche's emplacement. In turn, areas likely experiencing similar emplacement conditions might then be grouped at deposit (i.e., map) scale, ultimately allowing for a straightforward delineation of a given deposit into areas of varying emplacement behaviours and a general emplacement history to be developed. Multiple VDA events might also then be qualitatively compared to recognize likely similarities/differences in their emplacement behaviours.

Several distinct geomechanical stages of the general emplacement model introduced above can be identified; in turn, each of these stages is generally recognizable as a zone of distinct character on the surface of a given deposit, if present. In total, these stages represent the complete geomechanical evolution of a VDA from failure initiation to deposition.

4.3.2.1. Frictional block sliding stage

The initial stage of the general model, after the first instance of failure, is characterized mainly by frictional block sliding of a relatively intact failure mass (Voight *et al.*, 1983; Glicken, 1998; Reubi and Hernandez, 2000). Overall avalanche body deformation is likely to be relatively insignificant though brittle fracture and disaggregation of the initial rock mass with associated bulking/dilation is likely taking place, representing the period where Voight *et al*. (1983) suggest global rock mass strength is significantly reduced. Avalanche body extension too, is minimal, though may be in the early stages of development through by large-scale faults developing in upper unsaturated zones (Voight *et al.*, 1981; Voight *et al.*, 1983). Significant deposition of material is likely also limited as the generally coherent failure mass is travelling relatively intact with considerable kinetic energy. This stage is best described as the *frictional block sliding* behavioural stage and is recognized at deposit scale by the general absence of significant deposition of material within the proximal confines of the known limits of the deposit (Zone A).

4.3.2.2. Main extensional stage

As emplacement evolves rock mass fracture and dilation are relatively complete as the failure begins to organize itself into a steady flow at the base of the failed edifice, representing the next general stage of emplacement (Ui and Glicken, 1986; Endo *et al*., 1989; Glicken, 1991, 1998; Siebe *et al*., 1992; Schneider and Fisher, 1998; Belousov *et al*., 1999; Clavero *et al*., 2002). Disaggregation of large blocks likely progresses through evolving horst and graben-type processes and the general separation of previously fractured blocks (Voight *et al.*, 1981; Voight *et al.*, 1983; Siebert, 1984; Abele, 1997; Shea *et al.*, 2008). It is at this point, where considerable horst and graben and associated normal fault offset develop, that the overall length of the avalanche likely begins to significantly extend (Siebe *et al*., 1992; Clavero *et al*., 2002). From the most proximal point of this stage, large-scale intact blocks, torevas, are deposited as momentum is continuously lost. Progressively smaller blocks deposit with distance; continuous block disaggregation and basin material interaction likely leads to the development of the distinct block and matrix facies (Glicken, 1991, 1998; Takarada *et al*., 1999). This stage of emplacement, termed the *main extensional* stage, likely represents the majority of the behaviour of a VDA not significantly affected by runout basin topographic highs. Recognition of this stage as a deposit scale zone (Zone B) may be most easily done by the distinct block facies, represented by progressively smaller torevas and hummocks on the deposit surface with

distance from source. Many block groups may also possess a macroscopic jigsaw fit across contacts and linear blocks are most often aligned perpendicular to the principle direction of emplacement (Glicken, 1991, 1998; Siebe *et al*., 1992). Longitudinal lineations, furrow and ridge features are additional distinguishing features of this zone (Wadge *et al*., 1995; Belousov *et al.,* 1999; van Wyk de Vries *et al*., 2001; Kelfoun *et al*., 2008).

4.3.2.3. Progressive deposition stage

As blocks are deposited and the proportion of saturated matrix material increases, the avalanche likely attains a character defined less by frictional sliding, block faulting and disaggregation but by matrix deformation and flow, marking a transition to the next stage of emplacement (Crandell, 1989; Takarada *et al.*, 1999). It is early in this stage where avalanche mobility is likely at its peak (not including possible downstream lahars) as turbulence among the now smaller particles of the failure mass is at its highest and/or significant saturated matrix material has been entrained (Voight *et al.*, 1983; Schuster and Crandell, 1984; Francis and Self, 1987; Glicken, 1998; Reubi and Hernandez, 2000). Increased mobility leads to zones containing increased deformation of surface features, such as random or flow-parallel alignments of hummocks and hummock trains (Siebert, 1984; Ui, 1989; Glicken, 1998; Clavero *et al*., 2002; Shea *et al*., 2008). Complex hummock shapes of relatively lower amplitudes might also be increasingly common (Siebe *et al*., 1992; Clavero *et al*., 2002). However, as the early part of this stage likely represents a peak of avalanche mobility, it might also signify a general transition to a decline in overall avalanche energy due to momentum loss, dependent on the properties of material constituents involved. Therefore, as this period likely represents a progressive transition to depositional behaviour in ideal cases, it is referred to here as the stage of *progressive deposition*. As mentioned above, this stage is identifiable as a deposit scale zone (Zone C) by a shift towards randomly or flow-parallel orientated hummock features. A reduction in the jigsaw fit of large-scale blocks and the clearly recognizable block facies in general may be another distinguishing characteristic, as observed by Siebe *et al*. (1992).

4.3.2.4. Compressional deposition and lahar conditions stage

Avalanche behaviour during the progressive deposition stage likely becomes increasingly dependent on material yield strength and/or saturation levels. Where each of these properties is moderate, deposition most likely ensues from a progressive reduction in

momentum, identifiable at deposit scale as generally featureless margins. Where yield strengths are considerable, deposition may develop more abruptly through upward aggradation or material 'freezing', producing steep-sided or slightly raised margins (Robin and Boudal, 1987; Belousov *et al.*, 1999; Richards and Villeneuve, 2001; see also Section 2.4). As margins of this type often contain imbricate thrust structures, they can be thought of as compressional stress regime margins, thus defining a fourth stage of emplacement, *compressional deposition* (Voight *et al.*, 1983; Siebe *et al.*, 1992; Glicken, 1998). More obvious instances of compressional deposition develop from an avalanches' encounter with adjacent topographic highs, which may deflect the failure mass considerably and produce significant thrust fault and fold structures often discussed in the literature and likely observable at deposit scale (Zone D; Voight *et al*., 1983; Siebe *et al*., 1992; Wadge *et al*., 1995; van Wyk de Vries *et al*., 2001; Kelfoun *et al.*, 2008). Bulldozer facies may be another clear indication of compressional conditions (Siebe *et al*., 1992; Belousov *et al*., 1999). Where material yield strength is low and/or the failure mass sufficiently saturated, a stage of debris flow or *lahar conditions* may develop down-valley or after general deposition of the main avalanche body (Voight *et al.*, 1983; Schuster and Crandell, 1984; Siebert *et al.*, 1987; Glicken, 1991; McGuire, 1996, 2003). Such an event was witnessed after the 1980 Mount St. Helens VDA and suggested for the Mount Shasta (Voight *et al.*, 1983; Crandell *et al*., 1984; Siebert, 1984; Siebert *et al.*, 1987; Crandell, 1989). At deposit scale, development of lahar behaviour might be most easily recognized by flat, featureless distal margins and/or clear transitions into down-valley watershed drainages (Zone E; e.g., Mount St. Helens and Mt. Shasta per Voight *et al*. [1983] and Crandell [1989], respectively).

The stages of VDA emplacement and associated deposit features that might be used to recognize these distinct behaviours at deposit scale are summarized in Table 1 and the generalized schematic shown in Figure 10. It should be noted that Table 1 is meant only as a general and provisional guide for using debris avalanche deposit features as a means of identifying likely emplacement behaviours occurring in specific areas of the failure body. There are, of course, important components that are not universal to a general VDA emplacement scenario and therefore not recognized in this deposit behaviour recognition scheme, such as intense topographic reflection (e.g., Socompa, Section 4.2.3), blast involvement (e.g., Mount St. Helens, Section 4.2.1), retrogressive collapsing (e.g., Mount St. Helens, Section 4.2.1), and significant basin material entrainment (e.g., Chimborazo, Section 4.2.8). These aspects likely have significant effects on avalanche emplacement behaviour and would subsequently result in deposits with varying character. For instance,

an immense blast may add significant energy to the avalanche system and result in highly shattered avalanche material, leading to significantly different emplacement behaviour than a system where blast energy might not be involved and initial avalanche material was comprised of relatively large-scale and intact blocks not affected by blast energy. With this in mind, the emplacement behaviour recognition scheme discussed here is designed to reflect an idealized scenario where these complicating factors are generally neglected and only the deformation sequence of an edifice slope with a listric failure geometry, to result in an extended and thinned deposit at the base of the failed edifice, is considered. The effects of any factor considered to be outside of the common deformation sequence must be considered on a case-by-case basis.

Though not verified in the field directly, the classification system discussed here has been developed from the body of literature discussing VDA emplacement mechanics specifically, the central theories of which are directly based on concentrated field interpretations. Likely avalanche behaviours are based on the most reasonable mechanics to have created each particular deposit scale recognition feature. For instance, toreva block structures bound by normal faults are assumed to be created trough extensional mechanics, not by some other inexplicable means. As VDA emplacement is an extremely complex and spatially variable phenomenon, departures from the simplified classification system presented in Table 1 most certainly exist. Furthermore, if a behaviour or stage recognition feature is noted in one stage, it does not necessarily mean it is unique to that particular stage as most processes are continuously changing and evolving over the entire period of emplacement. For example, frictional block sliding likely occurs to some degree throughout the entire duration of avalanche emplacement; it is in the early stages, however, where this type of behaviour is most prevalent and/or dominant (Voight *et al.*, 1983; Glicken, 1998; Reubi and Hernandez, 2000). All other behaviours and stage recognition features are classified in a similar manner: where they are likely most prevalent and/or dominant. Even with the above limitations in mind, the classification system presented in Table 1 can be considered as a generally consistent guide for recognizing various avalanche emplacement behaviours and evolving emplacement mechanics at deposit scale.

Table 1 – Emplacement behaviour stages and associated deposit zones representing the evolution of emplacement behaviour and associated deposit morphology.

Emplacement behaviour stage (Deposit scale zone)	Likely dominant avalanche behaviour	Deposit scale recognition features
Frictional block sliding (Zone A)	• Frictional block sliding	• General absence of proximal deposition
	• Disaggregation/fracture of in situ material	
	• Development of extensional (normal) and strike-slip faulting	
Main extensional (Zone B)	• Progressive reduction in frictional sliding	• Longitudinal features (furrows, ridges, lineations)
	• Progressive disaggregation of block material	• Normal faulting perpendicular to flow direction
	• Progressive development of matrix facies and fluid-like flow/spreading	• Strike-slip faulting parallel to flow
	• Progressive development of basal shearing/deformation layer	• Horst and graben development
	• Progressive entrainment of basin material	• Lack of compressional features (thrust faulting, low flow perpendicular ridges)
	• Transport-parallel extensional strain	• Toreva block deposition
		• Jigsaw fit of large-scale blocks
		• Block linearity perpendicular to flow direction
Progressive deposition (Zone C)	• Initial increased mobility	• Reduction in number of blocks/hummocks perpendicular to flow direction
	• Progressive deposition if not sufficiently saturated or yield strength controlled	• Increase in random orientation of hummocks
	• Progressive increase in the influence of yield strength	• Increase in conical and complex hummock shapes with lower amplitude and diffuse outlines
		• Increase in number of blocks parallel to flow direction
		• Reduction in large-scale block jigsaw fit
Compressional deposition (Zone D)	• Relatively abrupt deposition through upward aggradation or yield strength 'freezing'	• Compressional features (i.e. thrust faulting, complex folding, flow perpendicular ridges and bulldozer facies)
	• Abrupt movement cessation upon encountering topographic barriers	• Raised margins
	• Transport-perpendicular compressional strain	• General proximity to topographic highs
Lahar conditions (Zone E)	• Turbulent, fluid-dominated mechanics	• Flat, featureless distal margins
	• Flow direction dictated mainly by topography (drainage)	• Narrow topographic channelling

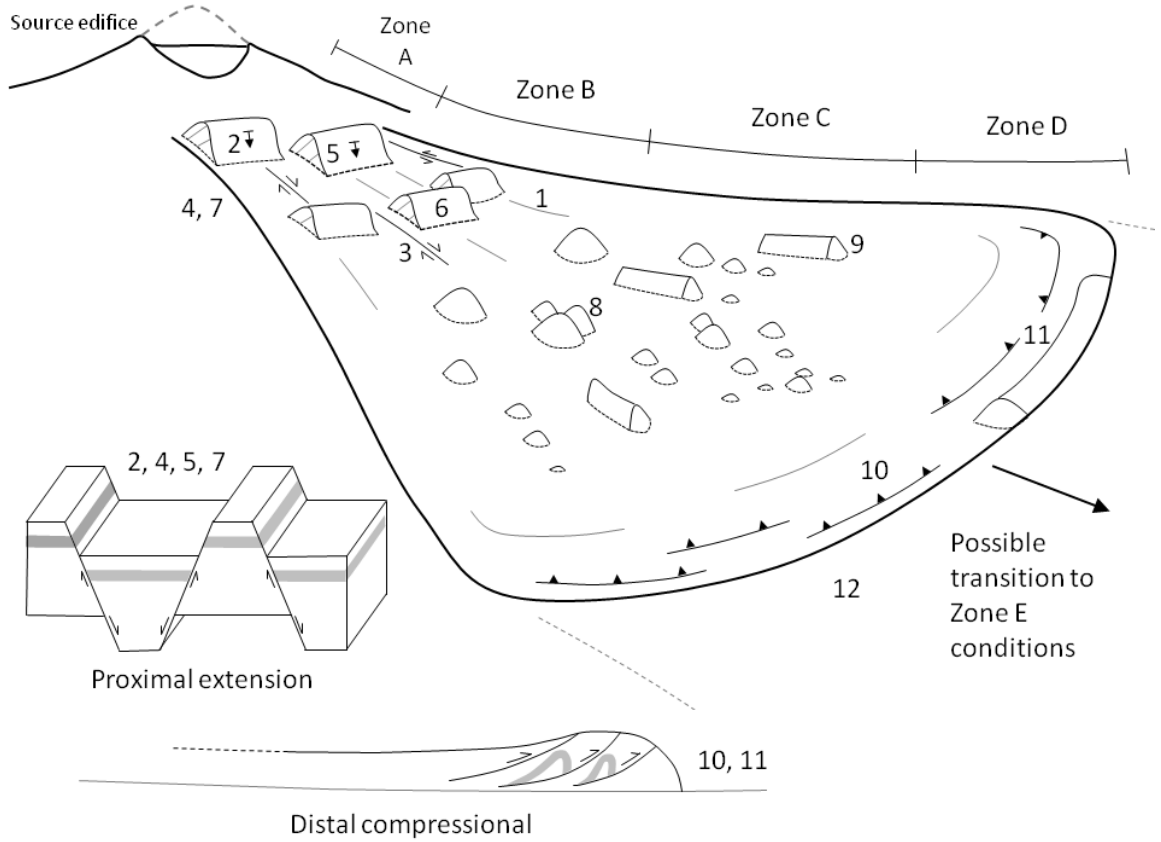

Figure 10 – Schematic of a generalized VDA deposit showing the zone features which might be used to recognize the emplacement behaviour stages discussed in this section, generally corresponding to the discussion summarized in Table 1. The insets show a basic diagram which depicts horst and graben development, as would generally be seen in the proximal area of the avalanche and subsequent deposit (proximal extension), and the manner in which raised margins, thrust fault complexes and stratigraphic folding might occur in the distal areas. Numbers depict 1) flow-parallel lineations; 2) flow-perpendicular normal faulting; 3) flow-parallel strike-slip faulting; 4) horst and graben development; 5) toreva block deposition; 6) jigsaw fit of proximal blocks (depicted here by a close spatial relationship); 7) flow-perpendicular block linearity; 8) conical and/or more complex hummock shapes; 9) flow-parallel block linearity; 10) compressional features (thrust faulting/folding); 11) raised margins, and ; 12) featureless distal margins if transitions to lahar conditions might occur (also denoted by distal gray dashed lines). Transport direction to the right from the source edifice, in the direction of the large black arrow. Dashed line on source edifice denotes the area vacated by the failure mass. Not to scale.

4.4. Discussion

The first part of this chapter went beyond the basic description of common VDA deposit features (Chapter 3) to consider them in a number of notable cases, representing the extent of the literature on this particular subject. The likely formation mechanisms of these features and the general emplacement sequences of each event, as hypothesized by the associated authors, have been summarized. Though many of the characteristic deposit

features have developed in a varying range of conditions and environments, their morphology, orientation and spatial variation are in most cases remarkably similar. A primary example of this phenomenon is toreva blocks which are always located in the proximal sections of the deposits and possess a steep-sided triangular morphology typical of horst and graben extensional systems. It is therefore reasonable to assume that the geomechanical processes that lead to the development of these features might be similar in each case and thus controlled mainly by a common deformation sequence. Based on this idea, a general VDA emplacement model has been discussed, which defines the controlling processes of VDA emplacement from failure initiation to deposition. The general emplacement model can be defined by several stages where geomechanical behaviour is thought to vary and/or be controlled by differing stress regimes: the frictional block sliding, main extensional, progressive deposition, compressional deposition and lahar condition stages. In turn, a general classification system whereby avalanche behaviour during these stages might be identified as distinct morphologic zones in a VDA deposit has been discussed. Zones are identified by common morphologies and spatial arrangements of the major characteristic features observed. These zones distinguish the key emplacement processes that are occurring during evolving VDA emplacement and can be considered generally universal to all cases, though their precise location, extent and specific characteristics may vary. Exceptions to this universal assumption are cases where topographic barriers are not encountered to develop compressional structures (Zone D) or saturation is not sufficient enough to develop distal lahars (Zone E). The general model is, however, sufficient to describe the fundamental geomechanical processes occurring during VDA emplacement. Mapping VDA deposits using the associated zone classification system outlined here may allow for valuable insight to be developed on debris avalanche emplacement evolution, including comparisons between events. The following chapter will apply this concept to several VDA deposits in order to test these ideas put forward above.

Chapter 5 - Orthophoto imagery analysis

The objective of this chapter is to examine high-resolution orthophoto imagery of VDA deposits and identify the spatial variations in the morphology of the characteristic features discussed in the previous chapters. As recognized in Chapter 4, changing morphologic characteristics can be used to identify various stages of the geomechanical evolution occurring during emplacement of a VDA. This chapter aims to identify the avalanche behavioural zones discussed in the Chapter 4 at several notable VDA deposits, thus testing the ideas put forward therein. Additionally, several quantification exercises are conducted to further distinguish the distinct geomechanical stages in the evolution of a VDA and recognize the characteristics that might be common to all cases considered.

Key questions:

- What is the spatial variation in the morphology and orientation of characteristic VDA features?
- Are the variations identified common to all cases considered?
- Are the characteristics of the common deposit features identified and mapped consistent with the emplacement model put forward in the previous chapter and what does this tell us about emplacement behaviour?

5.1. Introduction

According to the discussion in Chapter 4, VDA emplacement can be considered as an idealized sequence of evolving mechanics from proximal block sliding and disaggregation to more flowing but topographically controlled conditions distally. These processes are reflected in deposit morphology, which is best observable at deposit scale. High-resolution orthophotographic imagery is the most practical tool for this approach as it allows both qualitative and quantitative observations to be made in regards to avalanche emplacement kinematics and morphologic characteristics. Qualitative methods of this nature have been used successfully by previous authors (Wadge *et al.*, 1995; Kelfoun *et al.*, 2008; Shea *et al.*, 2008) at Socompa and other large-scale rock and debris avalanches and are extended here to additional VDA deposits which display macroscopic features particularly useful for developing insight into emplacement processes.

5.2. Methods

Six deposit images were analysed in this exercise: Mt. Shasta, Socompa, Jocotitlan, Shiveluch, Parinacota and Tata Sabaya (Bolivia). These particular deposits were chosen for several reasons. First, each deposit displays features, such as toreva blocks, hummocky topography and surface expressions of faults that are easily visible on the deposit surface. In this sense the deposits have either been generally preserved or not significantly concealed by subsequent volcanic or fluvial deposits and/or vegetation. Secondly, each of these events has been thoroughly considered in the literature with significant discussion based on field investigation. This is particularly true in the case of Socompa though an exception to this point is the Tata Sabaya VDA deposit which has thus far been only briefly discussed (e.g., Francis and Wells [1988] and Francis and Oppenheimer [2004]). This deposit does, however, show striking morphologic features easily visible on a large scale and is thus included here. The infamous Mount St. Helens deposit is not included due to its heavy valley confinement and significant deposition of post-emplacement eruptive materials which has obscured key features at the available orthophoto resolution.

With the exception of Mt. Shasta, mapping of each deposit was accomplished by image interpretation using data obtained by the Advanced Spaceborne Thermal Emission and Reflection Radiometer (ASTER) aboard NASA's Terra satellite, launched in 1999. ASTER provides high-resolution (15-90 m) visible and near-infrared (NIR) imagery with a swath width of 60 km (Abrams, 2000; Stevens *et al.*, 2004). The Terra satellite has been collecting ASTER data since February 2000 with a 16-day orbital repeat cycle (Stevens *et al.*, 2004). The ASTER imagery was obtained from NASA's Land Processes Distributed Active Archive Center (LP-DAAC) website (NASA, 2008). False-colour composites were created using bands 1 (green), 2 (red) and 3N (NIR, near infrared). These bands use the finest spatial resolution of all ASTER bands, 15 m, whilst the use of NIR reduces the effects of atmospheric haze and maximises contrast. Terra's orbital altitude (≈ 705 km) results in negligible geometric and terrain distortions which for the purposes of this study were ignored.

Data from the National Agriculture Imagery Program (NAIP) was used for imagery interpretation of Mount Shasta deposit. This 1 m resolution orthophoto (planimetrically correct, with image and terrain distortions removed) was obtained from the California Spatial Information Library (CaSIL) as a county mosaic acquired during the 2005 survey (CaSIL, 2009). The intention of the NAIP, which has been in development since 2001, is

to obtain peak growing season 'leaf on' orthophotos for agricultural purposes for the whole of the continental United States (NAIP, 2009).

Following the summaries given in the preceding chapter, the notable topographic features and kinematic indicators of each deposit are first described. In the case of the Tata Sabaya VDA, which has not been thoroughly detailed in the literature, only a brief summary can be given to accompany the imagery analysis. Morphologic features are then mapped onto each image with ESRI's ArcGIS ArcMap software. The first step in this process was to transfer features mapped by previous authors onto each image, including deposit area (outline/extents), fold and fault structures, torevas and hummocks and any additional features which may have been discussed and/or mapped in the literature. Topographic maps and additional spatial imagery tools, such as Google Earth©, were used to supplement the mapping where available. Toreva structures, if observed, are marked in red and hummock features are marked in blue. This is in a sense arbitrary; a toreva can be regarded as a large-scale hummock in the proximal area of the deposit with its long axis perpendicular to the principal emplacement direction. This distinction is done simply to highlight the existence, scale and location of toreva blocks; where hummock statistics such as area and number documented are given, torevas are included. The location and limits of these kinematic structures and features may differ from the locations mapped by previous authors or actual cases to some degree as a result of reduced image resolution, topographic interpretation and general uncertainty due to image scale. The measured values obtained, however, are generally similar to those presented in the literature and may therefore represent updated constraints on feature scale (e.g., areal extent, Table 2). In some cases, dimension measurements of some of the more notable deposit features are performed and compared to the values obtained in previous studies for validation purposes. Reasonably distinguishable morphologic features not shown specifically in maps within the literature, but perhaps discussed, were then mapped, including hummocks and toreva blocks. Similar to the field exercises of previous authors (Siebert, 1984; Siebe *et al.*, 1992; Glicken, 1998; Clavero *et al.*, 2004; Shea *et al.*, 2008), length and orientation of the long and short axes of all features were recorded, allowing any systematic variation in these metrics with emplacement distance to be investigated (Figure 11). The location and nature of these features represent key kinematic indicators when considered on deposit scale; smaller-scale features not visible within the given image resolution were likely unrecognizable and have therefore been mapped as groups rather than individually.

Each deposit is then separated into the emplacement behaviour zones as introduced in Section 4.3.2. The internal limits of these zones have been mapped with each of the associated recognition feature criteria in mind, though a degree of uncertainty exists. Transitions from one zone to the next likely represent a progressive abruptness. For instance, the transition from frictional block sliding (Zone A) to the main extensional stage zone (Zone B) are likely much more gradual than the transition from progressive depositional behaviour (Zone C) to a compressional stress regime (Zone D) as a travelling avalanche may rapidly come into contact with adjacent topographic barriers. The transition to more fluid-like lahar situations (Zone E), however, likely always represents a gradual and progressive process as the avalanche deposits blockier material and increasingly develops finer-grained matrix material through disaggregation, pulverization and the entrainment of fine-grained and potentially saturated basin sediments. Lastly, based on the combinations of kinematic indicators recognized in the literature and orthophotos, hypothetical flow lines are then qualitatively drawn as best interpretations of emplacement course. These lines represent likely emplacement directions and are included to give the reader a general sense of avalanche motion in each case; they have not been specifically verified in the field.

In the case of Mount Shasta, Parinacota and Tata Sabaya, the collapse scar has been filled in by post-collapse volcanic materials. Hypothetical headwall scars have therefore been included on these images to indicate likely collapse direction and scale. The zone of frictional block sliding (Zone A) in these examples begins at an arbitrary point downslope from hypothetical collapse amphitheatres. If marked accordingly by previous authors, the distal extent of Zone A projects into the deposit margins to the point where block deposition is observed. If deposit margins have not been marked in the literature, Zone A extends to the proximal limit of the deposit denoted on each image by proximal block deposition. When applying the zone distinctions to each deposit, open space is occasionally left (i.e., no zone distinction given) at the most distal axial and lateral points as the deposit margins are often unclear in the literature or not distinct at image scale. Such may be the case where a deposit margin is not clearly defined by topography or steep slopes. Distances given are in the general direction of principal flow and measured from the summit, or hypothetical summit, of each edifice.

Table 2 – Areas covered by particular VDA deposits, both calculated from ArcGIS measurements and presented in the literature. Slight deviations from the documented deposit area values are likely due to image resolution, topographic interpretation, observational subjectivity and the fact that some authors may have included the collapse scar as part of the deposit area calculations, thus increasing those values. Areas calculated here do not include collapse amphitheatres with the exception of the 1964 AD Shiveluch event as this collapse amphitheatre is commonly included in the deposit area in the literature.

Deposit	Calculated area (km^2)	Published area (km^2)	% Difference
Mt. Shasta	680	675	0.8
Socompa	529	550	3.5
Jocotitlan	73	80	8.8
Shiveluch	105	100	5.6
Parinacota	133	150	10.8
Tata Sabaya	282	331	15.0

Figure 11 – Hummocks of the Mount Shasta VDA deposit showing axis definitions. Feature long axes (white) were regarded as the largest dimension and short axes (red) were taken as the largest dimension perpendicular to the long axis. Axis length and orientation were recorded for each surface feature reasonably distinguishable at the given orthophoto resolution.

5.3. Case studies

5.3.1. Mount Shasta

The Mount Shasta VDA deposit presents one of most remarkable examples of hummocky topography with hundreds of large, extraordinarily conical features present over the area of the deposit, which often influence the location and construction of modern infrastructure, such as roads and settlements. In the most comprehensive description of this event, Crandell (1989) discusses the obvious behavioural differences of the block and matrix facies; proximal/medial deposition of less mobile blocks to form conspicuous hummocks and ridges and subsequent draining of highly mobile, potentially saturated matrix into distal debris flow. Unfortunately, structures clearly indicative of emplacement kinematics (folds and faults) are either only briefly explained by previous researchers or not visible at image scale. This fact is likely due to: A) erosion as a result of the older age of the deposit (300,000 – 380,000 ybp), or B) the distinct contrast between the potentially saturated matrix and block facies where low matrix cohesion may have resulted in a lack of structure formation, as opposed to a generally cohesive failure such as Socompa. With this in mind, hummock geometry and orientation is used as the principal kinematic indicator.

Hummocks at Mount Shasta are typically covered by vegetation unlike that of the inter-hummock area and are therefore clearly visible on the orthoimage, due in part to the higher quality of this particular image (1 m resolution) (Figure 12). Therefore, features could be mapped with a high degree of accuracy (Figure 13, Table 3). Opposed to the majority of the VDA descriptions below, toreva blocks have not been mapped as separate entities at Mount Shasta, though large-scale blocks with a similar morphology (triangular flow-perpendicular shape, intact source edifice stratigraphies, back-tilting) are present. This was done because though the morphology is similar to that described for torevas, they are located in the medial section of the deposit, rather than the most proximal areas adjacent to the collapse amphitheatre, such as at Socompa, Jocotitlan, Parinacota and Shiveluch. The features discussed are the medial ridges striking perpendicular to flow direction (Figure 14), which are detailed by Crandell (1989), who notes a 9 km length for the largest feature (point X on Figure 13). Though it is possible that this feature represents a single intact block system, clear separation of various sections of the feature are observed on topographic maps and it is therefore mapped as a series of blocks here. The dimensions of a number of blocks have been recorded (Table 4). The jigsaw fit of these blocks, which can be visually re-fit across contacts, is analogous to the large proximal ridge system

observed at Jocotitlan (Siebe *et al.*, 1992) and may represent the progressive disaggregation of a single large block. A series of eight ridge or hummock clusters similar to that shown on Figure 14 has been mapped by Crandell (1989) which is likewise suggested to represent the break-up of once much larger blocks of source edifice material (Figure 13).

Hummock/toreva size has been recorded by measuring the length of the long and short axes of each reasonably visible feature and plotted versus emplacement distance (Figure 15). A decrease in feature size with distance is observed though there is a rise in feature size towards the medial area of the deposit, the location of the major ridge complex discussed above. The decrease in long axis length is much steeper than that of short axis length, reflecting a change from linear to conical morphology with emplacement distance. Feature orientation, in relation to the principal flow direction (N21W, as estimated from orthophoto) is plotted in Figures 16A-C. Though overall orientations are fairly uniform, an increased number of long axes are aligned in the approximate direction of flow and short axes aligned perpendicular, indicating a stretching of blocks in this direction and/or preferential alignment upon deposition.

Table 3 – Number and area of the clearly discernible hummocks measured at the Mount Shasta VDA deposit.

Number of hummocks documented	Total area covered (km^2)	Percentage of total deposit area covered (%)	Dimensions of largest feature (m*m)[a]	Area of largest feature (km^2)[a]
1203	118.3	17.4	1200*3151	2.8

[a]Feature I in Figure 14.

Figure 12 – Example of the hummocky topography clearly visible on the orthoimage. Notice the conspicuous changes in vegetation on the hummock surface (outlined by dashed black lines). Both simple and more complex hummock forms are visible, in the west and east of the figure, respectively. General location noted on Figure 13. Lateral extent of the deposit indicated by solid yellow line.

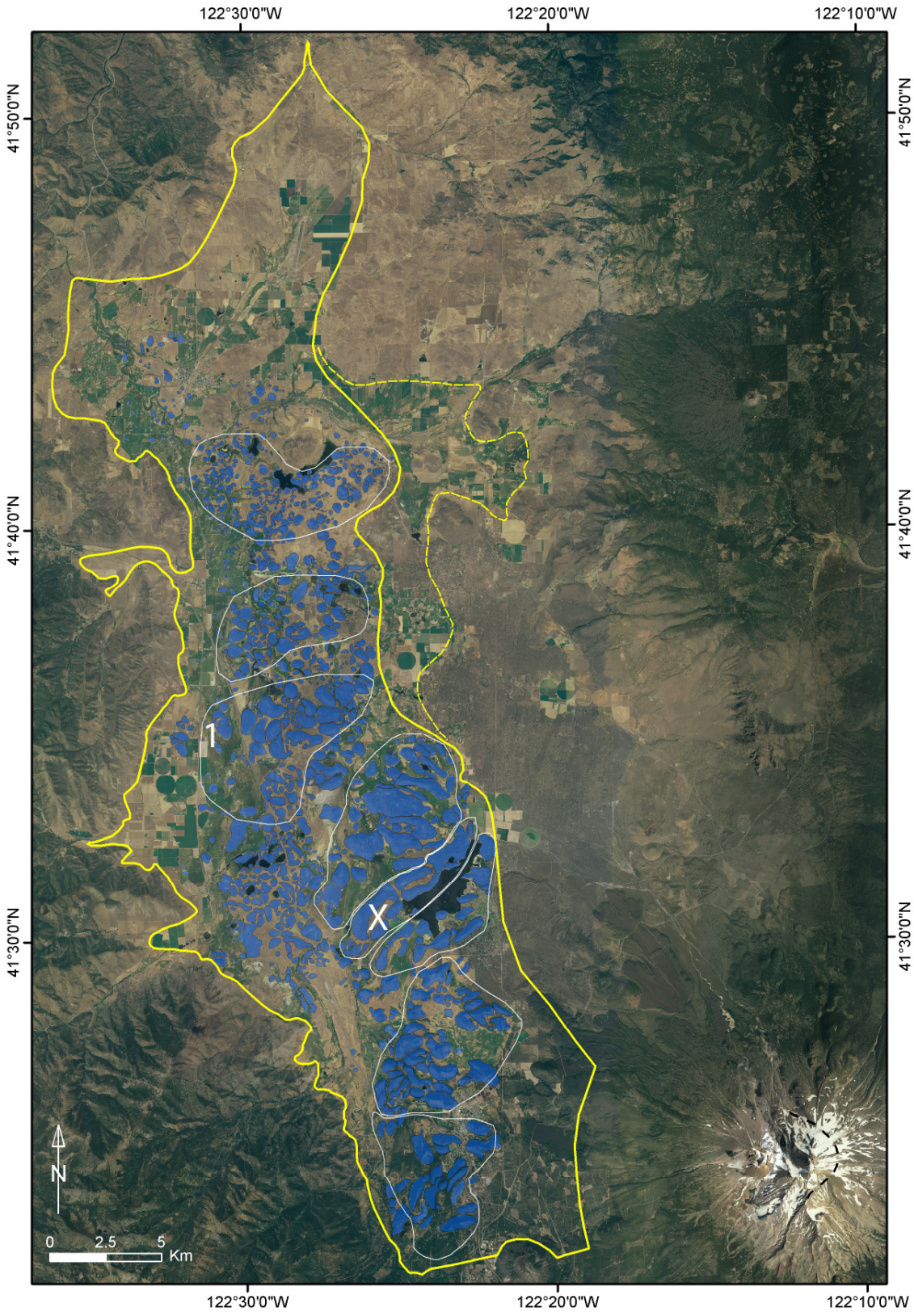

Figure 13 – Mapped distribution of hummocks and ridge features (blue) within the Mount Shasta VDA deposit (solid yellow outline). Uncertain deposit extents at the deposits eastern margin are represented by the dashed yellow line. The white outlines represent the high-standing, flow perpendicular ridge systems of Crandell (1989) and suggest the disaggregation of even larger blocks of the initial edifice. The black dashed line on the source edifice represents a likely failure geometry. The point 'X' denotes the large medial ridge block as discussed in the text, the point '1' refers to the general location of Figure 12.

Figure 14 – Medial ridge blocks aligned perpendicular to the principal flow direction, boundaries denoted by dashed black lines. General location noted by the 'X' in Figure 13, which represents the position of the large ridge block discussed by Crandell (1989). The maximum dimension of this feature was noted as 9 km by Crandell (1989), though that length has been significantly shortened here as it has been split into three separate blocks as outlined. Letters A-I note the position of the blocks measure in Table 4 with the exception of feature I, whose metrics are noted in Table 3. Solid and dashed yellow lines represent approximate lateral extents of the deposit and alternative deposits.

Table 4 – Dimensions of large medial ridge blocks, locations noted in Figure 14.

	Dimensions (m*m)	Area (km^2)
A block	700*2760	1.9
B block	545*1750	0.8
C block	500*1920	0.8
D block	805*2305	1.8
E block	400*1415	0.6
F block	420*1640	0.6
G block	990*2325	1.2
H block	515*2505	1.2

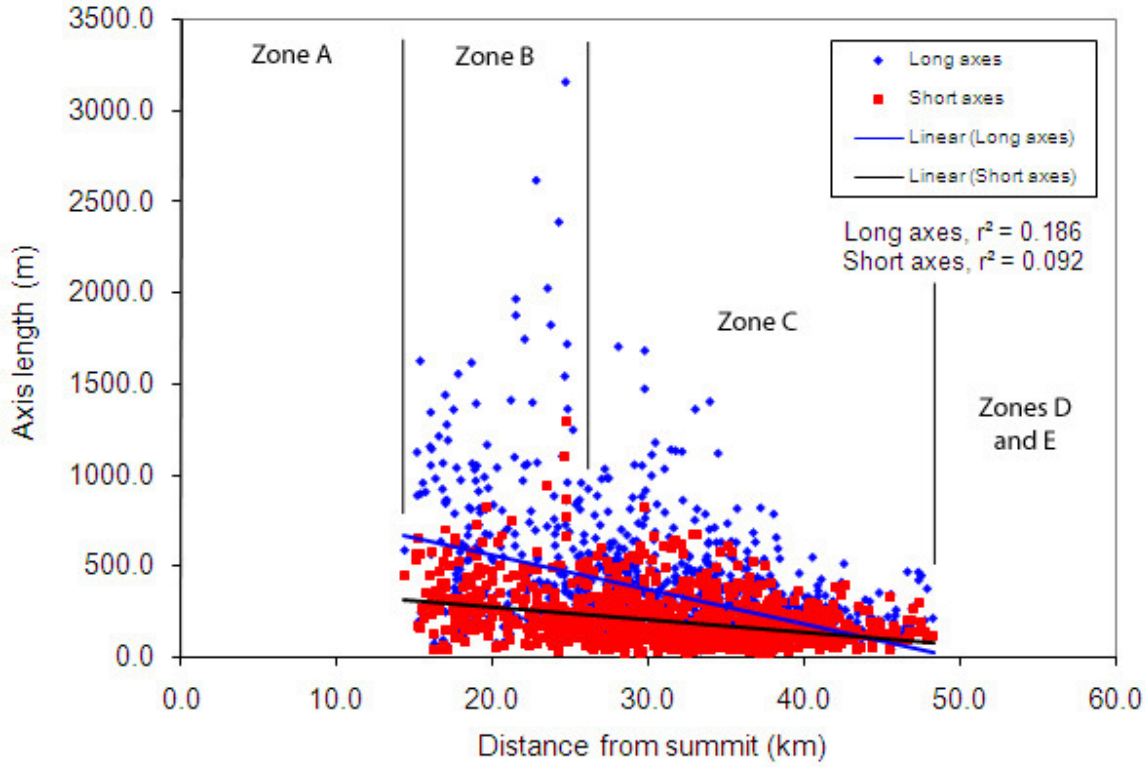

Figure 15 – Relationship between topographic feature long and short axis length versus emplacement distance from current edifice summit, Mount Shasta VDA deposit. Kolmogorov-Smirnov and Shapiro-Wilk normality tests performed in the statistical package *SPSSv.15.0* indicate non-normal distribution in this particular data set; subsequent Spearman correlation for non-parametric data sets results in a significant but weak correlation between feature axis length and distance from source (r = -0.418 and -0.303 for the long and short axes, respectively, p-value < 0.001 for both cases). Linear regression trendline used to represent the general decrease in feature size with emplacement distance. Zone distinctions based on the mean extent of each zone shown in Figure 17 and referred to in the relevant discussion.

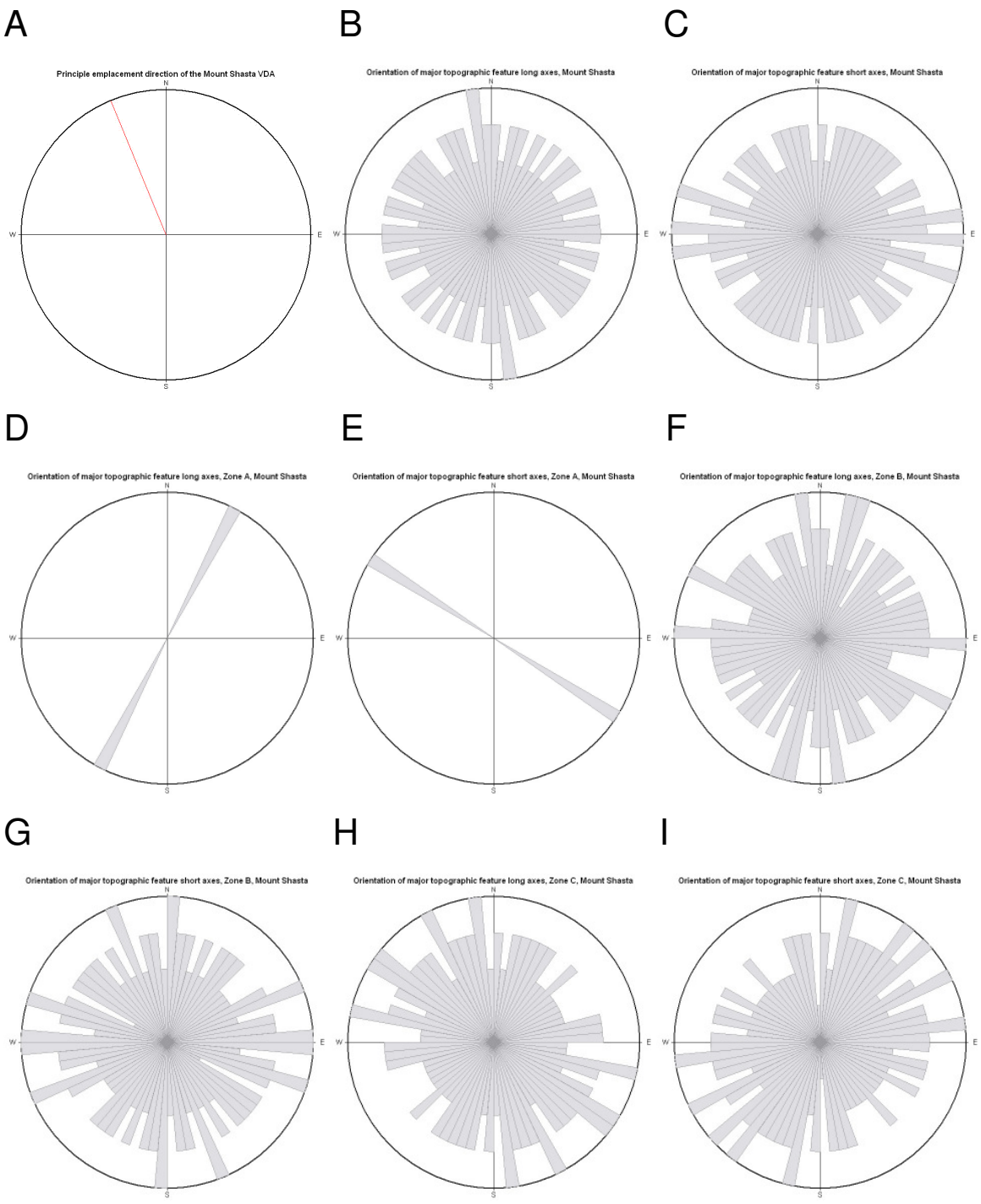

Figure 16 – Surface feature (hummock/toreva) orientation plots for the Mount Shasta VDA. Rose diagrams were generated with the software Rose, available from http://mypage.iu.edu/~tthomps/programs/home.htm. A) Orientation of the principle emplacement direction; B) Orientation of major topographic feature long axes, total deposit; C) Orientation of major topographic feature short axes, total deposit; D) Orientation of major topographic feature long axes, Zone A; E) Orientation of major topographic feature short axes, Zone A; F) Orientation of major topographic feature long axes, Zone B; G) Orientation of major topographic feature short axes, Zone B; H) Orientation of major topographic feature long axes, Zone C; I) Orientation of major topographic feature short axes, Zone C.

The emplacement of the Mount Shasta VDA is relatively straight forward in that it appears it did not encounter any topographic barriers 'head-on' but may have been gently directed

down-valley by the adjacent topographic highs. In this sense the Mount Shasta VDA represents both confined and unconfined flow and can be divided into the emplacement behaviour zones discussed in Section 4.3.2 as mapped in Figure 17. The area of frictional block sliding (Zone A) is represented by the most proximal area of the deposit as mapped by Crandell (1989) and the area immediately adjacent to the failed edifice, which has since been filled in by post-collapse materials and is therefore unrecognizable. This area extends to approximately 14 km from the source, a significantly longer distance than observed at other VDA deposits, representing either an increased amount of initial energy in the failure system or favourable runout surface geometry and/or material properties. Likewise, an influential fluidising mechanism may be partially responsible. Only one major surface feature is recognizable in this zone; its long and short axes are orientated perpendicular and parallel, respectively, to early emplacement direction (Figures 16D and 16E).

The main extensional zone (Zone B) generally begins with the first encounter of proximal large-scale blocks at approximately 14 km from source. Due to topographic confinement on the western margin of the emplacement basin, Zone B behaviour extends to only 19 km in the proximal parts of the deposit but up to 30 km down-valley (northwards). This zone is characterized by large hummocks and ridges which can easily be re-fit across contacts, representing clear progressive disaggregation and deposition of block material. Overall, long axes are randomly orientated though a slight preferential alignment in the approximate principal emplacement direction can be recognized (Figures 16F and 16G). This may be misleading for two reasons: A) initial emplacement may have been approximately perpendicular to the principal down-valley emplacement direction, resulting in topographic features aligned perpendicular to the early emplacement but parallel to principal emplacement, and; B) an abundance of smaller scale features relative to the largest blocks which are aligned perpendicular to the principal direction of emplacement. Therefore, preferential block alignment can be considered perpendicular to principal flow in this zone. Layered blocks commonly reveal normal faulting representative of extensional stress regimes (Ui and Glicken, 1986). As suggested by Crandell (1989), the southernmost hummock cluster outline shown in Figure 13 likely represents a slide block involved in the first stages of failure but was deposited in the western topographic low of the emplacement basin and not involved in subsequent movement along the principal flow direction. Zone B contains the large ridge structures surrounding Lake Shastina previously discussed and transitions into Zone C progressive depositional behaviour where the jigsaw fit of the blocks becomes generally indistinguishable. Zone C behaviour is also represented by random hummock orientations with a slight tendency toward alignment

subparallel to the principal direction of emplacement, representing further stretching of the avalanche body, deposition of the block facies and draining of the saturated matrix material (Figures 16H and 16I). As the Mount Shasta VDA was directed more to the northwest, Zone C is more prevalent on the western margin of the basin which defines the valley topographic low. Zone C behaviour likely also exists on the eastern margin of the deposit but is not mapped here as the eastern extents are questionable due to the deposition of post-emplacement volcanic and sedimentary materials. Though the Mount Shasta VDA was generally confined, compressional Zone D behaviour is for the most part not recognized in the deposit structure and morphology. The most likely occurrence of compressional conditions exists on the western margin of the deposit which is defined by a north-trending topographic high, which would have been most influential during early emplacement stages. The avalanche encountered this topographic high at approximately 20 km, likely deflecting the failure northwards. No evidence of significant disturbance in terms of topographic run-up or avalanche body/block deformation is discussed in the literature or observed on the orthoimagery. Some large blocks have been observed to 95 m above the current ground surface level along the western margin of the deposit but cannot explicitly be classified as material involved in this particular failure (Crandell, 1989). Compressional conditions may have also existed as the failure turned towards the northwest into a distal river gorge.

It is suggested that the distal reaches of the Mount Shasta VDA transitioned into lahars due to the heavy saturation and subsequent mobility of the matrix material. This change is represented in Figure 17 by the transition to Zone E behaviour beginning at approximately 36 km from source and generally marks the end of the deposition of the hummocks and block facies as mapped by Crandell (1989). This most distal point of the deposit (≈ 55 km) is mapped after Crandell (1989) and represents the movement of the mobile debris flow material into the valley of Willow Creek.

The flow lines drawn in Figure 17 represent the generally simple emplacement of the Mount Shasta VDA northwards into the emplacement basin. The early stages of emplacement along the proximal, western margin of the basin are likely to have been the most topographically affected though further encounters with topography along this margin may have occurred as the failure progressed northwards. The south-to-north distribution of the block facies (i.e., hummocks and ridges) likely represents the progressive, sequential failure of the edifice (Crandell, 1989). In this respect distal blocks represent material originally at the toe of the failed edifice while proximal blocks represent material derived

from the more internal sections of the collapse headwall. Initial emplacement may have been directed towards the west, as indicated by the flow lines drawn. However, the avalanche may have also had more of a north-northwestern initial direction but this is uncertain as the collapse scar has since been filled in by post failure materials and the deposit extents are uncertain on its eastern margin. In any case, the majority of the failure was likely directed towards the west-northwest, as suggested by the high percentage of axial block facies along this direction; the flow lines drawn reflect this behaviour.

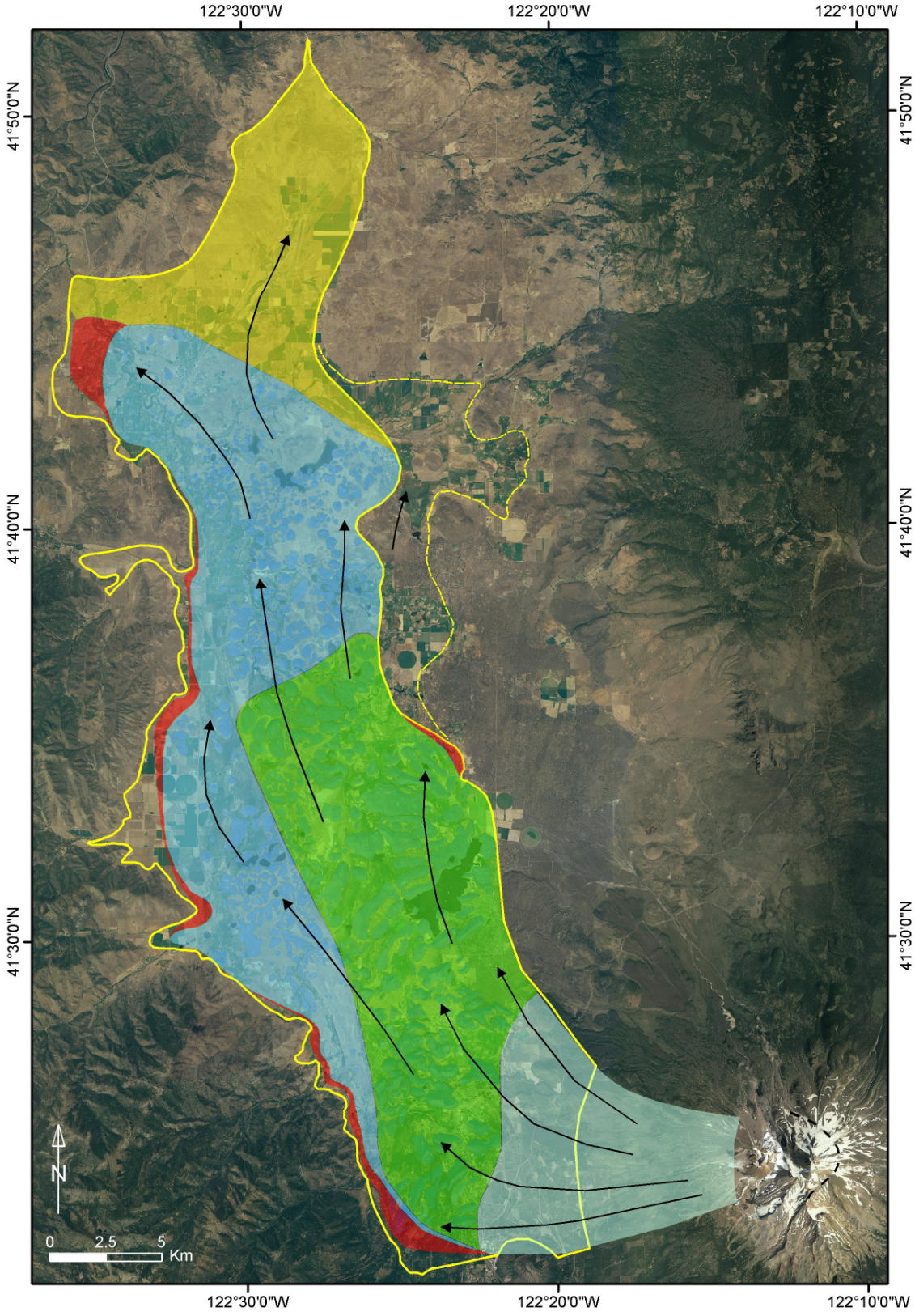

Figure 17 – Emplacement behaviour zone separation of the Mount Shasta deposit. From proximal to distal – Zone A (white), Zone B (green), Zone C (blue), Zone D (red), Zone E (orange). The black flow lines represent a likely emplacement direction scenario.

5.3.2. Socompa

The Socompa VDA is one of world's most well-studied large-scale avalanche events due is its exceptional preservation and clear mobility/emplacement process indicators. Several authors have used orthoimagery to study this deposit in a similar approach to that presented here (Wadge *et al.*, 1995; Kelfoun and Druitt, 2005; Kelfoun *et al.*, 2008; Shea and van Wyk de Vries, 2008); this section builds on those studies by considering their findings in relation to the emplacement evolution processes presented in Section 4.3.

Visible surface structures have been mapped on the Socompa deposit, including fault, fold and toreva structures recognized by previous authors (Figure 18). In cases where previous authors have mapped relatively small-scale and/or complex structures (e.g., Kelfoun *et al.*, 2008) perhaps not visible at the available orthoimage resolution, only the largest structures or approximate locations which reveal the given deformation sense have been mapped here. More detailed information on specific structures can be found in the references herein. Unlike the majority of other mapping efforts described in this chapter, individual hummocks have not been mapped at Socompa as their low relief and generally small size (< 10 m) make them difficult to discern at the given image resolution. However, the locations of the hummocks as described by Wadge *et al.* (1995) and Kelfoun *et al.* (2008) are discussed in the text. In the place of hummock structures, large-scale intact blocks have been mapped following the work of Kelfoun *et al.* (2008) as these structures are key kinematic indicators useful for dividing the deposit into the emplacement behaviour zones discussed in Section 4.3.2.

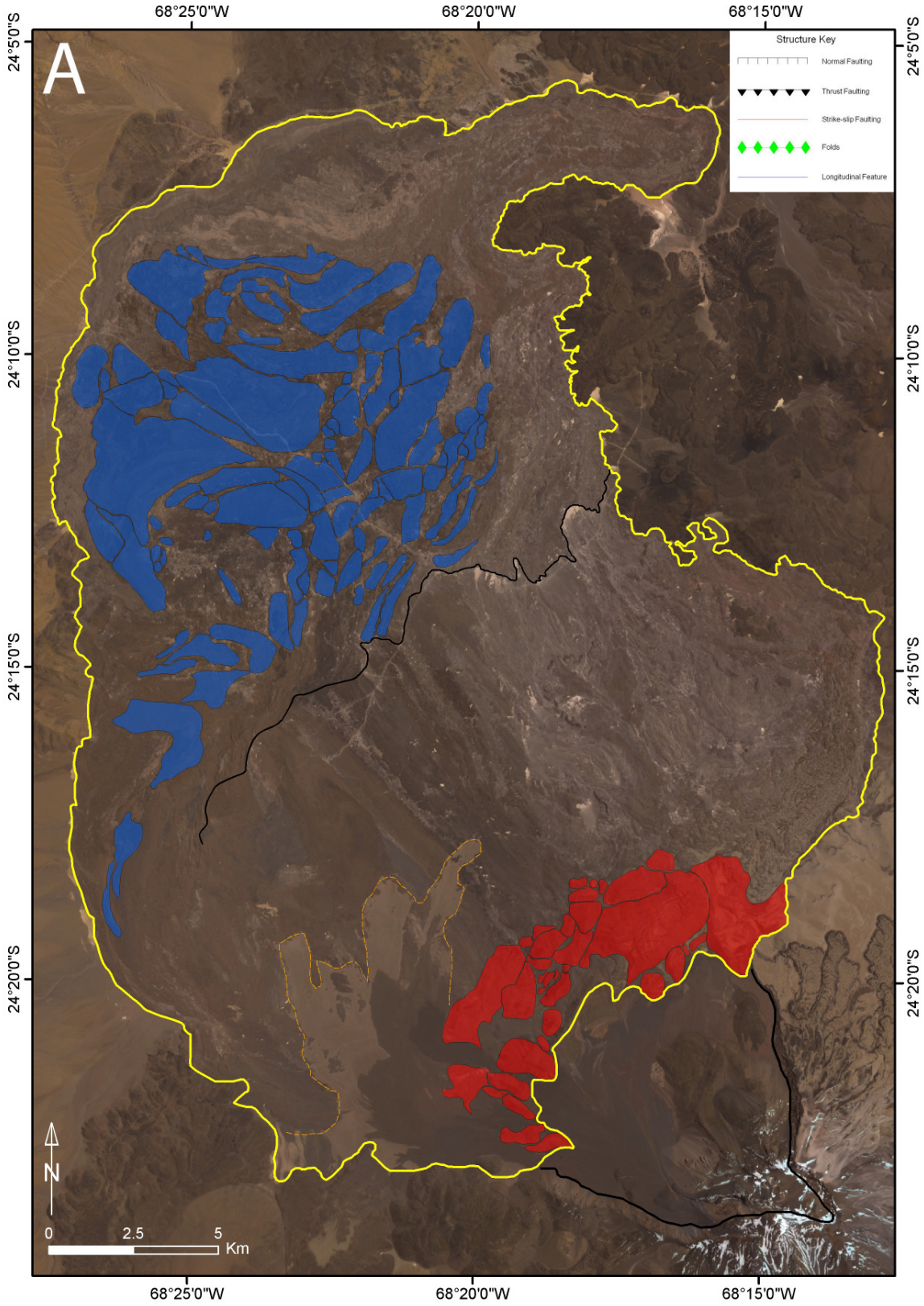

(Figure 18 continued on following page)

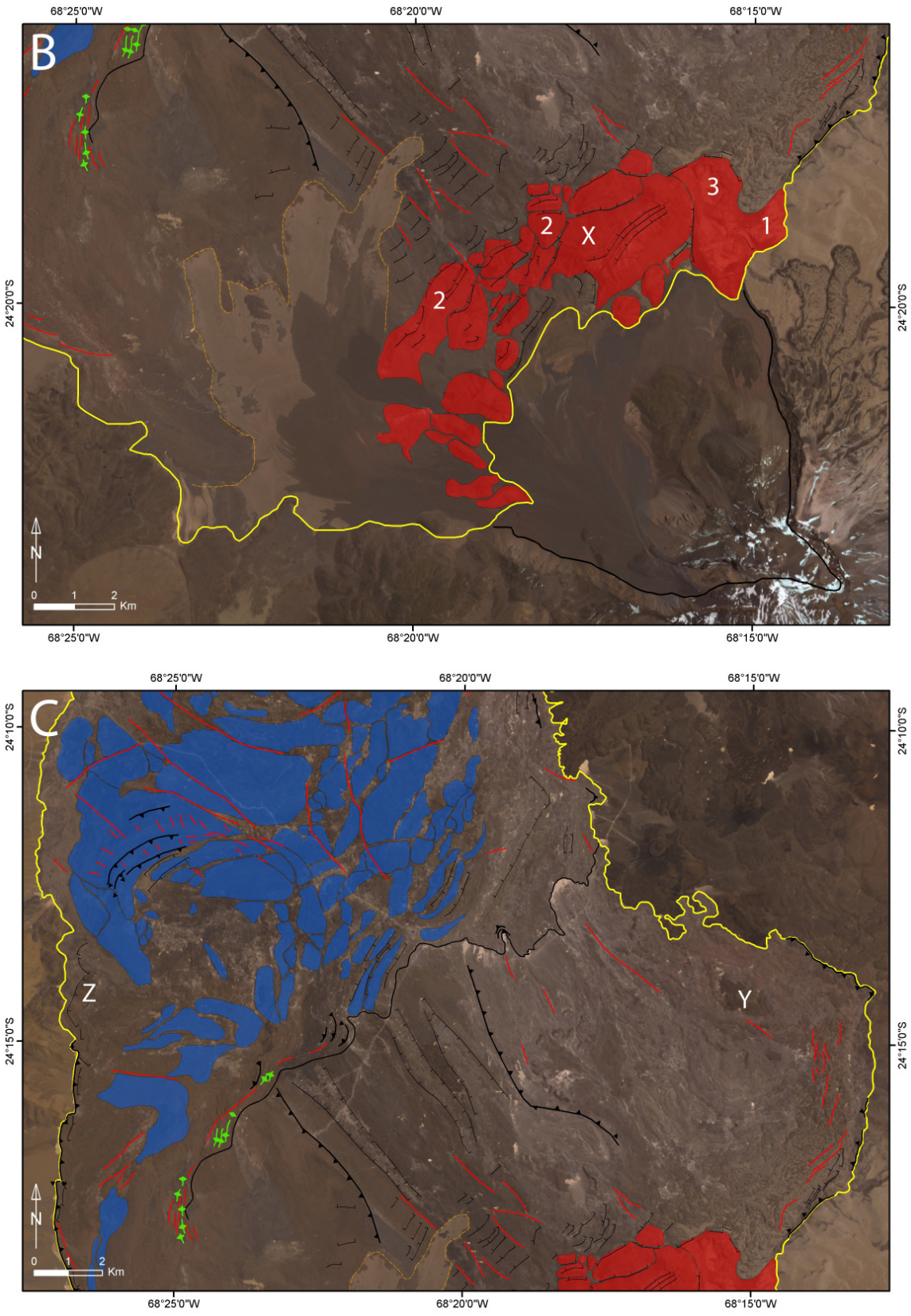

(Figure 18 continued on following page)

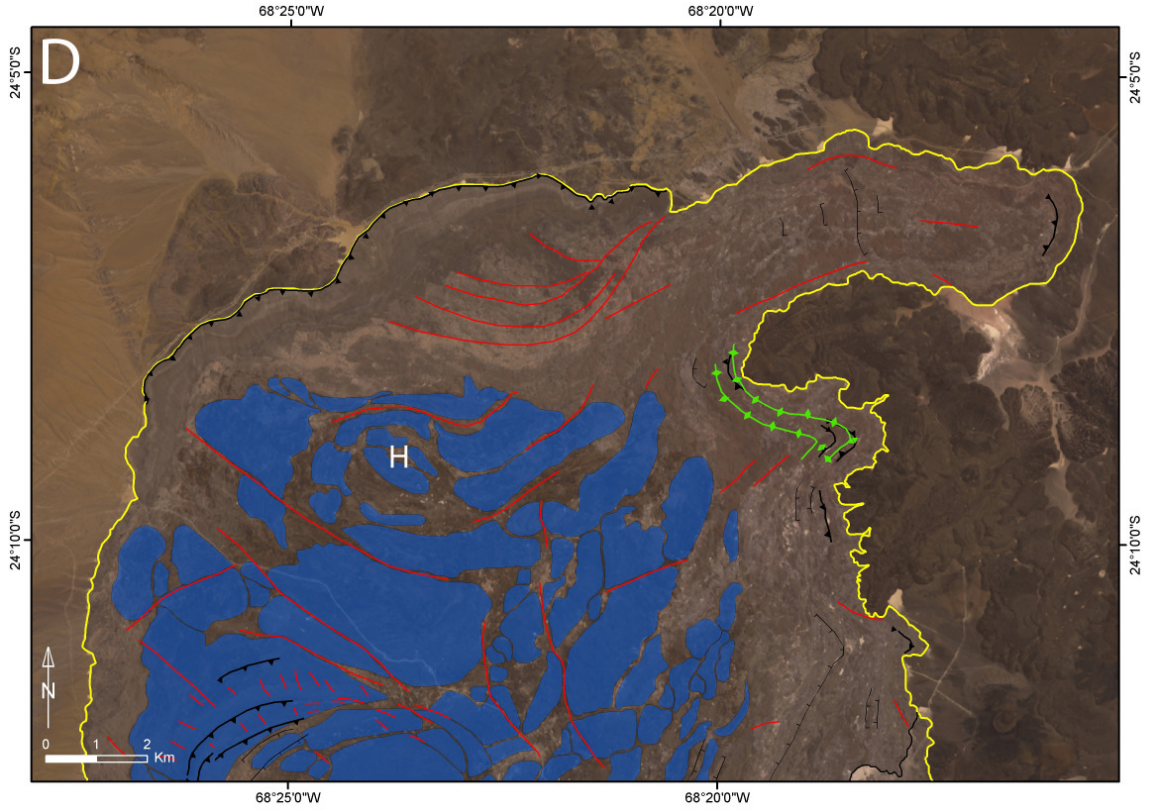

Figure 18 – Structural interpretation of the Socompa VDA deposit, modified after Kelfoun *et al.* (2008) and Shea *et al.* (2008). (A) Full area of the deposit, blue areas denote rafted lava block material after Kelfoun *et al.* (2008) and Shea *et al.* (2008), red areas signify the proximal toreva blocks after Wadge *et al.* (1995); (B) Proximal area of the deposit; the three toreva morphologies introduced by van Wyk de Vries *et al.* (2001) and discussed in Section 3.3.2 are indicated by the numbers 1, 2 and 3, respectively; (C) Medial area of the contrast between proximal extension and the overlapping of the reflected distal failure to create the medial escarpment. The location of the margin shown in Figure 6 is the margin due east of the topographic high marked by 'Y'; (D) Distal area of the deposit which highlights the rifted rafts of block material and their interaction with a topographic high after reflecting off the western margin (point 'H').

The toreva blocks highlighted in Figure 18B are considered to be a quintessential example of this type of structure (Wadge *et al.*, 1995). They are bounded by imbricate normal faults on their proximal and distal sides and transverse or strike-slip faults laterally; scarps of up to 400 m are recognized between the blocks (Francis and Wells, 1988). As discussed in Section 4.2.3, a total of 11 km^3 of material is thought to be contained in the toreva blocks. These structures are key indicators of frictional sliding with little disturbance; the fact they were emplaced intact to distances of 5-9 km from their source is attributed both to the high cohesion of the constituent materials (interbedded lavas and pyroclastic flows) and low angle of emplacement (Wadge *et al.*, 1995). Wadge *et al.* (1995) suggest that the toreva blocks have slid into place from a point high on the north slope of the source edifice *after* displacement of the forward avalanche material, while van Wyk de Vries *et al.*, (2001) note the relationship of mobilised substratum material and the torevas, suggesting

their emplacement occurred *coincidental* with the avalanche event. Wadge *et al.* (1995) also describe a further 23 km^3 of blocks which broke off the amphitheatre walls after the failure of the main avalanche (and torevas) and deposited in the collapse scar. As these structures have been significantly buried by post-collapse materials and are debated by subsequent authors (van Wyk de Vries *et al.*, 2001), they have not been included here. Toreva dimensions measured from the orthoimage are presented in Table 5 and Figure 19. A general decrease in toreva size with emplacement distance is observed in Figure 19; linear ridge morphology is represented by the fact that the two linear regression trendlines remain a clear distance apart from one another. The orientation of these features in relation to the principal emplacement direction of the avalanche (N36W) is shown in Figures 20A-C. It is clear from these figures that the majority of the torevas are aligned with their long axes orientated perpendicular to the principal flow direction. A number of the western torevas, however, are aligned generally parallel to flow. While this observation may represent a true flow-parallel alignment of torevas in this area, deposition of syn- or post-emplacement materials may mask their true orientation.

Table 5 – Number and area of the clearly discernible toreva blocks measured at the Socompa VDA deposit. Dimensions are in general agreement with previous authors.

Number of torevas documented	Total area covered (km^2)	Percentage of total deposit area covered (%)	Dimensions of largest toreva (m*m)[a]	Area of largest toreva (km^2) [a]
37	27.8	5.3	1714*3534	6.4

[a]Location denoted by the letter 'X' on Figure 18B.

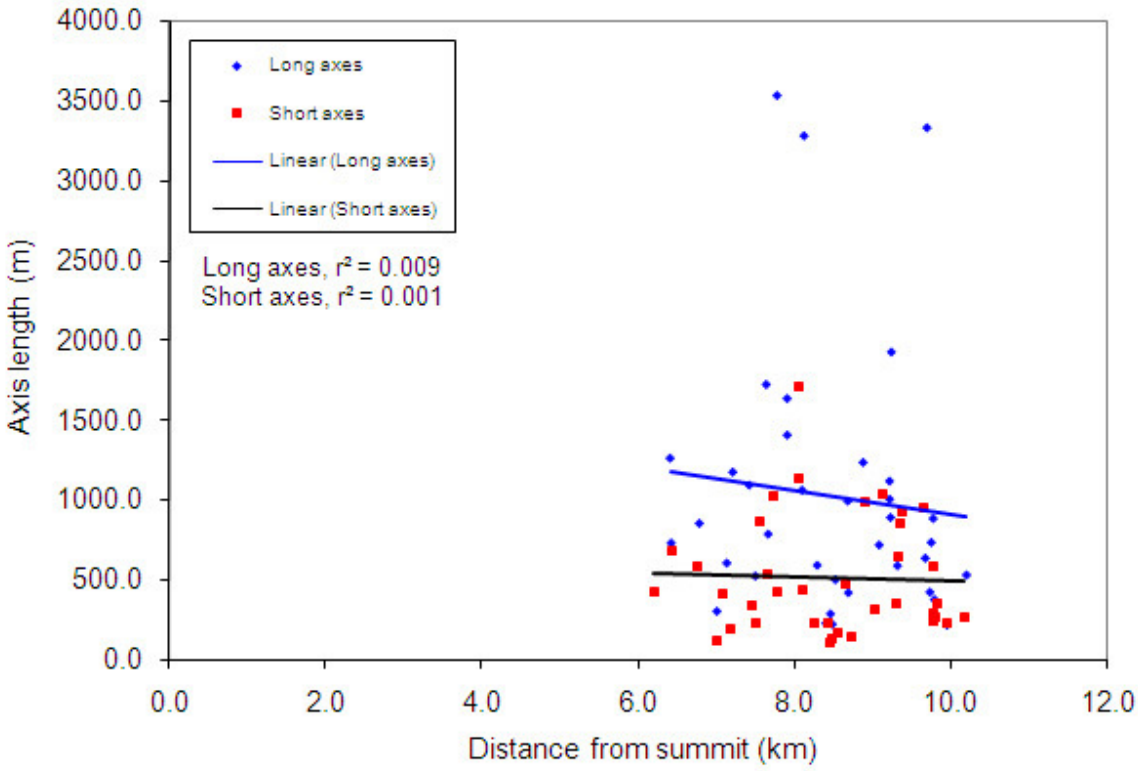

Figure 19 – Relationship between toreva block long and short axis length versus emplacement distance from current edifice summit, Socompa VDA deposit. Kolmogorov-Smirnov and Shapiro-Wilk normality tests performed in the statistical package *SPSSv.15.0* indicate normal distribution in this particular data set; subsequent Pearson correlation for parametric data sets results in a weak correlation between feature axis length and distance from source (r = -0.094 and -0.035 for the long and short axes, respectively). t-tests result in p-value > 0.05 for both cases, however, indicating that the relationship between feature axis length and emplacement distance is not statistically significant in this case, which might be expected due to the limited data set analysed here. Linear regression trendline used to represent the general decrease in feature size with emplacement distance. All features considered here are located in Zone B (see Figure 21).

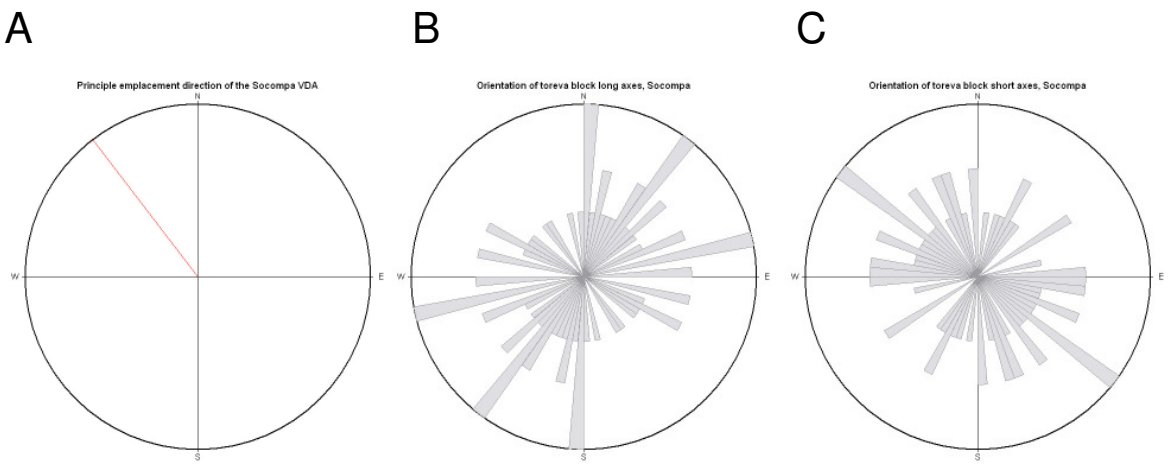

Figure 20 – Surface feature (toreva) orientation plots for the Socompa VDA deposit. A) Orientation of the principle emplacement direction; B) Orientation of major topographic feature long axes, total deposit; C) Orientation of major topographic feature short axes, total deposit.

Based on the structures mapped in Figure 18, the Socompa deposit has been divided into the emplacement behaviour zones described Section 4.3.2 (Figure 21). It is immediately clear from this figure that the majority of the avalanche was dominated by extension (Zones A and B). Zone A frictional sliding is generally confined to the collapse scar, though, if large blocks have collapsed into this region as described by Wadge *et al.* (1995), this zone might be eliminated altogether. As these structures have not been mapped here, Zone A is therefore included. Zone B extension dominates the Socompa deposit. This zone can be divided into three regions to the south of the median escarpment: east, central and west. The east of the zone is characterized by a roughly textured area consisting mainly of disaggregated lavas and basement materials (reconstituted ignimbrite facies [RIF] of van Wyk de Vries *et al.* [2001]) and generally represents the El Cenizal unit of Wadge *et al.* (1995) and proximal lineated terrane (P2) of Kelfoun et al (2008). This area is generally characterized by normal (particularly in more proximal areas) and strike-slip faulting, showing compressional characteristics only near suspected topographic highs (Kelfoun *et al.*, 2008). The velocity and thickness of this part of the failure are both suspected to have been reasonably low, suggesting both a more fluid behaviour dominated by relatively low yield strength (Wadge *et al.*, 1995; Kelfoun *et al.*, 2008). The central part of this section is likely dominated purely by extension as shown by intense normal (dipping away from source) and transverse faulting in the direction of motion and the strong flow-parallel lineations and elongate ridges clearly visible on the orthoimage. In the field, the lineation features are observed as trains of low-relief hummocks parallel to flow direction (Kelfoun *et al.*, 2008). During emplacement, this part of the failure is suggested to have been moving at relatively high speeds with a fluidized RIF base moving faster than a brittle upper section composed mainly of competent lava material (van Wyk de Vries *et al.*, 2001; Kelfoun *et al.*, 2008). The western section is also characterized by extensional features but shows increasing evidence of interaction with a topographic high on its western margin. Increasing deformation (folding and thrust and transverse faulting) is observed in the northern part of this section as the failure interacted with the western topographic high and began to fold over itself at approximately 20 km (Figures 18A and 18B). The texture of this section is relatively smooth as it too is suggested to have been travelling at a relatively high velocity (Kelfoun *et al.*, 2008). The central and western sections generally represent the proximal Monturaqui unit and lineated terrane (P1) of Wadge *et al.* (1995) and Kelfoun *et al.* (2008), respectively.

Zone B north of the median escarpment can be separated into two areas: northwest and north, each representing secondary or late stage emplacement. These areas generally

correlate to the distal Monturaqui units of Wadge *et al.* (1995) and secondary terranes of Kelfoun *et al.* (2008). The northwest area is generally characterized by the break-up of large, mechanically competent, rafted blocks of dacitic lavas originating from the source edifice (Socompa breccia [SB] per van Wyk de Vries *et al.* [2001]). The emplacement direction of the blocks is oblique to the primary travel direction representing material that has deflected off the topographic high at the west-northwest margin of the emplacement basin and rifted to various degrees before settling in the deeper part of the basin (Kelfoun *et al.* 2008). The upper surface of this section of the deposit is characterized by large-scale brittle blocks with fluidized, ductile RIF material underneath, the latter having been ejected from underneath the source edifice with sufficient energy to deflect the avalanche mass from its primary travel direction (van Wyk de Vries *et al.*, 2001). As observed in Figure 18D, some of the large brittle blocks have deflected further around a topographic high before settling. The deposit to the north and east of the represents the final stages of emplacement as the largest blocks have been deposited and the failure moved towards its eastern and north-eastern margins. Though increasing depositional conditions are envisaged as the failure moved further into these areas, extensional structures remain dominant. The furthest extents of the failure to the northwest represent a tongue of material that was deposited in the very latest stages of emplacement (Kelfoun *et al.*, 2008). The majority of the areas north-northwest of the median escarpment posses a rough surface texture in comparison to the deposit south of the escarpment, suggesting a relatively slow emplacement velocity for the secondary deflected avalanche (Kelfoun *et al.*, 2008).

Due to the involvement of a significant amount of potentially fluidized, ductile material (≈ 80% by volume per van Wyk de Vries *et al*. [2001]), the Socompa VDA is thought to be a very high energy, mobile avalanche which encountered topographic highs at a number of locations. The significant reflection off of the topographic high at the northwest margin of the emplacement is evidence of this high mobility. Therefore, Zone C behaviour, where the avalanche progressively comes to rest due to momentum loss, is thought to be relatively non-existent as the avalanche likely moved with high velocities in an extensional regime (Zone B) to abruptly encounter topographic highs and quickly transition to compressional deposition conditions (Zone D). Therefore, the most likely areas for the existence of Zone C behaviour are located at a significant distance from the source but still well away from topographic highs at the margins of the deposit. The areas classified as Zone C areas in Figure 21 meet these criteria as well as not possessing significant amounts of extensional or compressional structures, at least by what is apparent in the maps and discussions of previous authors and the available imagery. As the Socompa deposit does

not possess stereotypical large-scale hummocks, associated depositional indicators could not be considered. It is entirely likely that extensional or compressional conditions exist to some degree in these areas, particularly in the eastern area of the deposit where several smaller-scale but significant topographic highs exist in this area (point 'Y' on Figure 18C; Kelfoun *et al.*, 2008). In the centre of the secondary deposit north of the median escarpment, depositional conditions likely exist though significant extension is still apparent through the presence of normal and transverse fault structures. As such this region remains classified as Zone B.

Zone D compressional depositional behaviour generally exists around the entire deposit margin as it is more or less confined in the basin by higher topography. This margin is generally characterized by steep, abrupt levees with a notable amount of transverse and thrust fault structures at various scales. Bulldozed facies are also observed at the deposit's western margin (van Wyk de Vries *et al.*, 2001). Several compressional stress regime areas, however, deserve further attention. The first is the western margin to the west-northwest of the median escarpment (point 'Z' in Figure 18C). In this area the steep margin exists but is separated from the remainder of the deposit body by large normal faults with significant offset (> 100 m), often with an oblique component (Kelfoun *et al.*, 2008). These structures are interpreted by Kelfoun *et al.* (2008) to be the result of initial compression of the primary avalanche material against the high topographic margin and extension as the failure deflected into the basin to the northeast. Thus, the margin remained behind as the main failure body moved away. A second Zone D area worthy of additional discussion is the median escarpment which crosses the lateral extent of the deposit at 20 km (Figures 18A and 18C). Significant folding, transverse and thrust faulting is observed in the topographically higher secondary avalanche material to the west-northwest of the escarpment as it represents a 'frozen wave' of material that folded back onto itself and progressively deposited over the primary avalanche material (see Section 4.2.3). To this end, the median escarpment itself represents a thrust structure. Significant folding, transverse and thrust faulting is observed near the western limits of this structure, representing initial deformation of the deflected avalanche, transitioning to more extensional conditions as the secondary avalanche travelled to the east-northeast. Unequivocal evidence for a distal transition to lahar conditions (Zone E) is not thoroughly discussed in the literature and therefore this zone has not been included here.

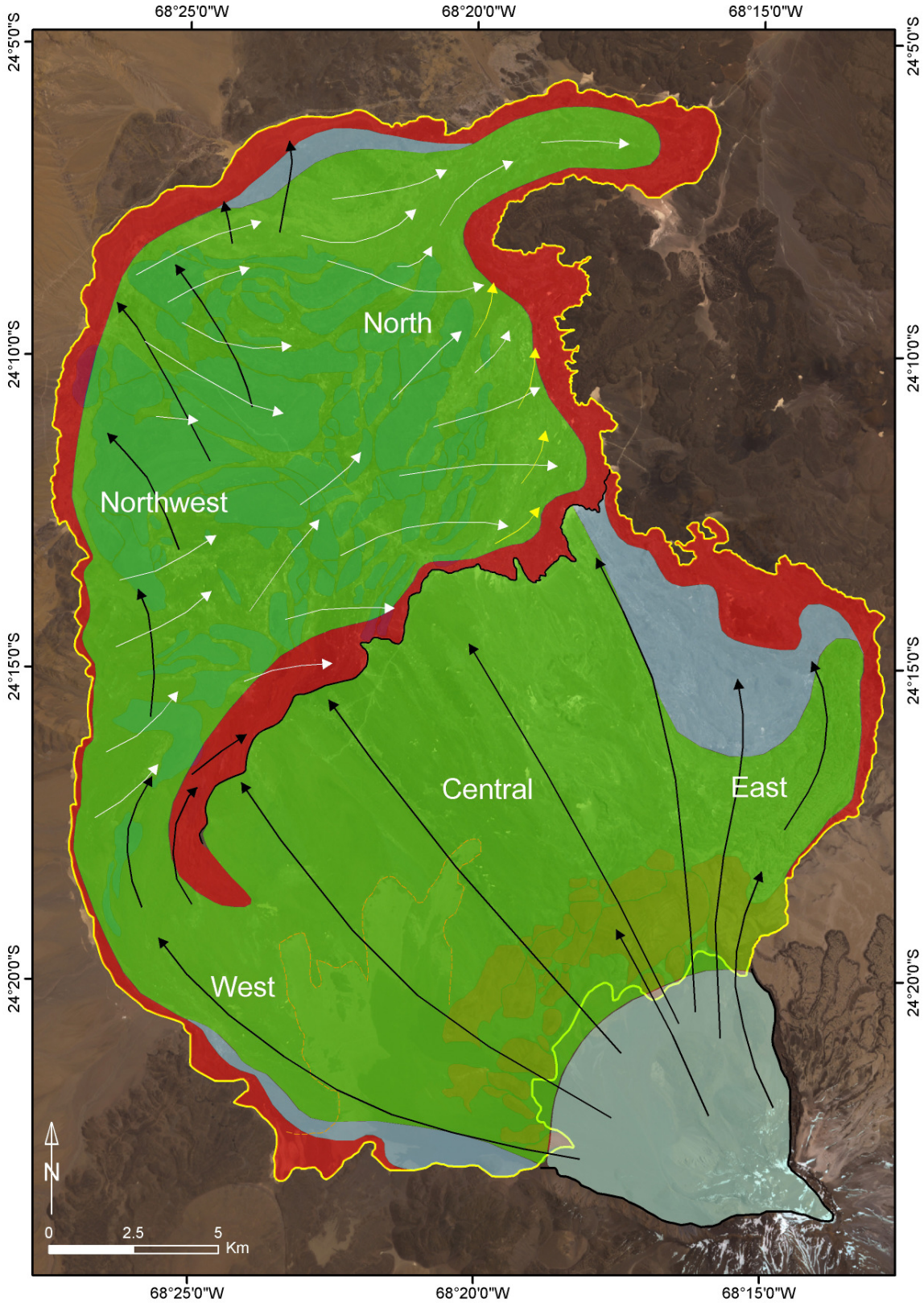

Figure 21 – Emplacement behaviour zone separation of the Socompa deposit. From proximal to distal – Zone A (white), Zone B (green), Zone C (blue), Zone D (red). The black flow lines represent a likely emplacement direction scenario, the white flow lines represent the secondary direction of the avalanche as it reflected off the high western margin and the yellow lines represent secondary or late stage flow along topographic highs at the basins' eastern margin.

The flow lines displayed in Figure 21 generally represent those of previous authors (e.g., Francis *et al.* [1985] and Wadge *et al.* [1995]) with all kinematic indicators discussed in mind. The origins of the flow lines within the collapse scar represent the proposed source regions for the deposit material following the suggestions of Wadge *et al.* (1995); the flow line representing the torevas structures suggests a source region at the rear of the failure amphitheatre and toreva deposition in the latter stages of emplacement or after the failure of the remainder of the avalanche material. The suggested distance travelled by these structures leads to an associated *H*/*L* ratio of 0.14, a considerably low value for such large features (Wadge *et al.*, 1995).

5.3.3. Jocotitlan

The most striking characteristic of the Jocotitlan VDA deposit is the exceptionally large and steep toreva ridges and conical hummocks. A total of 191 hummock and toreva block structures were mapped here in comparison to 246 discussed by Siebe *et al.* (1992), 235 of which were mapped by those authors. The discrepancy in these values lies in the difficulty of recognizing smaller scale features at the given image resolution. General feature metrics are shown in Table 6. Also shown in Table 6 are dimension values for the largest and most distinct topographic features as discussed and measured by Siebe *et al.* (1992) but repeated here to both confirm the original measurements and to provide a check on the orthoimagery approach described herein. The values are in good general agreement with the exception of the hummock diameter presented by Siebe *et al.* (1992) and maximum dimension as measured here. This difference is due to the difficulty in interpreting exactly what dimension was measured by Siebe *et al.* (1992); maximum dimension was measured in this study, so differences in values are large where the features are more linear and converge as a more conical form is taken.

Table 6 – Number and metrics of the clearly discernible hummocks and toreva blocks measured at the Jocotitlan VDA deposit. This table also includes measurements the maximum dimensions and areas of the hummocks and toreva ridges that were also measured by Siebe *et al.* (1992), in parentheses, which in most cases are similar. With hummocks, Siebe *et al.* (1992) measured the diameter whereas the maximum dimension has been measured here, which in the case of circular features are the same. Also, Siebe *et al.* (1992) did not note the specific dimensions they considered, making it difficult to replicate the measurements. These two points are the main source for any discrepancies.

Number of hummocks and torevas documented	Total area covered (km^2)	Percentage of total deposit area covered (%)	Dimensions of largest feature[a] (m*m)	Area of largest feature (km^2)[a]
191	14.8	20.2	795*3016.7 (2700)	2.0

[a]Loma Alta ridge

	Feature name	Max. dim. measured here (m) (Siebe *et al.* [1992] measurement)	Area (km^2)
Hummocks	Cerro Xitejé	561.2 (600)	0.19
	Cerro San Miguel	335.8 (500)	0.12
	Cerro Faldo	470.1 (500)	0.24
	Cerro La Cruz	390.5 (400)	0.15
	A	328.6 (400)	0.08
	B	1000 (1000)	0.4
	D	1171 (350)	0.39
	E	1290 (400)	0.14
	F	611 (350)	0.19
	G	643 (350)	0.23
	H	475 (300)	0.11
Ridges (torevas)	Loma De Enmedio	2168.0 (2150)	0.57
	C	1736.7 (1750)	0.5

All hummock and toreva features were mapped following Siebe *et al.* (1992) (Figure 22) and clearly display the two morphologically distinct areas recognized by these authors: subparallel linear ridges (toreva blocks) separated by closed depressions located in the east of the deposit and steep, conical hummocks in the west. The majority of the largest

features are located within the proximal section of the deposit (within 3-8 km of the 12 km total length) and give way to smaller hummocks and hummock clusters of low relief distally. Surface feature measurements are presented in Figures 23 and 24. A general decrease in surface feature size is observed in Figure 23, representing progressive disaggregation of original material. The relatively high number of large dimensions recognized in medial section of this deposit is a reflection of the significant lateral spreading which occurred here; large-scale toreva features are in fact located more proximally than other features but have travelled in a generally different direction (distance is measured directly from the current edifice summit). The observation that the long axis length linear regression trendline lies at a relatively flat angle is reflection of the two differing deposit morphologies. In the eastern part of the deposit, linear feature form, aligned perpendicular to the principal emplacement direction, is prevalent in the proximal deposit area and transitions to more conical forms distally. However, the opposite is observed in the western area of the deposit, where proximal hummocks are highly conical and become linear with distance with long axes now generally aligned parallel to flow. Plots of overall surface feature orientation reveal preferential alignment both parallel and perpendicular to the principal emplacement direction (N27E, Figures 24A-C).

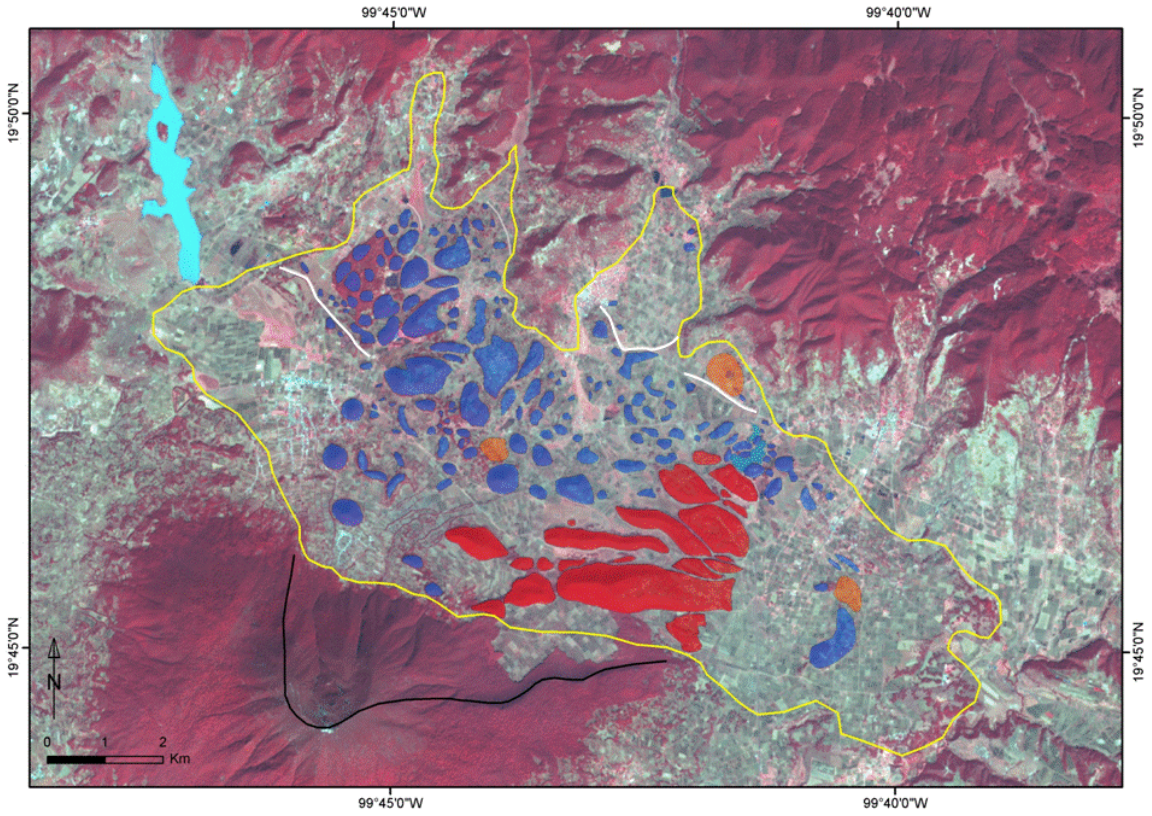

Figure 22 – Mapped hummock (blue) and toreva block (red) distribution at the Jocotitlan VDA deposit, modified after Siebe *et al.* (1992). The solid yellow line represents the deposit margins; the solid black lines represent the collapse scar. Orange shaded features denote the location of closed circular depressions; solid white lines represent steep breaks in slope after Siebe *et al.* (1992), suggesting a limit of deposition of high yield strength material.

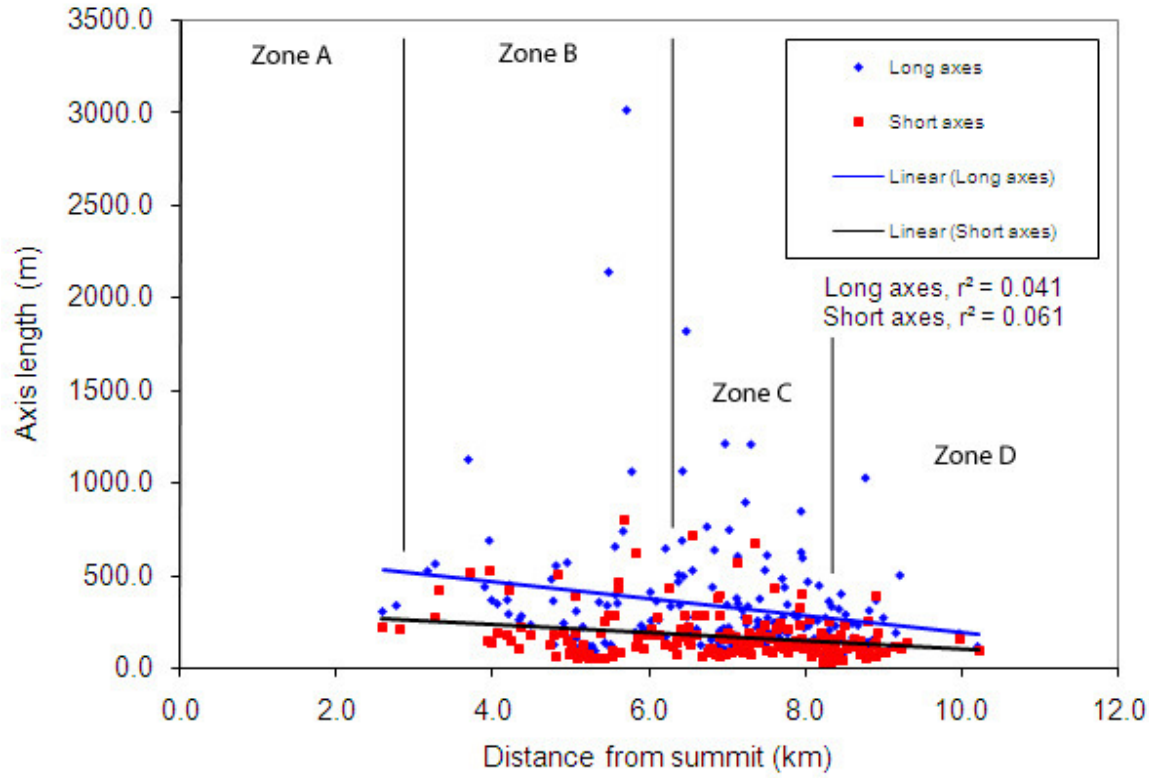

Figure 23 – Relationship between topographic feature long and short axis length versus emplacement distance from current edifice summit, Jocotitlan VDA deposit. Kolmogorov-Smirnov and Shapiro-Wilk normality tests performed in the statistical package *SPSSv.15.0* indicate normal distribution in this particular data set; subsequent Pearson correlation for parametric data sets results in a significant but weak correlation between feature axis length and distance from source (r = -0.201 and -0.247 for the long and short axes, respectively, p-value < 0.01 for both cases). Linear regression trendline used to represent the general decrease in feature size with emplacement distance. Zone distinctions based on the mean extent of each zone shown in Figure 25 and referred to in the relevant discussion.

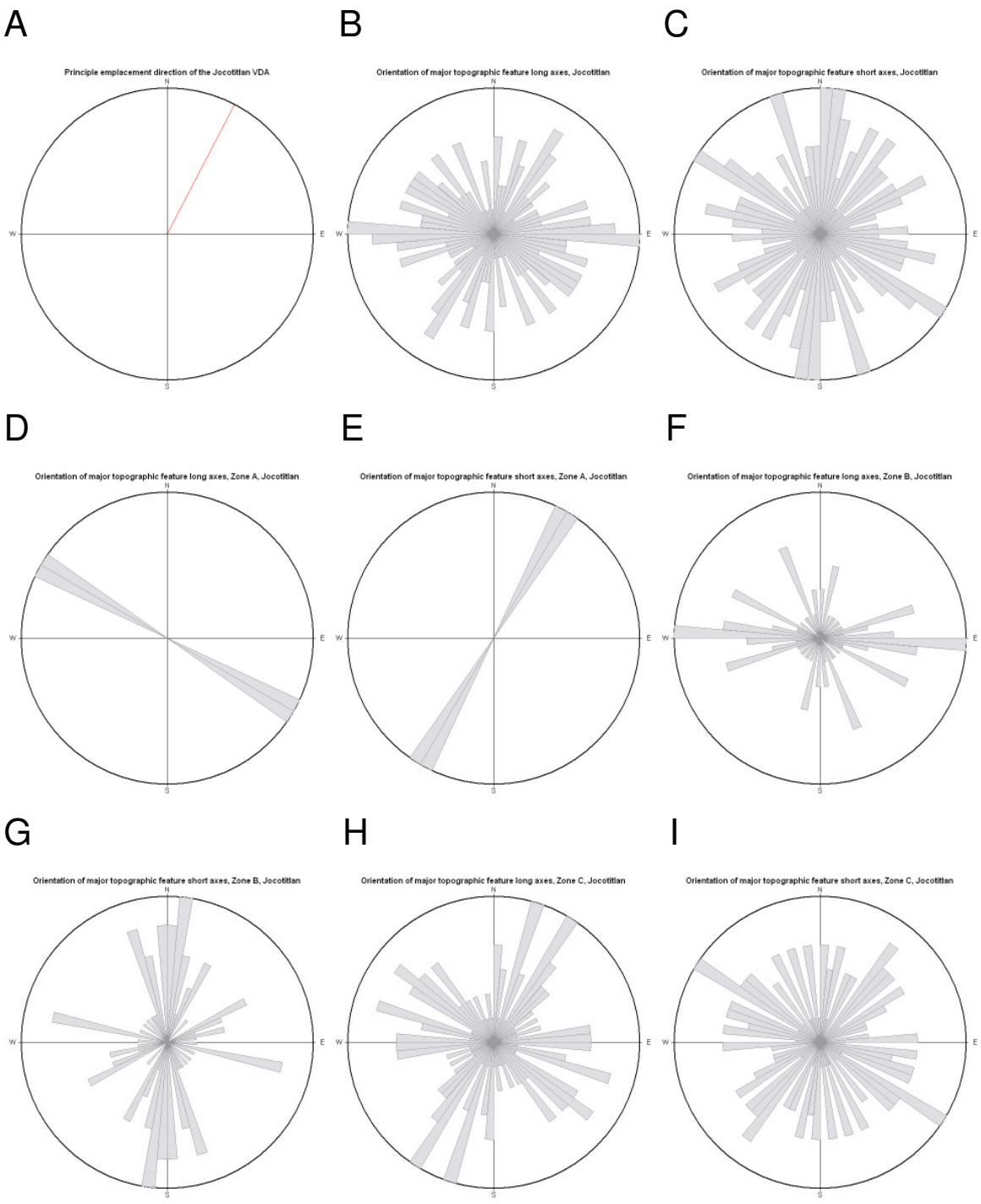

Figure 24 – Surface feature (hummock/toreva) orientation plots for the Jocotitlan VDA deposit. A) Orientation of the principle emplacement direction; B) Orientation of major topographic feature long axes, total deposit; C) Orientation of major topographic feature short axes, total deposit; D) Orientation of major topographic feature long axes, Zone A; E) Orientation of major topographic feature short axes, Zone A; F) Orientation of major topographic feature long axes, Zone B; G) Orientation of major topographic feature short axes, Zone B; H) Orientation of major topographic feature long axes, Zone C; I) Orientation of major topographic feature short axes, Zone C.

Though fold and fault features were not mapped by previous researchers, it is possible to delineate the Jocotitlan deposit into the emplacement behaviour zones discussed in Section 4.3.2 based on the shape of the hummock and toreva blocks (Figure 25). As large blocks

are observed at approximately 2.7 km from the source, Zone A frictional sliding is in this case confined to the collapse scar area and that immediately adjacent to it (< 3 km). The few surface blocks present in this zone are aligned with their long axes perpendicular to the principal emplacement direction (Figures 24D and 24E). Zone B extensional stage behaviour extends from roughly 3-8 km, less so in the centre and west of the deposit as compared to the east where the toreva ridges qualitatively appear to have progressively separated into continuously smaller blocks. As the large conical hummocks in the west of the deposit (Cerro San Miguel, Cerro La Cruz, Cerro Xitejé) appear to form a broad hummock train, it is possible these features disaggregated from a single block during deposition. The majority of the features in Zone B are aligned with their long axis perpendicular to the principal direction (Figures 24F and 24G). The features located in Zone C (8-11 km) generally lose their orientation perpendicular to flow direction as orientations become principally aligned parallel to flow direction (Figures 24H and 24I). Complex hummock clusters also become more common, particularly in the northwest of the deposit where the avalanche appears to have spilled into a topographic low to deposit a large proportion of blocks (i.e., hummocks). In the northeast of the deposit, just distal from the large separating ridge sequence, deposition of blocks appears to have been heavily influenced by the adjacent topographic high as block orientations quickly change from flow perpendicular to random within a short distance (< 0.25 km), representing the transition to compressional conditions of Zone D. Though the locations are not clear, Siebe *et al.* (1992) note intense thrust faulting and folding in this northeast section. Similar compressional features, including deformation of basal lacustrine sediments and bulldozer facies, have also been noted at the north-northwest margin of the deposit by Siebe *et al.* (1992). These features represent compressional conditions in high yield strength material, which likely increases in intensity near the topographic highs at the deposits' northern margin. At the eastern margin, the avalanche was generally unconfined and able to spread freely, depositing few significant features. Siebe *et al.* (1992) note the presence of a steep deposit margin here (15-50 m high) which represents deposition of a high yield strength material in unconfined conditions. Clear indications of Zone E lahar behaviour is not easily recognizable in the orthophotos, nor discussed in the literature.

Flow lines included in Figure 25 distinguish emplacement of the two morphologically distinct areas of the deposit. Emplacement in this manner may suggest separate stages of failure of the original edifice within a short time period (or simultaneously) in generally different directions, perhaps indicative of pre-failure topographic or stress conditions. As suggested by Siebe *et al.* (1992), the various blocks can be re-fit together and to the source

edifice with varying degrees of uncertainty. This observation suggests source regions in the east and west of the source edifice for each respective morphologic area, and, in the east of the deposit, progressive disaggregation of an initially large block. In this sense the most proximal ridges likely represents material from higher up and within the failed edifice while more distal feature are comprised from material originally located on near the slope toe. Qualitatively, frictional sliding behaviour representative of initial extensional emplacement appear to have persisted longer in the east of the deposit as compared to the west and may not have reached full fluid-like spreading potential as the avalanche was rapidly influenced by distal topography.

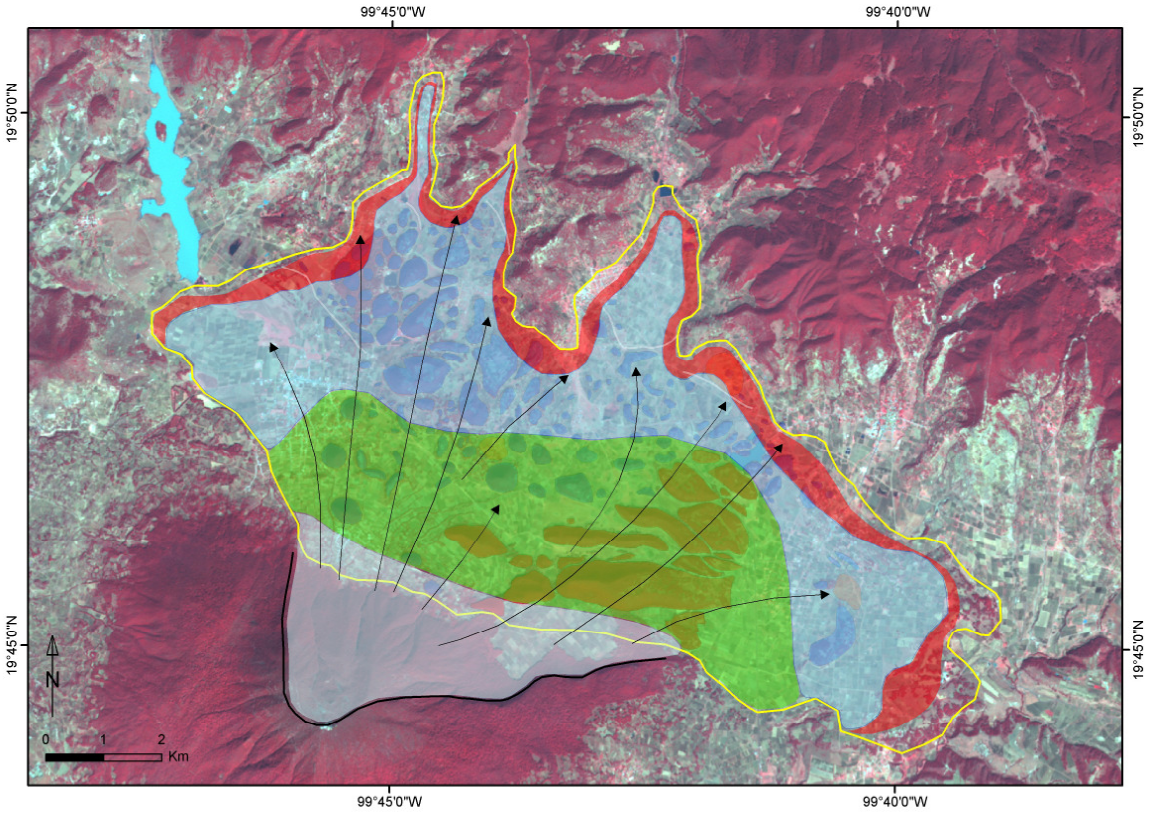

Figure 25 – Emplacement behaviour zone separation of the Jocotitlan deposit. From proximal to distal – Zone A (white), Zone B (green), Zone C (blue), Zone D (red). The black flow lines represent a likely emplacement direction scenario.

5.3.4. Shiveluch

The most recent VDA event at Shiveluch (1964 AD) possesses the best examples of kinematic indicators as it is not significantly covered by post-emplacement materials. Further information concerning the large hummock blocks of the 30,000 ybp collapse event can be found in Belousov *et al.* (1999). These authors describe the entire 1964 deposit as being covered by hummocks < 10 m amplitude; too small to be visible in the

available orthoimage. Therefore, only the large proximal toreva structures have been mapped and measured here (Figures 26-30 and Table 7). Normally offset scarps separating these torevas form three distinct 'steps' in the proximal section of the deposit, which are > 1 km long and up to 150 m high (Figure 27; Melekestsev, 2006; Ponomareva *et al.*, 2006). A general decrease in long/short axis length with distance is observed and long axes are generally aligned perpendicular to the principal emplacement direction (S8W, Figures 28 and 33A-C). These immense blocks are back-tilted towards the source edifice and thought to have been emplaced during deceleration as their movement was restricted by the distal part of the failure which disintegrated downslope to form the main body of the VDA (Belousov *et al.*, 1999). The torevas mapped in Figures 26 and 27 are flanked by longitudinal levees 10-30 m high and > 1 km long which mark the proximal flow boundary and increase in length with distance (Figure 29; Belousov *et al.*, 1999). The levees are aligned subparallel to the principal emplacement direction (Figures 30D and 30E).

Table 7 – Number and area of the clearly discernible toreva blocks measured at the Shiveluch 1964 AD VDA deposit. Dimensions are in general agreement with previous authors.

Number of toreva documented	Total area covered (km^2)	Percentage of total deposit area covered (%)	Dimensions of largest feature (m*m)	Area of largest feature (km^2)
8	1.7	1.6	437*1018	0.5

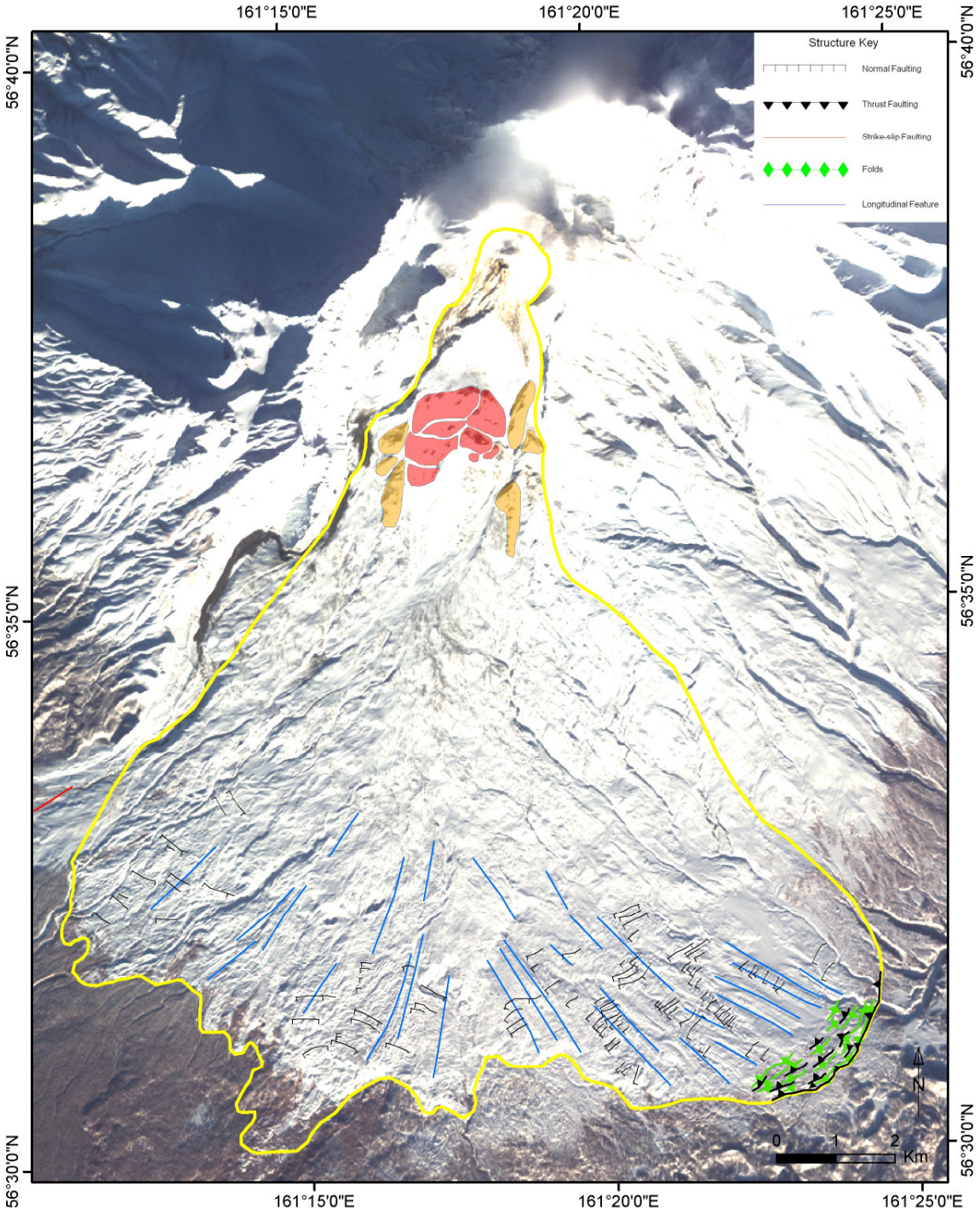

Figure 26 – Extents of the 1964 AD Shiveluch VDA deposit (solid yellow line). This deposit includes the collapse amphitheatre as it is commonly mapped in this manner in the literature. Toreva blocks are shaded red and large lateral levees are shaded orange.

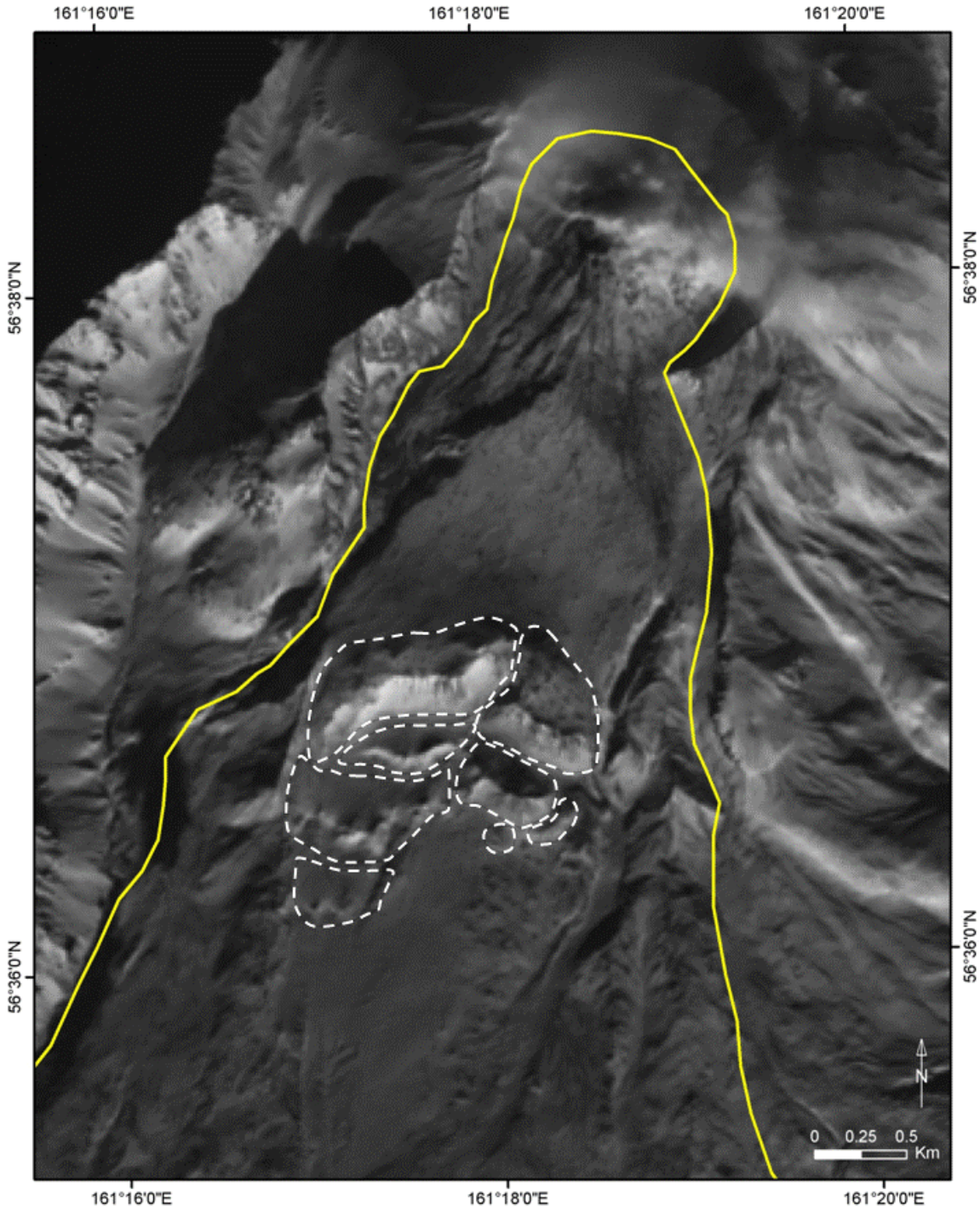

Figure 27 – Zoom view of the proximal section of the 1964 AD Shiveluch deposit highlighting the large toreva structures at the mouth of the collapse amphitheatre (outlined by the dashed white lines). The deposit extents are represented by the solid yellow line. Only the B2 (visible red band of the electromagnetic spectrum) image is displayed in this image for clarity.

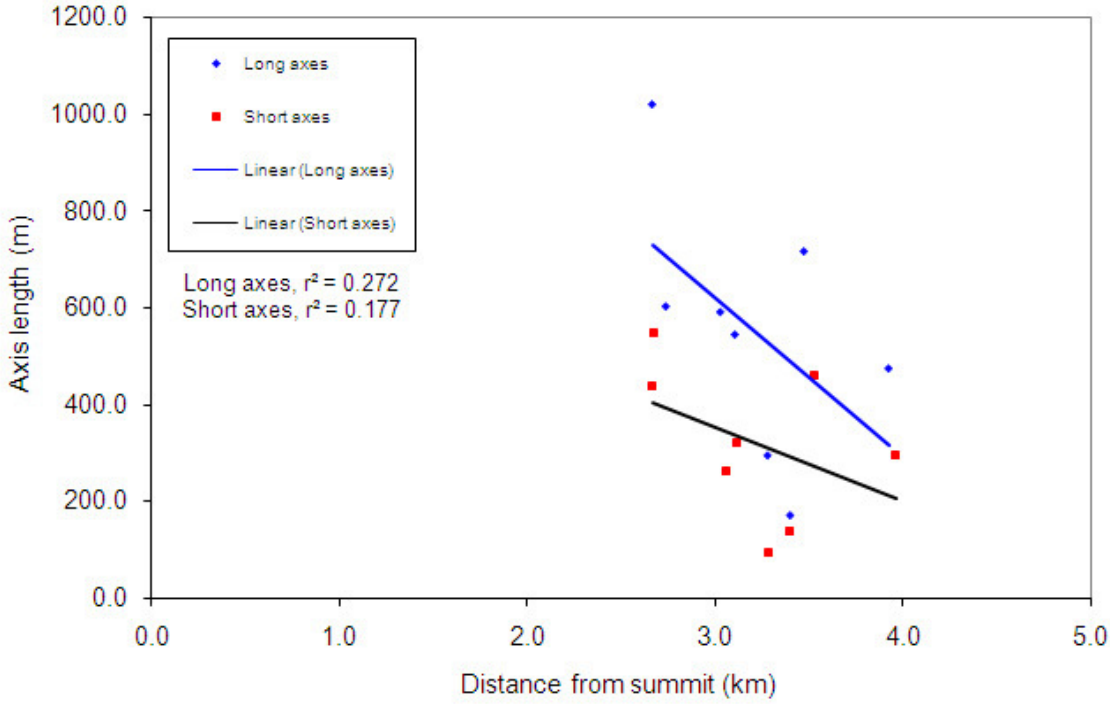

Figure 28 – Relationship between toreva block long and short axis length versus emplacement distance from current edifice summit, 1964 AD Shiveluch VDA deposit. Kolmogorov-Smirnov and Shapiro-Wilk normality tests performed in the statistical package *SPSSv.15.0* indicate normal distribution in this particular data set; subsequent Pearson correlation for parametric data sets results in a weak correlation between feature axis length and distance from source (r =-0.522 and -0.421 for the long and short axes, respectively). t-tests result in p-value > 0.05 for both cases, however, indicating that the relationship between feature axis length and emplacement distance is not statistically significant in this case, which might be expected due to the limited data set analysed here. Linear regression trendline used to represent the general decrease in feature size with emplacement distance. All features considered here are located in Zone B (see Figure 31).

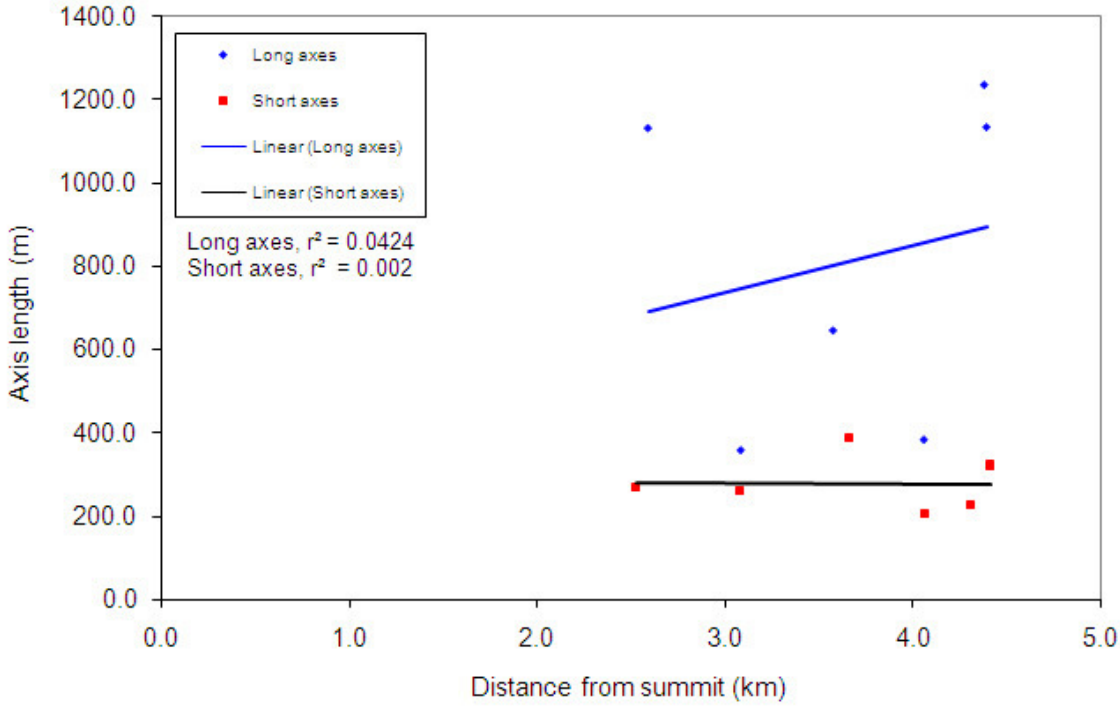

Figure 29 – Relationship between lateral levee long and short axis length versus emplacement distance from current edifice summit, 1964 AD Shiveluch VDA deposit. Kolmogorov-Smirnov and Shapiro-Wilk normality tests performed in the statistical package *SPSSv.15.0* indicate normal distribution in this particular data set; subsequent Pearson correlation for parametric data sets results in a weak correlation between feature axis length and distance from source (r = 0.206 and -0.039 for the long and short axes, respectively). t-tests result in p-value > 0.05 for both cases, however, indicating that the relationship between feature axis length and emplacement distance is not statistically significant in this case, which might be expected due to the limited data set analysed here. Linear regression trendline used to represent the general decrease in feature size with emplacement distance. All features considered here are located in Zone B (see Figure 31).

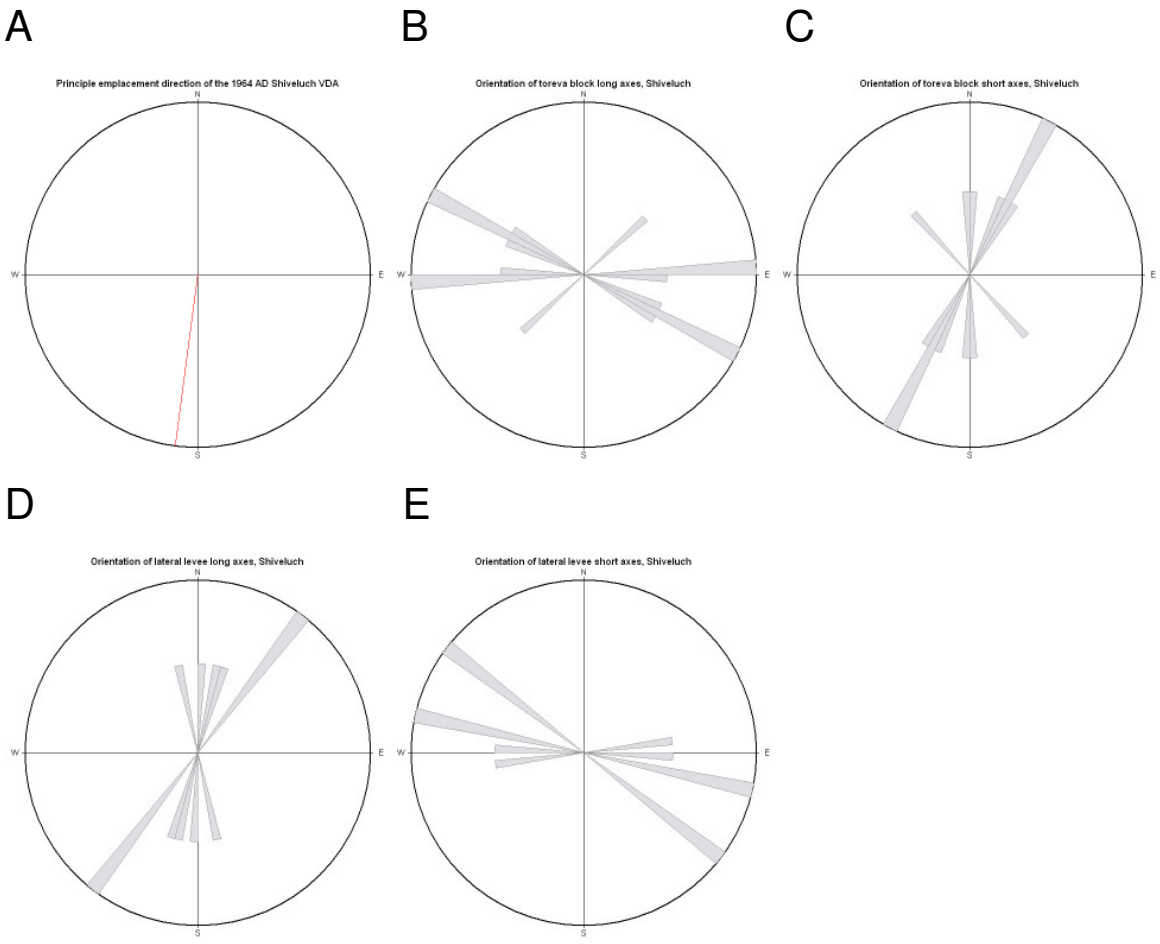

Figure 30 – Surface feature (toreva) orientation plots for the 1964 AD Shiveluch VDA deposit. A) Orientation of the principle emplacement direction; B) Orientation of toreva block long axes; C) Orientation of toreva block short axes; D) Orientation of lateral levee long axes; E) Orientation of lateral levee short axes.

The locations of significant structures indicative of emplacement kinematics are shown in Figure 26. This includes longitudinal furrows in the medial and distal areas of the deposit which are subparallel to the principal flow direction and radiate outwards from the failure source. These features are 1-30 m wide, 0.3-10 m deep and several kilometres long and suggested to have been formed from extensional strain in the cohesive avalanche body (Belousov *et al.*, 1999). Also shown in medial and distal areas of the deposit are normal faults striking perpendicular to flow representing predominantly extensional mechanics. On the surface these structures are viewed as horsts ridges 2-15 m high and graben trenches perpendicular to the longitudinal furrow structures to form a 'net-like' pattern as described by Ponomareva *et al.* (1999). Conical hummocks are present on the surfaces of both the longitudinal furrows and the transverse ridges (Ponomareva *et al.*, 1999). Additional kinematic structures are mapped on the southeastern margin of the deposit as thrust faults and folds perpendicular to the principal flow direction which represents a zone of intense compression. This zone is approximately 6 km long and 1.5 km wide and

composed not of avalanche body material but of pyroclastic and earlier VDA deposit material sediments scraped up by the 1964 event and compressed at the distal margin as a 'bulldozer' facies (Ponomareva *et al.*, 1998; Belousov *et al.*, 1999). The undulating ridges of low relief are likely surface expressions of low angle thrust faults and folds (Belousov *et al.*, 1999).

Figure 31 shows the delineation of the 1964 Shiveluch VDA deposit into emplacement behaviour zones discussed in Section 4.3.2. This classification is relatively straightforward as a result of emplacement onto a generally unconfined and gentle slope. Zone A frictional sliding behaviour occurs from the collapse edifice to the proximal point of toreva block deposition, indicating a point where the avalanche began to disintegrate into the debris avalanche. Zone B extensional behaviour begins at approximately 2 km with toreva blocks and dominates the remainder of the deposit. This is again indicative of the unconfined emplacement conditions where the avalanche was able to spread freely on the gentle slope. The longitudinal furrows and low-relief horsts and grabens in the medial and distal portions of the deposit are characteristic of this zone. As this avalanche was generally comprised of relatively smaller extrusive dome block material as compared to other VDA events, progressive disaggregation of large-scale blocks is not observed at the resolution of the available orthoimage. A narrow zone of (< 1 km) Zone C behaviour exists at the southern, southwestern and western boundaries of the deposit where the avalanche may have deposited due mostly to momentum loss. Though the adjacent margins appear to be relatively steep (to 10 m), which might suggest yield strength freezing, significantly raised topography, thrust fault and fold structures which would suggest clear compressional stress regimes in these sections are not discussed in the literature nor visible on the orthoimage (Siebe *et al.*, 1992; Belousov *et al.*, 1999). Therefore, these margins are classified as Zone C progressive deposition areas in Figure 31. Additionally, Melekestsev (2006) suggests the steep morphology indicates a slow rate of emplacement in these areas, consistent with momentum loss depositional behaviour. Zone D compressional behaviour, however, is clearly defined by the bulldozer facies zone at the southeastern distal margin of the deposit. As discussed, this area is mainly composed of material scraped up by the travelling avalanche but compressional conditions were likely transmitted proximally due to this interaction. According to both Ponomareva *et al.* (1999) and Belousov *et al.* (1999), no evidence of a distal transition to lahar conditions (Zone E) is observed.

The emplacement direction flow lines, which radiate outwards from the source area as mapped in Figure 31 are reflective of the fan-like morphology of the deposit and again

represents the unconfined emplacement of the avalanche onto the generally featureless and gentle deposition slope.

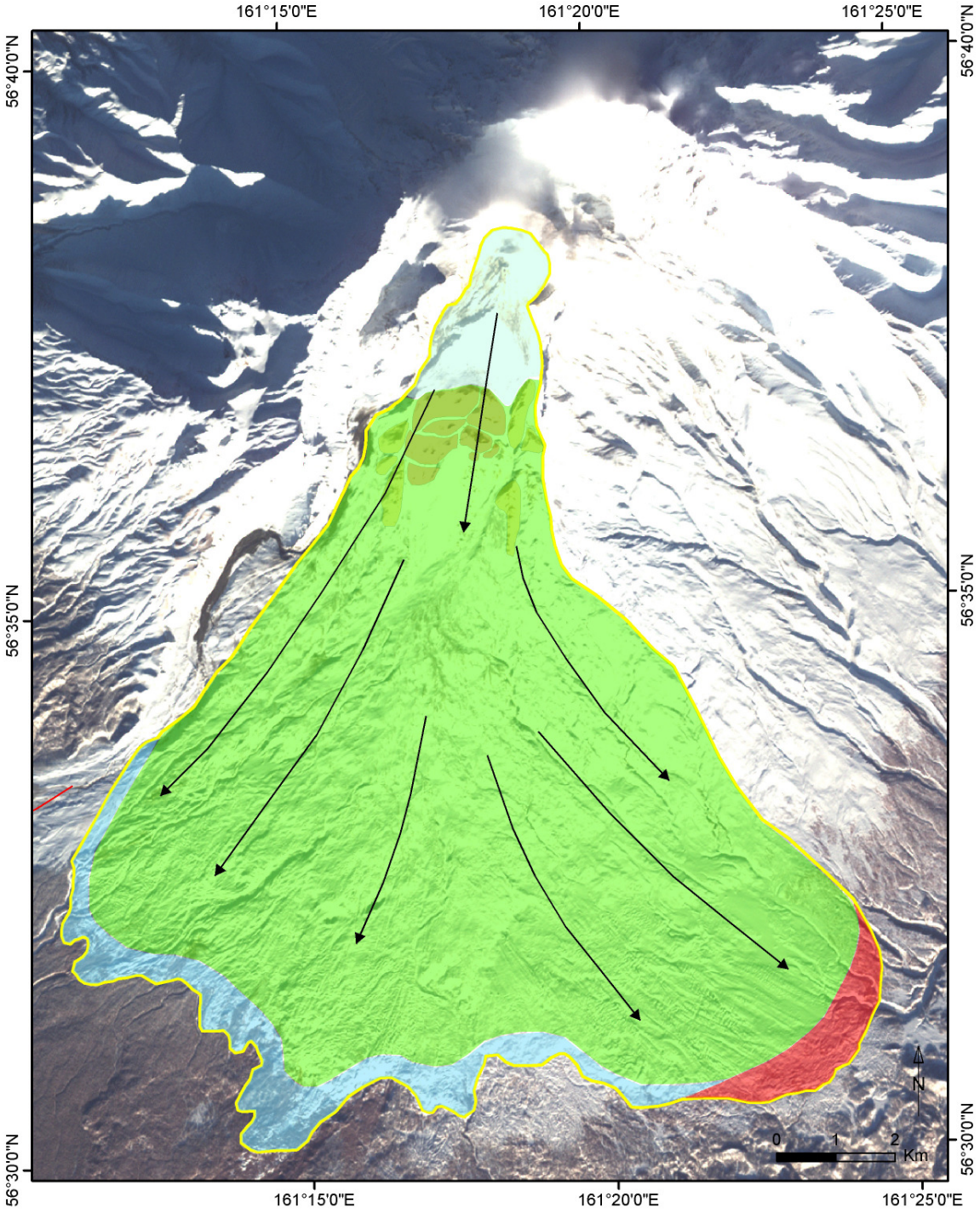

Figure 31 – Emplacement behaviour zone separation of the 1964 AD Shiveluch VDA deposit. From proximal to distal – Zone A (white), Zone B (green), Zone C (blue), Zone D (red). The black flow lines represent a likely emplacement direction scenario.

5.3.5. Parinacota

The failure of Parinacota volcano involved the emplacement of approximately 6 km^3 of rhyodacitic and andesitic lava material into the partially confined Lauca basin filled with lacustrine, fluvial, glacial and volcaniclastic materials (Francis and Wells, 1988; Clavero *et al.*, 2002). Disintegration of the initial edifice material into the extraordinary hummocky deposit is thought to have occurred preferentially along planes of weakness present in the pre-failure edifice (i.e., the 'domains' concept of Clavero *et al.*, 2002). Proximal toreva blocks and more distal hummocks are generally composed of different materials which represents the sequential failure of the edifice, rhyodacite blocks and assorted lava breccias, respectively (Clavero *et al.*, 2002). Measured characteristics of 150 of these features (volume, diameter, height, size of largest block) by Clavero *et al.* (2002) show a progressive decrease in each of these values with distance from source. The basic characteristics of the largest and most discernible toreva and hummock features as measured on the orthoimage are given in Table 8 and mapped in Figure 32 and generally agree with dimension values suggested by Francis and Wells (1988) and Clavero *et al.* (2002). The outlines of many of the smaller scale, low amplitude hummocks are difficult to discern at the given image resolution. These hummocks are visible, however, in better resolution images (such as Google Earth©) and the map of Shea and van Wyk de Vries (2008) and are therefore mapped in Figure 32 as continuous hummock fields rather than individual hummocks. Progressively distal hummocks generally have more diffuse outlines, low relief, compound shapes and generally lack internal structure (Siebe *et al.*, 1992; Clavero *et al.*, 2002). Plots of surface feature (hummock and toreva) long and short axis lengths are shown in Figure 33 and show a decrease in feature size and linear form with emplacement distance. The overall orientation of surface features shows general uniformity with a slight preferential alignment of features perpendicular to the principal emplacement direction (S88W, Figures 34A-C).

Table 8 – Number and area of the clearly discernible hummocks and toreva blocks measured at the Parinacota VDA deposit. Dimensions are in general agreement with previous authors.

Number of toreva and hummocks documented	Total area covered (km^2)	Percentage of total deposit area covered (%)	Dimensions of largest feature (m*m)	Area of largest feature (km^2)
407	21[a], 47.9[b]	15.8[a], 36.0[b]	552*1591	0.9

[a]Not including small-scale hummock fields

[b]Including small-scale hummock fields

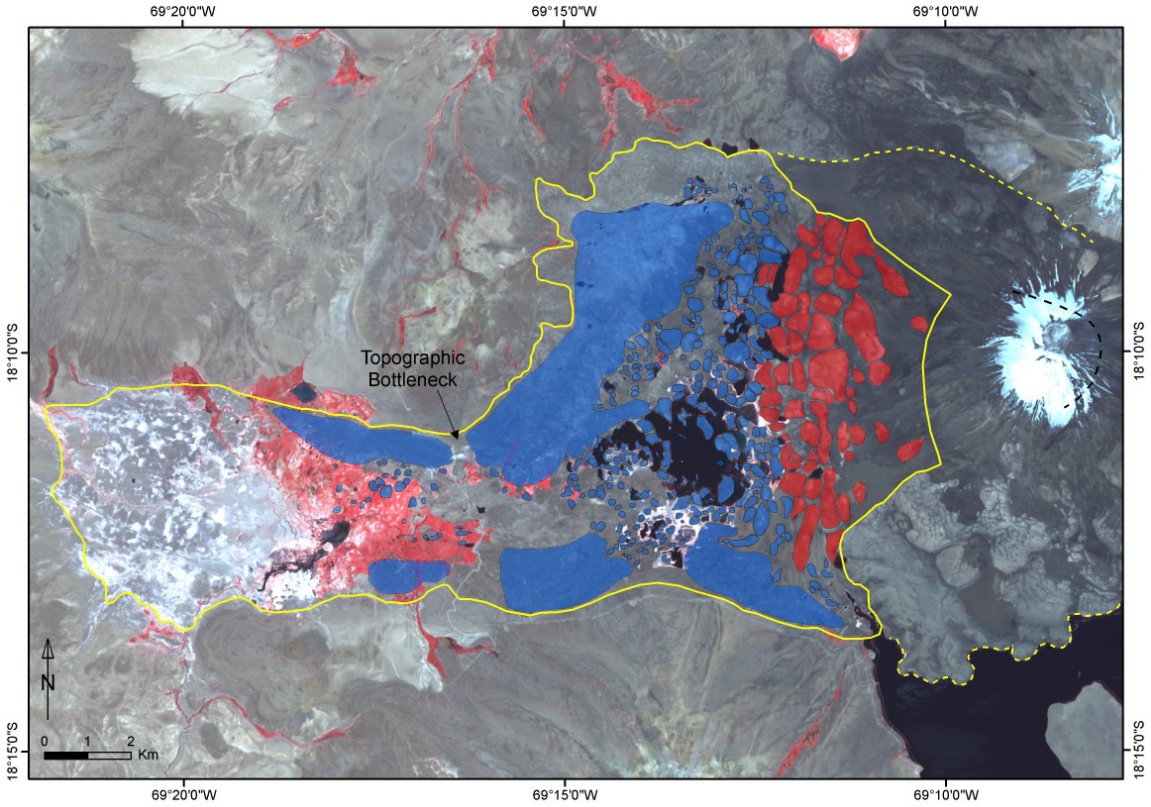

Figure 32 – Mapped hummock (blue) and toreva block (red) distribution at the Parinacota VDA deposit, modified after Clavero *et al.* (2002). The large areas blue-shaded areas represent areas where hummocks exist with relief too low for their margins to be discernible at the available image resolution.

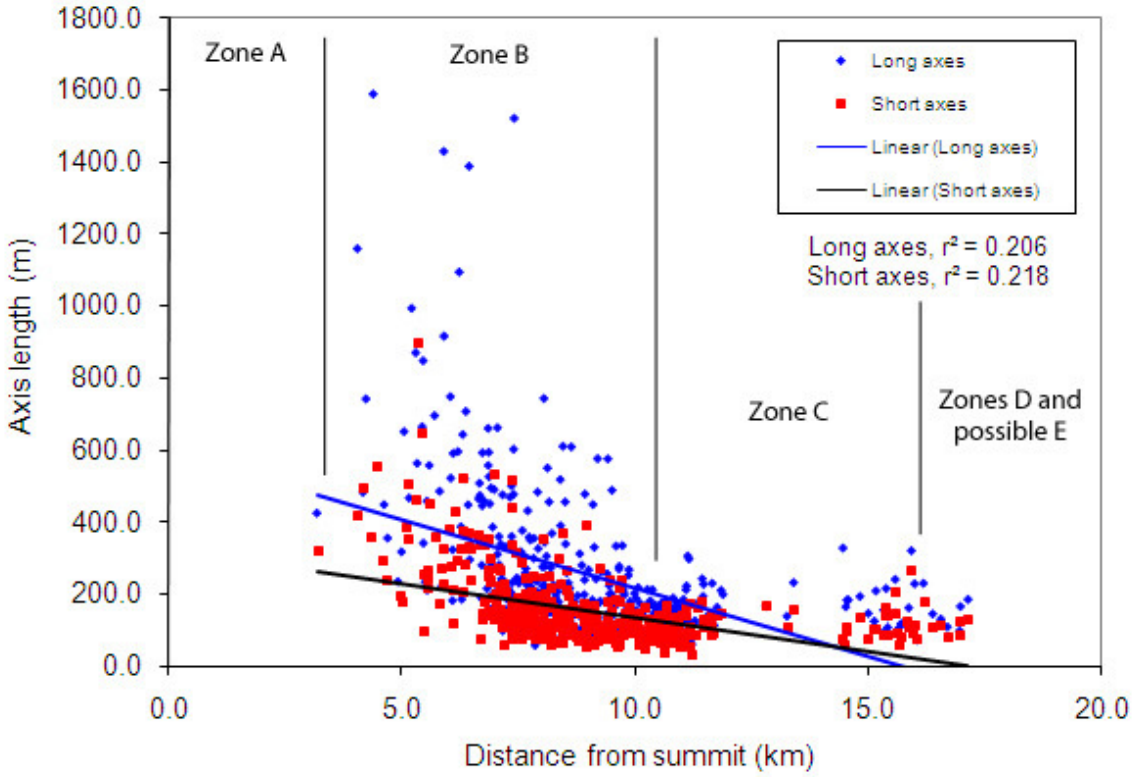

Figure 33 – Relationship between topographic feature long and short axis length versus emplacement distance from current edifice summit, Parinacota VDA deposit. Kolmogorov-Smirnov and Shapiro-Wilk normality tests performed in the statistical package *SPSSv.15.0* indicate normal distribution in this particular data set; subsequent Pearson correlation for parametric data sets results in a significant but weak correlation between feature long axis length and distance from source (r = -0.453 and -0.467 for the long and short axes, respectively, p-value < 0.01 for both cases). Linear regression trendline used to represent the general decrease in feature size with emplacement distance. Zone distinctions based on the mean extent of each zone shown in Figure 36 and referred to in the relevant discussion.

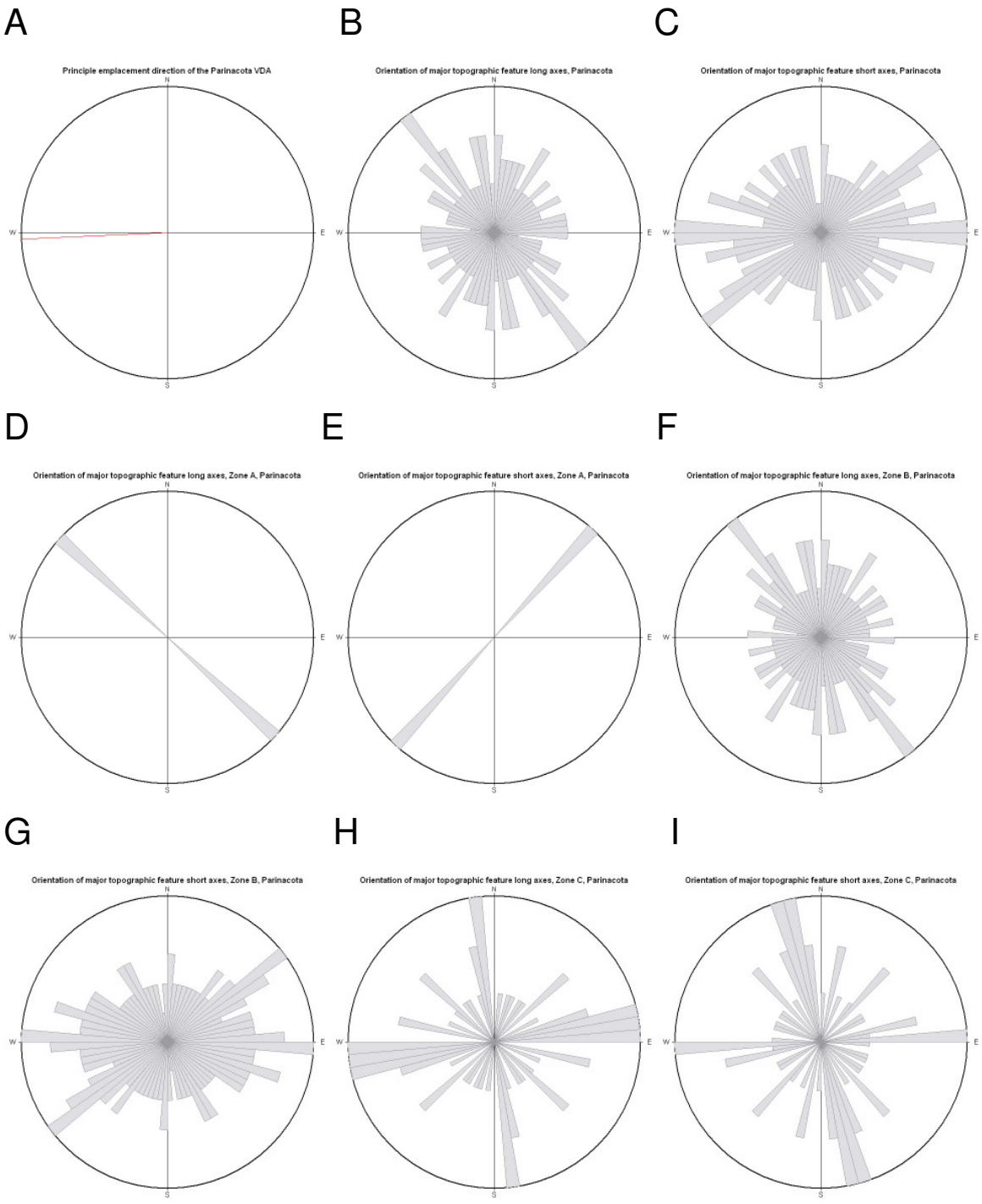

Figure 34 – Surface feature (hummock/toreva) orientation plots for the Parinacota VDA deposit. A) Orientation of the principle emplacement direction; B) Orientation of major topographic feature long axes, total deposit; C) Orientation of major topographic feature short axes, total deposit; D) Orientation of major topographic feature long axes, Zone A; E) Orientation of major topographic feature short axes, Zone A; F) Orientation of major topographic feature long axes, Zone B; G) Orientation of major topographic feature short axes, Zone B; H) Orientation of major topographic feature long axes, Zone C; I) Orientation of major topographic feature short axes, Zone C.

The progressive break-up of the failure material is qualitatively recognizable in Figure 32. Large-scale toreva blocks, generally aligned perpendicular to flow, dominate the proximal deposit from 3-6.5 km, representing the lower unit rhyodacitic back-tilted domes of

Clavero *et al.* (2002). These structures give way to progressively smaller hummocks in the medial and distal areas of the deposit with the inter-hummock depressions in the medial area now holding the Cotacotani Lakes. The failure encountered the Guane Guane Hill topographic high at approximately 11 km and was either stopped or diverted down-valley to the southwest. Hummocks are generally absent after the topographic bottleneck at 13 km, representing a general decrease in system energy and deposition of the block facies due to momentum loss and the topographic restriction. Hummocks after this point occur as small fields on the margins of the deposit or isolated axial blocks.

Structures indicative of emplacement kinematics have been mapped by Shea and van Wyk de Vries (2008). The general location of these structures has been included in Figure 35 and demonstrates a transition from predominantly extensional emplacement (normal faulting) to a more compressional regime (thrust faulting) as the avalanche encountered the Guane Guane Hill topographic high. Thrust faulting is dominant in the distal sections of the deposit both near Guane Guane Hill and as the avalanche was diverted to the southwest. Distal from the topographic bottleneck thrust faulting is observed along the deposit margin and in the most distal reaches as emplacement was influenced by adjacent topographic highs and momentum loss, respectively. Transverse faulting indicative of general but differential extension throughout the avalanche body as it spread is visible throughout the deposit. This is especially clear along the axis of the medial area of the deposit.

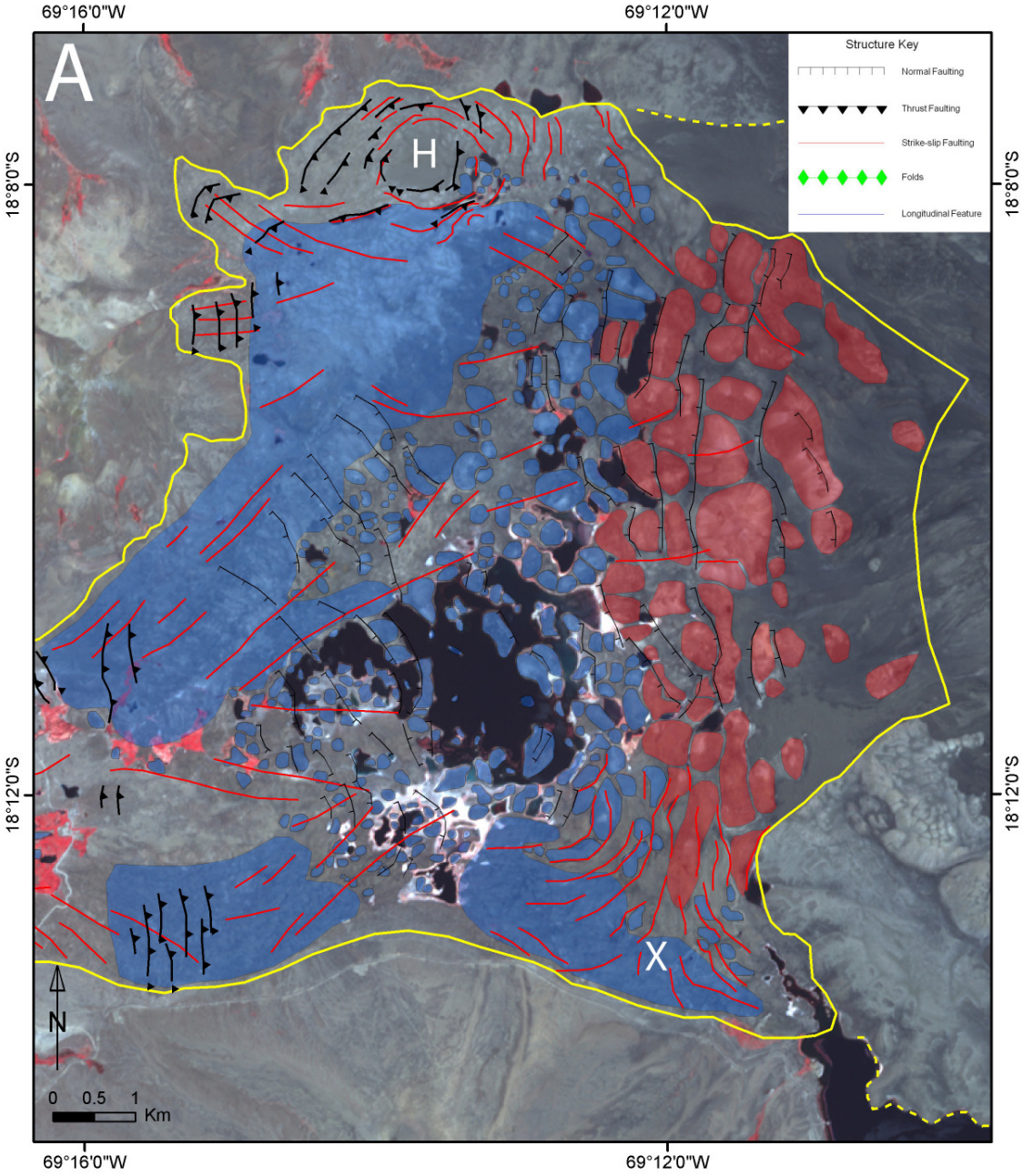

(Figure 35 continued on following page)

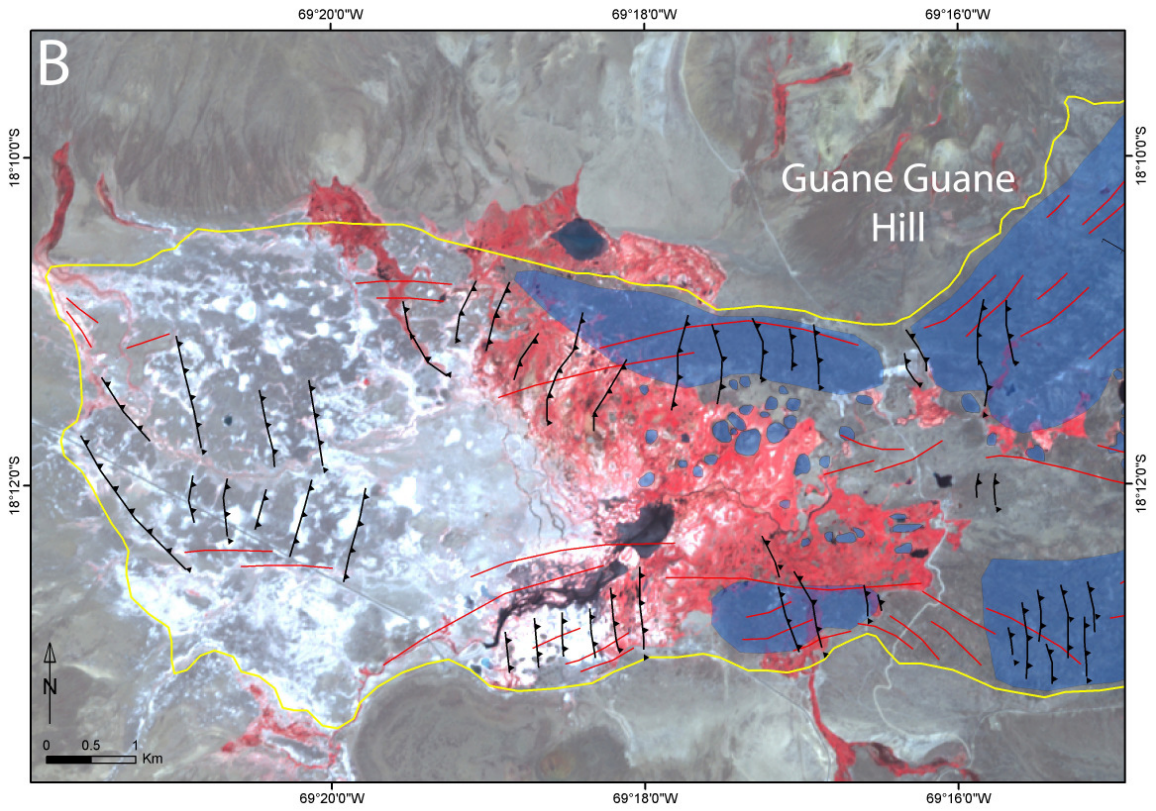

Figure 35 – Structural interpretation of the Parinacota VDA deposit, modified after Clavero *et al.* (2002) and Shea *et al.* (2008). (A) Proximal area of the deposit, the letters 'H' and 'X' refer to areas containing structures which suggest high mobility of the failure, as described in the text; (B) Distal area of the deposit. Notice separate scales for each figure.

The Parinacota avalanche has been separated into the emplacement behaviour zones outlined in Section 4.3.2 as depicted in Figure 36. As at Mt. Shasta, the collapse scar has since been filled in by latter eruptive materials and the zone of frictional block sliding, Zone A, is restricted to the most proximal area adjacent to the hypothesized failure scar (< 3 km). Zone A ends at the location of toreva block deposition but includes some large structures possibly involved in the collapse. As these structures are significantly covered by post-failure materials their origin is not clearly known though they are included here as torevas and are orientated generally perpendicular to the principal emplacement direction (Figures 34D and 34E). Zone B extensional behaviour extends from the location of the toreva blocks (3 km) to a location which generally marks the end of clearly recognizable block facies deposition (additional block facies, or hummocks, are present distally but are generally too small to be mapped at the given orthophoto resolution). What might be a symmetrically radial emplacement pattern is affected by the confinement of lateral and distal topographic highs and the distal down-valley diversion. Thus, Zone B ranges from 3-8 km in the extreme north and south of the deposit (affected by topographic confinement) and 3-13 km along the axis of the deposit as the failure extended down-

valley. Topographic features in this zone are for the most part aligned perpendicular to the principal emplacement direction (Figures 34F and 34G). Zone C represents areas where general deposition has occurred due to loss of initial downslope momentum in the emplacement basin; structures (extensional or compressional) are less conspicuous in this section. This zone is larger axially as emplacement is less affected by topographic influences. Distal hummocks recognizable in Zone C are generally aligned parallel to the principal direction of emplacement (Figures 34H and 34I). In some cases, the Zone C behaviour extends close to the deposit margins as emplacement was generally unaffected by confinement in these areas. These areas represent flat, wedge-shaped margins merging into areas of scattered blocks and small isolated hummocks as described by Clavero *et al.* (2002), as opposed to steep margins generally controlled by yield strength and/or topographic confinement, mainly located along the more proximal/medial margins. Significant compression (Zone D) is suggested by the thrust fault structures mapped by Shea and van Wyk de Vries (2008) and shown in Figure 35, representing influence of the topographic highs along the margins of the deposit. These areas are larger along the northwestern margin of the deposit as the avalanche likely travelled undeterred across the Lauca depression to meet these hills head-on. Indeed, the avalanche has been noted by Clavero *et al.* (2002) as having climbed over 200 m vertically up this margin. Significant run-up is also noted at the southern deposit margin (≈ 100 m). As significant water is thought to have been present in the Parinacota failure, featureless distal margins may represent localized draining of saturated matrix material and may represent Zone E lahar behaviour. However, this behaviour has not been discussed specifically in the literature and therefore is not mapped here.

A clear representation of avalanche mobility is observed in the most northern reaches of the deposit as the avalanche encountered a topographic high and was diverted to either side (point ‘H’ in Figure 35A). In the southeast of the deposit, high mobility is again suggested as the avalanche spilled out to the south-southeast, perpendicular to the principal flow direction, into a topographic low at the southern margin of the basin (point ‘X’ in Figure 35A).

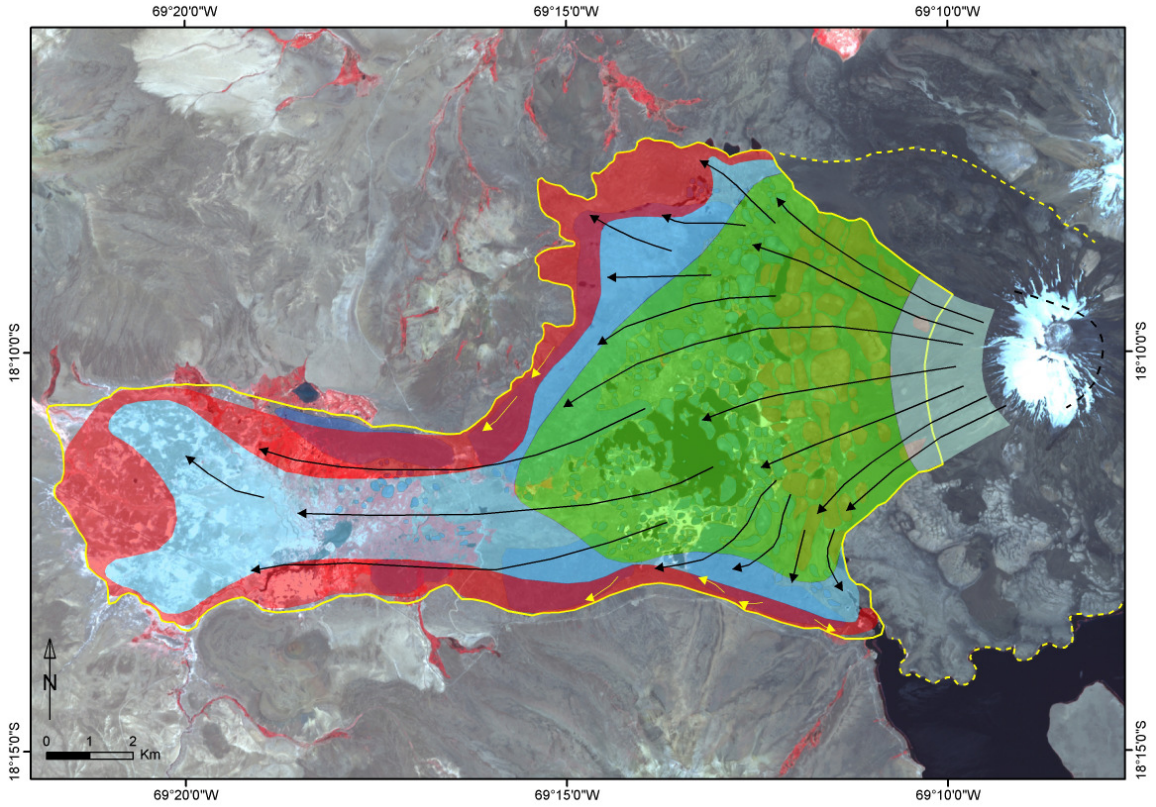

Figure 36 – Emplacement behaviour zone separation of the Parinacota VDA deposit. From proximal to distal – Zone A (white), Zone B (green), Zone C (blue), Zone D (red). The black flow lines represent a likely emplacement direction scenario; yellow flow lines represent flow along margin.

5.3.6. Tata Sabaya

The collapse of Tata Sabaya (< 12,360 ybp, L > 25 km, A = 331 km^2) represents a remarkable example of hummocky topography, highly visible on image scale due to the distinct contrast between the dark-coloured andesitic lava hummocks and the white evaporite deposits of the Salar de Coipasa playa (Figure 37). Surprisingly, only brief descriptions of this collapse event can be found in the literature (Francis and Wells, 1988; Francis and Oppenheimer, 2004) and therefore it was not detailed in Section 4.2. Similar to Mount Shasta and Parinacota, the collapse scar has since been filled in with post-failure volcanic materials and only a small trace of the failure scarp can now be observed (Francis and Wells, 1988). The true distal extent of the deposit is also unknown as it has since been covered by post-emplacement evaporite deposits.

The conspicuous nature of the Tata Sabaya hummocks allow for straightforward orientation and geometry measurement (Table 9). As shown in Figures 37 and 38, a reduction in hummock size is observed both distally and laterally towards the avalanche margins. The observation that high long axis length values are observed in the more

proximal and distal areas of the deposit reflects the linear nature of features in this area though overall size and orientations may change. Qualitatively, compound hummocks forms of low relief are often observed in distal areas. An overall preferential alignment of hummock forms perpendicular to the principal direction of emplacement (S14E) is revealed by Figures 39A-C. The most distal reaches of the southeastern and southwestern deposit are characterized by fields of low lying hummocks indiscernible at the given image resolution. At many of the locations, indicated by patches of dark debris material spread over the evaporite deposits, hummock forms do not appear to be present due to the resolution of the available orthophoto and therefore have not been mapped in Figure 37. This approach differs from the small-scale hummock fields mapped at Parinacota, because in that case, hummocks forms were either partially visible on the image or mapped by previous authors.

Table 9 – Number and area of the clearly discernible hummocks and toreva blocks measured at the Tata Sabaya VDA deposit.

Number of toreva and hummocks documented	Total area covered (km^2)	Percentage of total deposit area covered (%)	Dimensions of largest feature (m*m)	Area of largest feature (km^2)
1735	38.4	13.6	350*1695	0.8

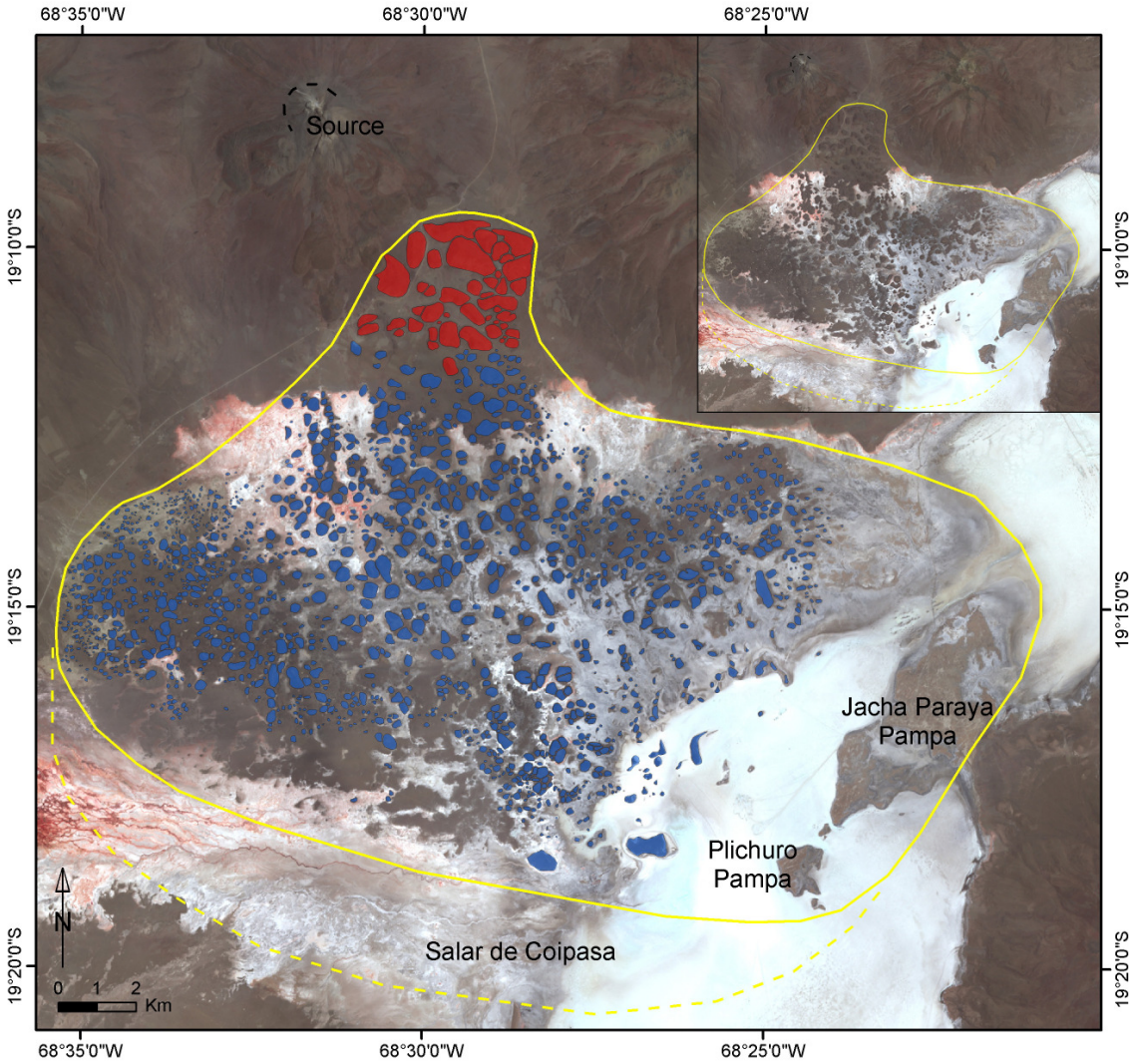

Figure 37 – Mapped hummock (blue) and toreva block (red) distribution at the Tata Sabaya VDA deposit. The solid yellow line represents the likely limits of the deposit; the dashed yellow line represents the uncertain limits of the distal section of the deposit which has been covered by post-VDA emplacement evaporite deposits. The inset shows the deposit without the hummock/toreva shading, highlighting the clear contrast between the dark hummocks and the white evaporite deposits. Place names per Francis and Wells (1988).

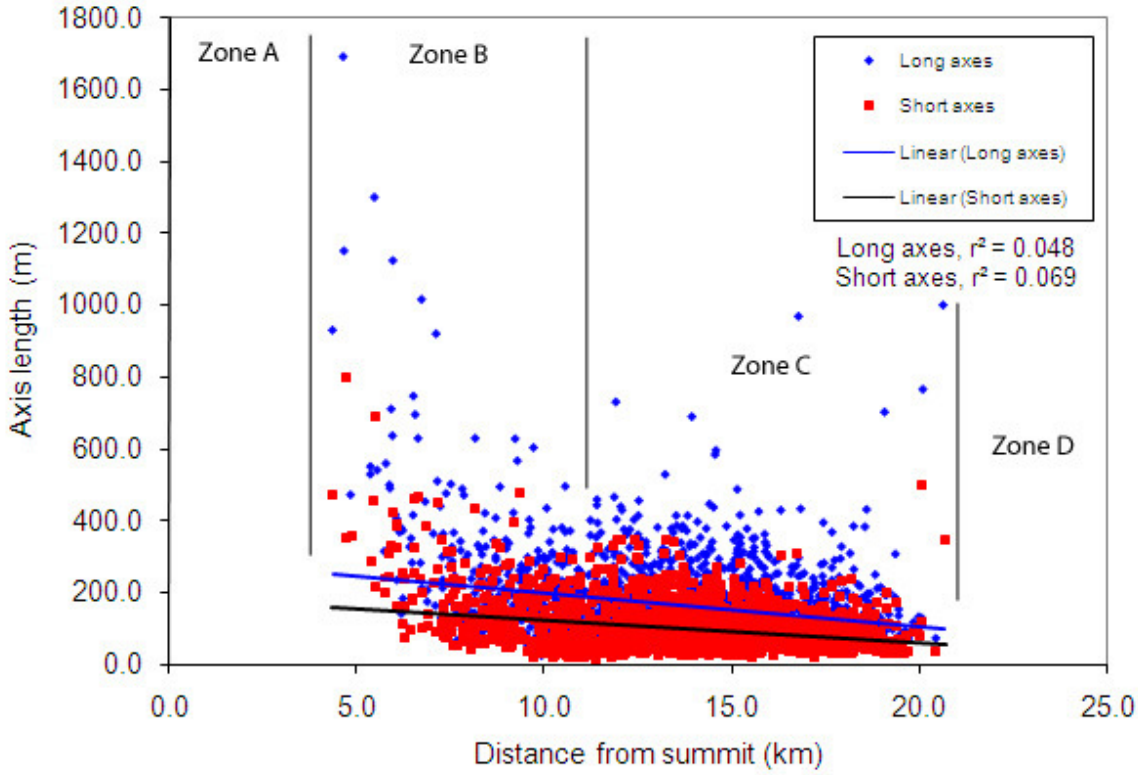

Figure 38 – Relationship between topographic feature long and short axis length versus emplacement distance from current edifice summit, Tata Sabaya VDA deposit. Kolmogorov-Smirnov and Shapiro-Wilk normality tests performed in the statistical package *SPSSv.15.0* indicate normal distribution in this particular data set; subsequent Pearson correlation for parametric data sets results in a significant but weak correlation between feature axis length and distance from source (r = -0.220 and -0.263 for the long and short axes, respectively, p-value <0.01 for both cases). Linear regression trendline used to represent the general decrease in feature size with emplacement distance. Zone distinctions based on the mean extent of each zone shown in Figure 40 and referred to in the relevant discussion.

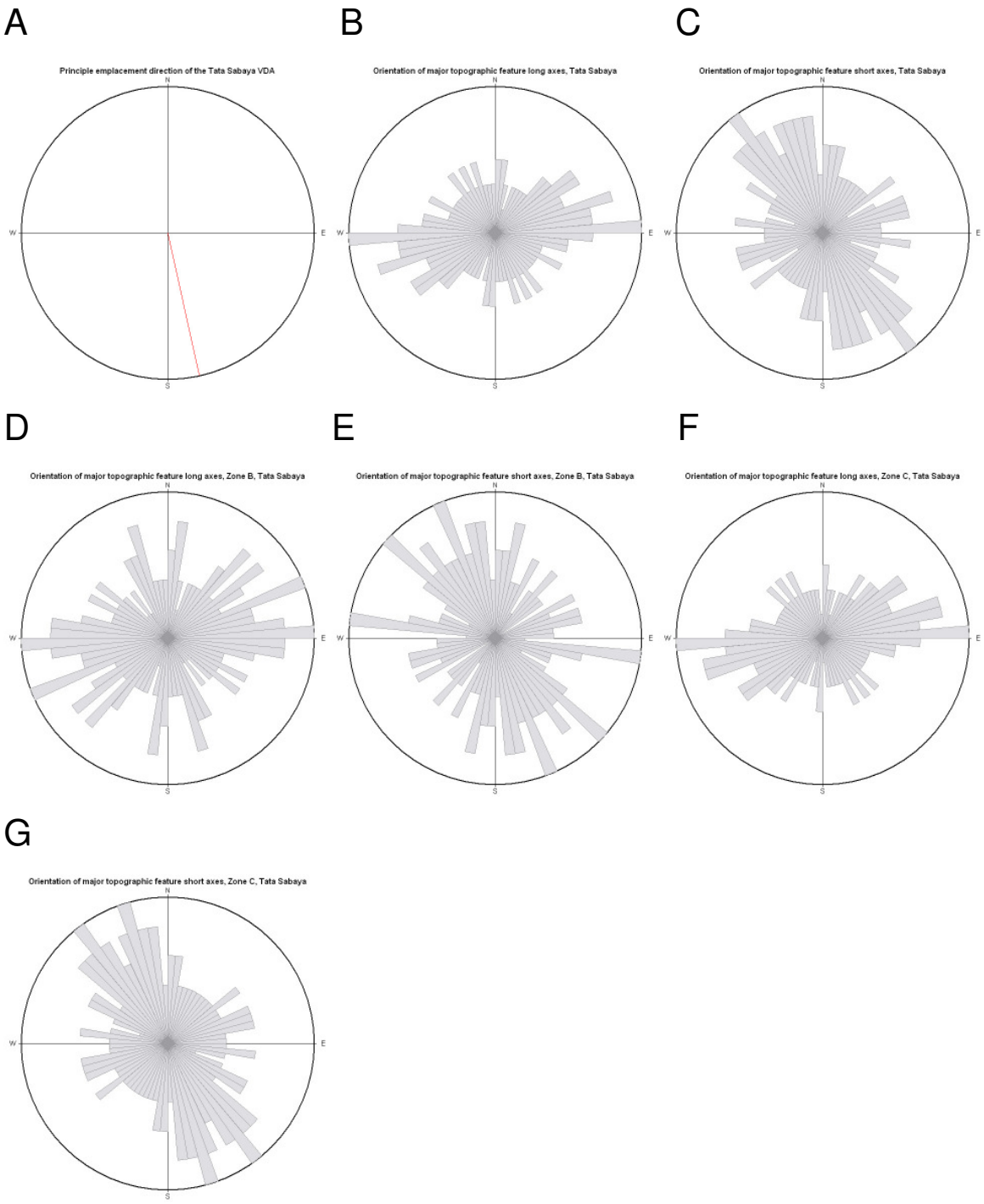

Figure 39 – Surface feature (hummock/toreva) orientation plots for the Tata Sabaya VDA deposit. A) Orientation of the principle emplacement direction; B) Orientation of major topographic feature long axes, total deposit; C) Orientation of major topographic feature short axes, total deposit; D) Orientation of major topographic feature long axes, Zone B; E) Orientation of major topographic feature short axes, Zone B; F) Orientation of major topographic feature long axes, Zone C; G) Orientation of major topographic feature short axes, Zone C.

The emplacement of the Tata Sabaya VDA appears to have been a relatively straightforward event as it does not appear to be significantly affected by topographic influences. As at Mount Shasta, structural kinematic indicators such as faults and folds are

either absent, not visible at available orthophoto resolution or not discussed in the literature and therefore deposit shape and hummock presence, geometry and orientation are the main kinematic indicators. As shown in Figure 40, the emplacement behaviour zones as discussed in Section 4.3.2 are arranged in a generally symmetric pattern reflecting the unconfined and symmetric nature of deposition. Zone A frictional sliding behaviour exists from the hypothesized point of the failed cone to the first location of large toreva blocks at approximately 4 km, marking the proximal extent of the deposit and the transition to Zone B extensional behaviour. A topographic high on the eastern margin of this proximal section may have both directed the main deposit southwards into the emplacement basin and/or restricted toreva movement, influencing near source block deposition and representing the possibility of compressional behaviour (Zone D). Progressive block disaggregation and block deposition occurred from the 4 km mark southwards into the emplacement basin to approximately 13.5 km down the central axis of the deposit. As the main flow direction was generally towards the south, lateral disaggregation in Zone B was generally restricted. Topographic features in Zone B are generally aligned with their long axes perpendicular to flow though a noticeable proportion are aligned at random directions or with their long axes parallel to flow (Figures 39D and 39E). The transition to progressive depositional behaviour (Zone C) is marked by a reduction in block (i.e., hummock) size and clustering of hummocks to form compound shapes. Evidence of Zone C behaviour is prevalent over the majority of the distal area of the deposit as the failure lost momentum and slowed in the generally featureless emplacement basin, unaffected by topography. Increased lateral spreading is observed almost directly parallel to the principal flow direction. Surface feature orientations in Zone C generally mirror those of Zone B in that significant proportion are aligned perpendicular to the principal emplacement direction (Figures 39F and 39G). This may be misleading, however, as significant lateral spreading perpendicular to the principal emplacement direction occurred here in both easterly and westerly directions (qualitatively visible in Figures 37 and 40). Therefore, distal hummock alignment can be regarded as generally parallel to flow. Though the most distal reaches of the deposit are now covered by evaporite deposits in the south and southwest, a series of low ridges arranged with their long axes perpendicular to the principal flow directions suggests the likely presence of compressional Zone D behaviour to the southeast (Figure 41). These structures may be surface expressions of low angle thrust faults resulting from the avalanche's encounter with a distal topographic high as observed at other VDA deposits, such as Shiveluch and Socompa (Belousov *et al.*, 1999; Kelfoun *et al.*, 2008; Shea and van Wyk de Vries, 2008). Structures of this type also suggest a degree of avalanche material yield strength. Transition to compressional Zone D behaviour likely

occurs underneath the evaporite deposits at approximately 20 km. If any transition to lahar conditions (Zone E) occurred at Tata Sabaya it is either not noted in the literature or not visible on the orthoimage due to the presence of post-emplacement evaporite deposits. The symmetric flow line geometry presented in Figure 40 reflects the mostly unconfined emplacement conditions as the avalanche was likely free to spread laterally into the playa basin.

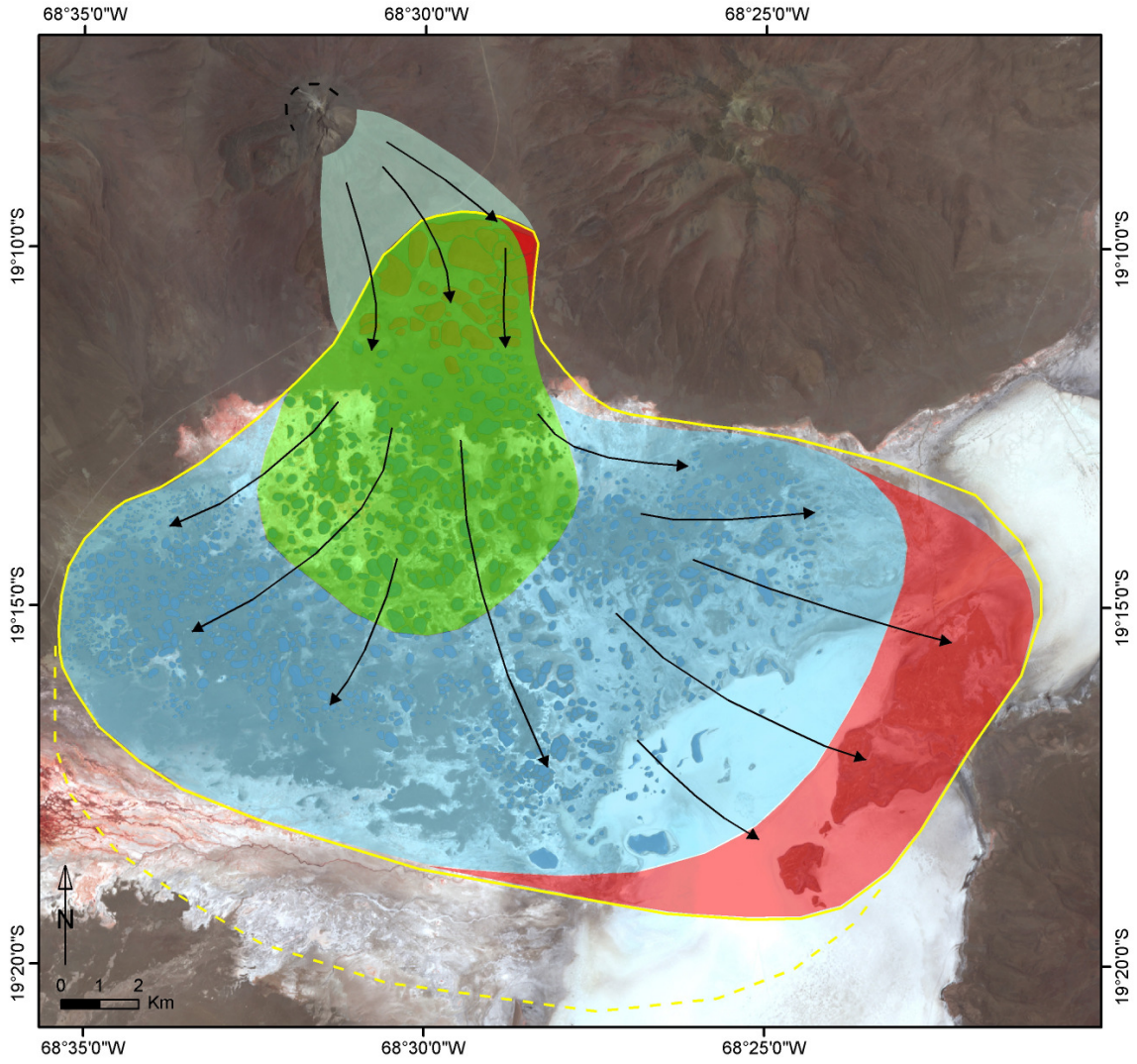

Figure 40 – Emplacement behaviour zone separation of the Tata Sabaya VDA deposit. From proximal to distal – Zone A (white), Zone B (green), Zone C (blue), Zone D (red). The black flow lines represent a likely emplacement direction scenario.

Figure 41 – Zoom view of the island of Jacha Paraya Pampa showing the low linear hummock ridges striking perpendicular to the principal avalanche flow direction, which are likely surface expressions of low-angle thrust faulting (thrusts likely dip to the northwest). Location of Jacha Paraya Pampa shown in Figure 37. Figure generated via Google Earth©.

5.4. Discussion

Orthoimagery interpretations combined with literature descriptions have been used in this chapter to develop further insight into avalanche behaviour. These observations are generally similar in each case and consistent with those discussed in Section 4.3, thus providing tentative support for the general emplacement model and emplacement behaviour zones discussed therein. The most notable observation concerns the apparent progressive disaggregation of intact material and the development of characteristic structures. After failure initiation, emplacement progresses with a period of relatively little disruption of the avalanche body (Zone A). Breakup of the initial material occurs to a minimal degree as this period is mostly characterized by frictional block sliding (Voight *et al.*, 1983; Glicken, 1998; Reubi and Hernandez, 2000). Zone A behaviour covers an average of 20% of the most proximal areas of the VDAs considered. Progressive disaggregation and deposition of the initial slide block or blocks then begins to occur; larger blocks, torevas, are deposited proximally while continually smaller blocks are deposited distally, marking a transition to Zone B extensional behaviour. Constituent blocks appear to retain their relative spatial positions; blocks originating in the slope toe become distal hummocks while internal or headwall material is deposited proximally as

large intact blocks. Most proximal blocks form ridges aligned perpendicular to the principal emplacement direction and display steep-sided triangular horst morphology characteristic of toreva structures. Large-scale block features of this nature are also observed in the more medial deposit areas, at Mount Shasta in particular. A significant proportion of blocks remain aligned perpendicular to the principal direction of emplacement throughout Zone B, which appears to dominate the majority of the events considered and suggests extension as the major general emplacement behaviour regardless of basin geometry. This observation is consistent with the general emplacement model discussed in Section 4.3. Accordingly, extensional structures appear to be predominate: normal and strike-slip faulting, horst and graben systems and flow parallel lineations and furrows. These structures are particularly noticeable in the more proximal sections of the deposits but decrease in prominence with distance. Zone C progressive depositional behaviour is generally characterized by velocity reduction due to momentum loss and a general shift in block long axis orientation parallel to the principal direction of emplacement due to increased influence of the more mobile matrix material. Increasingly random orientations of hummocks are also observed. A decrease in block size and jigsaw fit with distance (Zone A → Zone C) is observed to the distal limit of Zone C, which generally marks the end of deposition of the block facies (Figure 42). Plots showing this relationship are similar to those presented in the literature (Siebert 1984; Siebe *et al.*, 1992; Glicken, 1998; Clavero *et al.* 2002, 2004; Shea *et al.*, 2008). Also, surface feature (hummock/toreva) shapes shift from linear to conical with distance, recognizable in each plot of long/short axis length with distance by distally converging linear regression trendlines (long/short axis length ratios → unity). While extension structures remain dominant in Zone C, they are not as conspicuous as those observed proximally.

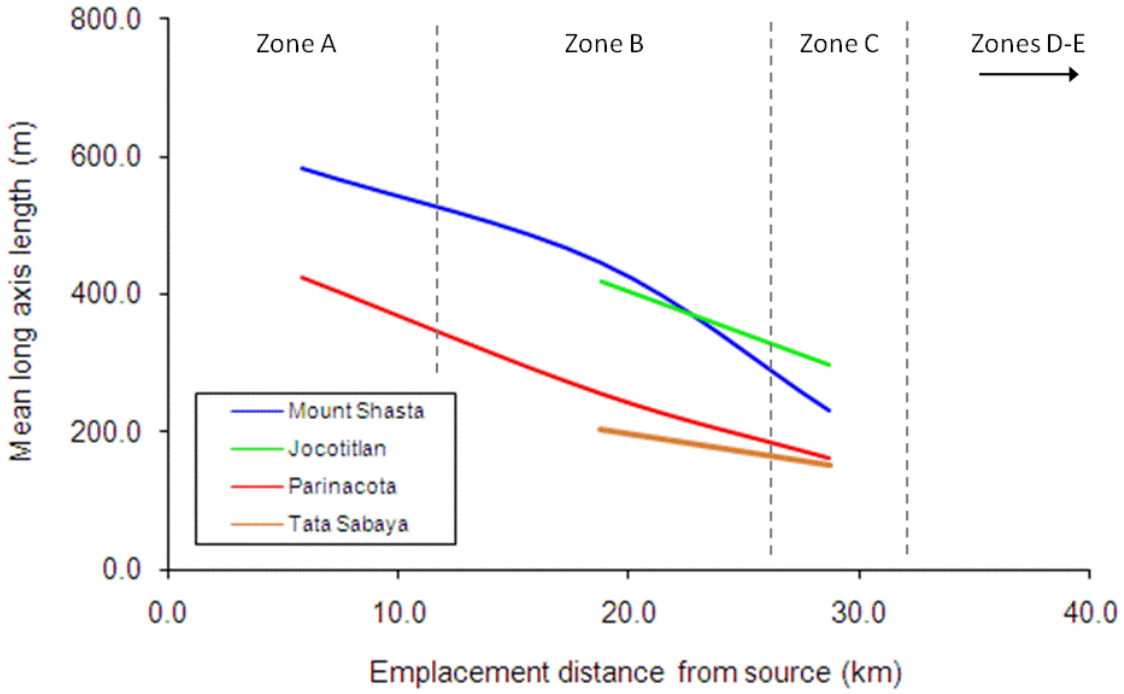

Figure 42 – General reduction in mean block size, defined by long axis length, per emplacement behaviour zone. Only those deposits which show a statistically significant decrease in long axis length with distance are included. Additionally, only those zones which contain a significant number of features across all deposits are included (i.e., blocks from Zone D have not been considered). An exception to this statement is Zone A of the Tata Sabaya deposit, which does not contain any blocks; this deposit was still included, however, due to the large number of measurable features in distal zones (B and C). Zone extents are only qualitative and have been determined from each respective emplacement behaviour zone map and scaled according to the Mount Shasta VDA deposit, the longest of the deposits considered here; individual zone extents were then combined and averaged to produce the general extents shown here. The blocks in Zone for the Mount Shasta and Parinacota VDAs represent features that were difficult to discern at the given resolution of the available orthophotos; they appear as torevas but are outside of the proximal limits of the deposit as drawn by previous authors.

Progressive disaggregation and block deposition likely result in a distal avalanche dominated by matrix behaviour (Zone B → Zone D). These periods define the majority of emplacement and, if a basal shearing/deformation layer mechanism is to develop, might progressively do so during this time. Momentum loss would likely lead to continuous deposition and increased response to topographical barriers, recognized at deposit scale by the prevalence of compressional structures such as thrust faults and folds. Steep and often raised margins may define deposit limits, formed through momentum loss/yield strength influence (Zone C), topographic influences (Zone D) or a combination of each of these factors. Depending on the saturation level of the matrix facies, if present, the most distal reaches of the avalanche may transition to lahar behaviour (Zone E), resulting in flatter and more featureless distal margins.

It should be stated that the emplacement behaviour zonation exercises discussed here have been developed exclusively through orthoimagery interpretation and have not been verified in the field. Thus, a certain amount of error may exist in the precise locations and extents of the zones discussed and they should therefore be regarded only as provisional and first-order classifications of avalanche behaviour. However, the observations made do appear to agree with the general emplacement model described in Section 4.3. Variations in feature dimensions and orientation have been quantified and are generally consistent in all cases considered. The spatial relationships of the emplacement behaviour zones mapped in each example considered are also generally consistent in each case. These observations support the hypothesis that a general deformation sequence, described by the general emplacement model, is likely the most influential factor in resulting deposit morphology and may be universal, to some degree, in most instances. Extension is the major process observed and it is this motion that creates a great deal of the deposit features observed: toreva blocks and hummocks, progressive reduction in block (i.e., hummock) size, normal/strike-slip faulting and longitudinal features. Compression occurs only in certain regimes where topographic barriers are met or avalanche yield strength dominates macroscopic flow behaviour. It is in these local instances that compression related structures might develop, such as complex margins and thrust complexes.

Chapter 6 - Distinct element modelling

The objective of this chapter is to introduce distinct element modelling as tool for the investigation of large-scale debris avalanche emplacement. Earlier studies using DEM for similar purposes are reviewed and the numerical operations of the method are introduced. Limitations are also briefly discussed.

Key questions:

- What is the distinct element method and how has it been used for similar previous studies?
- How does the distinct element method operate?
- What are the general limitations of distinct element modelling?

6.1. Introduction

Though general, mostly qualitative descriptions of emplacement processes can be given, large-scale avalanche emplacement behaviour remains a poorly understood phenomenon. Based on literature interpretations and orthophoto analysis, a common VDA deformation sequence has been hypothesized in the previous chapters to explain the formation of common deposit morphologic features and has been observed to be relatively consistent in all cases considered. However, the precise mechanisms that lead to the formation of characteristic features such as horst blocks, hummocks and basal deformation layers can only be contemplated with a degree of uncertainty. This is due to the fact that events of this nature are relatively rare, often occur in remote locations, and, as unstable slopes and volcanic scenarios may be involved, conditions would likely be too hazardous to make worthwhile analysis practical and safe. Consequently, previous investigators have adopted various modelling approaches to further our understanding on avalanche behaviour, including experimental (Hutter and Savage, 1988; Savage and Hutter, 1989; Drake, 1990; Iverson *et al.*, 1992; Davies and MacSaveney, 1999; Shea and van Wyk de Vries, 2008), theoretical (Savage, 1984; Hutter *et al.*, 1993; Campbell, 1989; Iverson, 1997) and numerical (Hakuno *et al.*, 1989; Cleary and Campbell, 1993; Campbell *et al.*, 1995; Crosta *et al.*, 2001, 2003; Voight *et al.*, 2002; Staron, 2008; Vezzoli *et al.*, 2008) studies. Of these methods, numerical modelling offers significant advantages because of its versatility and ease of quantification and reproducibility for parametric studies. A wide variety of numerical techniques are discussed in the literature; in avalanche emplacement studies

depth-averaged continuum schemes are often employed (Hungr, 1995; Crosta *et al.*, 2003; Kelfoun and Druitt, 2005). This study, however, employs an innovative technique, distinct element modelling (DEM), to simulate avalanche emplacement and thus develop further insight into the geomechanical processes that might control characteristic deposit feature development and the general emplacement evolution sequence recognized in previous chapters. DEM is advantageous over continuum methods because its discrete nature allows the emergent and complex behaviour of a multitude of particle interactions to be considered and is thus directly applicable to granular material studies (Cleary and Campbell, 1993; Campbell *et al.*, 1995; Cleary *et al.*, 2007). DEM also has the ability to simulate the large deformations necessary to model avalanche emplacement over great distances. In these respects DEM is considered to have the capabilities necessary to model the most fundamental aspect of VDA emplacement behaviour as recognized in Chapters 4 and 5: progressive disaggregation of brittle material over large distances based on evolving stresses throughout the failure body.

DEM is a predictive tool widely used to analyze the behaviour of granular materials under applied stresses or gravitational forces (Cleary *et al.*, 2007). Numerous fields, including but not limited to, rock mechanics, slope/foundation studies, mining, industrial design and structural geology have found useful applications for DEM (Morgan, 1999, 2004; Morgan and Boettcher, 1999; Ord, 2003; Seyferth and Henk, 2003; Victor, 2003). Because of its outstanding ability to predict deformation in difficult-to-study environments, DEM is most widely used in the fields of mining, rock mechanics and geotechnical engineering. This and similar methods have also been used by a number of previous authors to consider the mass failure of Earth materials (Hakuno *et al.*, 1989; Cleary and Campbell, 1993; Campbell *et al.*, 1995; Calvetti *et al.*, 2000; Barla and Barla, 2001; Crosta *et al.*, 2003; Deluzarche *et al.*, 2003; Gonzalez *et al.*, 2003; Preh *et al.*, 2003; Tomassi *et al.*, 2003; Preh and Poisel, 2006; Kuraoka and Makino, 2007; Lorig *et al.*, 2007; Staron, 2008; Utili and Nova, 2008). Similar to the work described here, a number of authors have applied the DEM approach to volcanic edifice stability problems (Morgan and McGovern, 2003, 2005a, 2005b; Morgan, 2006; Ward and Day, 2006; Uttini *et al*., 2006, 2007). The majority of these studies, however, have used DEM to consider only the initial stability of edifice slopes as opposed to catastrophic emplacement processes, though Ward and Day (2006) do use a form of DEM to investigate the development of macroscopic VDA deposit morphology. Several of these DEM publications particularly relevant to this study are reviewed below.

This study aims to build upon these previous works by considering the specific debris avalanche emplacement processes that lead to the development of characteristic deposit features and commonly observed morphologies. The widely used commercial DEM software Particle Flow Code PFC^{2D}, available from HCItasca, is employed for this purpose. *PFC* is available in two (PFC^{2D}) or three (PFC^{3D}) dimensional versions though only the two-dimensional version is considered here. A loan of PFC^{2D}, subject to yearly progress reports, was generously offered by HCItasca for the duration of this research. A detailed description of the governing principles and operations of this code is given below.

6.2. Review of notable DEM avalanche emplacement studies

Campbell *et al.* (1995) present an early yet important paper using DEM to investigate the factors that may influence the long runouts observed in large-scale failures. These authors briefly describe a range of hypothesized mobility mechanisms as discussed in Section 2.4, including the often discussed basal shearing layer mechanism, ultimately proposing an alternative. A series of pseudo-laboratory experiment simulations were performed where assemblages of 5,000 – 1,000,000 particles were released down an angled planar chute and allowed to come to rest on a horizontal runout surface. Particles were regarded as rigid disks of a uniform size. A horizontal layering was included to the initial mass to make qualitative observations on deformation.

Upon failure, particles initially at the lowest part of the failure accelerate most, initiating a straining of the deposit. Due to frictional resistance at the base, however, the material at the free surface overtakes the lower portion, creating a folding-over effect. Stratigraphy which was initially horizontal and at an angle to the failure plane aligns itself parallel to the basal surface; material initially on top of the failure eventually covers the full length of the deposit. This last observation leads the authors to suggest this upper material was 'handled gently' and thus would preserve surface block features as observed in natural landslide deposits. Stratigraphic order is preserved throughout. When larger failures were compared with smaller ones the centre of gravity of the deposit shifted proximally (i.e., did not travel as far). Additionally, in the larger failures, the upper layers did not have time to completely cover the entire length of the failure and a portion of each stratigraphy was thus represented on the surface. Spatial velocity measurements show the proximal region comes to rest well before the distal end, which possess the largest relative velocity. Additionally, the volume effect as discussed in Section 2.4, where a decreasing drop height

to runout length ratio (*H*/*L*) is observed with increasing failure volume, is reproduced by Campbell *et al.* (1995).

Campbell *et al.* (1995) also measured the amount of stress experienced by the basal surface due to the emplacement of the failure. Intuitively, it is observed that the largest stresses experienced occur as the failure enters the circular arc which transitions the inclined plane to the horizontal runout surface. Each aspect of stress, normal and shear, is seen to fluctuate greatly for the time period the failure is moving. A certain frequency is observed in this fluctuation though it believed to be much too small to represent the acoustic fluidisation long runout mechanism of Melosh (1979, 1982, 1986). Furthermore, as increasing failure surface friction had no influence on the stresses observed and larger failure showed a noticeable decrease in *H*/*L* ratio, Campbell *et al.* (1995) suggest an additional long runout mechanism must be affecting larger-scale slides. The mechanism subsequently proposed is based on shearing throughout the depth of the failure. In vertical velocity profiles created during the beginning, middle and end of emplacement, the mass is seen to be completely sheared throughout its depth at the beginning and middle of emplacement but travelling relatively together just before deposition. Shearing throughout the entire failure depth is also noted in the DEM simulations of Hakuno *et al.* (1989) and Tomassi *et al.* (2003). In other words, the upper particles are travelling faster than the lower ones which are more influenced by basal friction. Campbell *et al.* (1995) suggest this observation rules out the need for a basal shear layer as this behaviour would preserve jigsaw fracturing in blocks and original stratigraphy, which is indeed observed in rock and debris avalanche deposits. When similar velocity profiles were created for failures of increasing size (i.e., volume), the maximum velocities recorded were nearly identical, signifying decreasing shear rates with increasing failure size. The authors suggest that avalanche energy dissipation is therefore based on shear rate; higher rates (smaller slides) dissipate energy faster and consequently have smaller runouts. Therefore, a basal shearing layer would not necessarily be needed to explain long runout or many characteristic deposit features. Ultimately, Campbell *et al.* (1995) concede that granular flow remains poorly understood and most likely operates in a complex regime transitional between rapid and quasi-static.

Crosta *et al.* (2001) used DEM to simulate the runout of a general granular avalanche. Their simulations were designed to replicate the laboratory experiments of Hutter *et al.* (1995) in which an assembly of plastic disks was released down a chute to study general avalanche mechanics and deposit formation. Because particles are treated as disks of a

specific thickness, the DEM simulation is considered as a 'slice' of the actual experiment. A suite of variables was tracked throughout the avalanche simulation and recorded in the deposit: global kinetic energy, position and velocity of the centre of the flowing mass, coordination number (number of disk to disk contacts) and position and velocity of the front and rear of the travelling avalanche. The particles were released from a relatively high position on the runout chute and therefore acquired a large degree of kinetic energy. It is interesting to note that the initial and final stages of emplacement are characterized by a relatively tight packing with long lasting frictional relationships while the intermediate period displays a dispersion of particles where collision predominates (Crosta *et al.*, 2001). Crosta *et al.* (2001) carried out a sensitivity analysis to observe the effects of contact parameters on avalanche runout and deposit characteristics. Contact stiffness is observed to have an insignificant effect on avalanche deposit characteristics. Particle friction coefficient (μ_p), however, had a noticeable effect: centre of mass runout and global kinetic energy both decreased significantly with increasing μ_p. This effect was less pronounced for the highest μ_p values as particle sliding capability decreases and rotation increased due to frictional coupling. The influence of chute wall friction, μ_w, was also considered and showed similar effects as μ_p.

Crosta *et al.* (2001) calibrated the DEM simulation by choosing material properties identical to those used by Hutter *et al.* (1995) and varying the numerical damping parameter to reproduce shape and position of the deposits produced in the laboratory experiments. Once good agreement was reached between the numerical and experimental models in terms of deposit characteristics, the numerical models were used to investigate the influence of chute geometry variation and the number and size constituent failure particles. It was observed that an increase in chute inclination leads to a decrease in flow length and increase in kinetic energy. An increase in particle number leads to larger energy dissipation and a reduction in the runout distance of the centre of mass, as observed by Campbell *et al.* (1995). Increasing the size of the avalanche particles did not significantly affect the avalanche travel or deposit characteristics.

Using the damping parameter found to accurately reproduce the laboratory experiments, Crosta *et al.* (2001) then attempted to reproduce a real world avalanche event, the Val Pola rock avalanche which occurred in the Swiss Alps in 1987. Particle size distribution (uniform) was chosen from observations of the in situ deposit and microproperties were chosen to match the constituent rock mass. Bonds were installed at particle contacts though it is unclear if these have been contact or parallel bonds. Failure was induced by

two methods: A) instantly removing bonds, and; B) progressively removing bond strength until failure was triggered. Travel and deposit characteristics are little affected by the method used. Method A represents a more 'granular' flow with higher kinetic energy. Using method B, remaining bonds were progressively destroyed during emplacement. In either case, good agreement between the numerical simulations and real world event was observed in terms of velocity attained, overall emplacement time and deposit geometry. The main discrepancy lies in the deposit thickness; the numerical simulation deposit was thicker as expansion in the third dimension (out-of-plane) was not possible. The position of several individual particles located in different areas of the failure was tracked throughout emplacement, allowing the following observations to made (Crosta *et al.*, 2001):

- The shortest runouts are experienced by particles close to the rupture (i.e., ground or failure) surface.

- Travel distance decreases with vertical depth in the initial failure, i.e. a 'cascading' effect was observed. This observation exemplifies a vertical velocity gradient and a thinning and stretching of the avalanche body.

Additionally, stratigraphic layers were introduced by varying particle colour to make qualitative observations on emplacement where an overall 'vertical inversion' of layers was observed as layers on the upper surface of the initial failure were located on the bottom of the deposit, and vice versa.

Ward and Day (2006) employed a DEM technique following the same general mechanical operations as those presented above, though with some distinct differences. This method can be described as DEM as it employs a particulate assembly, each particle with its own material properties and the ability to separate from its neighbours. Additionally, the assembly loses energy due to frictional and velocity-dependent deceleration. This technique differs from those presented above, however, in that it utilizes very few particles and is displayed in the xz plane (map view) rather than the xy plane (cross-sectional). An advantage of this model is that it uses a base which mimics natural topography, allowing avalanche/topography interactions to be more realistically considered.

Ward and Day (2006) applied their DEM model to the 1980 Mount St. Helens VDA to investigate the spatial distribution of the deposit as well as its kinematic history. The post-

collapse scar is reconstructed to its pre-collapse geometry with particles possessing material properties, namely frictional, representative of those found in the deposit. As the Mount St. Helens VDA was observed to initiate as three separate blocks (Voight *et al.*, 1983), those of the DEM model were separated into three spatial groups and released at 30 s intervals. Simulations reproduced the deposit of the VDA in terms of deposit thickness and distribution. High friction particles designed to represent competent blocky material came to rest in the more axial/proximal areas of the deposit, as observed in the actual deposit. Low-friction material representative of matrix material was found primarily distal of a prominent break in slope, again similar to the actual deposit (see Section 4.2.1). The model was not able simulate the portion of the deposit that spilled over a prominent topographic high (Johnston Ridge) or match the overall emplacement duration accurately. These simulations did, however, agree with kinematic constraints presented by actual seismic records in terms of timing of collision into Johnston Ridge, reversal of acceleration and forces generated (Ward and Day, 2006). A number of similar models have been produced by Ward (2009) for the purpose of analyzing large-scale failure, particularly in relation to tsunami generation.

6.3. DEM operation

PFC^{2D} and the DEM method in general are based on the rock mechanics work of Cundall (1971) and subsequent soil/granular material study of Cundall and Strack (1979). This technique models the movement and interaction of stressed assemblies of rigid, circular particles joined together by a network of contacts and can be classified in the wider scheme of *discrete element modelling* (Cundall and Hart, 1992; Itasca, 2004a). The term *distinct element modelling* refers to a specific class of discrete element modelling which uses deformable contacts and explicit, time-stepping solutions of the equations of motion (Cundall and Hart, 1992). In short, DEM simulates the dynamic relationship of an assembly of stressed, rigid particles by calculating the contact forces and subsequent displacements of each individual particle in response to its interaction with its neighbours (Itasca, 2004a). Particle contact forces and displacements of a group of particles, the result of disturbances caused by specified wall or particle motion and/or body forces, are found by incrementally monitoring the movements of each individual constituent particle (Itasca, 2004a). DEM simulations are typically considered to be fluid-free, 'dry' granular flow simulations (Campbell *et al.*, 1995).

PFC^{2D} operates under the following assumptions (Itasca, 2004a):

- Particles are circular, rigid bodies occupying a finite amount of space ('clumping' may be used to define entities of arbitrary shape).

- Particle contacts occur over a vanishingly small area.

- A soft-contact approach characterizes each contact where rigid particles may overlap one another. The amount of particle overlap at a contact is related to contact force by the force displacement law. Overlaps are small in comparison to particle size.

- Bonds may exist at particle contacts.

With these assumptions in mind, *PFC*^{2D} models granular assemblies particularly well as deformation results from the sliding and rotation of rigid bodies and the opening and interlocking of interfaces between discrete particles (Itasca, 2004a).

The movement of individual particles in an unstable assemblage is determined through an explicit timestepping scheme where the timestep is theoretically chosen to be so small that disturbances cannot transmit further than the immediate neighbours of a particular particle. In this manner the forces acting on a specific particle are determined exclusively by interactions with particles it is immediately in contact with. The speed at which disturbances propagate is a function of the material properties of the particles. This explicit numerical technique means the nonlinear interaction of a large number of particles can be considered without excessive memory requirements (Itasca, 2004a).

Two calculations are performed at each timestep. First, Newton's second law of motion ($F = ma$) is applied to each particle to determine its movement (position and velocity), and that of its contacts, due to the contact and body forces acting on it. Particle and wall positions and velocities are updated by integrating this equation twice (acceleration → velocity → displacement) (Lorig *et al.*, 1995). Next, a force-displacement law is used to update the contact forces stemming from the relative motion of the two particles (or particle and wall) that make up a contact. These contact forces are then used to determine subsequent particle movement, and the cycle continues to the next time step. If force is in

equilibrium, no motion occurs. A summary of the governing force equations used in this process, after Itasca (2004a) and Potyondy and Cundall (2004), is detailed as follows.

The overall contact force vector, F_t, which represents the force of one ball against another, can be decomposed as:

$$F_t = F_n + F_s \tag{2}$$

where F_n and F_s are the normal and shear component vectors, respectively. The magnitude of F_n is calculated by:

$$F_n = k_n U_n \tag{3}$$

where k_n denotes the normal stiffness at the contact and U_n is the amount of particle overlap. k_n is a function of the stiffness of each constituent particle, defined as:

$$k_n = k_{nA} k_{nB} / (k_{nA} + k_{nB}) \tag{4}$$

where k_{nA} and k_{nB} denote the user defined normal stiffnesses of the constituent particles *A* and *B* (i.e. any two particles in contact). k_n is a secant modulus, representing *total* displacement and force experienced throughout a given simulation.

The magnitude of the shear force (F_s), however, is calculated *incrementally* (hence Δ) at each timestep as:

$$\Delta F_s = -k_s \Delta U_s \tag{5}$$

where k_s is the contact shear stiffness and ΔU_s denotes the change in particle overlap from one timestep to another. k_s is calculated in a manner similar to that in shown in (3). F_s is calculated by adding the new shear force, ΔF_s, to that present at the beginning of the timestep:

$$F_{s(new)} = F_s + \Delta F_s \tag{6}$$

The *translational* motion of an individual particle is determined from the force, F_t. A particles' *rotational* motion, however, is related to the moment acting on a particle, which is in turn a function of a particles' radius, shape, mass and angular acceleration (Itasca,

2004a). A detailed description of the numerical operation of the PFC^{2D} calculation cycle, including a full explanation of the procedures used to account for rotational motion, can be found in Itasca (2004a) but is withheld here due to the mathematical complexity of the discussion. The basic concepts needed to understand the operations of the code are, however, are given throughout this section.

Walls are assigned normal and shear stiffness and friction values of their own (k_{nw}, k_{sw}, μ_w, respectively) and may interact only with particles and not each other. Any desired model geometry may be created with a number of wall segments.

6.3.1. Timestep

For computational stability in PFC^{2D}, a critical timestep must not be exceeded. Because PFC^{2D} behaves in a mechanical fashion similar to an assemblage of particles and springs, associated spring behaviour equations can be used to determine the critical timestep (Itasca, 2004a):

$$t_{crit} = \sqrt{\frac{m}{k_{tran}}} \text{ (translational motion)} \tag{7}$$

$$t_{crit} = \sqrt{\frac{I}{k_{rot}}} \text{ (rotational motion)} \tag{8}$$

where m = particle mass, k_{tran} = translational stiffness, k_{rot} = rotational stiffness and I = the moment of inertia of a particular particle. k_{tran} and k_{rot} are functions of particle radius, contact forces present and particle stiffness as detailed mathematically in Itasca (2004a). PFC^{2D} applies these equations automatically to each degree of freedom for every particle in a given assemblage and the final value of t_{crit} is taken to be the minimum of every value calculated. To ensure computational stability, the timestep used in a given simulation is then taken to be some fraction (typically ≈1/3) of this value of t_{crit}.

6.3.2. Damping

Energy contributed to a particulate system in PFC^{2D} is dissipated only through frictional sliding, which in some cases may not be sufficient to reach a steady-state solution in a reasonable period of time (Itasca, 2004a; Potyondy and Cundall, 2004). For this reason,

some form of numerical damping must be applied to the particulate system, several forms of which are available in PFC^{2D}. The default form, termed *local* damping, is applied as a function of the unbalanced force in the assembly and applied to each particle. Local damping is best used for quasi-static, compact assemblies and thus not appropriate for dynamic granular flow-type simulations. For this type of model, *viscous* damping, applied to each particle contact is most suitable (Crosta *et al.* 2001; Morgan and McGovern, 2003; Tomassi *et al.*, 2003; Itasca, 2004a). Viscous damping simulates the effect of adding normal and shear dashpots at each contact, active only in the instance of particle contact (i.e., impact), and is characterized by the critical damping ratio, which in turn is relatable to a measured value of the coefficient of restitution, a common material property. This relationship can be obtained by simulation drop tests performed in PFC^{2D} (Tomassi *et al.*, 2003; Itasca, 2004a). Though local and viscous damping models may be combined to reach equilibrium more quickly in some cases, only viscous damping is applied in this study.

6.3.3. Contact model

In PFC^{2D}, the constitutive model acting on a particular particle-particle contact is composed of three parts: a stiffness model, a slip model and a bonding model (Itasca, 2004a, 2004b). As introduced in equations 2-6, the contact stiffness model defines the elastic relation between contact force and associated displacement. Though user defined models may be implemented, two general models are available in PFC^{2D}, linear and Hertz-Mindlin. The linear contact model, defined by normal and shear particle as detailed above, is used exclusively in this study as the Hertz-Mindlin model is undefined for bonded model simulations as discussed in Chapter 8. The slip model is an inherent property always active between two particles in contact. This model dictates that no normal force is present when two particles are in tension and allows slip to occur by a limiting shear force, defined by the lowest friction coefficient value (μ_p) possessed by either of the two particles. The limiting shear force is defined as:

$$F_{max} = \mu_p F_n \tag{9}$$

If the shear force that develops between two particles experiencing shearing motion is greater than F_{max}, irreversible slip occurs.

The third contact property present is a bond model, a unique but powerful tool in *PFC*^{2D}. This feature allows a 'glue' or 'cement' like bonding of two particles in contact that possess certain normal and shear strength properties, that if exceeded, break (Figure 43). This is important as it has the ability to simulate fracture processes in a rock mass; individual bonds break and combine with other broken bonds in an overstressed area to form macroscopic fractures and faults, depending on model scale. This process allows emerging brittle behaviour to develop based on the realistic evolution of intergranular force chains, as would occur in a natural rock material under stress. Several authors have shown that this system does indeed replicate the majority of significant behaviours observed in fracturing rock systems (Potyondy and Cundall, 2004; Schöpfer *et al.*, 2008; Utili and Nova, 2008).

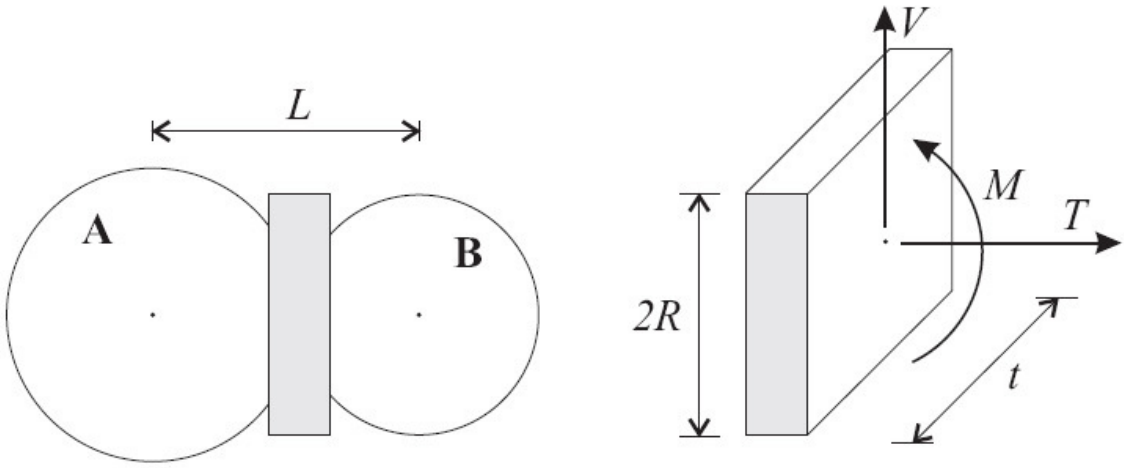

Figure 43 – Idealization of a parallel bond modified from Itasca (2004a). The left of the figure shows the idealized bond between two particles A and B and the distance between their centres, *L*. The right of the figure details the axial (*T*) and shear (*V*) forces and moment (*M*) acting on the interparticle bond. The size of the bond, *2R*, is user specified but in this case equals the diameter of the smallest particle involved in the bond. The bond thickness, *t*, is also user defined and remains equal to 1, the thickness of the disks involved, throughout this study.

Two bonding models are available in *PFC*^{2D}, contact and parallel bonding, though user specific models may be defined. Contact bonds act as a glue at a vanishingly small contact point and transmits force, but not moment. Parallel bonds, in contrast, which act as a brittle elastic glue of finite size, do transmit moment and are therefore most appropriate for most rock mass simulation models. For this reason parallel bonds are used exclusively in this study and thus described here. Further information on the principles of contact bonding can be found in Itasca (2004a).

A parallel bond is considered to act as a set of elastic springs uniformly distributed over a rectangular cross-section centred at a particle-particle contact, as in Figure 43, and defined by a constant normal and shear stiffness (Itasca, 2004a, 2004b). Individual particle motion causes both force (normal stress) and moment (shear stress) to develop within the bond that if it exceeds the normal and/or shear strength of the material, breaks the bond. Frictional slip properties are then called upon to define the contact.

6.3.4. Microproperty characterization

A bonded particle model is characterized by particle mass density, size distribution, packing arrangement and particle and bond properties (Potyondy and Cundall, 2004). To ensure realistic packing arrangements in the particle assembly (and in keeping with the methods recommended by Itasca [2004b]), a uniform particle size distribution is used throughout this study, both in calibration exercises and subsequent simulations. Particle and bond properties are important in defining the deformation characteristics of a simulated rock mass. The behaviour of a simulated rock mass is defined by (Potyondy and Cundall, 2004):

E_c, k_n/k_s, μ_p – particle properties (10)

E_{cb}, k_{nb}/k_{sb}, λ, σ, τ – parallel bond properties (11)

where E_c and E_{cb} are the Young's moduli of the particles and bonds, respectively, and k_n/k_s and k_{nb}/k_{sb} are the normal to shear stiffness ratios for the particles and bonds, respectively. The symbols λ, σ and τ represent the bond radius, normal and shear strength, respectively. As before, μ_p represents intergranular particle friction.

For future macroscopic rock mass calibration purposes, it is important to note that in two dimensions (Potyondy and Cundall, 2004):

$$E_c = k_n /2t \text{ or } k_n = E_c /2t \quad (12)$$

where t = disk thickness as shown in Figure 43 (particle thickness as particles are herein treated as disks). The value of t typically equals one, therefore $k_n = E_c /2$.

6.3.5. Material genesis and calibration

DEM differs from other numerical modelling techniques in that it represents a discontinuum of individual particles, each characterized by specific microproperties. Macroscopic material properties (e.g., rheologic) cannot be simply entered directly based on known or measured values as can be done with many continuum methods. For this reason Itasca has developed a material genesis and calibration procedure designed to relate particle microproperties with the desired macroproperties, such as peak strength and deformation characteristics (Itasca, 2004c; Potyondy and Cundall, 2004). It is most often these macroproperties that users are typically interested in simulating.

The calibration procedure involves the simulation of laboratory tests commonly implemented in reality to define rock strength, namely Brazilian and biaxial (PFC^{2D})/triaxial (PFC^{3D}) tests (Sitharam and Nimbkar, 1997; Itasca, 2004c; Potyondy and Cundall, 2004). The tests are implemented by driver files and functions provided by Itasca. The material genesis procedure is shown Figure 44. First, a rectangular (2:1 height:length ratio) is created in the PFC^{2D} environment from a series of four frictionless walls. Second, a number of frictionless particles are generated in rectangular space and their radii are expanded to produce a compact assembly where each particle is in contact with its nearest neighbour or wall. As tight packing is desired, a uniform particle size distribution is used to achieve a porosity of roughly 16% (Potyondy and Cundall, 2004). This procedure produces unfavourable internal stresses so particle radii must then be manipulated to produce a specified isotropic stress throughout the sample, which is set to a low value relative to overall material strength. To produce a dense network of bonds, it is then desirable to remove all particles which have fewer than three contacts with neighbouring particles, termed ‘floaters’. The test specimen is completed by installing particle friction coefficients and bonds and removing the specimen from the production rectangle, if desired. A fully bonded, tightly compacted specimen with low locked-in isotropic stresses and equilibrium forces is now achieved.

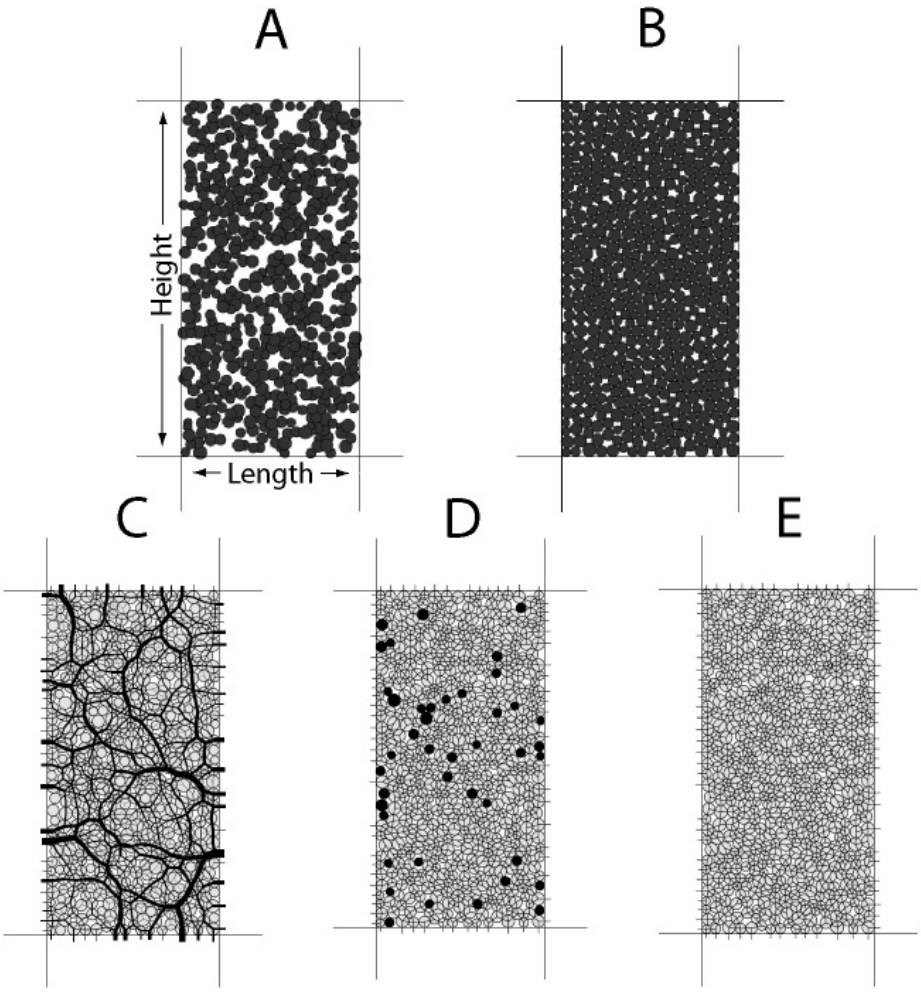

Figure 44 – Test sample genesis procedure per Itasca (2004c). (A) Initial particle assembly generated in random positions at half of their final size; (B) Particle assembly after model cycling, particles initially in contact are repulsed from one another to occupy distinct positions; (C) Compressive contact force distribution after radii expansion to achieve a low isotropic stress state; (D) Identification of 'floater' particles, those with fewer than three contacts; (E) Final assembly after each floater has been removed and bonds have been installed, if desired. Scale is dependent on the desired material to be tested, in this case the average radius, $R_{avg} \approx 1$ mm.

Simulation laboratory tests are then conducted on the specimen by loading the rectangular specimen with the top and bottom walls, thus applying axial stress. As in a real world test, the positions of the lateral walls are automatically adjusted by a servo-mechanism to keep a constant confining stress, if present. Stresses and strains acting in the specimen are measured by both wall-derived quantities and measurement circles and evaluated to observe the associated macroproperty values. An example of the PFC^{2D} uniaxial test simulation is shown in Figure 45.

A

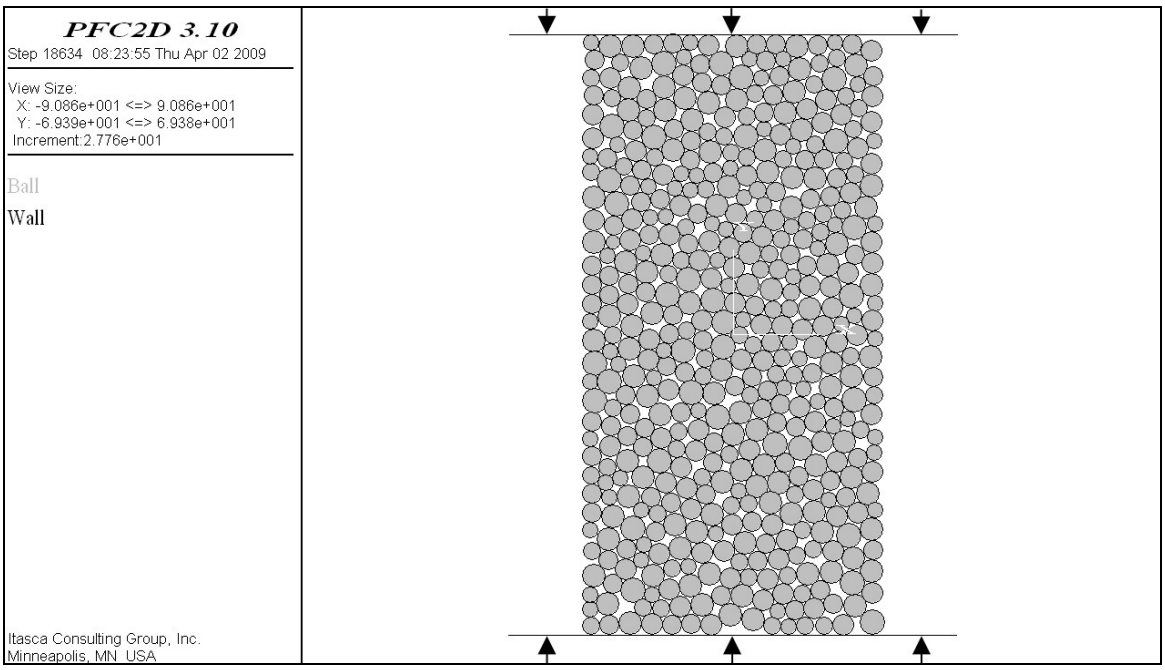

B

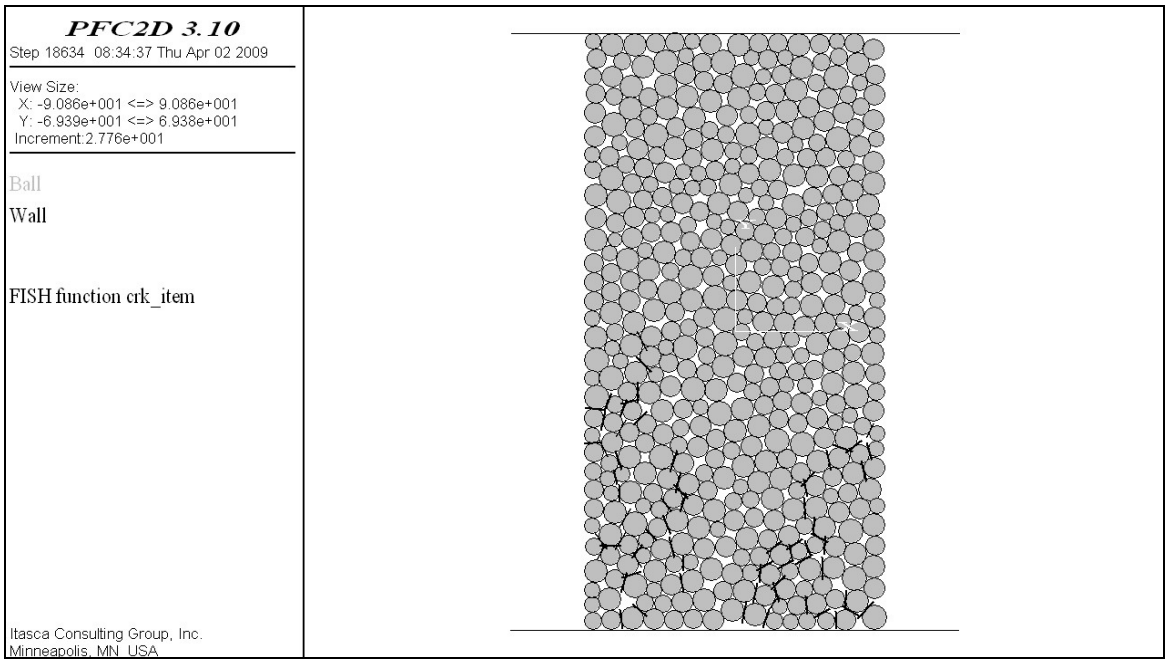

(Figure 45 continued on following page)

C

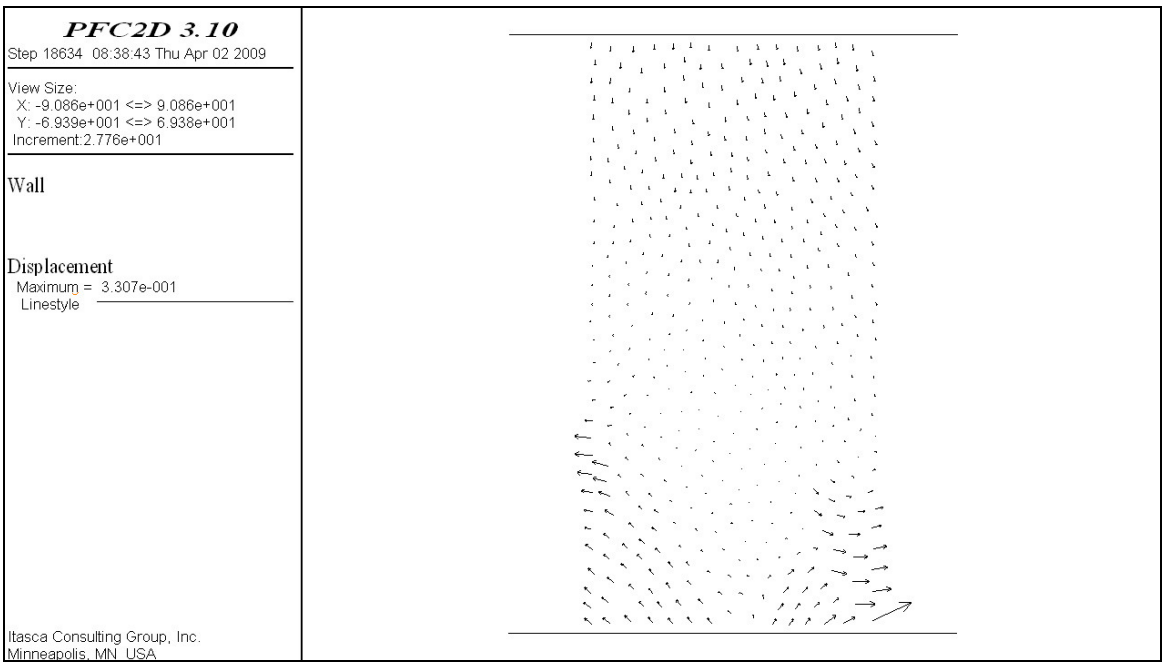

D

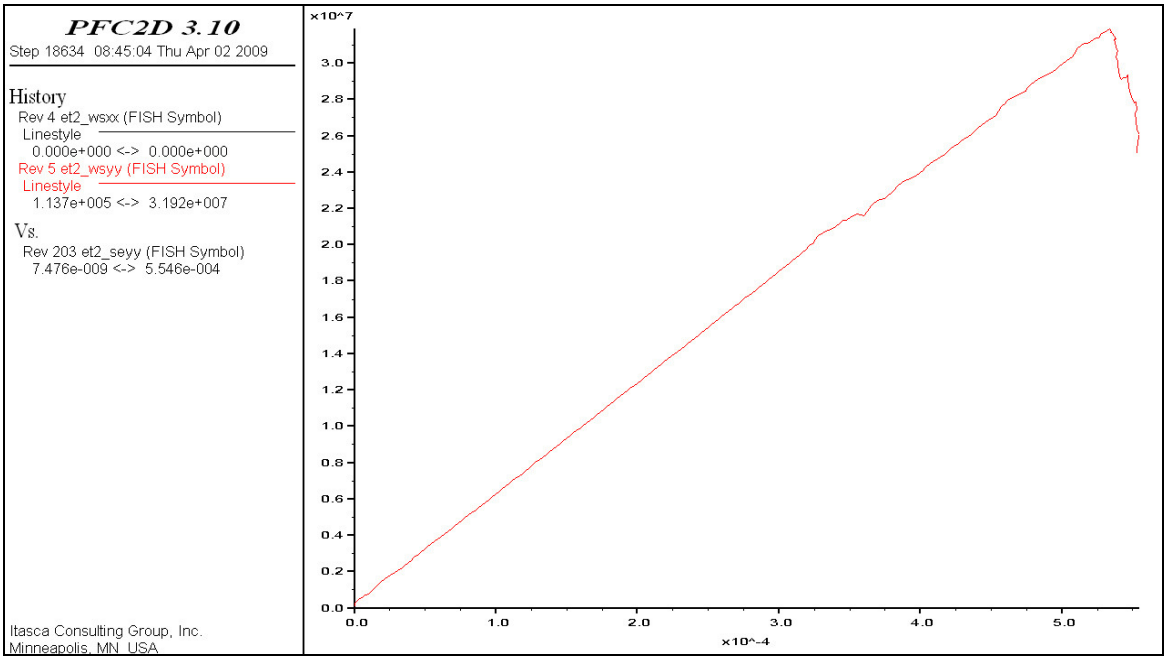

Figure 45 – *PFC*^{2D} uniaxial test for material calibration process. (A) Initial assembly, with axial loading indicated by loading platen movement arrows; (B) Development of tensile fractures within the bonded assembly, denoted by black 'infill' between particles, which signifies and individual broken bond ; (C) Particle displacement; (D) Plot of axial stress versus axial strain indicating failure of the bonded specimen; in this case UCS = 31.9 MPa. Figures generated by *PFC*^{2D}.

To reach the desired macroproperty values, a series of iterative steps are performed (Itasca, 2004c):

1. In an unconfined scenario, material strengths are set to high values and E_c and E_{cb} are varied to produce a desired macroscopic elastic modulus, E_m. Desired Poisson's ratio (v) values are then achieved by varying the k_n/k_s and k_{nb}/k_{sb} values.

2. Unconfined compressive strength (UCS or σ_{ci}) is then found by setting the standard deviation of material strengths to nil and varying mean material strength.

3. After peak strength has been matched, crack initiation stress (σ_{ini}) is obtained by varying the standard deviation of material strengths.

4. Post-peak behaviour may then be matched by varying μ_p.

5. A strength envelope can then be created by performing a number of biaxial tests at increasing levels of confinement. Brazilian tensile strength may also be found at this point.

Strength envelopes are computed by the following Hoek-Brown relation:

$$\sigma_f = \sigma_3 - \sqrt{s\sigma_c^2 - \sigma_3\sigma_c m} \tag{13}$$

where σ_f = peak strength, σ_3 = confining pressure at failure, σ_c = unconfined compressive strength (when s = 1) and m and s are dimensionless material constants (Potyondy and Cundall, 2004). It should be noted that achieving an accurate strength envelope in DEM is a topic of ongoing research (Itasca, 2004c; Potyondy and Cundall, 1999, 2004; Schöpfer *et al.*, 2008; Utili and Nova, 2008). Potyondy and Cundall (2004) show that, when implementing the material calibration procedures above to simulate known laboratory behaviour, UCS values match closely but the slope of the simulation strength envelope is much lower than that found through actual laboratory testing. These authors suggest this observation may be the result of using circular (or spherical in three dimensions) grains in the model. Additional experiments have therefore been conducted by these authors using clustered grain assemblies, which do not break internally and interlock with neighbouring clusters as would occur in actual assemblies of irregular grains. Subsequent results show

an increase in strength envelope slope though it remained lower than the desired (i.e. actual) slope. Additionally, variation of the bond normal to shear strength ratio (σ/τ) has a noticeable effect on the strength envelope slope; as this ratio increases, the strength envelope decreases. This observation is the result of failure mode: materials with smaller σ/τ ratios fail predominantly in a brittle (tensional) manner where normal strength is exceeded and larger σ/τ indicate predominantly ductile (shear) failure as shear strength is exceeded (Itasca, 2004c; Preh and Poisel, 2006). Ultimately, it is stated by the authors mentioned that the subject of replicating the strength of envelope for a particular material needs significant further research. Therefore, bonded materials in this study were calibrated by an unconfined scenario where no strength envelope was produced, though accurate E_m, v and UCS values are still be obtained (Jaeger and Cook, 1979; Potyondy and Cundall, 2005). Furthermore, crack initiation stress (σ_{ini}) information was not available for the materials being calibrated and was therefore neglected. Though some information is neglected, this approach is a reliable means of calibrating the macroscopic response of a bonded particle assembly in PFC^{2D}, particularly at the large-scale of the models in question (DeGagne, 2008).

6.4. Limitations

Lorig *et al.* (1995) describes both mechanical and computational limitations of DEM (and PFC^{2D} specifically): mechanical limitations are considered to be the lack of knowledge about material microproperties whereas computational limitations have largely since been overcome my modern computers. PFC^{2D} is, in this case, a two-dimensional discontinuous medium and thus possesses additional limitations. Only two force and one moment components exist; the out-of-plane force and moment components are not considered; stress and strain must be determined through averaging procedures. The effects of lateral spreading and associated margin structures therefore cannot be examined. Staron (2008), however, notes that the lack of third dimension movement does not considerably affect the flow dynamics of the simulation avalanches in the principal (downslope) flow direction.

Additional limitations exist in assuming model packing, porosity and mass properties (Itasca, 2004b). Furthermore, constituent particles are circular or spherical in shape which may vary considerably from real world situations (Crosta *et al.*, 2001). The effect of this has already been discussed by the lower than desired slope of the simulated strength envelope; another effect may be the unwanted influence of particle rolling. This factor will be discussed in further detail in later chapters. Also, surface damage and wearing effects

are not simulated during particle interaction buy may have a notable effect on real world particle properties (Crosta *et al.*, 2001). The influence of fine-grained or saturated sediments and dynamic flow conditions often suggested for large-scale avalanche emplacement is also thus far difficult to consider. As the only source of energy dissipation in a DEM model is friction, non-elastic dissipation mechanisms cannot be modelled directly and must be done so through numerical damping procedures, such as viscous damping as described previously. Lastly, Crosta *et al.* (2001) point out that, without significant user code manipulation, DEM is generally not able to consider many of the more dynamic mechanisms typically considered to be influential in governing avalanche runout, such as fluid/gas interaction, granular temperature or block fragmentation. PFC^{2D} particles are rigid blocks and retain their size and geometry no matter the state of stress present; real world blocks and grains would likely be altered to some fashion. However, both bonding effects and user-written definitions can be employed to take this effect into account (to some degree).

DEM, particularly in two dimensions, is therefore limited in its ability to simulate every mechanism that may be occurring in a given rock or debris avalanche situation and results should therefore be regarded as first-order approximation in any case. This technique is nonetheless valuable for its ability to capture the general mechanics of real world problems and represent simplified cases of often very complicated events (Barla and Barla, 2001). As put by Crosta *et al.* (2001, p. 15), "…the numerical results can be considered satisfactory….due to the model capability to catch the basic aspects of the phenomenon, which resides in the discrete and frictional nature of the flowing material". The ability of this method in capturing the processes occurring during large-scale catastrophic debris avalanche emplacement specifically will be considered in the conclusion to this thesis.

6.5. Discussion

DEM is a powerful and versatile numerical method used in a number of industries, particularly in those where the mechanical behaviour of rock and soil must be understood. The discrete nature of this method makes it ideal for investigating the behaviour of granular materials, and subsequently, avalanche emplacement processes specifically. A review of notable DEM studies conducted with a similar to purpose to that of this thesis have therefore been discussed. These studies have established the capability of DEM for analyzing avalanche emplacement mechanics, such as evolving vertical velocity profiles and the relationship between material properties and runout length. The numerical

operation of DEM (PFC^{2D} specifically) has also been reviewed, including the best practices for macroscopic material calibration, which will be considered again in Chapter 8 specifically for purposes of this study. Though limitations of DEM exist, the ability of the method to capture first-order mechanical processes is exceptional, particularly in relation to other numerical methods, and it can therefore be considered an appropriate tool for investigating the geomechanical processes occurring during VDA emplacement.

Chapter 7 - Unbonded DEM modelling

The objective of this chapter is to build upon the introduction to DEM given in the preceding chapter and develop an initial avalanche simulation model capable of simulating the general geomechanical behaviours identified in Chapters 3-5. A simple unbonded scenario is used here to develop an understanding of basic model controls and simplistic avalanche behaviour through a number of quantitative and qualitative simulations analysis methods. The ultimate objective of this chapter is to consider the findings of the unbonded avalanche simulations performed here in relation to previous studies (Chapter 6), general VDA geomechanical behaviour and the formation of commonly observed deposit features and morphologic characteristics (Chapters 3, 4, 5).

Key questions:

- What are the basic controls and model parameters affecting the DEM simulations?
- Are observations stemming from simulations conducted here consistent with those of previous authors?
- What insight might be developed from the unbonded simulations in relation to the formation of commonly observed deposit features and morphologic characteristics?
- What are the limitations of the unbonded simulations in reproducing the observed deposit features?

7.1. Introduction

Previously conducted studies (Section 6.2) have shown DEM to be valuable tool with which to investigate avalanche emplacement mechanics. This chapter builds upon those studies by developing an avalanche simulation model representative of a volcanic flank collapse scenario and considering a number of quantitative and qualitative aspects of its behaviour during emplacement. These exercises are similar in many respects to those of Campbell *et al.* (1995) and Crosta *et al.* (2001). In this manner, many of the experiments of these authors can be repeated and/or modified to ensure consistent simulation behaviour and develop further understanding of the behaviours recognized by those authors. Starting with a simple model also allowed for an opportunity to learn the controls and operations of the PFC^{2D} system. Furthermore, as an initial intention of this study was to explore the particle bonding capability of PFC^{2D}, which adds significant complexity to the avalanche

model, the processes occurring in a simple unbonded avalanche system must first be established. Analysis of the mechanical processes occurring during emplacement is also undertaken here by utilizing software tools and analysis methods previously not available or considered. These tools, many exclusive to PFC^{2D}, allow for recognition of the spatial and temporal evolution of stresses, strains and other properties within the deforming avalanche body. The intention of this exercise is to specifically consider the implications of these observations in regards to overall VDA geomechanical behaviour, the formation of characteristic deposit features and the areas where an unbonded DEM model may lack the capabilities necessary to develop such features.

As this study represents a first attempt at DEM modelling for the author, sensitivity analyses on all parameters and operation controls used in PFC^{2D} were first conducted, including exploration of various numerical damping techniques, particles size ranges and particle/wall stiffness/friction values. In many cases, little dependency on the parameter or control being monitored was observed; hence, only the most pertinent observations are discussed below. This exercise was conducted mainly in order to gain familiarity with the operation of the chosen software and to recognize the most critical parameters controlling this particular model. In total, this effort was carried out by performing a large number of simulations, several hundred, which, including final interpretation on the simulation discussed below, took place over approximately 1.5 years. Each simulation discussed in this chapter takes approximately four to five hours of run-time.

7.2. Model setup

The simulation avalanche model design was based on typical volcanic edifice collapse scenarios as observed by post-collapse scar geometry (Figure 46; Siebert, 1984; Glicken, 1998; Voight, 2000). The use of this pre-defined failure surface is favoured for several reasons: (1) this study is concerned only with the processes that occur *after* flank failure and failure mechanisms are not considered; (2) little is known about the location of major discontinuities within volcanic edifices (Reid *et al.*, 2000); and (3) using additional particles to create a complete cone significantly increases computing time and prohibitively increases run-time. Furthermore, this study has been based on those of Campbell *et al.* (1995) and Crosta *et al.* (2001), which both use a pre-defined failure scenario to analyze the deformation of the failure mass specifically. Morgan and McGovern (2003) use a similar approach in their DEM simulations of Martian flank collapses. The edifice depicted in Figure 46 has a maximum height of 1,000 m and a slope

angle of 30°, a flank angle typical of large stratovolcanoes (Schuster and Crandell, 1984). The failure space is created by defining a wall element surface which rises at an initial angle of 7° to the horizontal following the models of Voight and Elsworth (1997) and Voight (2000). The steep angle of the back headwall is representative of that observed in natural scenarios (50-80°) (Siebert, 1984). The resultant failure would be representative of the geometry of the first slide block of the retrogressive failure at Mount St. Helens as discussed in Section 4.2.1. The runout surface is horizontal.

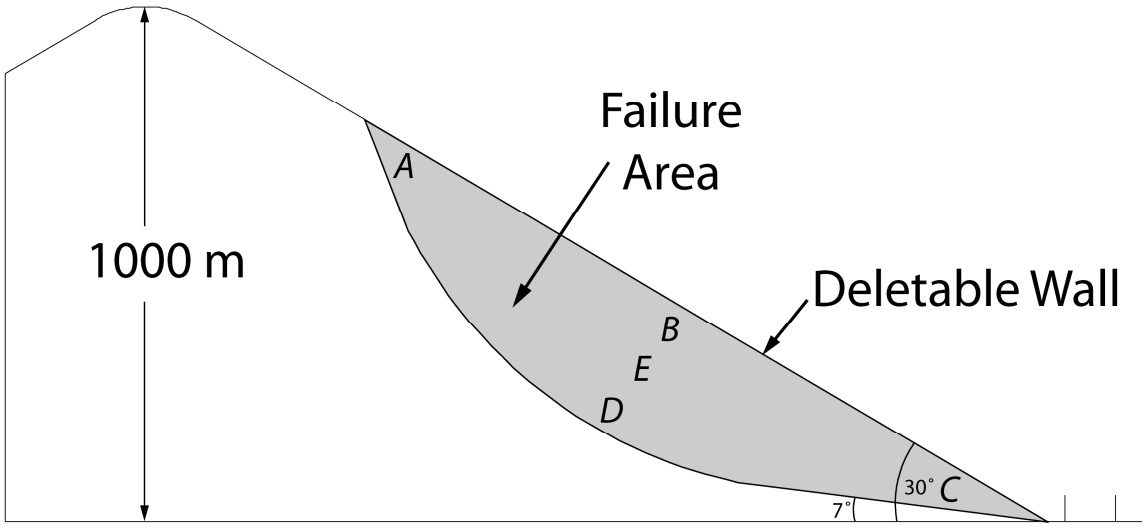

Figure 46 – Pre-failure simulation edifice. Letters A-E depict the locations of particles included in the mechanical analysis as described in Section 7.3. The grey area represents the particulate mass.

Particles are filled into the failure space and subjected to gravity until they reach equilibrium though they remain restrained by the deletable wall shown in Figure 46. Though a certain degree of stress builds up in the toe of the failure due to this procedure, it does not significantly affect the emplacement process as long as the particles remain unbonded. The final pre-failure model consists of 16,578 particles with a uniform size distribution ranging in size from 3.2 to 5.3 m in diameter (particle size ratio of 1.66 per Itasca [2004a]). No specific assumptions are made as to the initial material properties of the particles in the model and consequently assumptions are avoided with respect to the nature of the rock mass involved. The pre-failure avalanche mass is simply a particulate assembly at a certain initial geometry where each particle is in contact with its immediate neighbours and/or the failure surface. Gravity is the only force to which the assembly is subject. As a result size-scaling procedures are not necessary. The size range and distribution for the particles used in the model represent a balance between model resolution and practical simulation processing time since it is virtually impossible to

accurately represent the particle number and size distribution likely to be present in reality. Avalanche behaviour at particles size ranges other than that specified was not investigated. As introduced in Section 6.4, particles inevitably roll during emplacement due to their circular shape and frictional coupling effects, both in relation to each other and the runout surface. As a result, a small number of particles separate from the distal extent of the avalanche mass after deposition of the main avalanche body, particularly at higher values of particle and basal wall friction. These few particles were not included in any displacement, velocity or energy evaluations; runout distances are measured from the original location of the slope toe to the distal extent of the main avalanche body. Particle rolling was not restricted here for two reasons: (1) consistency with previous studies which have used DEM (Campbell, 1990; Crosta *et al*., 2001) or laboratory methods (Drake, 1990) to investigate avalanche emplacement where particle rotation was not controlled, and; (2) block rolling, to some degree, occurs in real world rock and debris avalanches and it is therefore unsuitable to fully ignore this motion and consider emplacement exclusively as particle sliding. Several earlier studies have investigated slope mechanics using restricted particle rotation (Morgan and McGovern, 2003, 2005a, 2005b; Tomassi *et al*., 2003; Morgan, 2006). In most of these studies, however, the static gravitational deformation of large-scale slope flanks was being examined rather than dynamic downslope avalanche motion. In the case of Tomassi *et al.* (2003), downslope motion was considered though only through frictional sliding. As it seems inappropriate to completely inhibit particle rotation, a more realistic model for avalanche behaviour may entail a closer investigation of the effects of rolling and the dependency of this motion on material frictional properties. With the above limitations in mind, simulation results presented here should only be regarded as first-order approximations of natural events.

A sensitivity analysis was conducted to observe the effects of various initial basal wall (μ_w) and particle (μ_p) friction coefficients on the characteristics of the final avalanche deposit, namely: runout, displacement of the proximal section, maximum thickness and the horizontal location of the section of maximum thickness. Similar back-analysis, or retrodictive, approaches have been used in previous numerical avalanche simulations (e.g., Le Friant *et al.*, 2006). Consequently, the results presented below are based on findings from simulations conducted at a single combination of μ_w (0.1, $\varphi = tan^{-1}\mu = 6°$) and μ_p (0.75, $\varphi = 37°$) except where specified otherwise. These values are chosen as they represent median values of those tested and produce a deposit with similar empirical relationships to those observed for large-scale volcanic debris avalanches ($H/L \approx 0.12$, Ui [1983]). Contradictory to the observation of Crosta *et al.* (2001), this analysis showed that μ_p had

little effect on the final characteristics of the deposit, while the influence of μ_w was significant in affecting avalanche runout (in line with Crosta *et al.* [2001]) (Figure 47). To observe the influence of uninhibited particle rolling, a simulation was conducted at this combination of material friction values where particle rotation was completely restricted. The resultant particulate deposit was significantly different to that produced when rolling was not restricted as runout decreased, resulting in a thicker, shorter deposit ($H/L = 0.19$). However, as the deposit could not settle into a compact arrangement due to frictional coupling between adjacent particles, an unrealistic packing arrangement was observed. It is therefore confirmed that complete particle rolling restriction may be inappropriate and an approach whereby rolling is dependent on particle friction or material stiffness may be the best approach for future studies.

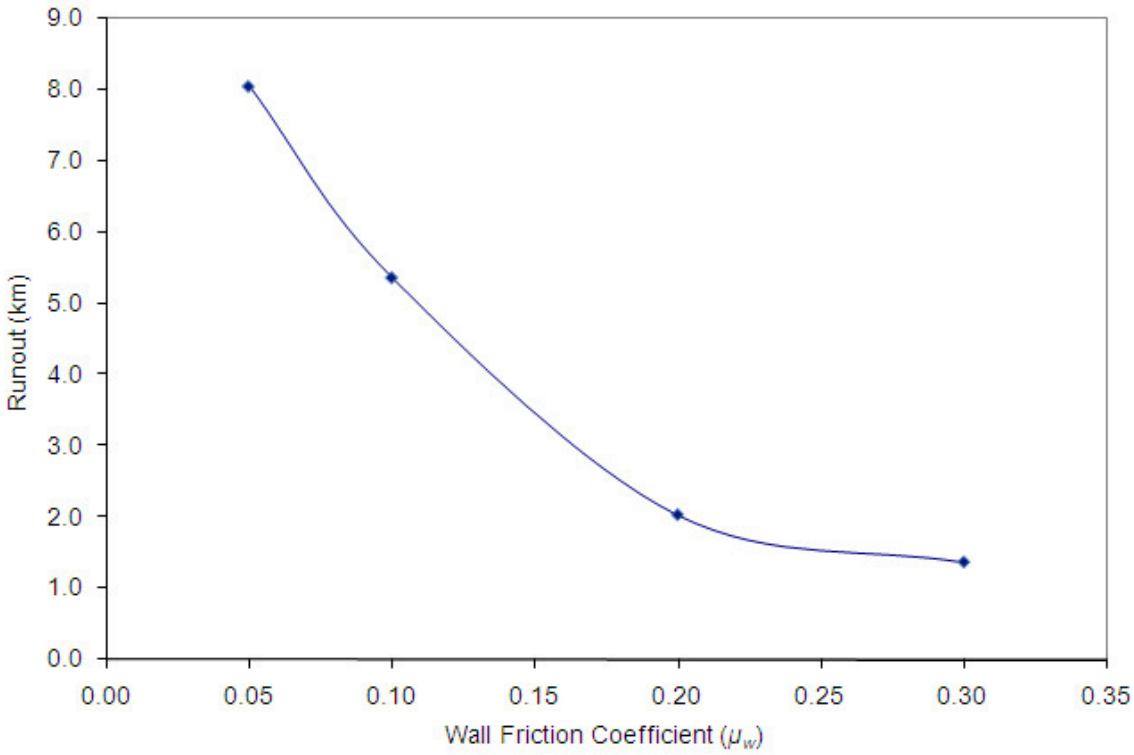

Figure 47 – The observed change in mean avalanche runout distance with increasing wall friction coefficient, μ_w. Each data point represents the mean runout distance for a range of μ_p values 0.25-3.0 measured at each value of μ_w. Runout distance is measured from the pre-failure slope toe to the distal section of the main failure mass.

The model properties are presented in Table 10 and were retained throughout all simulations. Particle normal/shear stiffness influences the computational timestep used and has a negligible effect on avalanche behaviour, therefore common values used by Itasca (2004) were employed. Wall normal/shear stiffness values were set equal to particle stiffness values for model stability. Particle density represents a common value for

competent rock material. As detailed in Section 6.3.2, a viscous damping technique was used within *PFC*^{2D} to ensure that the model reaches equilibrium within a reasonable time period and is most appropriate for dynamic conditions in that numerical energy damping is enforced only at the instant of particle-particle contact and free-motion is not damped (Itasca, 2004). The chosen value corresponds to a restitution coefficient appropriate for that of competent rock material, approximately 0.7, and was obtained through simulation drop tests (Figure 48; Azzoni and de Freitas, 1995; Itasca, 2004). Local damping, which applies a damping force to each ball proportional to the unbalanced force of the assembly, was not employed. Energy is also dissipated through friction when particles develop long-lasting contacts with each other or the basal runout surface using a linear contact model (Itasca, 2004).

Table 10 – Particle and wall properties used for all avalanche simulations.

Parameter	Value
Particle Normal/Shear Stiffness (N/m)	1e8
Wall Normal/Shear Stiffness (N/m)	1e8
Particle Density (kg/m^3)	2000
Viscous Damping Coefficient	1.0

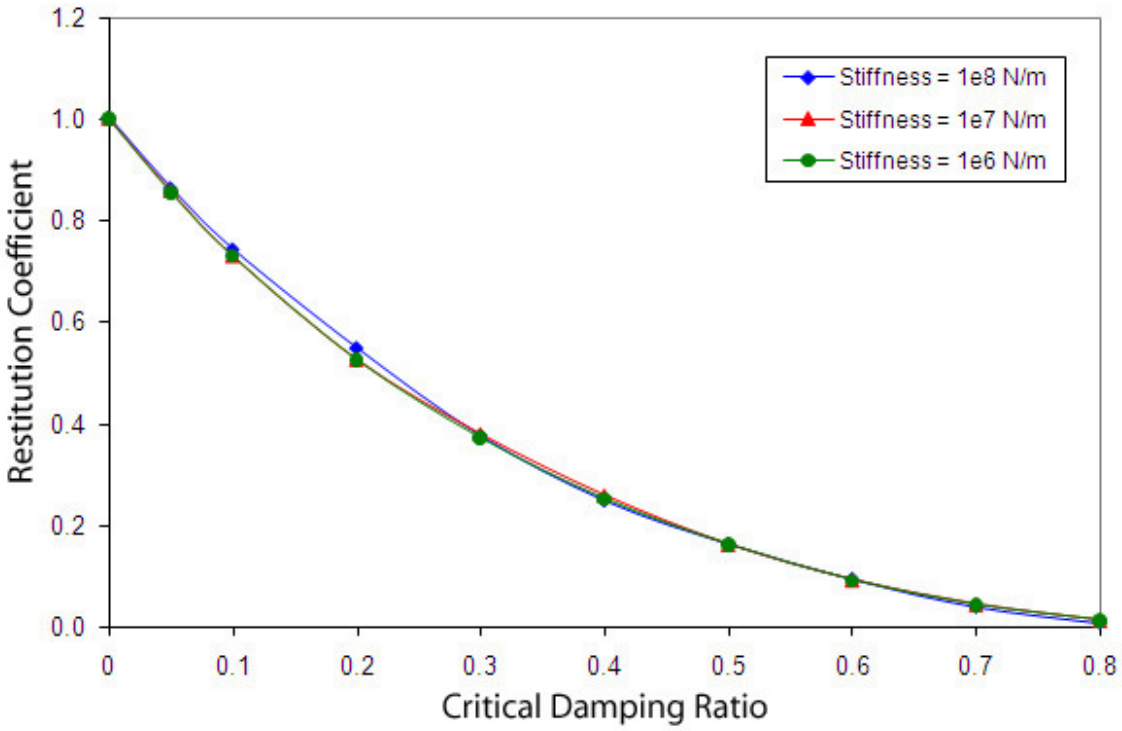

Figure 48 – Relationship between the critical damping ratio, which defines viscous damping in *PFC*^{2D}, and the restitution coefficient, as established in simulation drop tests per Itasca (2004a). A particle of 1 m diameter and 2000 kg/m^3 density was dropped from an 8 m height at critical damping ratios. The restitution coefficient is defined as the ratio of contact velocity before and after impact and calculated from the maximum rebound height of the particle (Itasca, 2004a). Particle and wall stiffness is seen to have little effect on the results.

After the pre-failure slope has been sufficiently filled with particles and cycled to equilibrium under gravity to ensure a steady-state condition where each particle is in contact with its neighbours and the assembly will not settle further, the flank wall is deleted to induce failure. The avalanche begins to travel as the model is cycled and is monitored until movement ceases at deposition (see Figure 54 for general deposit morphology).

7.3. Mechanical analysis

In order to observe the geomechanical behaviour of the travelling avalanche, a suite of variables was monitored throughout emplacement (Table 11), similar to the approach of Crosta *et al.* (2001). Each of these variables was monitored for a single particle located at five locations within the failure mass (A-E in Figure 46). These locations represent the head, toe, and top, middle, and bottom of the medial section of the avalanche and were chosen as their range of responses represents the full variation of avalanche behaviour in

terms of confinement, overburden, and influence of the ground and free surfaces. Only one particle from each section was used as a proxy for the whole section. To support this approach, identical mechanical variables were measured from several additional particles in each section. For instance, Figure 49 shows the x-velocity and xx-stress component variables previously described but measured from two other particles in close proximity to particles A, B, C, D, and E. Plots for the other variables mentioned in Table 11 show similar results. Though some variation is observed, results are generally consistent and therefore it is reasonable to assume that the effects experienced by one particle in a certain section of the avalanche can be used as a good approximation for the general behaviour of that section. The highest variability is seen in the stresses experienced by each particle as these values are originally highly erratic. Relative stress differences are generally preserved, however.

Table 11 – Variables monitored for mechanical analysis of the travelling avalanche.

Variable	Description
Stress (xx- component)	Time-dependent stress in xx-direction (MPa)
Stress (xy-component)	Time-dependent stress in xy-direction (MPa)
Stress (yy- component)	Time-dependent stress in yy-direction (MPa)
x-displacement	Total horizontal distance travelled by particle (m)
x-velocity	Time-dependent x-velocity (dimensionless)
y-displacement	Total vertical distance travelled by particle (m)
y-velocity	Time-dependent y-velocity (dimensionless)

A

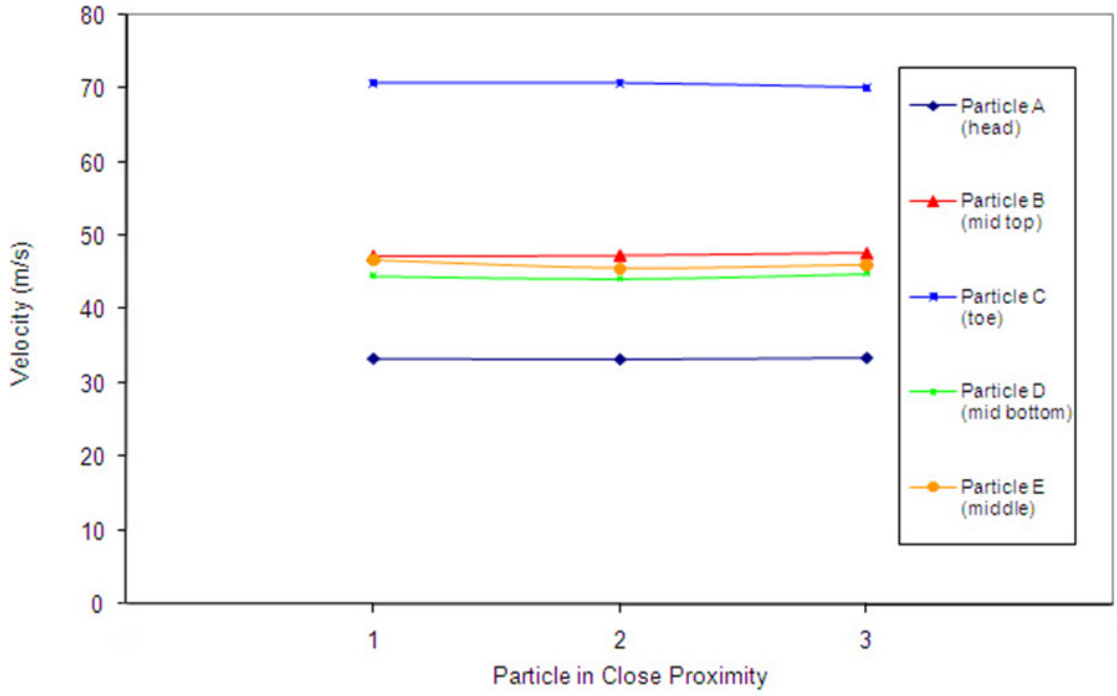

B

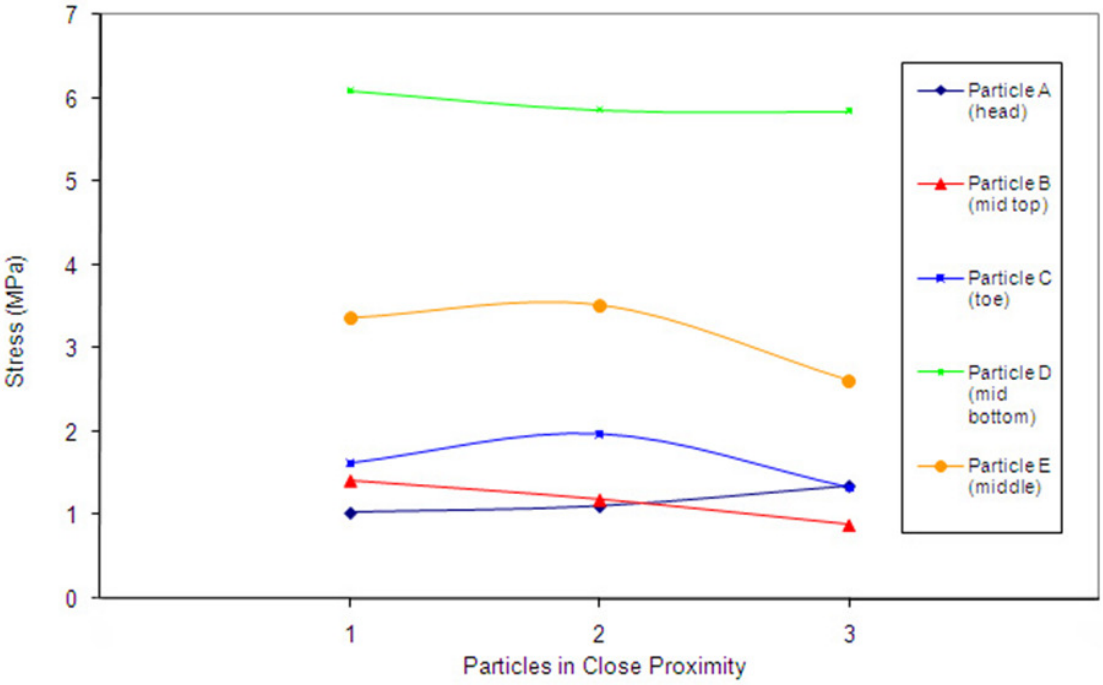

Figure 49 – Results of variables measured for particles in close proximity to five monitored particles. (A) Maximum x-velocity; (B) Maximum xx-component of stress.

It is difficult to recognize any clear trends in the plots of stress versus emplacement time; stresses in each sense (xx, xy, yy) are fluctuating and highly variable, as was observed by Campbell *et al.* (1995) (Figure 50). Stresses are measured for the particle only and not the

surrounding force chains, which carry the majority of the stresses present. Consequently the exact stress values are generally unimportant though the relative values remain significant. Stresses typically reach their highest absolute values and experience the highest fluctuations in the early stages of avalanche emplacement. Stress values and fluctuations typically decrease as the avalanche organizes itself into a steady flow across the horizontal runout surface. Particles located in the lower (D) and interior (E) of the avalanche experience greater stress fluctuations than do those particles locate on the free surface (A-C, Figure 51). In this case, stresses at the bottom and interior of the avalanche are 80-85% and 70-80% higher, respectively, than those at the free surface. A rock mass subject to such stress fluctuations will be more readily fractured and therefore both the early emplacement stages (time-dependent) and lower sections (location-dependent) of the avalanche represent situations where fracture and disaggregation are most likely to occur.

A

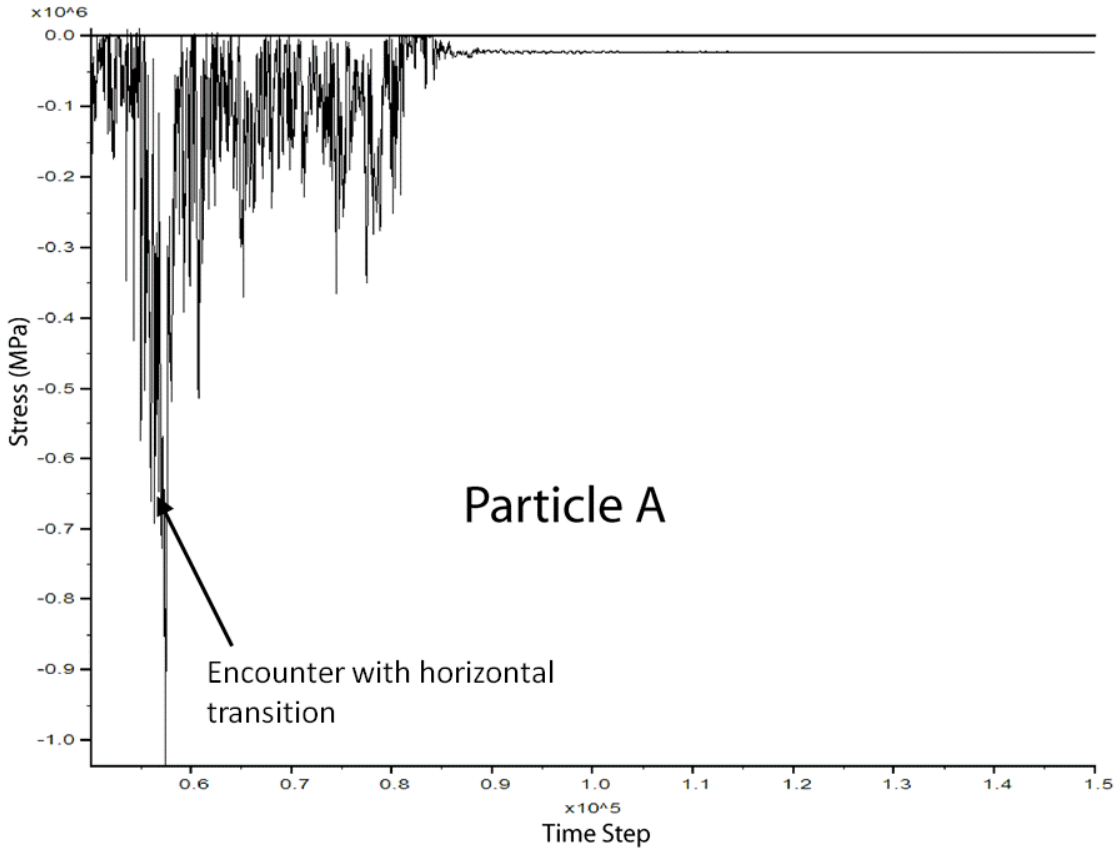

(Figure 50 continued on following page)

B

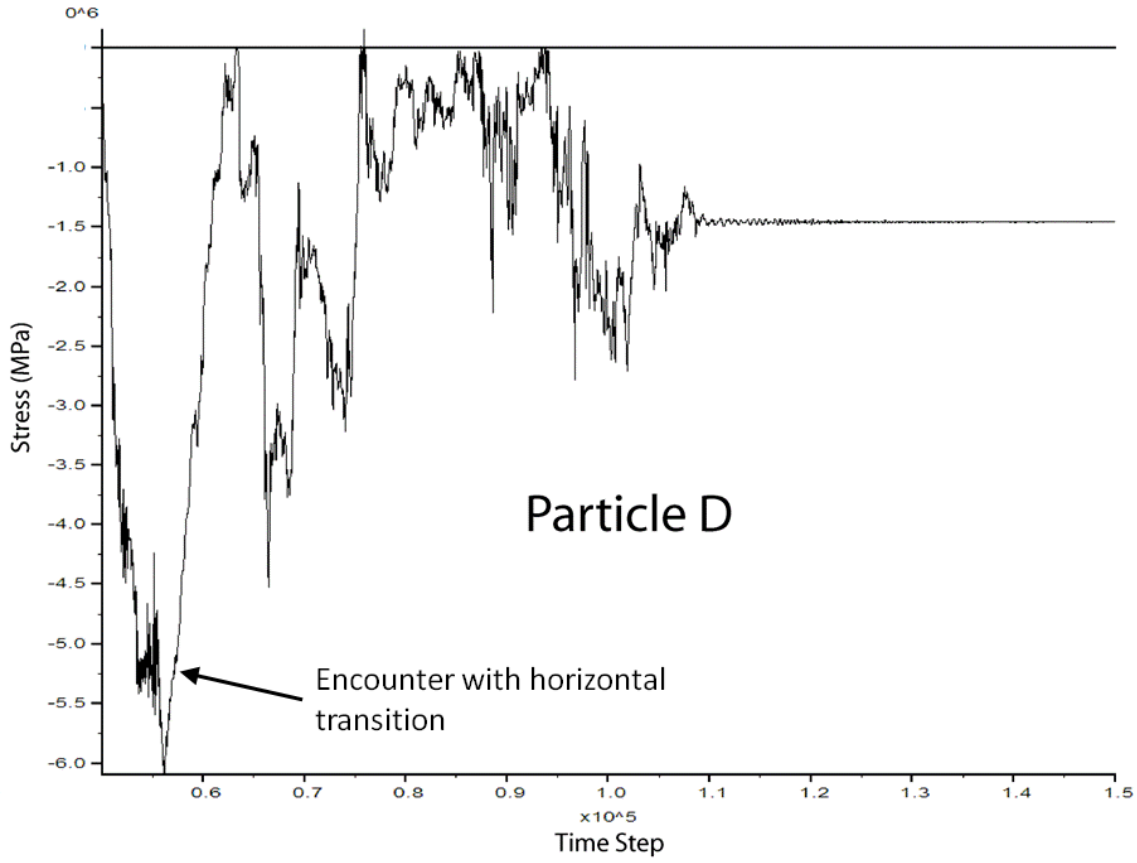

Figure 50 – Stress (xx-component) with time during emplacement for particles A (figure A) and D (figure B). Stresses for each particle monitored and in each sense (xx, xy, yy) behave in a similar fashion. Plot generated by *PFC*^{2D}.

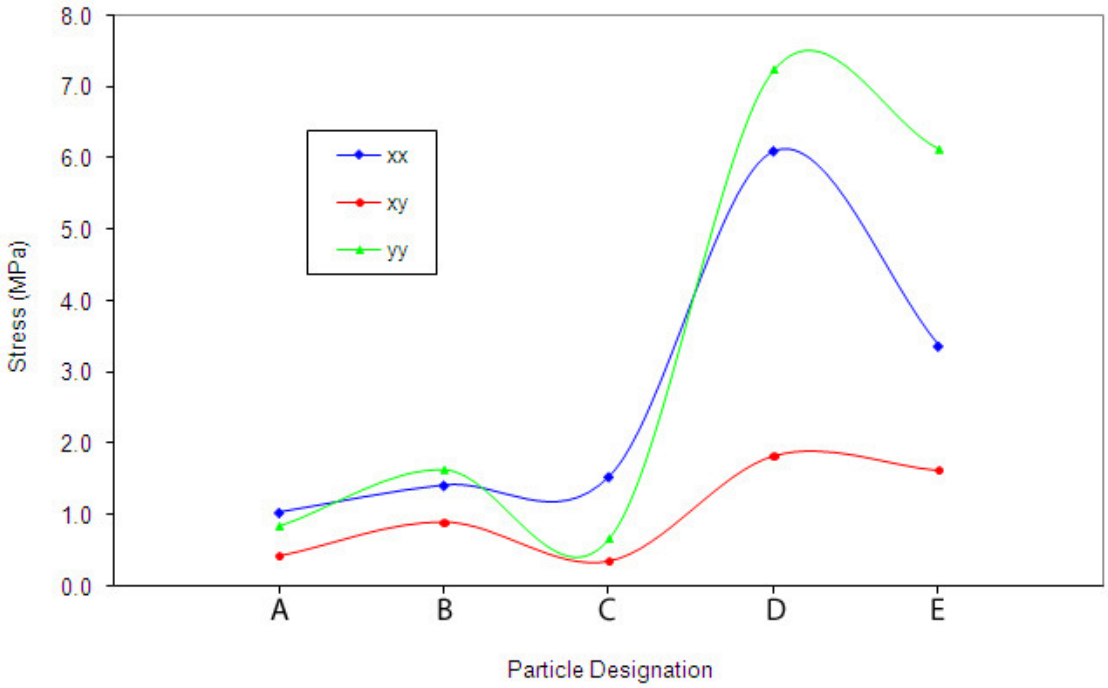

Figure 51 – Relative maximum stresses experienced by particles located in various parts of the avalanche during emplacement.

The horizontal displacement of the monitored particles shows an initially rapid increase which subsequently slows to a steady rate before declining rapidly immediately before movement ceases (Figure 52A). The increased initial rate of displacement reflects the chaotic moments just after failure where the avalanche begins to travel down-slope. Intuitively, the unrestrained particle at the toe of the failure (C) travels the greatest distance, the particle at the head of the failure the least distance (A) and those located in the medial section (B, D, E) travel comparable distances (Figure 52B). A similar observation was made by Campbell *et al.* (1995). Associated horizontal particle velocities (Figure 53A) initially increase steeply to a maximum then decline at a quickening rate. This observation reflects the increase in particle velocity as it moves down-slope before encountering the horizontal transition whereby it loses much of its kinetic energy and decreases in velocity until deposition. Similar plots are shown by Campbell *et al.* (1995), Crosta *et al.* (2001) and Staron (2008). A plot of relative maximum horizontal particle velocities shows a similar relationship to that of horizontal particle displacement; the toe of the failure travels the fastest, the head the slowest, and the medial section at a generally steady rate (Figure 53B). This observation represents the general extension and spreading of the avalanche body.

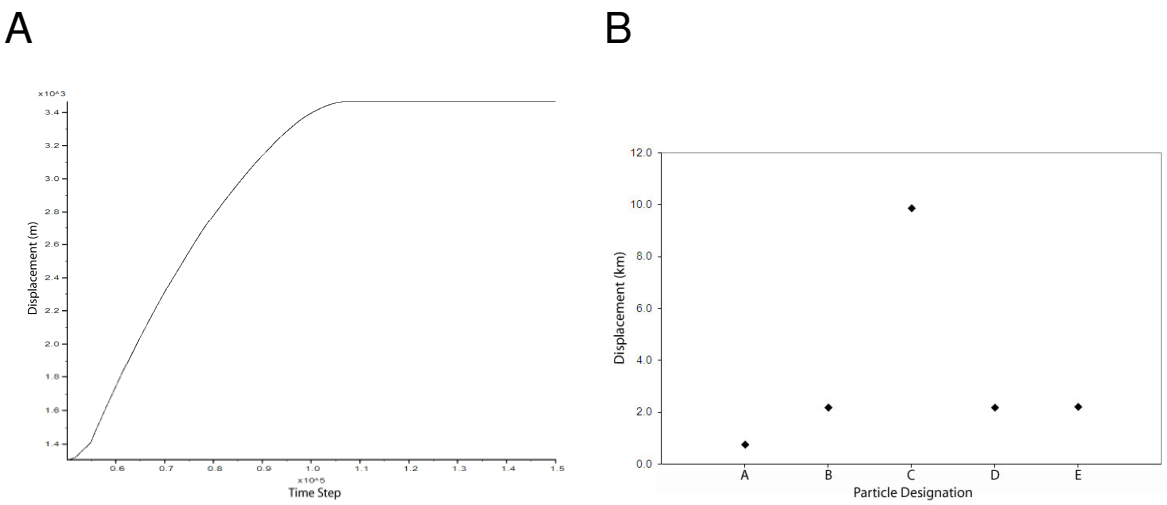

Figure 52 – (A) Horizontal displacement for particle D during emplacement. Each of the other monitored particles in the assembly behaved in a similar manner. Plot generated by *PFC*^{2D}; (B) Relative horizontal displacement for each of the monitored particles.

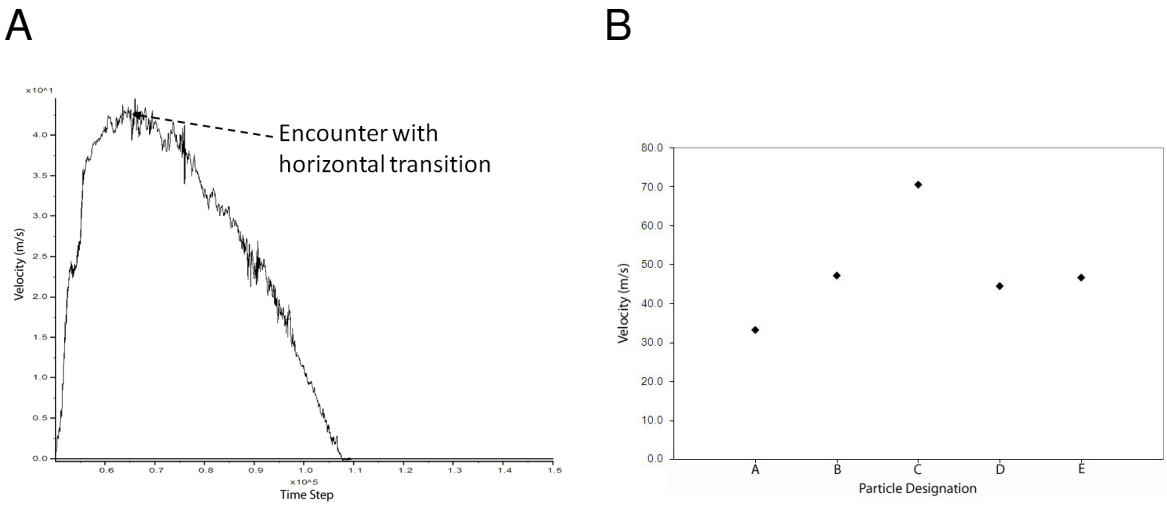

Figure 53 – (A) Horizontal velocity for particle D during emplacement. Each of the other monitored particles in the assembly behaved in a similar manner. The slight negative velocity observed on the plot of horizontal velocity indicates the particle momentarily moved backwards (towards the source).
Plot generated by *PFC*^{2D}; (B) Relative maximum horizontal velocity for each of the monitored particles.

Vertical particle displacements are merely a function of the original starting position of the particle within the failure; those starting from higher in the edifice travel further. The maximum vertical velocities obtained by these particles are also a function of particle starting position as those particles that travel furthest (i.e., those highest in the failure) are able to attain higher velocities.

7.4. Spatial property analysis

Additional observations of the travelling avalanche body were made with *PFC*^{2D}'s *measure* tool, which evaluates the change in a range of variables within user defined circles over a given period of time. Five locations were chosen to observe vertical and horizontal property changes within the avalanche (Figure 54). The positions of each circle remained constant as the avalanche passes through during failure simulation. The variables measured are presented in Table 12 and the results of this exercise are given in Figure 55.

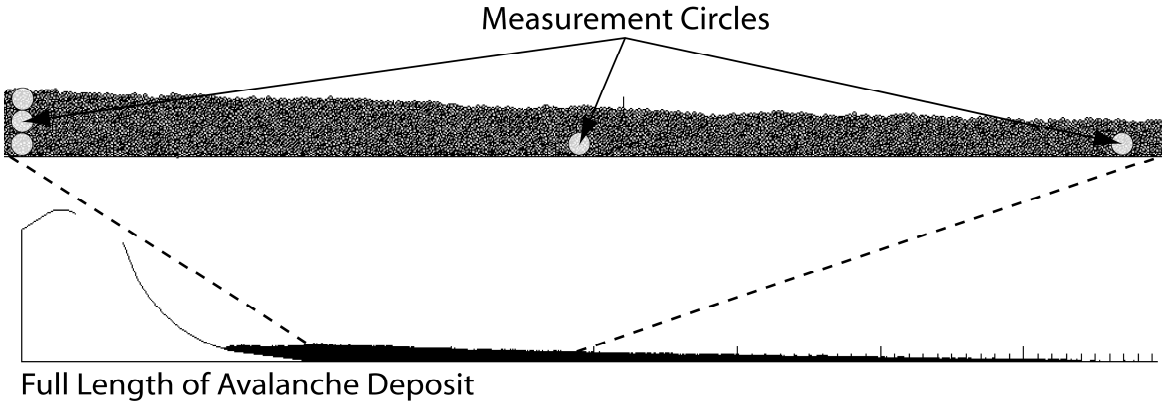

Figure 54 – Location of measurement circles (35 m diameter) used in the spatial property analysis.

Table 12 – Variables considered with *PFC*^{2D}'s measure command.

Variable	Description
Maximum stress	Maximum stresses averaged over the measurement circle (MPa)
Maximum strain rate	Strain rate tensors determined through lease squares method (Itasca, 2004a)
Porosity	Ratio of total void area within measurement circle to measurement circle area
Coordination number	Mean number of contacts per particle, averages over the measurement circle
Sliding fraction	Percentage of contacts which are slipping within the measurement circle

Figures 55A and 55B show that maximum stresses within the avalanche decrease with increasing vertical (y) height and horizontal (x) distance. Unlike the particle stresses discussed in the previous section, the stresses measured using the circle technique average all stresses within the circle, both particle and force chain. Therefore, this technique

provides a much better estimate of continuum average stress where values are significant. Maximum vertical stresses in this instance are 36.7% higher in the lower third of the failure than the upper third, while maximum horizontal stress is 28.3% higher. Vertical stress decreases by 66.8% from the proximal to distal portion of the avalanche, a function of a decrease in overburden, while horizontal stress decreases by 58.4%.

Strain rate results are a measure of the instantaneous velocity field and therefore what is measured is the maximum strain rate occurring in each respective section of the avalanche throughout emplacement on the horizontal section of the runout surface. It is not a cumulative measure of left-over strain. Results indicate strain is highest in the interior of the deposit and decrease toward both the free and ground surfaces (Figure 55C). Strain rate decreases linearly with horizontal distance (Figure 55D). These results may suggest that rock block and stratigraphic deformation is more likely in the interior, proximal section of the particular avalanche.

Both porosity (Figures 55E and 55F) and coordination number (Figures 55G and 55H) indicate a tighter packing at the lower, proximal section of the avalanche; a function of the increased stresses in this area. The mean values of these properties in the pre-failure slope assembly are 0.17 (range 0.14-0.19) and 3.7, respectively. Sliding fraction results (Figures 55I and 55J) reveal increased instability in lower proximal section of the avalanche as an increased number of contacts are slipping in this area, also a function of increasing stress with depth.

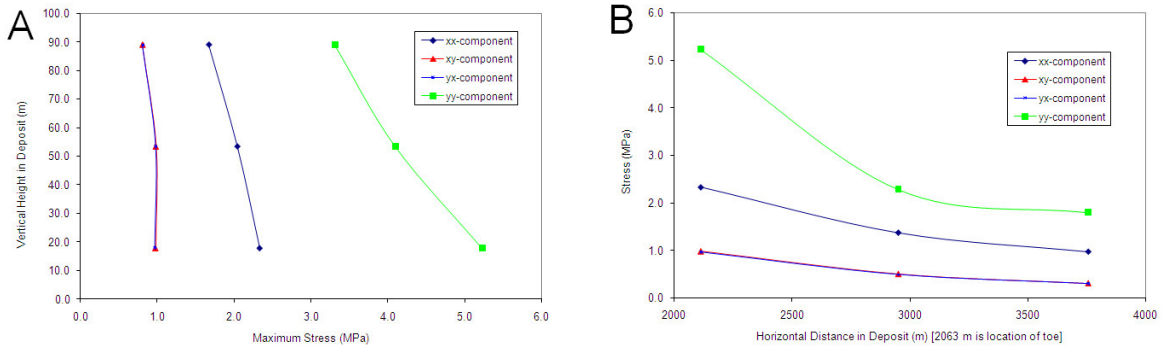

(Figure 55 continued on following page)

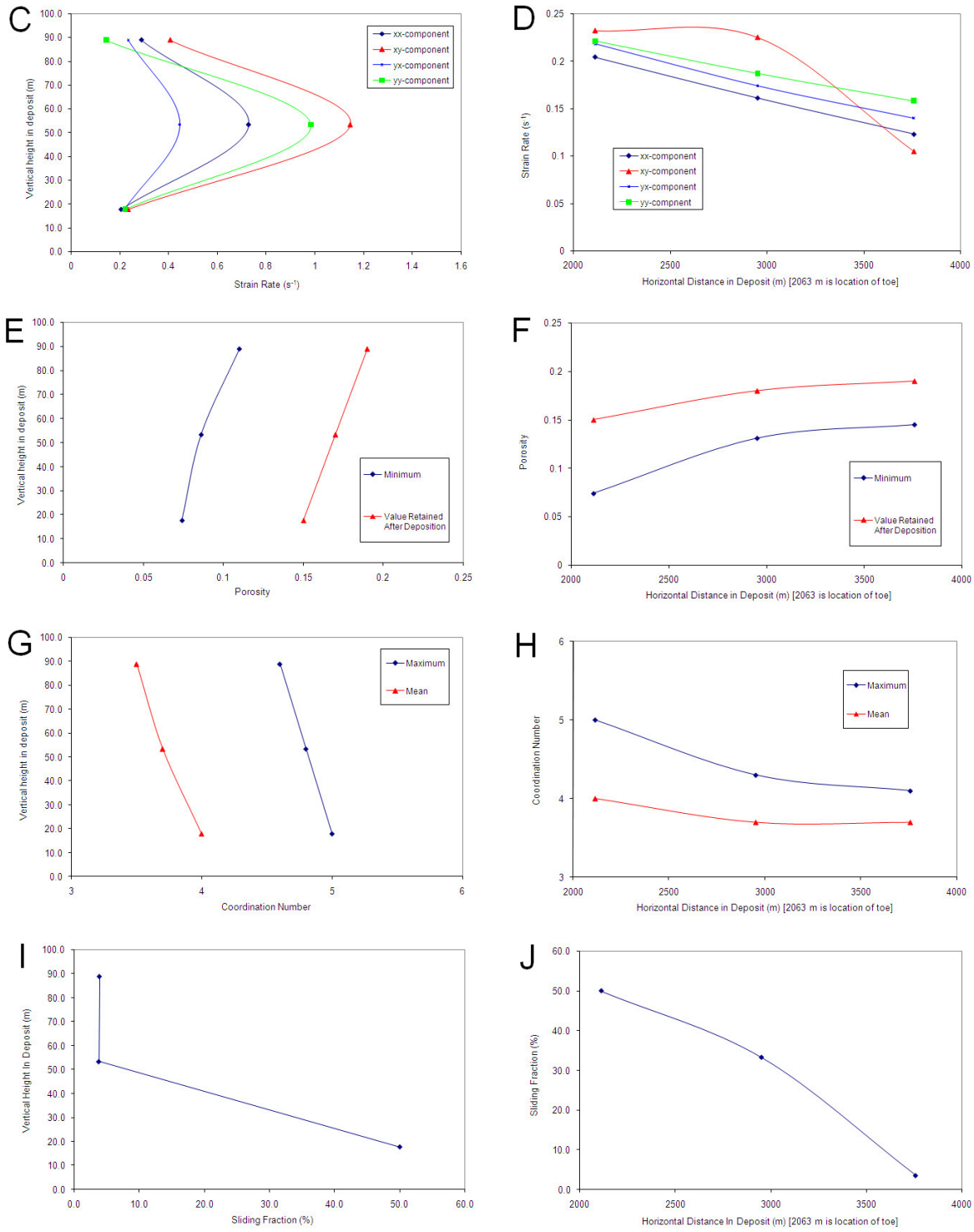

Figure 55 – Graphical results of the spatial property analysis – (A) Maximum stress versus vertical position; (B) Maximum stress versus horizontal position; (C) Maximum strain rate versus vertical position; (D) Maximum strain rate versus horizontal position; (E) Porosity versus vertical position; (F) Porosity versus horizontal position; (G) Coordination number versus vertical position; (H) Coordination number versus horizontal position; (I) Maximum sliding fraction versus vertical position; (J) Maximum sliding fraction versus horizontal position.

7.5. Energy analysis

Certain aspects of the avalanches' energy regime can be evaluated by PFC^{2D} (Table 13). The energy variables evaluated here constitute the basic forms of energy readily measured in PFC^{2D}; other important forms of energy potentially generated by VDAs, such as heat and seismic/acoustic energy are not as easily monitored and were therefore neglected here. These topics do, however, provide and interesting topic for future research. As opposed to the previous exercises, observations were recorded while varying both wall and particle friction (μ_w and μ_p). Figure 56A shows a rapid increase and gradual decrease in gravitational work indicating that at a given point gravity begins to contribute little energy to the simulation system; that is momentum has increased, switching from potential to kinetic energy. The decrease in the influence of gravity observed with increasing μ_p (Figure 56B) and μ_w (Figure 56C) suggests that gravity does not complete a full break-down of the avalanche body as particles are held together by increased frictional strength. Energy dissipated by friction rises steeply to a maximum and gradually decreases with time (Figure 56D), showing the amount of energy dissipated decreases as it is continually being expended. As the initial amount of energy in the system is always the same, the fact that the amount of energy dissipated decreases with increasing μ_p (Figure 56E) and μ_w (Figure 56F) suggests there is further energy left in the avalanche system (as potential energy) that has not been expended through emplacement. The curve in Figure 56D assumes the same general shape with increasing μ_w though the rate at which the energy dissipated through friction rises (i.e., curve steepens). This fact suggests energy is dissipated at a more rapid rate with increasing μ_w. At $\mu_w = 0.1$ the mean energy dissipated is higher than that at $\mu_w = 0.05$, intuitively (Figure 56E). However, at $\mu_w = 0.2$-0.3 the amount of energy dissipated through friction decreases, most likely signifying the onset of particle rolling as a significant process.

Table 13 – Assemblage energy variables monitored. Energy tracing begins at the instance of failure and ends at motion cessation.

Energy variable	Description
Body	Total accumulated work done by all body forces on the assembly; gravity is the only body force in this experiment
Frictional	Total energy dissipated by frictional sliding at all contacts in the assembly
Kinetic	Total kinetic energy of all particles in the assembly (translational and rotational motion)
Strain	Total strain energy of the entire assembly stored at all contacts

Figure 56G shows the change in the kinetic energy with time during emplacement. Kinetic energy increases rapidly to a sharp maximum, representing the movement of the main mass of the avalanche body down the failure slope and meeting the horizontal transition. Kinetic energy decreases gradually thereafter as the avalanche loses momentum and deposits in the runout area. This plot correlates well with that of horizontal particle velocity, itself a reflection of the avalanche's kinetic energy (see Figure 53). The relative proportions of translational and rotational kinetic energy are 72% and 28%, respectively, revealing that particle motion is mostly translational in this case (i.e., these particular values of μ_p and μ_w). The maximum kinetic energy attained by the system decreases with increasing μ_p (Figure 56H) and μ_w (Figure 56I), again suggesting energy is locked up as potential energy (less avalanche 'flow'). This suggestion is substantiated by a decreasing mean horizontal velocity with increasing μ_w (Figure 57). Similar kinetic energy relationships are shown by Crosta *et al.* (2001). The variation in total strain energy stored at all contacts in the assembly during emplacement was also monitored. Strain starts at a maximum and decreases regularly in a sinusoidal manner which decreases in intensity with time (Figure 56J). This observation perhaps suggests a 'pulsing' or 'caterpillar' type of avalanche movement as suggested by previous authors (Voight *et al.*, 1983; Schneider and Fisher, 1998; Crosta *et al.*, 2001). Maximum assembly strain decreases with increasing μ_p, perhaps again indicating increased particle rolling in the system (Figure 56K). Maximum strain increases with increasing μ_w (Figure 56L), however, which may indicate that strain is built up to higher levels within the avalanche body as the particles in contact with ground surface are bound by stronger contacts. This fact suggests that at higher values of material and boundary friction, energy within the moving avalanche is locked in the form of potential energy, an observation supported by the decreases in energy dissipated by friction and observed kinetic energy with increasing μ_p and μ_w described previously.

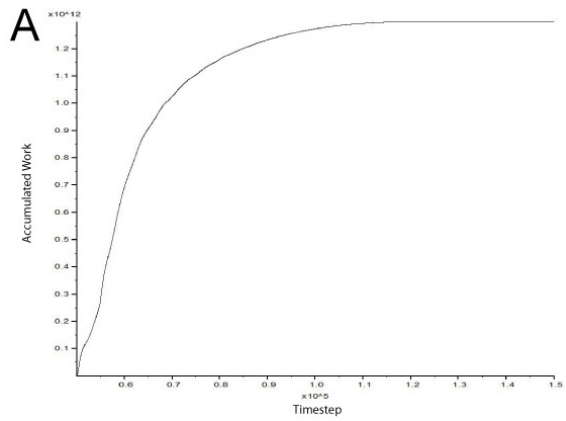

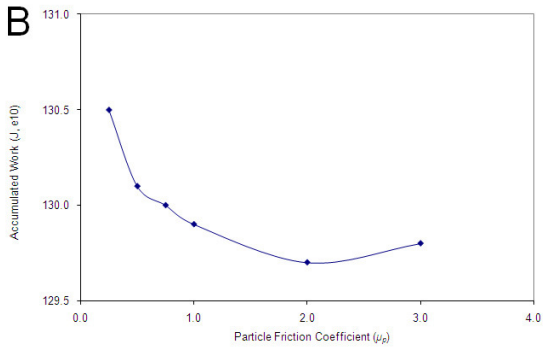

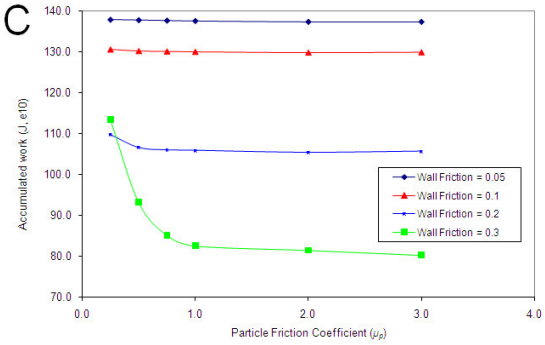

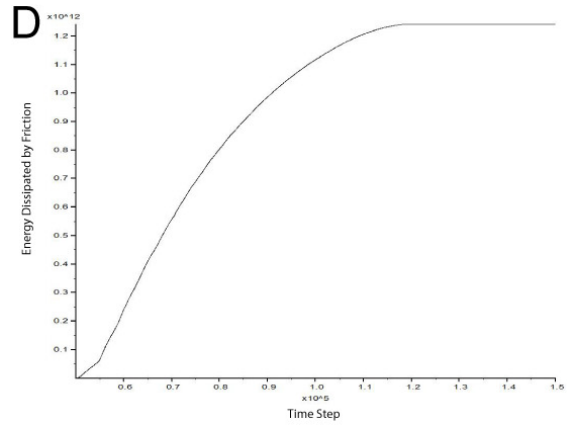

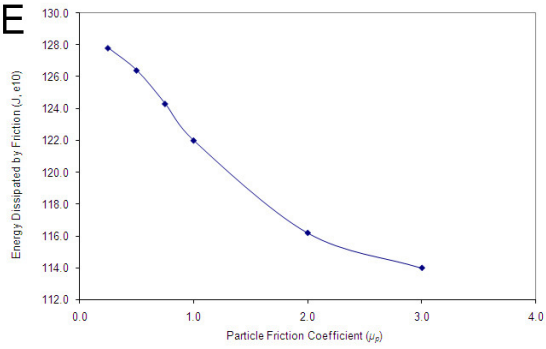

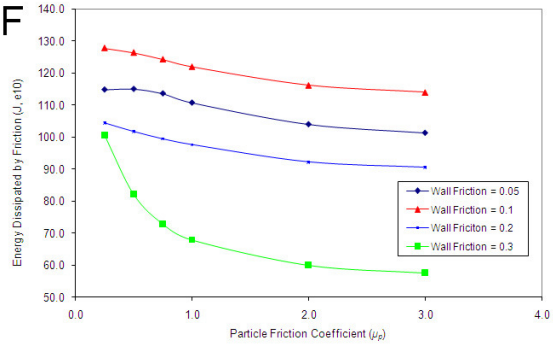

(Figure 56 continued on following page)

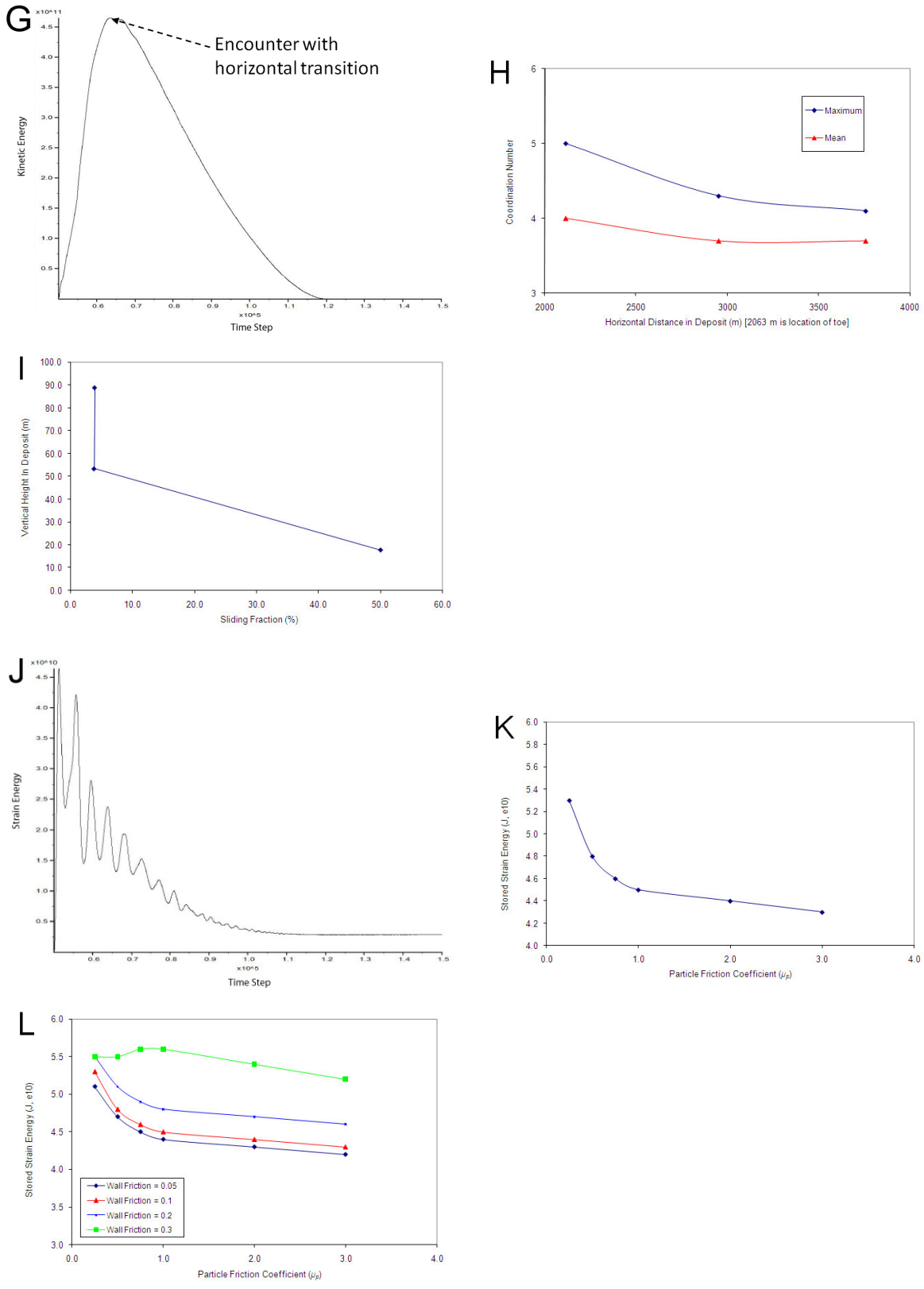

Figure 56 – Change in energy variables during emplacement. (A) Change in body energy, that done by gravity on the particle assembly, with time (Joules, $\mu_w = 0.1$, $\mu_p = 0.75$); (B) Accumulated work done by gravity forces on particle assembly with varying μ_p ($\mu_w = 0.1$); (C) Accumulated work done by gravitational forces on particle assembly for varying μ_p and μ_w; (D) Energy dissipated by frictional sliding at all contacts with time (Joules); (E) energy dissipated by frictional sliding at all contacts in the particulate assembly ($\mu_w =$ 0.1 only); (F) Energy dissipated by frictional sliding at all contacts in the particulate assembly (G); Changes

in total kinetic energy of all particles with time (Joules); (H) Maximum kinetic energy attained of all particles in the avalanche assembly (μ_w = 0.1 only); (I) Maximum kinetic energy attained of all particles in the avalanche assembly; (J) Change in strain energy stored at all contacts in the particulate system (Joules); (K) Maximum strain energy stored at all contacts in the particulate system (μ_w = 0.1 only); (L) Maximum strain energy stored at all contacts in the particulate system. Plots A, D, G and J generated by *PFC*^{2D}.

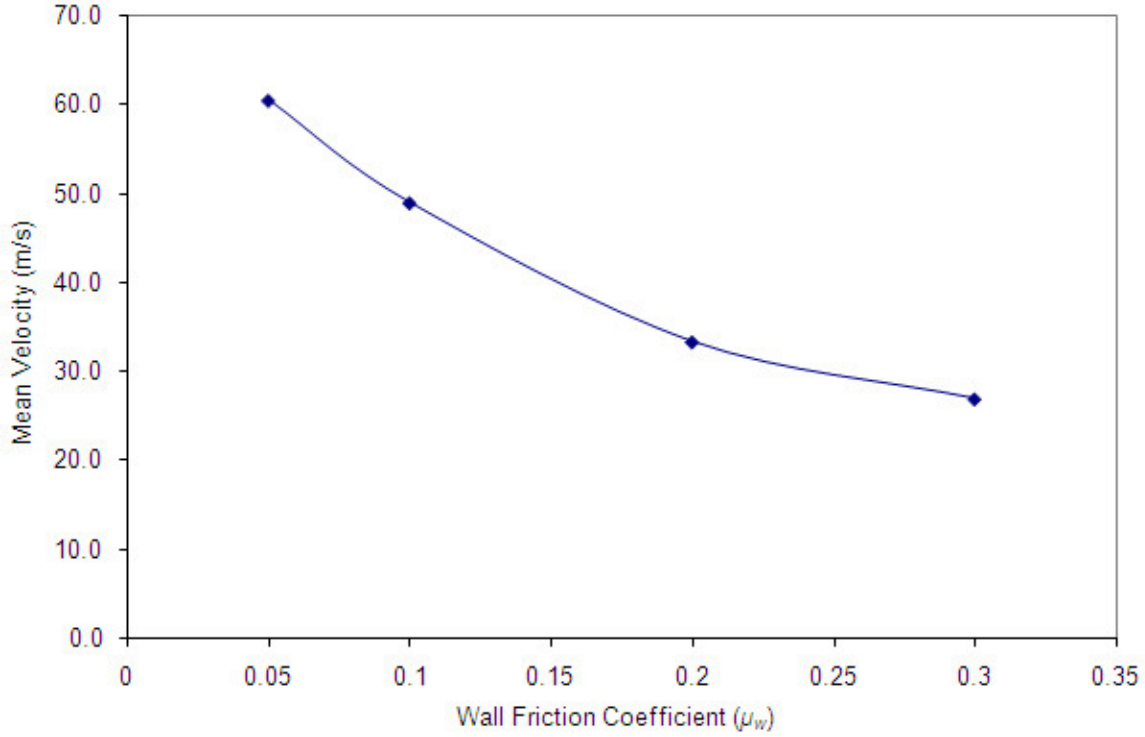

Figure 57 – Mean horizontal particle velocity versus increasing μ_w. Mean values are those for varying values of μ_w.

7.6. Deformation analysis

Further analysis of avalanche emplacement was performed by introducing coloured markers into each of the simulations detailed above following the models of Campbell *et al.* (1995) and Crosta *et al.* (2001). Both vertical stripes and a configuration generally representative of stratigraphic layers were used to obtain a qualitative understanding of avalanche body deformation during emplacement (Figure 58). Simulations were run in which each vertical stripe or stratigraphic layer possessed the same material properties as its neighbours and in which the properties varied between layers. Therefore, in the first case, stratigraphic layers were used only as a means of visualizing qualitative deformation. As performed for the energy analysis, changes in deformation were observed for various values of μ_p and μ_w. Ranges of μ_w values from 0.05-0.3 and μ_p values of 0.25-3.0 were considered.

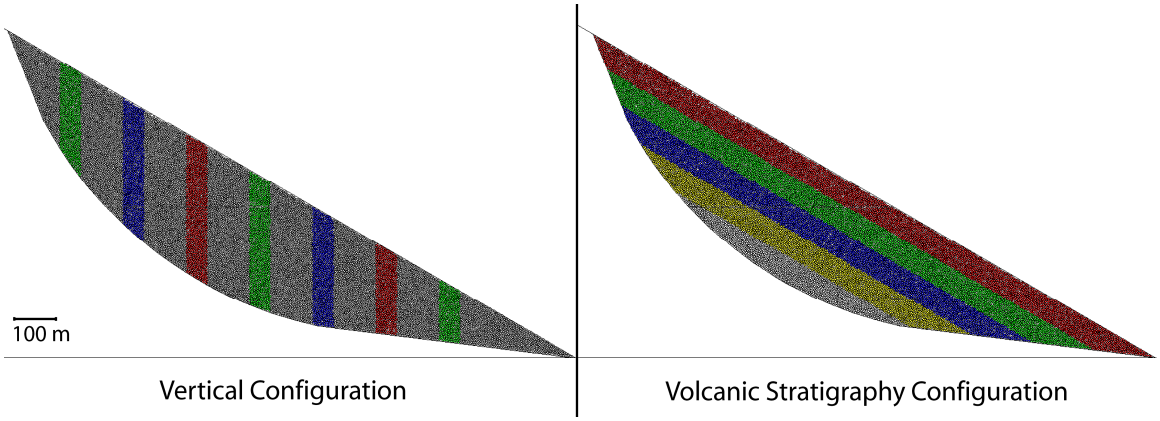

Figure 58 – Marker patterns used for deformation analysis. All layers possess the same material properties, colours added as a means of visualizing deformation only.

7.6.1. Uniform material properties

Deformation of the avalanche body during emplacement was first analyzed by using vertical stripes. At $\mu_w = 0.05$ (low wall friction), the lower region of proximal section of the avalanche moves more rapidly than the upper section down the failure slope (Figure 59). At a point in the medial section of the failure, the upper and lower sections travel together at the same rate. In the distal sections, the upper region of the failure near the free surface overtakes the lower region. This collective motion works to stretch and thin the failure and represents a changing vertical velocity gradient from proximal to distal sections of the avalanche. Increases in μ_p show the same general characteristics though deformation of the individual stripes appears to increase through compression of the medial section of the avalanche body as the failure slows upon reaching the horizontal transition. An up-welling of the medial particles is subsequently observed and retained after movement cessation (Figure 60A). Similar observations are made when μ_w is increased to 0.1, though to a lesser degree as the avalanche is not stretched as thinly. At higher levels of μ_p the compression and up-welling of the medial avalanche section is again observed just distally from the thickest segment of the deposit (Figure 60B). The up-welling feature increases in size with increasing μ_p and remains as μ_w is increased to 0.2, though stretching of the avalanche is less pronounced. Deformation in the proximal section of the slide is reduced at $\mu_w = 0.2$; deformation in the distal section increases, observed as particles in the upper regions cascading off the granular pile (Figure 61). The level at which particles cascade down the free surface rises vertically within the avalanche as μ_p increases. Similar behaviour is observed as μ_w is increased to 0.3 though mean particle displacement and failure deformation are further reduced as the failure mass is increasingly bound to the failure surface through greater frictional coupling. In summary, increases in μ_w decrease

the mean horizontal displacement of the failure mass while increases in μ_p decrease the depth at which particles cascade off the upper surface of the pile.

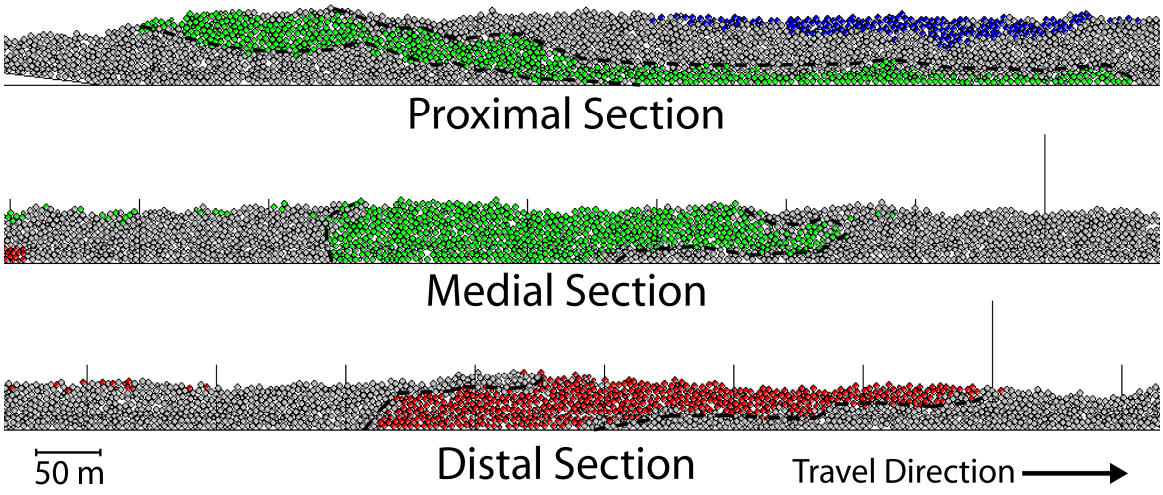

Figure 59 – Avalanche deposit at $\mu_w = 0.05$ showing differing spatial deformation. Stripes initially vertical. Refer to Figure 65 for a view of the full length of a simulation deposit. All layers possess the same material properties, colours added as a means of visualizing deformation only.

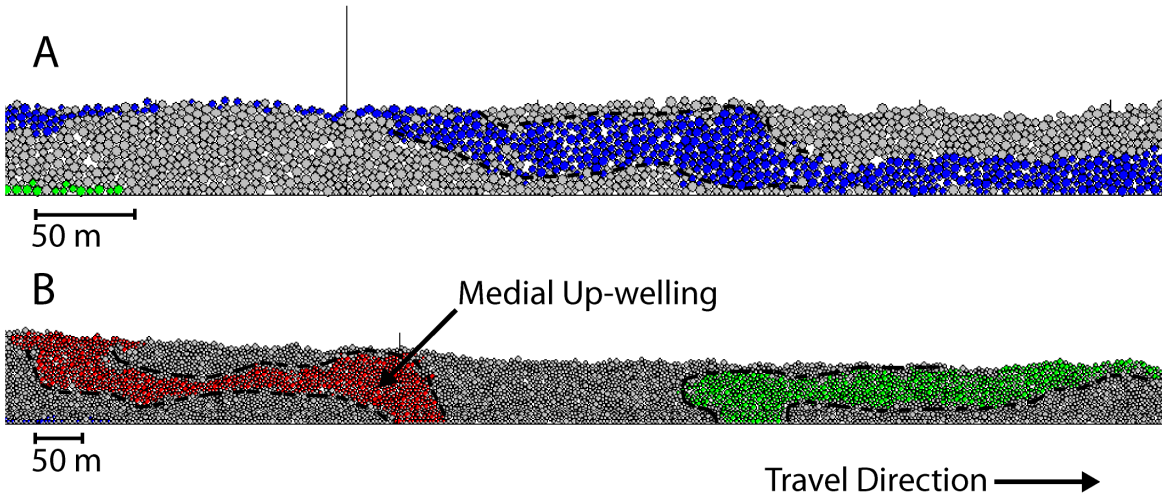

Figure 60 – (A) Compressional up-welling internal deformation structure ($\mu_w = 0.05$); (B) Up-welling of particles in medial section of the deposit. Notice the mode of deformation switching from left- to right-lateral just beyond this structure ($\mu_w = 0.1$). Refer to Figure 65 for a view of the full length of a simulation deposit. All layers possess the same material properties, colours added as a means of visualizing deformation only. Note separate scales.

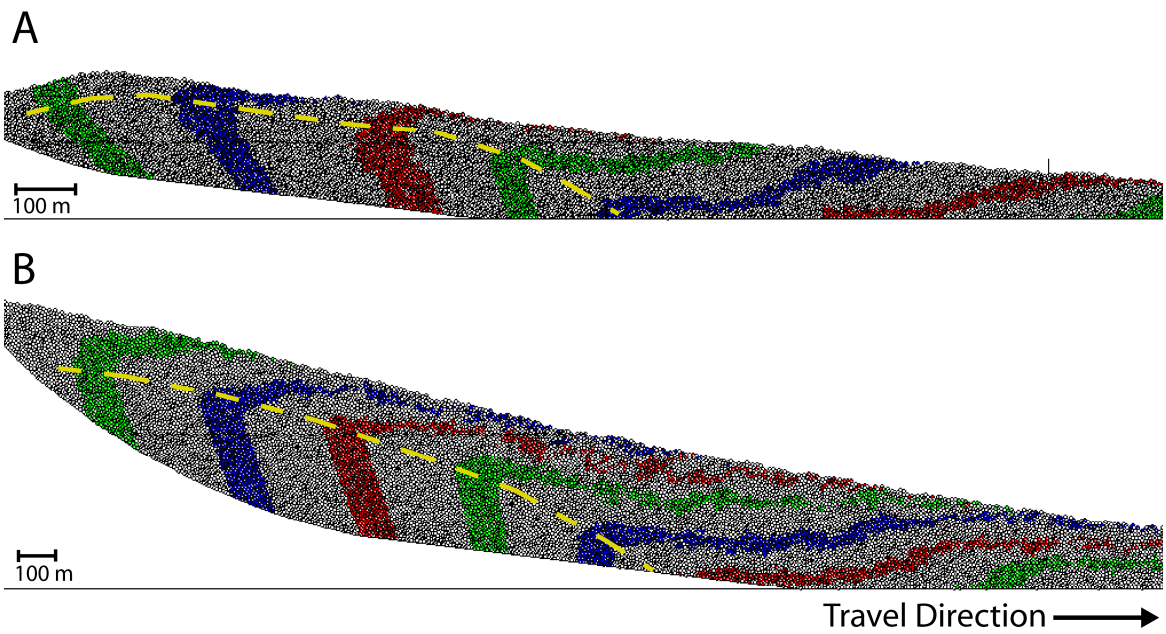

Figure 61 – (A) Avalanche deformation at $\mu_w = 0.2$. Dashed lines indicate denote vertical point where particles cascade distally from the granular pile; (B) Avalanche deformation at $\mu_w = 0.3$. Note separate scales for (A) and (B); $\mu_p = 0.75$ in each case. All layers possess the same material properties, colours added as a means of visualizing deformation only.

Using the geometry representing stratigraphic layers little in the way of deformation at lower values of wall friction ($\mu_w = 0.05$, Figure 62) was observed. Each layer is stretched thinly in the medial section of the deposit and thickens towards the proximal and distal edges but retain their original relative positions. Similar to the observation made by Campbell *et al.* (1995), layers located in the upper section of the original failure generally cover the entire length of the deposit. Little change in layer deformation is observed with increasing μ_p. Similar deformation observations are made as μ_w is increased to 0.1 though layer deformation generally increases. Stratigraphic layers undulate to a higher degree and the medial compressional up-welling feature is at its largest. Again, as μ_w is increased to 0.2, little change in deformation is observed. At the highest value of μ_w (0.3), the stratigraphic layers begin to fold over themselves as the lowest distal particles are bound to the failure surface, a phenomenon that increases with μ_p (Figure 63). Similar layer deformation was observed by Campbell *et al.* (1995).

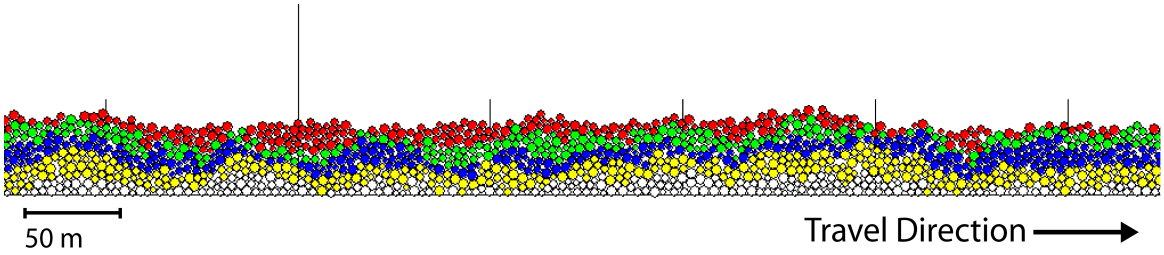

Figure 62 – Volcanic stratigraphic deposit in the distal section of the simulation deposit at $\mu_w = 0.05$. Vertical lines used to assess deposit thickness (tall lines = 100 m, small lines = 50 m). Refer to Figure 65 for a view of the full length of a simulation deposit. All layers possess the same material properties, colours added as a means of visualizing deformation only.

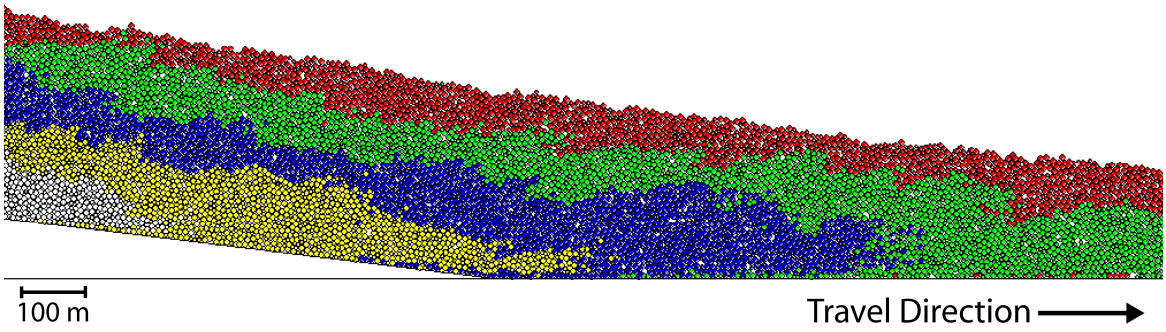

Figure 63 – Folding-over and deformation of stratigraphy in distal avalanche section at $\mu_w = 0.3$. All layers possess the same material properties, colours added as a means of visualizing deformation only.

7.6.2. Variable material properties

Here the material properties of the simulated volcanic stratigraphic layers were alternated such as would be found in nature. Variations of μ_p and particle mass density were considered individually as was the alteration of weak (low friction/low density), medium (medium friction/medium density), and strong (high friction/high density) layers.
In the cases where μ_p and mass density were altered, every other stratigraphic layer was given altered properties while the remaining layers retained their original properties. In the case of the weak, medium and strong layers, the properties of every other layer were alternated between the two material property combinations being considered. For instance, when the weak versus strong combination of material properties were under investigation, the stratigraphic pattern, from the bottom of the pre-failure slope, was weak layer-strong layer-weak layer-strong layer-weak layer-strong layer.

Increases in particle mass density lead to more structure being created in the internal layers within the deposit (Figure 64). This takes the form of a medial compressional up-welling structure with a series of similar structures of smaller-scale located distally. Visually, this feature is remarkably similar to cross-section sketches presented by Endo *et al.* (1989) in their description of hummock features at the debris avalanche deposit at Ontake volcano, central Japan and appear to deform the avalanche body in a right-lateral sense. Topography is gently undulating, reflecting and conformable with the layered stratigraphy below. Stratigraphy is generally preserved except for in the upper regions of the distal sections of the failure.

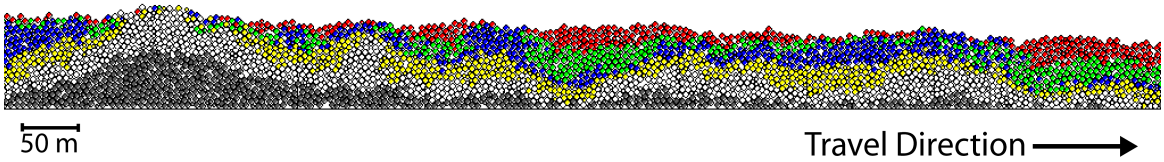

Figure 64 – Stratigraphic structure observed in the medial section of the simulation deposit as particle mass density is increased. Notice the addition of an additional stratigraphic layer (dark grey) as compared to Figure 58. Medial up-welling feature (left of figure) and associated distal layer deformation observed as μ_p is increased. Layers with increased density (3000 kg/m^3) are every other layer starting with the bottom-most (i.e., that in contact with the basal runout surface). Refer to Figure 65 for a view of the full length of a simulation deposit.

Increasing μ_p stems further development of the medial up-welling feature and internal layer deformation, particularly in more distal sections (as seen in Figure 64). The upper stratigraphic layers have been stretched so thinly they are completely separated. Topography is generally subdued and featureless; typically mirroring stratigraphic undulations below though some layer deformation is present in the distal sections of the deposit. When the weak ($\mu_p = 0.25$, density = 500 kg/m^3) versus medium ($\mu_p = 0.75$, density = 2000 kg/m^3) layer stratigraphies are analyzed, internal stratigraphic deformation is observed, which is generally reflected in the topography. This deformation increases as the medium versus strong ($\mu_p = 3.0$, density = 3500 kg/m^3) layer configuration is introduced and takes the form of highly undulating layers proximally, large medial up-welling structures and increasing distal stratigraphic deformation. Combining the weak and strongest layers reveals the most significant topographic undulations and internal deformation structures (Figure 65). Alternating the location of the weakest and strongest layers, where the weakest layer is in full contact with the failure surface, leads to a qualitative increase in stratigraphic deformation and associated topographic extremes

(Figure 66). However, common to all simulations is a series of compressional upwelling structures decreasing in scale distally. The travel characteristics (runout, deposit length and thickness) of the above stratigraphic simulations were also monitored; no clear trends were recognized though runout distances remained generally consistent. It is observed, however, that the longest avalanche runouts occur in the simulations with the largest material property differences (weak versus strong system). Runout generally decreases with increasing μ_p and particle mass density.

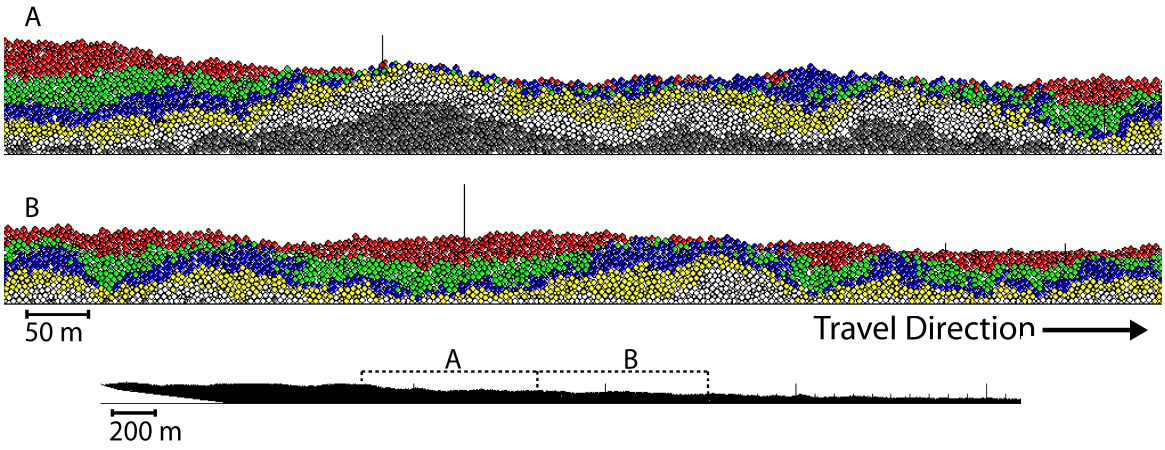

Figure 65 – Topography and close-ups of simulations with the largest material property differences (weak versus strong layers, starting with strong layer on bottom [adjacent to basal runout surface]). The medial upwelling structure is visible in the upper close-up (A). Notice separate scale for zoom.

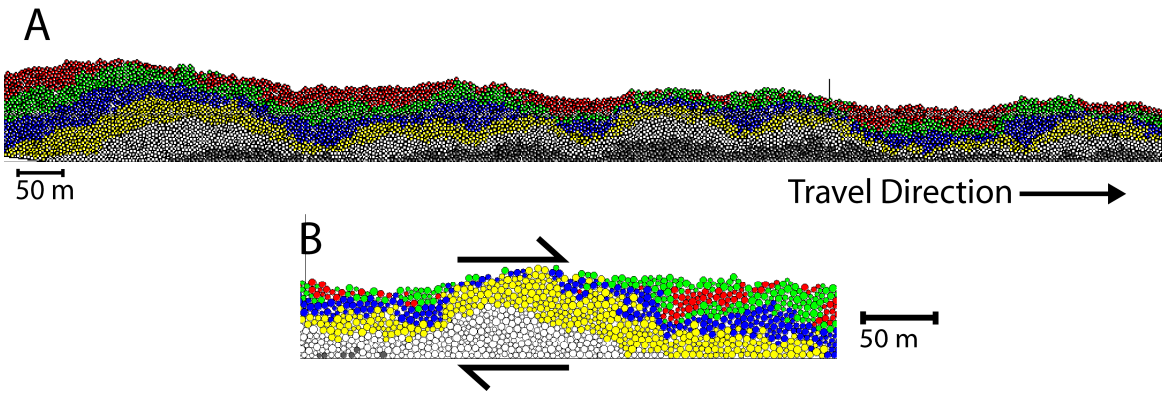

Figure 66 – Topography and structure observed when the weakest and strongest layers were alternated (i.e., weak layer on bottom, adjacent to the basal runout surface). (A) Large-scale structure of the medial section of the deposit; (B) Zoom view of a section of the deposit located off-page in the distal direction. This structure, along with many others, indicates an overall right-lateral sense of shear through the avalanche body. Similar features are shown by Campbell *et al.* (1995).

7.7. Discussion

The results of the unbonded avalanche simulations are consistent with those discussed by previous authors considering similar applications, thus validating the current approach: highly fluctuating stresses, friction-dependent runout, similar velocity and kinetic energy profiles and qualitative deformation observations. Several points worthy of further discussion which were not specifically considered by previous authors emerge from these exercises, including: (1) the temporal and spatial dependency of stresses within the avalanche body; (2) the evolution of the energy variables during emplacement and their relationship to material properties; and (3) the deformation of the in situ avalanche mass throughout emplacement. Specifically, the observations made have implications concerning the emplacement mechanics of VDAs and the formation of several of the commonly observed features in their deposits.

7.7.1. Stress evolution

Monitoring the evolution of stresses that the avalanche experiences during emplacement shows that the initial stages of failure are more variable than the latter stages. Stresses reach greater values with rapidly varying extremes both in space and time. The time period represented by this disorder is defined in the general emplacement model as that immediately following failure initiation as the avalanche body changes from its pre-failure, in situ state to a flowing mass of material. Stresses continue to fluctuate and remain at high levels as the avalanche reaches the transition to the horizontal runout surface and begins to organize itself into a steady flow. This is significant as rapidly varying, high stresses would facilitate rock mass fragmentation and disaggregation in natural rock and debris avalanches. Rarefaction processes, where fragmentation develops from the tensional forces created from the relief of brief but intense collisions, are likely to occur at this time (Glicken, 1991; Reubi and Hernandez, 2000). When considering large-scale VDAs, a number of previous authors have indeed suggested that these early stages of emplacement are most efficient in rock mass break with relatively minor fragmentation occurring during emplacement (Ui, 1983; Voight *et al.*, 1983; Ui and Glicken, 1986; Belousov *et al.*, 1999; Takarada *et al.*, 1999; Reubi and Hernandez, 2000). Such fragmentation processes may represent the evolution from block sliding to more dynamic flow conditions (Voight *et al.*, 1983). Furthermore, the implication of an evolution from early internal chaos to organized steady flow has implications as to the formation of commonly observed deposit features. For example, block-scale jigsaw fracture patterns

may possibly form during block-block or block-ground impacts and rarefaction effects at early stages of emplacement and be preserved during steady, organized motion in the latter stages.

Avalanche velocity and internal stresses are at their highest as the avalanche approaches the transition to the horizontal runout surface, as suggested by Figure 50. Kinetic energy, dependent on velocity, is also at its highest (Figure 56G). A similar observation was made by Campbell *et al.* (1995) by recording variations in basal stresses directly. Each of these quantities decreases in value thereafter, rather rapidly in the case of velocity and kinetic energy. The transition to horizontal motion therefore represents a key moment during emplacement as stress fields must readjust to accommodate this change, further promoting block/rock mass fragmentation. Based on observations made during field studies of large-scale VDA deposits, several authors have also concluded that the changing stress regime associated with this transition is influential in promoting block fragmentation (Ui *et al.*, 1986; Shea *et al.*, 2008).

The stresses and displacements observed also quantify the degree to which the toe and free surface of the failure are relatively unrestricted as compared to lower and interior sections of the avalanche. This is important for two reasons. First, an unhindered toe, or avalanche front, facilitates stretching and thinning of the avalanche body, allowing it to attain a higher energy and promoting long runout. Secondly, lack of stress at the top of the failure may help to preserve large angular blocks often found on the surface of large avalanche deposits, therefore explaining their presence and the possible development of reverse grading (Campbell *et al.*, 1995).

The degree to which stresses increase and vary due to overburden in the avalanche has been quantified. Avalanche stress increases of this nature have been inferred in field study descriptions by Takarada *et al.* (1999). In addition to stresses and instabilities (sliding fraction) being higher in the lower sections of the avalanche, they are also seen to be higher in the avalanches' proximal sections as it piles up at the horizontal transition. These observations have important implications for the crushing and fragmentation of the lower sections of the avalanche mass. Where high initial and rapidly fluctuating stresses may work to disaggregate the avalanche body on the whole, latter development of these spatially-dependent stresses increases may promote the development of fragmented or fine-grained basal shearing layers. A similar crushing mechanism due to large basal stresses has also been suggested by Strom (2006) (Section 3.3), who also suggests that the relative

fluidity of this crushed basal layer may lead to the subsequent development of hummock-type structures common in large-scale rock and debris avalanche deposits. This layer may accommodate much of the deformation taking place in the avalanche body during emplacement, allowing the material above to travel relatively undisturbed, and consequently allowing features such as stratigraphic relationships and jigsaw fractured blocks to be preserved upon deposition. Additionally, the basal shearing layer may facilitate increased mobility and long runout and is consistent with laminar plug flow hypotheses as discussed in Section 2.4.

In this DEM model, however, individual particles are rigid and cannot fragment. Therefore, a fragmented or fine-grained basal shearing layer cannot develop. As a result, the strain produced in this lower region, which one would expect to be the highest in the avalanche, cannot be relieved and may therefore be transferred upwards within the failure body. This may account for the increased strain rates in the interior of the travelling avalanche (Figure 55C). High strain rates cannot develop on the free surface of the avalanche and are therefore confined to the interior of the avalanche. Subsequently, increased deformation is observed in this interior region where it would most likely be accommodated by basal shearing layers in a natural setting. While this observation may initially appear to reveal a limitation in the modelling technique, it also highlights the importance of material properties on emplacement characteristics. In an avalanche of material composed of either weak or widely varying material properties, a basal shearing layer may be more likely to develop. In an avalanche comprised of either more robust and competent or homogeneous materials such as the rigid particles modelled in PFC^{2D}, however, basal shearing layers may be less likely to develop and shear and deformation may be more evenly distributed throughout the avalanche body. A similar suggestion has recently been discussed by Davies and MacSaveney (2008) who describe basally weak versus basally strong failures where a lower shearing layer may be more or less likely, respectively, to develop during emplacement. These authors refer to field observations where rock fragmentation has been observed both throughout the full depth of the resultant deposit (basally strong) or confined to basal section (basally weak). The DEM simulations conducted here would therefore be classified as basally strong.

7.7.2. Energy evolution

Description of the time-dependent energy terms indicates that gravity contributes to the initial potential energy of the avalanche system which increasingly develops into kinetic

energy as the failure nears the horizontal transition, decreasing thereafter. This may be intuitive, but is significant as it shows that gravity by itself can contribute all the initial energy needed to develop high, fluctuating stresses in the first stages of avalanche development. In volcanic flank failure situations, which may often complicated by complex tectonic, magmatic and/or phreatic influences, it is important to show that these forces might not necessarily be needed to develop high avalanche mobility or characteristic deposit features. The amount of energy dissipated is seen to decrease with increasing material friction as strain within the avalanche increases. This observation suggests that the avalanche's energy is not fully dissipated as friction increases, essentially locking the particles together with stronger frictional properties. Decreased avalanche runout with increasing basal wall friction (μ_w) supports this idea. These observations are noteworthy as they stress the importance of material properties in determining avalanche emplacement characteristics. For instance, more competent, high friction materials may tend to be deposited in more proximal locations where lower friction materials would travel further, giving the perception of increased mobility. Such a scenario was modelled by Ward and Day (2006) in their reconstruction of the emplacement of the 1980 Mount St. Helens debris avalanche.

A pulsing form of motion was also been observed in the simulations by monitoring the change in particulate assembly strain energy with time of emplacement. Though it is not particularly clear what mechanisms this may relate to in actual rock or debris avalanche, a 'stick-slip' type of movement is indicated by the strain variations observed in Figure 56J. Strain is highest as the avalanche descends from its in situ position to be temporarily relieved when frictional bonds along the basal failure surface are continually overcome. This behaviour continues as frictional coupling between the basal surface and the particles it is in contact with increases after a finite increment of avalanche motion. The mechanism is thus very similar to fault zone stick-slip dynamics. This form of motion in large-scale debris avalanches is difficult to comprehend as they are typically regarded to travel at high velocities (upwards of 70-100 m/s) with a certain degree of fluid mobility. Nonetheless, a pulsating motion of this type has been suggested by previous authors (Voight *et al.*, 1981, 1983; Sousa and Voight, 1995; Schneider and Fischer, 1998; Legros *et al.*, 2000) though it is unclear how relatable the observation made here may be. Additionally, developing high friction in this manner may be the source of friction-generated pseudotachylytes such as those observed by Legros *et al*. (2000) at Peru's Arequipa VDA deposit. The dependency of the sinusoidal behaviour on particle stiffness variation, of which strain energy is a function of, was not explored in detail in this study though it provides an interesting topic

for future research (Itasca, 2004).

7.7.3. Avalanche body deformation

Finally it is worth drawing attention to the qualitative deformation analysis. The general deposit shape is similar to that produced by Crosta *et al.* (2001) and Campbell *et al.* (1995) for their large volume failures where the centre of mass of the deposit is located more proximally than distally relative to the failure source. It is clear from deformation of the vertical coloured markers that macroscopic deformation shifts from left- to right-lateral, thus representing a change in the vertical velocity profile, at some point within the avalanche body. This point is generally in the proximal to medial section of the failure where the deposit is thickest. Proximally from this point the granular material appears to 'fall back' on itself while distally the material cascades off the pile, extending the avalanche in a right-lateral sense. An up-welling structure that generally defines the transition from left-lateral to right-lateral avalanche body deformation has been observed in a number of simulations, particularly when particle friction values are relatively high. These structures result from a degree of compression in the avalanche body as it reaches the horizontal transition, due both to the interruption of the avalanches downslope movement and the fact that the distal portion of the avalanche body is slowing due to momentum loss as the proximal section is still travelling downslope. Increased compression in this area is reflected by increased stresses observed during this time (Figure 50). Original stratigraphic relationships are retained upon deposition though individual layers have been drastically thinned and stretched, the top layers more so than those on the bottom. This phenomenon was also observed in the DEM experiments of Campbell *et al.* (1995) and is significant as the retention of original stratigraphic relationships is often observed in the deposits of large-scale rock and debris avalanches (Siebert, 1984; Schneider and Fisher, 1998; Clavero *et al.*, 2002; Shea *et al.*, 2008). Thus, the collective motion of the DEM simulation indicates how large-scale avalanches may spread out in an organized fashion from the base of the failure source, as suggested for natural events.

7.7.4. Final thoughts

The unbonded simulations are clearly valuable in their ability to develop insight into the mechanics of avalanche emplacement. It is also recognizable, however, that this approach is limited in its capacity to develop characteristic deposit morphologies discussed in the literature and visible on the orthoimagery, such as hummocks, steep margins, etc. The

topography created by the unbonded simulations consists only of broad undulations at its most extreme. The unbonded simulations also lack the ability to consider realistic situations such as particle and block fragmentation and effects these processes have on emplacement and deposit features. These processes are considered to be a fundamental aspect of large-scale avalanche emplacement and the associated mechanics should be considered in detail (Davies, 1982; Ui, 1983). Furthermore, as the runout area is a simple horizontal surface in this case, the influence of varying topography has not been considered. This was done in part for consistency with previous studies.

The unbonded avalanche simulation have provided a valuable foundation on which to design simulations more representative of real world processes such as the influence of material strength, rock mass fragmentation and topographic influence. Based upon this simple model, the introduction of these more complex scenarios through particle bonding and runout area topographic variation are described in the following chapter.

Chapter 8 - Bonded DEM modelling

The objective of this chapter is to build upon the insight developed in Chapter 7 by the addition of particle bonding to the DEM simulations, allowing emergent brittle behaviour to be considered. Material calibration exercises are first presented. In addition to a purely extensional emplacement scenario, a further objective of this chapter is to consider the influence of runout area topography on emplacement behaviour and the subsequent features developed. The ultimate objective of this chapter is to consider the insight developed from these simulations in relation to the formation of characteristic VDA deposit features and general emplacement mechanics as discussed in Chapters 4 and 5.

Key questions:

- What material properties should be given to the bonded particle system?
- How does the bonded avalanche system behave in a purely extensional scenario?
- How does runout area topography affect emplacement behaviour and the deposit features created?
- How do the features created in the DEM simulations relate to those observed in nature and what emplacement mechanics insight can therefore be developed?

8.1. Introduction

On the basis of the simulated unbonded avalanche behaviour, the next step in considering the geomechanical processes that occur during large-scale avalanche emplacement is to include particle bonding in the pre-failure particulate mass. As discussed in Chapter 6, the introduction of particle bonding can simulate stressed rock mass behaviour through bond breakage when sufficient stresses are applied, thus capturing the emergent properties of a deforming brittle rock mass. Such an approach has been considered by previous authors in slope stability modelling (Hakuno *et al.*, 1989; Barla and Barla, 2001; Crosta *et al.*, 2001; Deluzarche *et al.*, 2003; Preh *et al.*, 2003; Tommasi *et al.*, 2003; Preh and Poisel, 2006; Lorig *et al.*, 2007), however, bond breakage in these cases was mostly considered as a means to initiate slope failure, rather than a process that occurs progressively during emplacement. In any case, these publications have not specifically considered progressively disaggregating avalanche simulations and their resultant deposits in relation to their real world counterparts, a main objective of this study.

As discussed in Chapter 6, bonded models must be calibrated through simulation of laboratory experiments by adjusting particle/bond microproperties to match desired a macro-response. Because achieving a realistic response from the bonded particulate assemblage is dependent on the initial state of stress of the system to be analyzed, a new slope failure scenario also had to be designed before simulation experiments could be conducted. Emplacement behaviours described in the previous chapter, however, remain generally applicable. The process of material calibration and model setup are presented first.

The exercise discussed in this chapter represents approximately one year of effort in realizing the most appropriate methods for material calibration and model design and to conduct the subsequent avalanche simulations and interpretation. The run-time of the simulations discussed below was approximately 8-10 hours per simulation, a significant increase over the unbonded simulations discussed in the previous chapter due to the necessity for the program to track and update particle bond status as well as particle/wall status. In total, several hundred avalanche simulations on top of those discussed in Chapter 7 were conducted in order to achieve the results discussed below. Material calibration was also a time consuming process as it involves iterative trial-and-error in order to achieve the desired response.

8.2. Model design

8.2.1. Material calibration

Identifying appropriate rock mass parameters for use in the emplacement simulations presented a significant challenge to this study. Volcanic edifices are composed of a wide range of materials such as lavas (rhyolites, dacites, andesites, basalts), pyroclastic and ash materials (loose ash to welded tuffs) and soils (both unconsolidated and indurated). Furthermore, these materials vary spatially and are often heavily affected by joints, brecciation and/or hydrothermal alteration. Therefore, the difficulty in assigning values to the parameters discussed in Section 6.3 was to do so in a manner that reflected the geomechanical behaviour of the *entire* slope, not just a specific area or rock type. With this in mind, material calibration was guided by the geotechnical classification of volcanic material scheme (GCVM) of del Potro and Hürlimann (2008). The GCVM was created by these authors to address a fundamental lack of geotechnical parameters for volcanic edifice material in the literature. del Potro and Hürlimann (2008) simplify the range of materials

present in a given edifice by classifying a material as either a lava, autoclastic breccia, pyroclastic material or volcanic soil. These distinctions may be subdivided further based on degree of hydrothermal alteration, welding and interlocking. Geotechnical characterization of these materials was conducted by del Potro and Hürlimann (2008) at Tenerife's Teide volcano by a combined study of intact rock strength and rock mass quality measurements. For intact rock strength, Schmidt hammer, point load and uniaxial compressive tests were conducted on both in situ and laboratory specimens. Rock mass quality measurements were conducted by use of the geologic strength index (GSI) methodology of Sonmez and Ulusay (1999). Ultimately, del Potro and Hürlimann (2008) combined their own measurements with values discussed in the literature to create the GCVM, which is undoubtedly the most thorough geotechnical classification scheme of volcanic edifice materials to date.

The key aspect of the GCVM is the use of rock *mass* properties (i.e., GSI) to determine the behaviour of the constituent volcanic materials. As detailed by Thompson *et al.* (2008), GSI is a numerical description of rock mass quality based on discontinuity spacing and condition (roughness, clay lining, etc.). GSI is estimated by visual assessment of the rock mass in question and compared to the chart of Hoek (2007) to assign a quantitative description. This value is in turn used in the Generalised Hoek-Brown Criterion to determine failure in jointed rock masses as described by Hoek *et al.* (1995):

$$\sigma'_1 = \sigma'_3 + \sigma_{ci}\left(m_b \frac{\sigma'_3}{\sigma_{ci}} + s \right)^a \tag{14}$$

where σ'_1 and σ'_3 represent the major and minor effective principal stresses at failure, respectively, and σ_{ci} represents the uniaxial compressive strength (UCS) of the intact rock material. m_b is a reduced value of the material constant m_i, given as:

$$m_b = m_i \exp\left(\frac{GSI - 100}{28 - 14D} \right) \tag{15}$$

s and *a* are additional rock mass quality constants given by:

$$s = \exp\left(\frac{GSI - 100}{9 - 3D}\right) \tag{16}$$

$$a = \frac{1}{2} + \frac{1}{6}\left(e^{-GSI/15} - e^{-20/3}\right) \tag{17}$$

The parameter *D* in the above equations represents the disturbance factor which is dependent on the degree of disturbance to which a rock mass may have been subjected by blast damage and/or stress relaxation (Hoek, 2007).

As detailed by Hoek *et al.* (2002), the criterion described by (14) is highly applicable to local fracture propagation scenarios; however, in the case of large-scale rock masses such as volcanic slopes, the *overall* strength of the rock mass should be taken into consideration. Hoek and Brown (1997) therefore define the *global rock mass strength* (σ'_{cm}), a metric much more applicable to scales being represented in this study:

$$\sigma'_{cm} = \sigma_{ci}\left(\frac{(m_b + 4s - a(m_b - 8s))(m_b/4 + s)^{a-1}}{2(1+a)(2+a)}\right) \tag{18}$$

Both measured and available GSI and σ_{ci} values are used by del Potro and Hürlimann (2008) to determine σ'_{cm} values for each of the GCVM materials (Table 14). In fact, most of the parameters needed to define and calibrate a bonded *PFC*^{2D} material are conveniently presented by del Potro and Hürlimann (2008) (Table 14). Values not included in the GCVM of del Potro and Hürlimann (2008) but necessary for calibration in *PFC*^{2D} have subsequently been found through other means, as discussed in Table 14. It should be noted that the completed Table 14 has subsequently been discussed and verified with M. Hürlimann (personal communication, 2009). The influence of the GSI, which represents decreasing rock mass quality, is clearly evident in Table 14 as the maximum values for σ'_{cm} is only 31.6 MPa whereas intact strengths of some lavas are commonly greater than 200 MPa (Hoek and Brown, 1997).

Table 14 – GCVM values per del Potro and Hürlimann (2008) and additional sources. Values presented represent those necessary for *PFC*^{2D} bonded material classification.

Material	Sub-unit	Unit weight (kg/m^3)	σ'_{cm} (MPa)	E_m [f] (GPa)	Poisson's ratio	Friction angle (φ)
Lava	Fresh	2489	31.6	13.7	0.25	40
	Altered	2346	9.9	7.7	0.33	40[c]
Autoclastic breccia		1520	8.5	9.6	0.25[b]	39[c]
Pyroclastic rock	Strongly welded, fresh	1479	31.4	50.9	0.25[b]	39[c]
	Strongly welded, altered	1275[a]	4.5	2.5	0.25[b]	26[c]
	Weakly welded/interlocked	1347	4.6	19.5	0.11	39[c]
Volcanic soils		1479	1.0[e]	0.1[d]	0.2[b]	25[b]

[a]per Hürlimann (2009)

[b]per Coduto (1999)

[c]Calculated from method presented by Hoek *et al*. (2002)

[d]per USACE (1990)

[e]estimation per Thompson *et al*. (2008)

[f]E_m - deformation (i.e Young's) modulus, calculated per Hoek *et al*. (2002)

The values presented in Table 14, however, represent geotechnical classifications of specific materials potentially found within in a volcanic edifice. As volcanic slopes are composed of a wide and complex range these materials, modelling efforts are best designed with an intermediate combination of these properties representative of all the materials potentially present (Rodríguez-Losada *et al*., 2009). Therefore, bonded *PFC*^{2D} assemblies were calibrated to represent the strongest, mean strength and weakest materials presented in Table 14 (Table 15).

Table 15 – Initial *PFC*^{2D} materials calibrated. High and low values represent the strongest and weakest materials present in Table 14. Mean values represent either the mean of the Table 14 values (unit weight, σ'_{cm}), common rock values for rock materials (Poisson's ratio, friction angle) or values chosen represent a middle-ground material (E_m, where the high and low values have at least an order of magnitude difference).

Designation	Materials represented	Unit weight (kg/m^3)	σ'_{cm} (MPa)	E_m [a] (GPa)	Poisson's ratio	Friction angle (φ)
Strong	Strong, fresh lavas, welded tuffs	2500	32	51	0.3	40
Mean	All materials present	1700	13	1/15[a]	0.25	35
Weak	Weakly welded or highly altered material,	1300	1	0.1	0.11	25

[a]Young's moduli of both 15 and 1 GPa were tested

In order to keep the bonded models consistent with the unbonded model detailed in Chapter 7, an identical particle size range of 3.2-5.3 m diameter with a uniform distribution was used to calibrate the bonded materials. As it is ideal for calibration specimens to contain at least 10-20 particles across the lateral dimension (x-axis), the specimens tested here had a dimension of x = 63 m, y = 126 m (2:1 height to length ratio), thus containing 478 particles (Itasca, 2004c; DeGagne, 2008). Similar large-scale test specimen calibration exercises in PFC^{2D} are also performed by Preh *et al.* (2003) and Preh and Poisel (2006). By running a series of laboratory test simulations at various resolutions, i.e. particle size ranges, it has been observed that particle size has only a nominal effect on the macroscopic properties of the assembly (Itasca, 2004c). Likewise, Crosta *et al.* (2001) note that particle size variations have little effect on simulation avalanche emplacement and deposit properties (Section 6.2).

The iterative calibration process whereby input microproperties are varied to achieve a desired macroscopic response, as described in Chapter 5, was followed. In this case, the desired macroscopic responses are those presented in Table 15. Specimen unit weight is taken as that of the individual particles and therefore does not vary after input. Material friction, also, does not vary after input. Particle friction coefficients are again defined as μ_p where $\mu_p = tan\varphi$. It should be noted that though the friction angle, φ, is used to calculate μ_p, it is not representative of the bonded material strength envelope. The approach of calculating μ_p from φ has been adopted from the literature (Preh *et al.*, 2003; Preh and Poisel, 2006) and personal recommendation (D. DeGagne, personal communication, 2008). Ultimately, the physical meaning of this parameter is not clear in bonded models and is influential mainly after brittle failure (i.e., post-peak) or in unbonded scenarios (Potyondy and Cundall, 2005). Bond radius, λ, was also held constant at 1.0, thus equalling the diameter of the smallest particle present in a given bonded pair. Therefore, from equations (10) and (11), only E_c, k_n/k_s (particle properties) and E_{cb}, k_{nb}/k_{sb}, σ, τ (parallel bond properties) needed to be varied for calibration. This process was further simplified by setting $E_c = E_{cb}$ and $k_n/k_s = k_{nb}/k_{sb}$ following Itasca (2004c, 2004d) and Potyondy and Cundall (2005). Additionally, the mean bond normal and shear strengths, σ and τ, respectively, were initially set equal to one another in order for both tensile and shear failure to be possible (Potyondy and Cundall, 2005).

Due to the relatively small number of particles constituting each test specimen, multiple tests were conducted to obtain an accurate realization of the desired macroresponses. In each test, the random number seed was varied, changing the location where each particle is

generated. Thus, at each seed, particles in the assembly assume a different location, slightly affecting macroresponse. To identify the most ideal macroresponse, calibrations were performed 30 times for each material, as shown in Appendix A. The results of each realization have been normalized to the mean output and tallied to produce a quantitative means of identifying the most ideal specimen for use in the avalanche simulations (Table 16).

Table 16 – Material calibration results. Both the most and least ideal realizations, in relation to the target macroresponses from Table 15, are displayed.

	Material	Random number seed	Friction coefficient (μ_p)	Unit weight (kg/m^3)	Input E_c, E_{cb} (GPa)	Input k_n/k_s, k_{nb}/k_{sb}	Input σ (MPa)	Input τ (MPa)	Output σ'_{cm} (MPa)	Output E_m (GPa)	Output ν
Most ideal	Strong	1	0.84	2500	59.7	5.25	28.5	28.5	31.9	51.1	0.31
Least ideal		8			66.5	6.85	23.5	23.5	32.3	51.6	0.34
Most ideal	Mean (E_m = 15 GPa)	19	0.7	1700	9.0	3.0	9.0	9.0	13.0	15.1	0.23
Least ideal		25			9.2	2.8	10.5	10.5	13.1	14.9	0.21
Most ideal	Mean (E_m = 1 GPa)	2	0.7	1700	0.90	2.70	9.0	9.0	13.1	1.1	0.23
Least ideal		18			0.90	3.00	11.2	11.2	13.1	1.2	0.23
Most ideal	Weak	4	0.47	1300	0.59	1.30	0.75	0.75	1.1	0.1	0.11
Least ideal		14			0.58	1.41	0.74	0.74	1.2	0.1	0.12

8.2.2. Simulated edifice creation

The calibration process discussed above produces a specimen of bonded particles of relatively small dimension (x = 63 m, y = 126 m) in relation to the overall size of the model being examined. In order to investigate the behaviour of larger rock mass systems, a process of replication of the original calibrated specimen called Adaptive Continuum/Discontinuum (AC/DC) Logic has been designed by Itasca (Itasca, 2004c). This approach reproduces a single calibrated block, called a *pbrick*, of a desired macroresponse and fits it to an identical adjacent block, the sides of which are an exact negative image of the original block (Figure 67). This process is repeated until a size sufficient enough to accommodate the desired model geometry is reached. Initial contact force information is stored within each pbrick, which is already in force equilibrium (Section 6.3.5); thus, stresses are quickly transferred across the entire composite model resulting in a large-scale, calibrated block at equilibrium. An additional feature of the AC/DC logic is the ability to convert pbrick components not being analyzed into 'continuum' blocks, the properties of which are based on the overall stiffness of the initial block. Thus, in large-scale simulations where brittle deformation in only a certain area of the model is being investigated but the overall stress state must still be considered, processing can be made much more efficient as deformation of the continuum pbrick blocks is considered rather than response of each individual particle. An example of such a

problem given by Itasca (2004c) is an underground caving scenario where only deformation immediately around a newly constructed void is important (Figure 67). The complete AC/DC technique employing continuum blocks was not used in this study though it may provide a useful approach for future work.

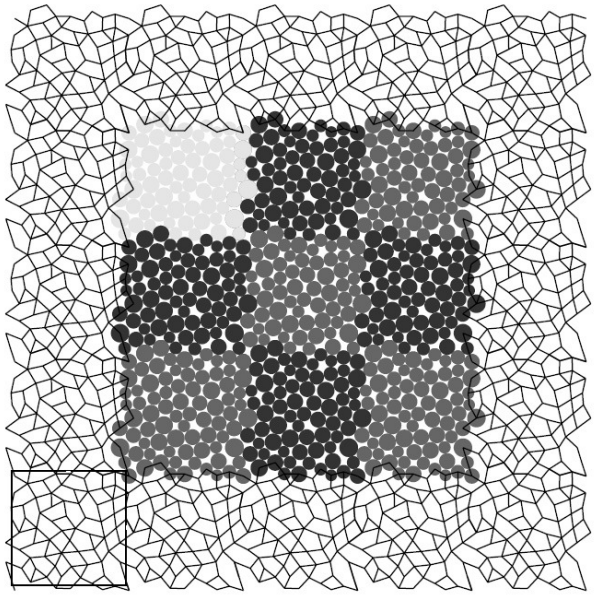

Figure 67 – System of nine identical pbrick components constructed to build a large block of material of a desired macroscopic response. Notice the precise fit of each block to its neighbours. The pbrick block is surrounded by a mesh representative of additional pbricks which have been converted to a matrix based on the overall stiffness properties of the initial pbrick. Only brittle deformation of the central part of the model is under consideration in this instance. Modified from Itasca (2004a).

For this study, pbricks calibrated to each of the macroscopic responses discussed in Section 8.2.1 were created and multiplied to build blocks large enough to accommodate a 1.0 km high volcanic cone with a 30° slope (3528 m base) (Figure 68). This geometry is consistent with that described in Chapter 7. A frictionless wall was then installed along the base of the block and a gravitational force (9.8 m/s^2) was induced. The model was then cycled for the block to adjust to the presence of the neighbouring blocks and the gravitational force; a realistic lithostatic stress field was thus created. In order to shape the calibrated block into a volcanic cone geometry, sections of the block above the cone were sequentially deleted, cycling the model in between each deletion to allow the cone to gradually adjust to the new stress field. Bond strengths were set to high values before cycling began to ensure that no deformation occurred during this process and returned to their original values after the desired geometry was created (Preh and Poisel, 2006). The resulting model is a bonded particle assemblage with a macroscopic response representative of a range of common volcanic materials with a geometry and stress field

representative of a volcano scenario. Such an approach is similar to that used by Itasca in design of their *Large Open Pit* research model (Itasca, 2009).

del Potro and Hürlimann (2008) note a vertical stress of approximately 40 MPa is likely experienced in the basal region of a volcanic edifice (unit weight ≈ 24 kN/m^3, 1800 m edifice). Similar to the exercise described in Section 7.4, a measurement circle (50 m diameter) was placed at the base of the cone to determine the stress in this area in relation to expected values. A ρgH calculation using the average unit weight from Table 15, ρ = 1833 kN/m^3, height, H = 975 m and gravity, g = 9.8 m/s^2 results in a lithostatic stress of 17.5 MPa. Stresses measured in *PFC*^{2D} range from 11-16 MPa, depending on the unit weight of the material; reasonable figures considering the smaller edifice height used and the porous nature of the material.

The *PFC*^{2D} code which automated and drove the sequence described above, along with the avalanche simulations discussed below, is presented in Appendix B.

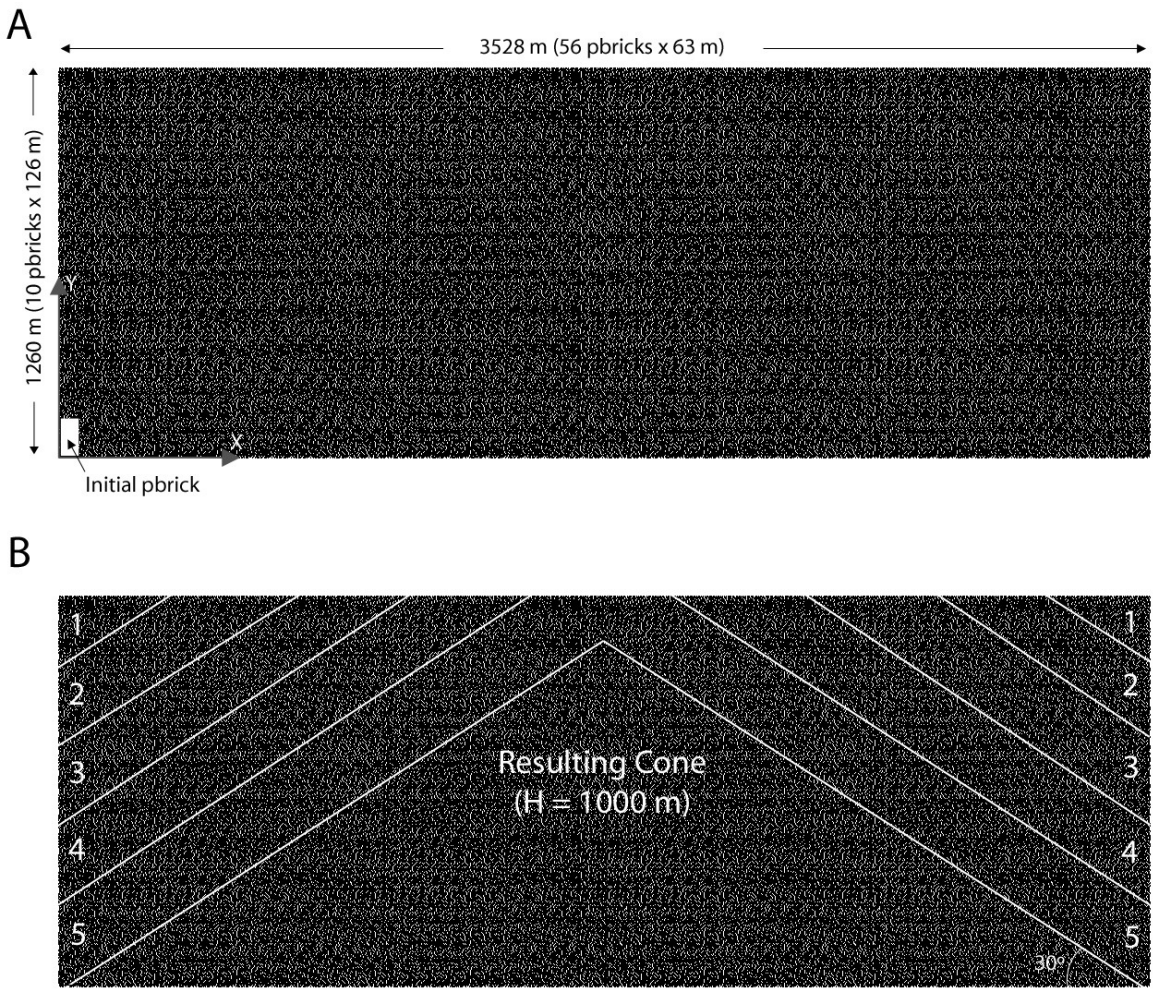

(Figure 68 continued on following page)

C

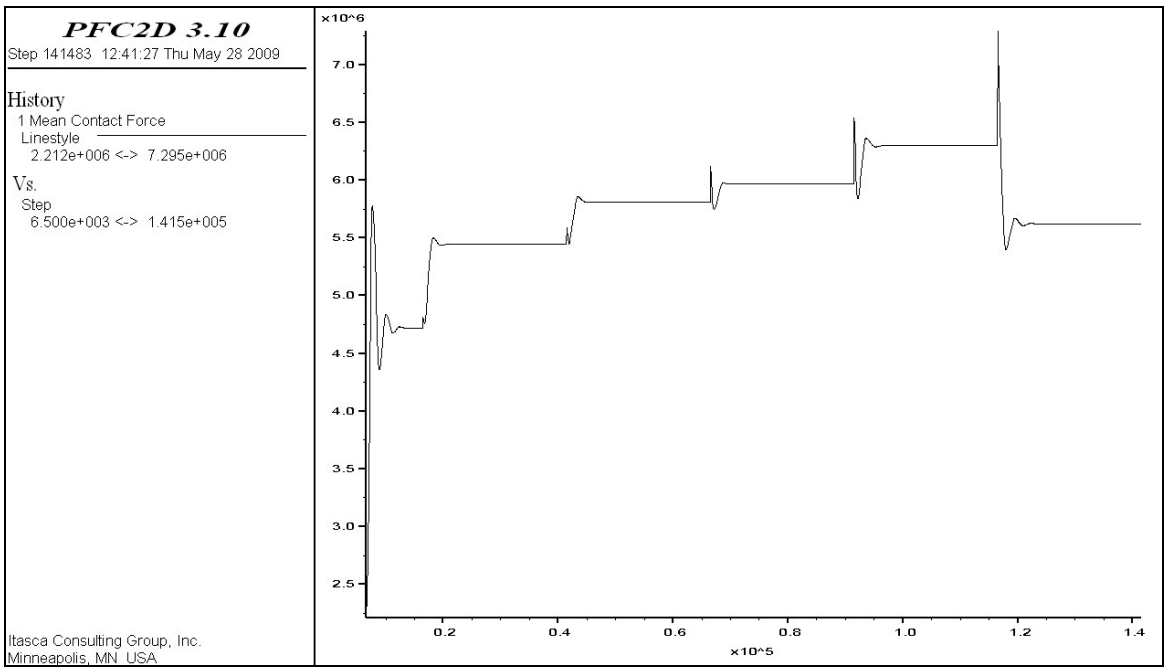

D

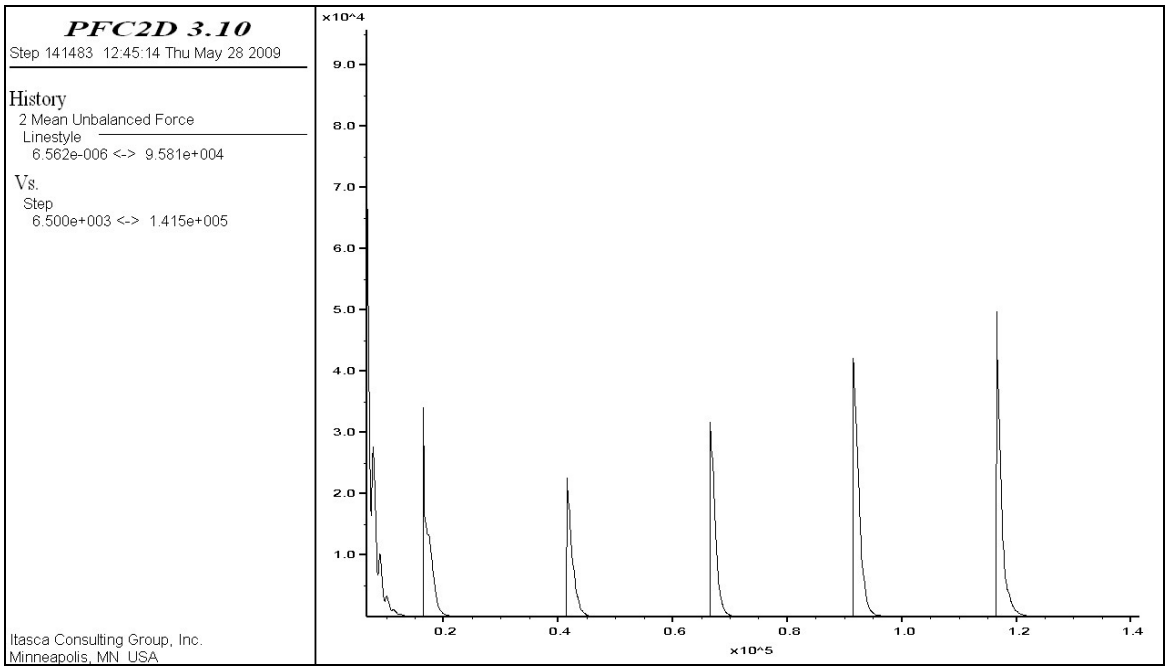

(Figure 68 continued on following page)

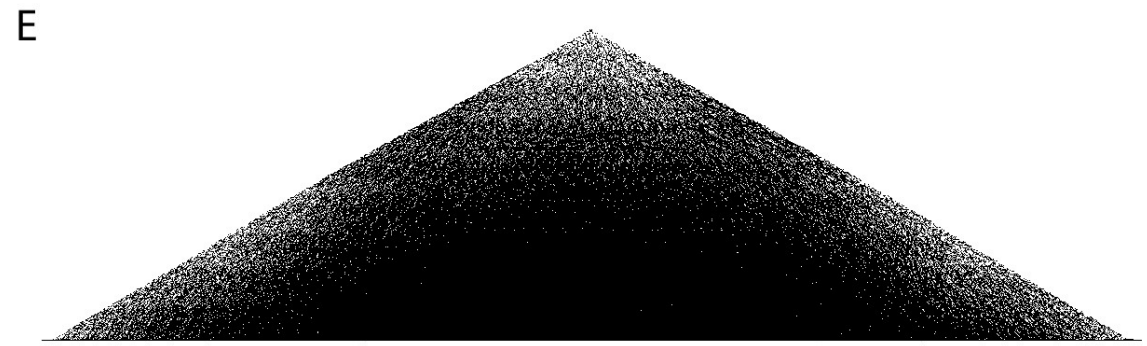

Figure 68 – Simulated volcanic cone creation process. (A) Large-scale block created from calibrated pbricks; (B) Sections of equilibrium block removed sequentially (1→5) to create the volcanic edifice geometry; (C) Evolution of the mean contact force in the particle assembly during sequential removal of overburden to create cone geometry. Increasing contact force is likely a function of consolidation of the assembly upon further cycling, a decrease in the final stage reflects the reduced overburden. Levelling-off indicates stability of the cone; (D) Evolution of the mean unbalanced force during cone creation, a measure of out-of-balance force components; return to a nil value indicates model stability; (E) Compressive stress field within the cone, stresses increase towards the bottom centre of the cone due to lithostatic loading, as would be expected. Similar observations were made for each material calibrated. Refer to Figure 70 for a detailed view of the internal particulate assembly structure as resolution is lost here due to the large size of the model and the large number of particles is contains. Final cone height is 1.0 km.

8.3. Debris avalanche simulation

8.3.1. Full cone collapse

The static stability of the simulated cone created above was investigated by cycling the model after the final geometry was created, thereby subjecting it to gravity. Cones with each of the calibrated strengths presented in Table 16 were considered with both a frictionless basal wall and basal wall with μ_w equal to that of each particle assembly. No indication of instability was observed for the strong or mean material strength cones. However, when the cone with the weakest material properties was considered, collapse resulted in the form of lateral spreading and reduction in cone height (Figure 69A). Retrogressive failure behaviour remarkably similar to that seen in real world scenarios was observed (Figure 69B, 69D and 69E). Behaviour variation was negligible at each value of μ_w. The occurrence, general location, and geometry of the faults which delineate each slide block are similar to those observed during the failure of Mount St. Helens (Figure 69C) and suggested for numerous other collapse events (Voight *et al.*, 1981, 1983; Schuster and Crandell, 1984; Siebert 1984; Glicken 1991, 1998; Sousa and Voight, 1995; Ward and Day, 2006). Additionally, the observation that collapse was only generated in the cone

with the weakest bonded material may help to constrain the properties of the natural materials which might be most influential in generating flank failure (del Potro and Hürlimann, 2008).

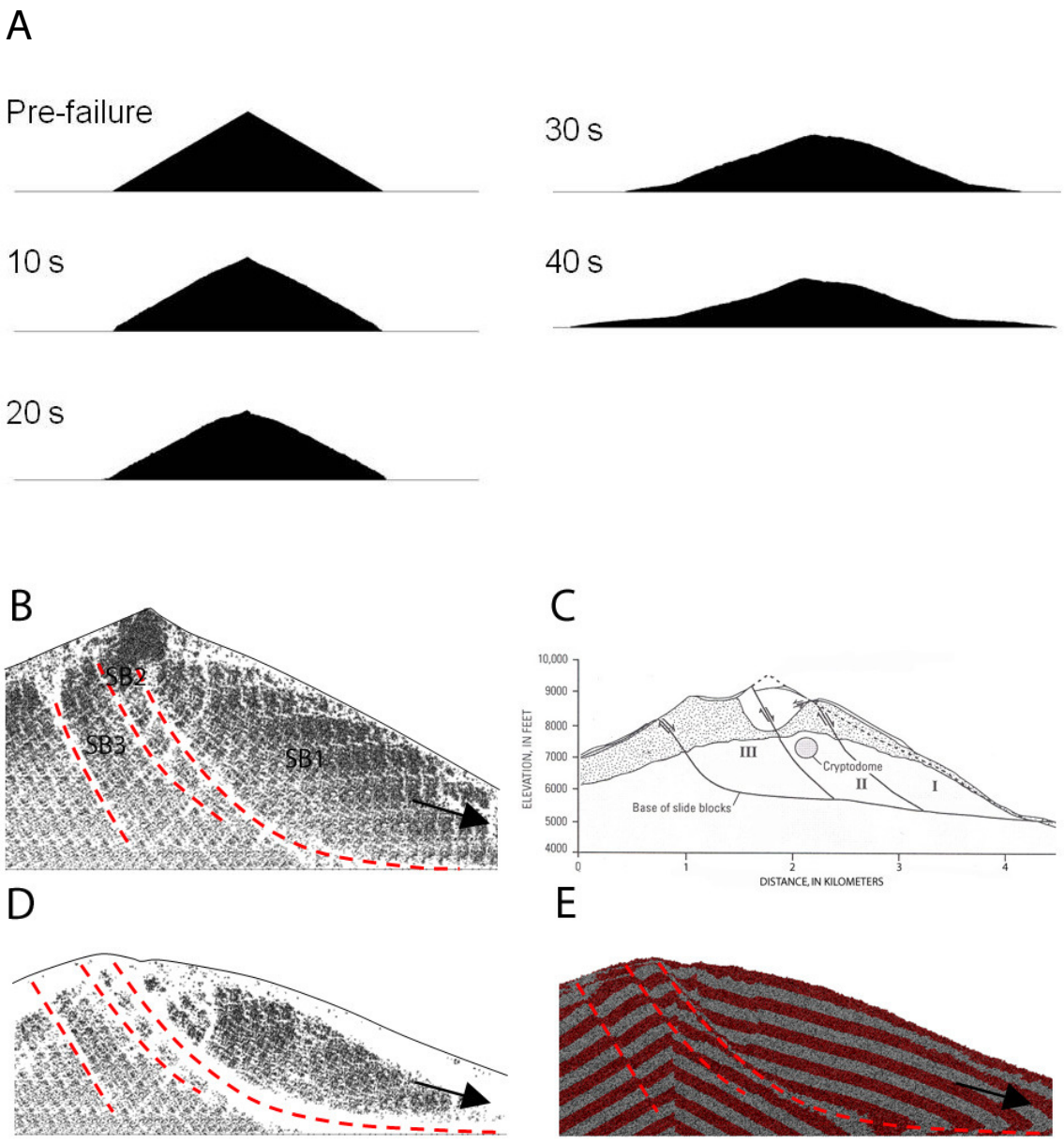

Figure 69 – Collapse of the simulated 1.0 km volcanic cone. (A) Collapse geometry from pre-failure edifice to 40 s; (B) Retrogressive listric faults developing within the cone at 10 s. Similar to the Mount St. Helens collapse, three slide blocks are observed (SB1-3). Figure shows particle bonds only for clarity; (C) Retrogressive failure of Mount St. Helens (modified from Glicken [1998]); (D) Evolving cone collapse at 30 s, bonds only; (E) Deformation of cone at 30 s viewed with hypothetical stratigraphic layering, notice normal offset of stratigraphy at each fault (red dashed line). Black arrows indicate displacement direction. Vertical offset in (E) is a product of the stratigraphy generation process and not created during collapse. Full cone simulations contain 114,053 particles; original cone height is 1,000 m.

Generation of retrogressive failure in the DEM simulation cone, however, involves deformation of the entire cone, which is unrepresentative of volcanoes where the remnants of the failed edifice remain and a distinct collapse scar is typically observed. The spreading edifice seen here likely affects the behaviour of the failure (or failures) considerably as the failure surface is ever-changing and essentially exerts a driving force on the underside of the initial failure. With these factors in mind, consideration of failure emplacement in detail is performed by use of a pre-defined failure surface as discussed below. This approach also allows consistency with the unbonded simulations detailed in Chapter 7 and efficient computation. The pre-failure geometry used, however, is based upon similar geometries to that observed here and in effect isolates the failures generated for a more detailed analysis. Isolation of the failure mass in this manner is consistent with the aims of this project in that it allows focus on avalanche emplacement behaviour rather than instability or failure initiation mechanisms. The reader is therefore referred to Morgan and McGovern (2003, 2005a, 2005b) and Morgan (2006) who consider lateral spreading of volcanic edifices by DEM simulation in detail. Though in-depth analysis of retrogressive collapse behaviour as observed here is beyond the scope of this study, generation of this phenomenon does provide an interesting topic for future research and verifies the ability of the DEM model to simulate real world geomechanical behaviour.

8.3.2. Pre-defined flank failure

To ensure a realistic state of stress was retained, the desired failure surface was installed through the calibrated cone assemblage after the gravitational settling procedure described above was complete. Particles below the failure surface walls, those that are not involved in the avalanche itself, were deleted before failure initiation. The failure surface installed inevitably crossed between the centroid and outer extent of many of the particles, and as particles are defined and deleted by the location of their centroids, a gap between the particle assembly and failure surface often resulted (Figure 70A). Upon failure, the few assembly particles which were in contact with the surface carried the weight of the assembly, resulting in unrealistic stress evolution and fracture development. Therefore, a particle insertion scheme was designed to install additional particles in the gap along the failure surface (Figure 70B). The newly inserted particles make contact with the failure surface wall and any surrounding particles and were given properties identical to those of the assembly. Bonds were then installed between the new particles and their neighbours based on the normal distribution of the existing bond strengths. This process results in a smooth interface between the bonded particle assembly (17,634 particles) and the failure

surface where the weight of the failure was realistically distributed along its length. This method was created in conjunction with Martin Schöpfer of the Fault Analysis Group at University College, Dublin and is shown in the *PFC*^{2D} code presented in Appendix B. Due to the presence of the failure surface, the particulate mass is inherently unstable and fails upon model cycling. As opposed to the horizontal runout surface beyond the slope toe used in Chapter 7, the runout surface here remained dipping at 7° and gradually curved towards the horizontal with distance; an approach thought to better simulate a natural emplacement basin. Wall friction, μ_w, was held constant at 0.1 (6°).

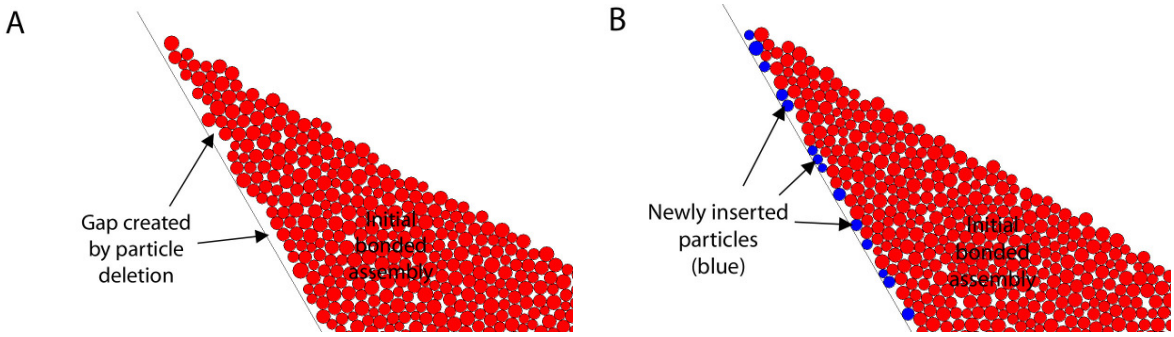

Figure 70 – Insertion of new particles to create a relatively smooth interface between the bonded particle assembly and the failure surface. (A) Head of particulate failure before particle insertion; (B) Newly inserted particles (blue) along failure wall. New particles are within the specified size range of the assembly and are in contact with any surrounding entity (particles and/or walls). This process is repeated until all gaps are reasonably filled; the new particles are then bonded to the assembly. Particle size range 3.2-5.3 m diameter.

Collapse simulations were then performed for each of the materials presented in Table 16 (most and least ideal scenarios). Results from this exercise were initially unsatisfactory as no realistic response was observed (Figure 71). In the case of the relatively stronger materials (strong and mean), flexure of the mass as it encountered the horizontal runout surface caused top-down tensile fracturing, behaving essentially as solid blocks of competent material. Bond breakage and fracture propagation were more widespread and the avalanche travelled further with each decrease in strength. In the case of the weakest material, the majority of bonds were broken within the earliest stages of emplacement; the avalanche subsequently behaved as an unbonded material. In this case, a small number of bonds do remain until stages of emplacement at the upper surface of the weakest material, however. The difference in behaviour between the most and least ideal materials was negligible.

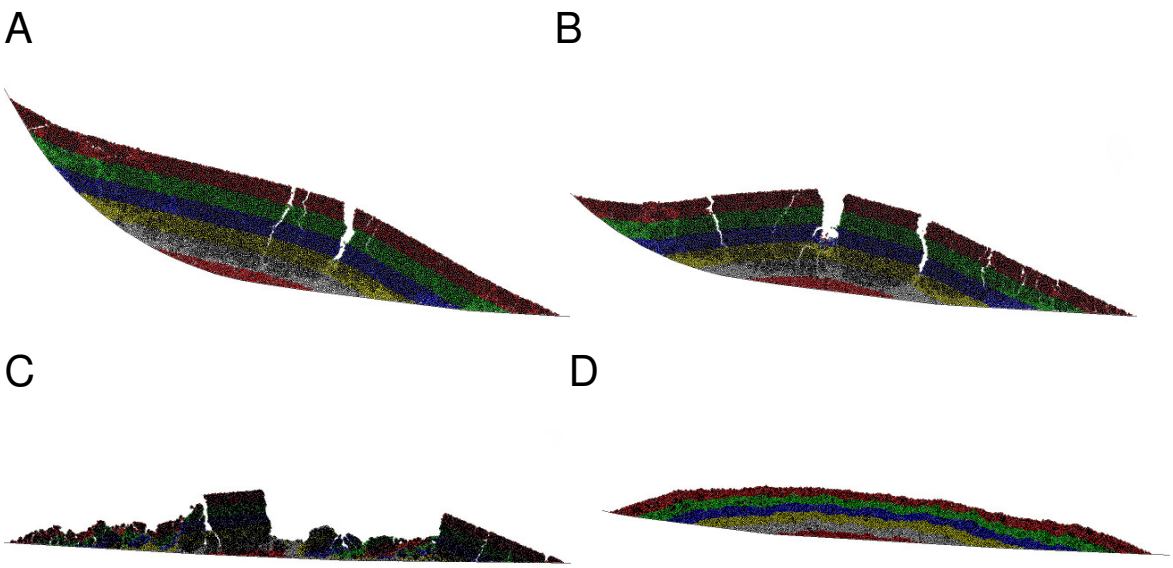

Figure 71 – Emplacement of each of the most ideal calibrated materials after 50 s; little bond breakage occurred after this point in each case. (A) Strong; (B) Mean (E_m = 15 GPa); (C) Mean (E_m = 1 GPa); (D) Weak. Black colouring in each figure indicates the presence of bonds. Direction of motion is to the right. Scale 0.5cm ≈ 100 m.

Strong material avalanche behaviour was therefore observed to be unrealistically rigid and weak material avalanches behaved essentially as those discussed in Chapter 7. In order to investigate the behaviour of materials spanning the identified strong to weak range, additional material calibration test were conducted to create bonded materials within this range (Table 17). Unit weight, v, and μ_p values were kept identical to those of the mean material strengths calibrated above while σ'_{cm} and E_m values were varied. Pbrick blocks were then created from the newly calibrated materials.

Table 17 – Materials calibrated to represent the identified strong to weak range of material properties given in Table 16.

Designation	Unit weight (kg/m^3)	σ'_{cm} (MPa)	E_m (GPa)	v	Friction coefficient (μ_p)
A	1700	10	10	0.23	0.7
B	↓	10	1	↓	↓
C		10	0.5		
D		10	0.1		
E		5	10		
F		5	1		
G		5	0.5		
H		5	0.1		
I		4	10		
J		4	1		
K		4	0.5		
L		4	0.1		
M		3	10		
N		3	1		
O		3	0.5		
P		3	0.1		
Q		2.5	10		
R		2.5	1		
S		2.5	0.5		
T		2.5	0.1		
U		2	10		
V		2	1		
W		2	0.5		
X		2	0.1		
Y		1	10		
Z		1	1		
AA		1	0.5		
BB		1	0.1		

Collapse simulations were conducted on each newly created material following the model generation process outlined in Section 8.1.2. All avalanches with high $E_m \geq 0.5$ GPa disaggregated in the initial stages of emplacement to subsequently behave as an unbonded avalanche; thus representing unrealistically stiff elastic values for this case. Additionally, any avalanche with $\sigma'_{cm} \geq 4$ MPa or ≤ 1 MPa was either too rigid or rapidly unbonded, respectively, leaving only the avalanches with $2 \geq \sigma'_{cm} \leq 3$ MPA and $E_m < 0.5$ GPa to be considered (designations P, T, X). The remaining avalanches display a realistic behaviour during emplacement where bond breakage occurs through fault initiation, propagation and widening and progressive disaggregation of bonded blocks. The main difference is that faults in weaker materials (T→X) widen at faster rates as bonds adjacent to these discontinuities are more easily broken, resulting in a more rapidly unbonding avalanche mass with behaviour approaching that described in Chapter 7. As the differences are subtle, only emplacement of the median case (designation T) is explored in detail below.

8.3.2.1. Extensional emplacement

The avalanche with the material properties identified above exhibits emplacement behaviour worthy of further attention. For this purpose, a series of emplacement 'snapshots' are described below, which detail the development and evolution of bond breakage within the avalanche body from failure initiation to deposition (Figure 72). These initial simulations are purely extensional in that no topographic barriers or irregularities were present in the runout space. The complete collapse sequence is shown in detail in Figure 73. The most significant events occur during the relatively early stages of emplacement (≤ 50 s) and descriptions below are therefore concentrated on this period.

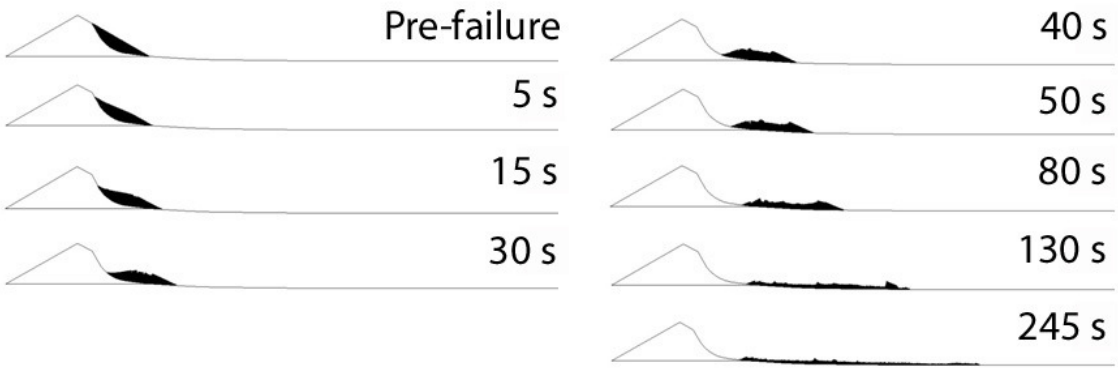

Figure 72 – Sequence of the bonded avalanche described. Complete deposition, cessation of all movement, occurs at approximately 245 s. The runout of the avalanche described is 5.9 km from source (H/L = 0.15). Original cone height is 1,000 m.

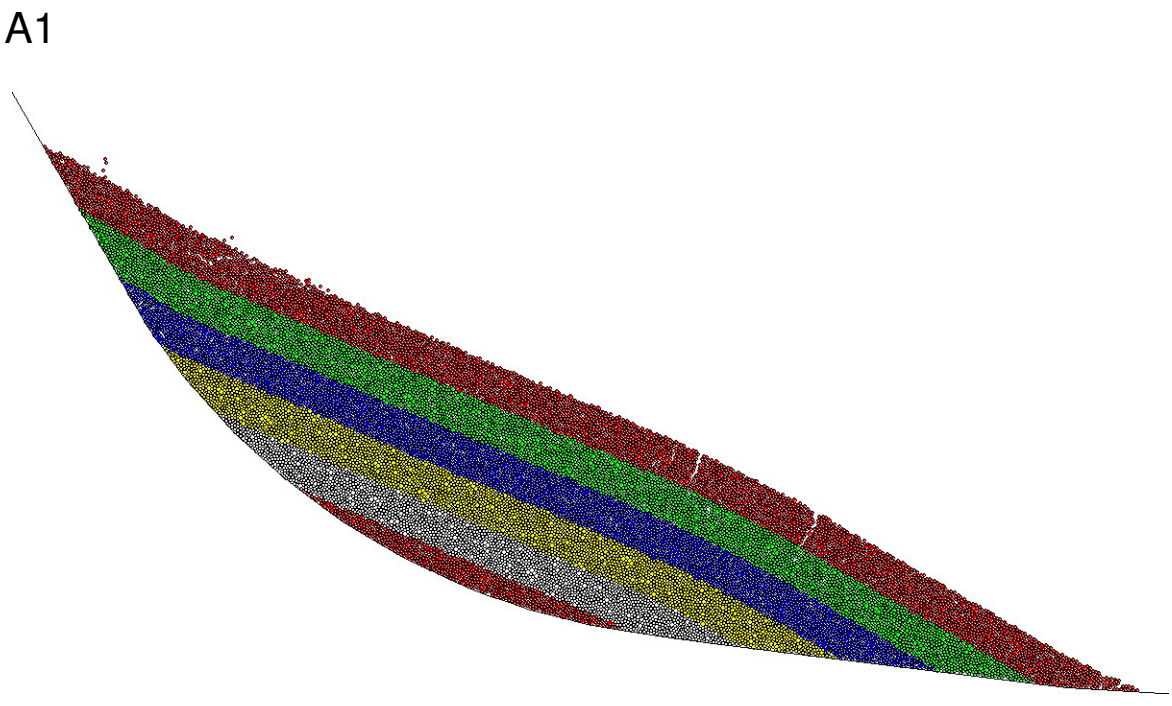

(Figure 73 continued on following page)

A2

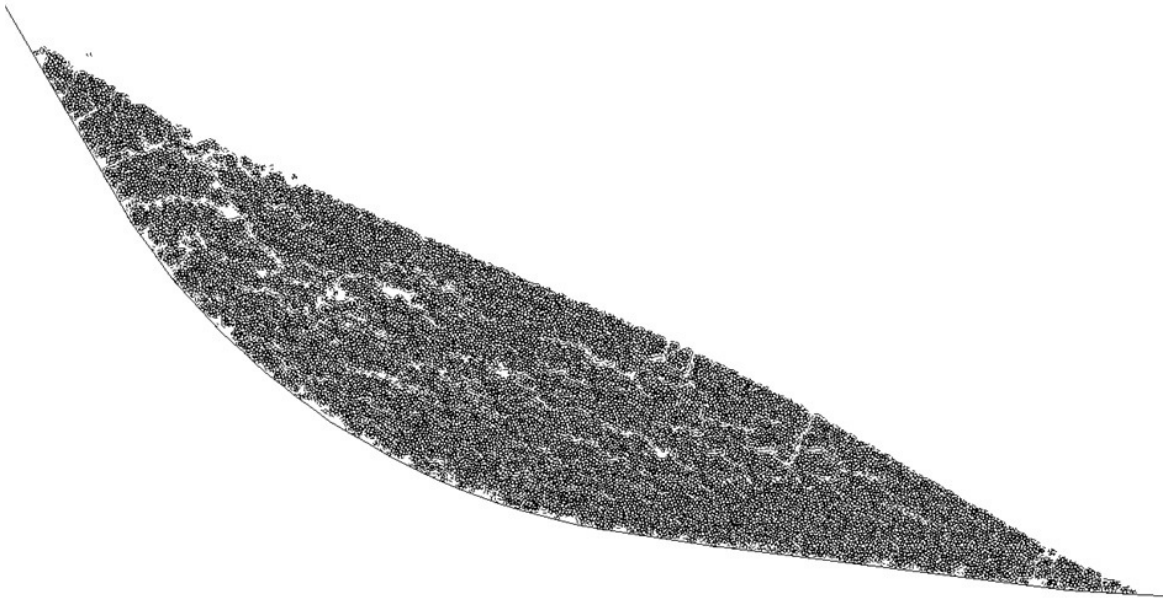

A3

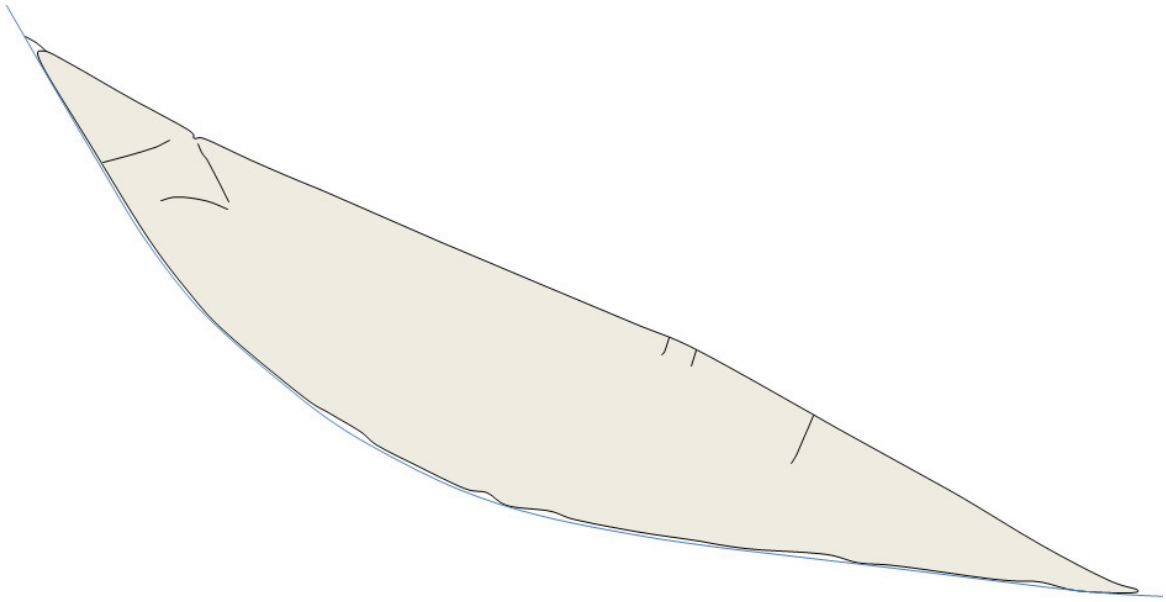

(Figure 73 continued on following page)

B1

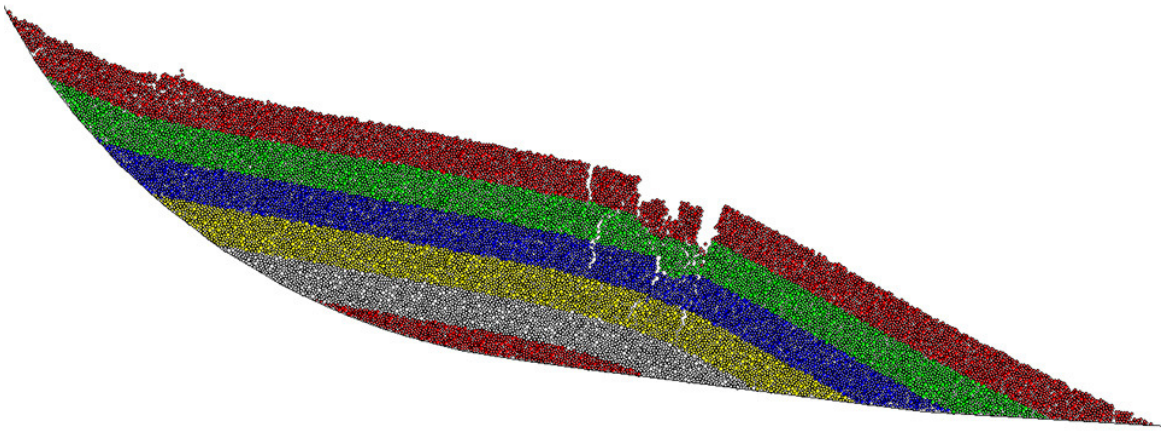

B2

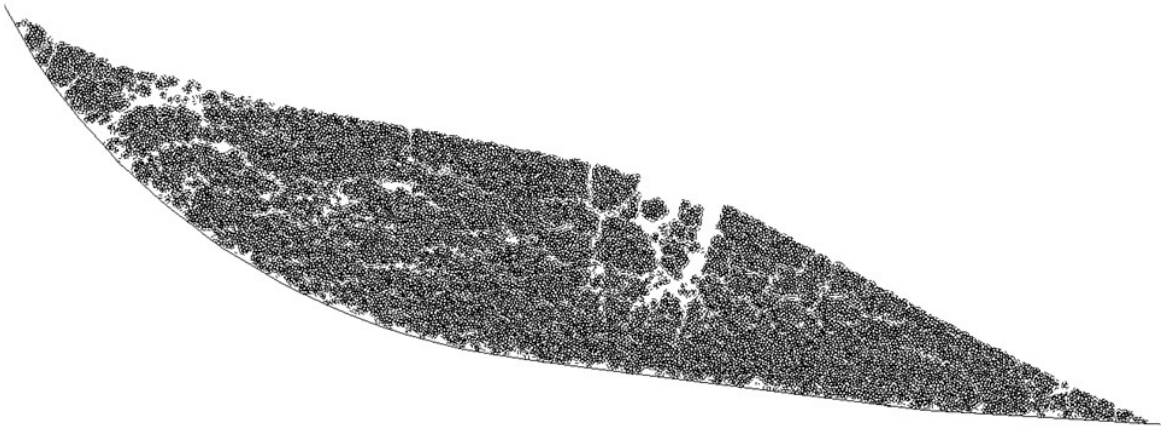

B3

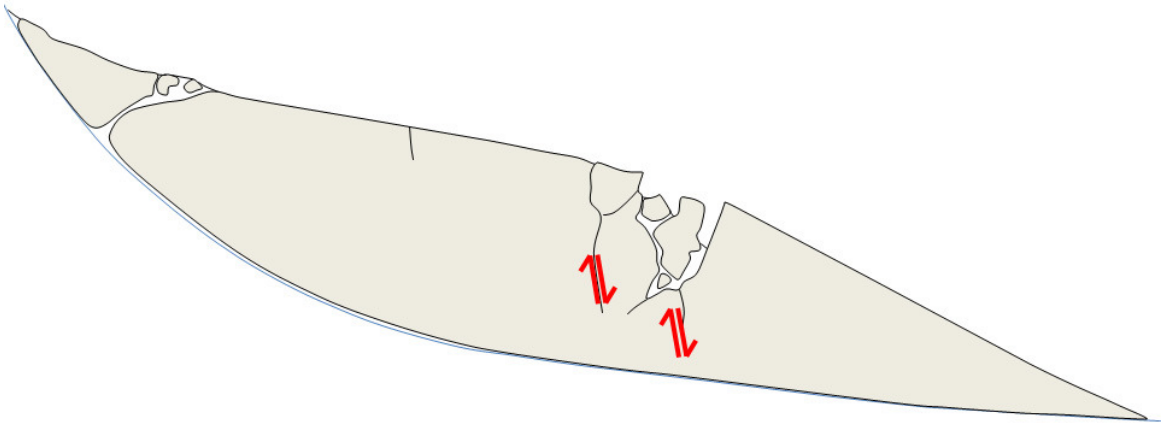

(Figure 73 continued on following page)

C1

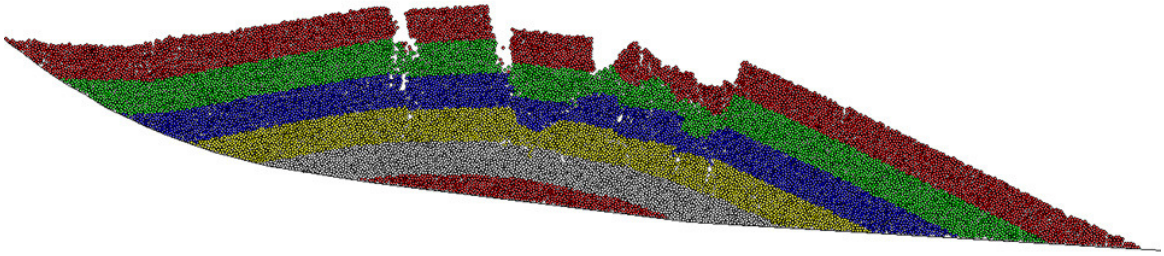

C2

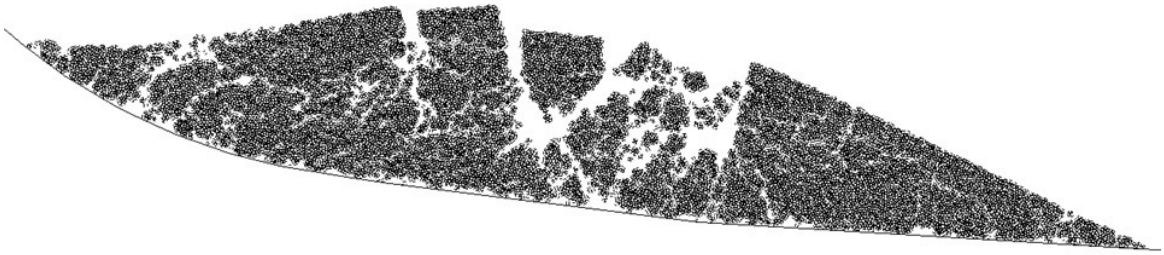

C3

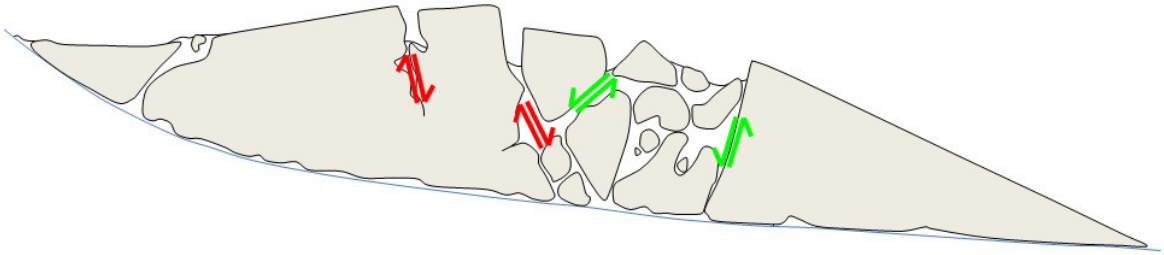

(Figure 73 continued on following page)

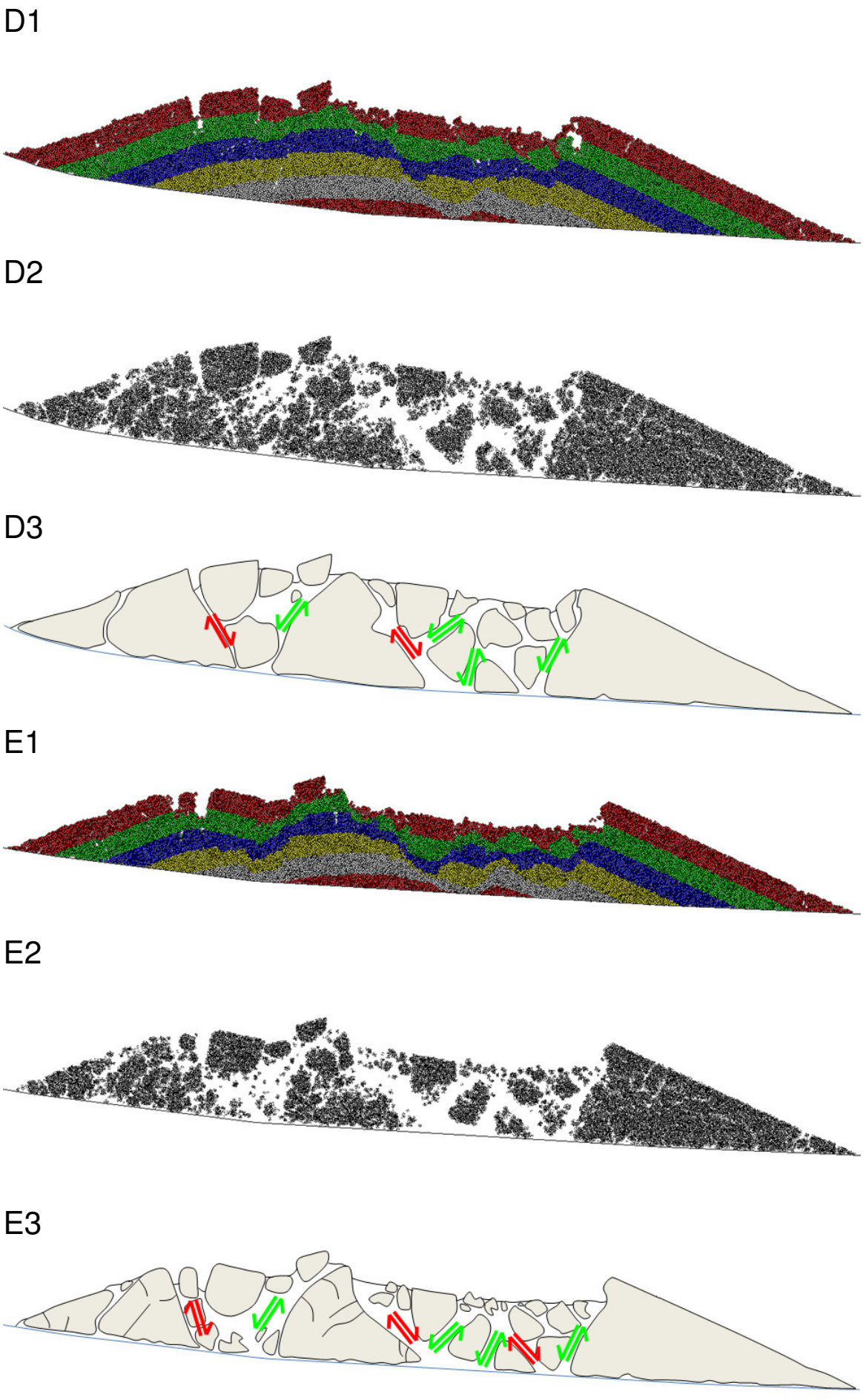

(Figure 73 continued on following page)

F1

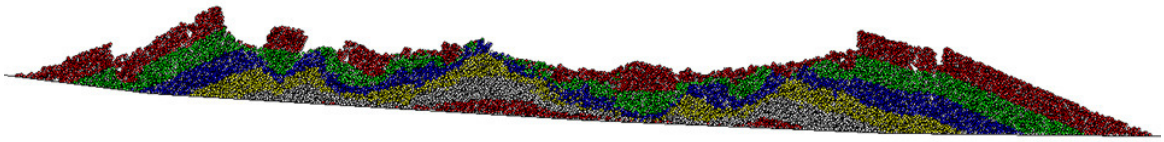

F2

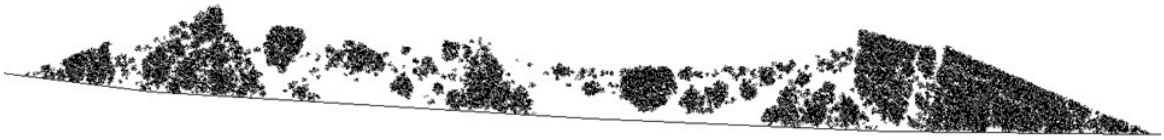

F3

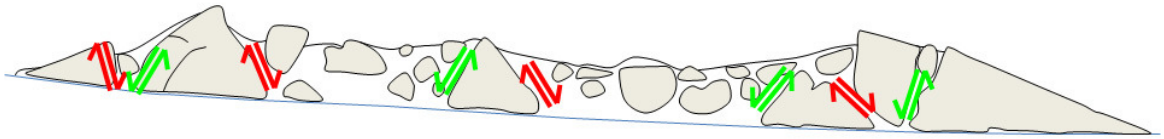

G1.

G2.

G3

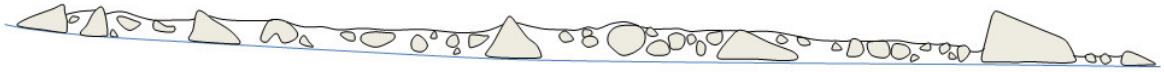

(Figure 73 continued on following page)

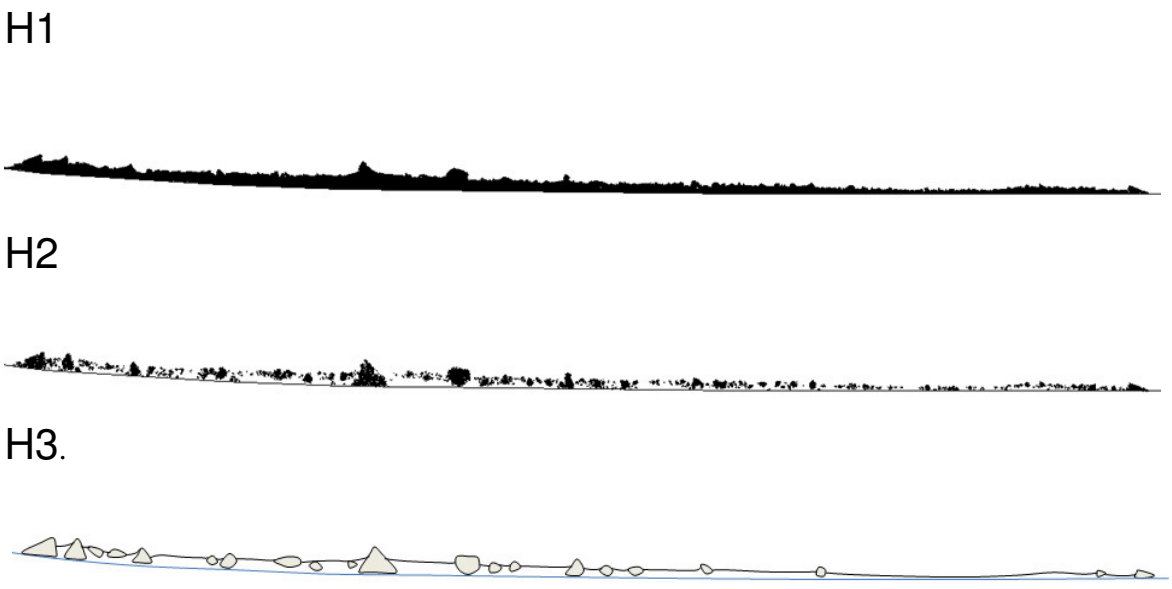

Figure 73 – Extensional emplacement sequence of bonded assemblage, emplacement direction is to the right. Three figures are presented for each sequence: (1) a bonded particulate assembly with pseudo-stratigraphy to better visualize deformation, (2) an assembly showing bonds only with the particles removed and, (3) a structural interpretation figure. (A) 5 s, scale ≈ 100 m; (B) 15 s, scale ≈ 100 m; (C) 30 s, scale ≈ 100 m; (D) 40 s, scale ≈ 100 m; (E) 50 s, scale ≈ 120 m; (F) 80 s, scale ≈ 175 m; (G) 130 s, scale ≈ 250 m; (H) 245 s, scale ≈ 450 m. Notice that scale decreases with increasing emplacement time as the viewing screen must be continually reduced to accommodate the increasing length of the avalanche body. Resolution of the model also decreases in order to view the entire length of the deposit and therefore stratigraphic layering is not visible in the latter cycles. This is acceptable as the majority of the significant deformation and brittle fracture occurs in the early stages of emplacement. In each structural interpretation figure gray colouring represents bonded material, white represents unbonded material.

Due to basal friction and the shape of the failure surface, a certain amount of contraction of the failure mass takes place during the initial stages of emplacement (≈ 5 s), resulting in a degree of tension on the upper surface of the failures' medial section (Figure 74). Likewise, compression occurs along the base of the failure. Bond breakage along the upper surface results from this process though not to a significant degree (Figure 73A2 and A3). Compression occurs in the proximal portion of the failure due to the shape of the failure surface and rotation of the failure mass. At 15 s much of the distal half of the failure reaches the runout surface and the mass subsequently begins to extend, representing a period of maximum avalanche body stresses and kinetic energy as described in Chapter 7. Extension is accommodated, and therefore stress is relieved, primarily by downward and distal propagation and widening of the fractures (dextral offset) developed during initial tension in the medial portion of the upper surface (Figures 73B1-B3). Initial compression at the proximal head of the failure has caused bond breakage but no significant offset. Small fractures parallel to the upper surface can be observed throughout

the failure mass, which may also accommodate extension of the body to some degree and suggest a tendency towards separation between upper and lower layers (Figure 73B2).

Figure 74 – Failure at 5 s showing tension (red) in the upper medial region of the failure and compression (black) in the lower portion. Thicker lines represent increasing stress intensity. Particles removed for clarity. Direction of motion is to the right. Scale 1cm ≈ 100 m.

At 30 s extension accelerates through further downward propagation and widening of the medial fracture zone to form distinct normal faults (Figure 73C1-C3). A large listric fault in the medial portion of the failure has reached the failure surface. Where previous faulting had been angled towards the nose of the failure, proximal-facing faults have now developed to create blocks in the disaggregating medial section (green offset arrows in Figure 73C3). A large fault with this sense of offset has also isolated the bonded distal part of the failure. Additional distal-facing normal faults begin to develop toward the proximal area of the failure with a similar geometry to those faults developed initially. Early bond breakage in the most proximal part of the avalanche caused by the failure surface shape has not developed significant offset. As observed in Figures 73C2 and C3 bonds along the failure surface interface begin to break. At 40 s body extension continues through widening and shallowing of normal faults. The disaggregated medial area of the failure has grown in width as faults widen and blocks fragment and pull apart from one another. In a similar sequence to that which occurred earlier in the medial area of the failure, distal-facing faults which developed toward the proximal area of the failure are followed by proximal-facing normal faulting to develop an additional disaggregated basin in the proximal section of the failure. The combined sense of offset in these areas is indicative of the development of a horst and graben extensional system (Figure 73D3). Further

extension of the avalanche at 50 s displays the horst and graben structure more clearly as the bonded, triangular horst are now separated by broad, block filled basins (Figure 73E3). Downward-propagating faults coalesce at the base of these basins to form unbonded lower and blockier upper sections (reverse grading appearance), perhaps indicating a degree of structural influence in basal shearing layer development. Additionally, bond breakage in the lower portion of the failure may be a function of increased stresses and instability in this area as recognized in the unbonded simulations. Bonds at the base of the triangular horsts remain mostly intact though some breakage has occurred.

Extension of the avalanche body beyond 50 s primarily sees further development of existing features though fault widening and block disaggregation. At 80 s, the most proximal horst feature begins to separate into a series of triangular features whose stratigraphy appears to be back-tilted, remarkably similar to toreva block features as described in preceding chapters (Figure 75). Though reduced in size through disaggregation, these features are retained at deposition (Figures 73H1-H3). Similar structures have developed in the medial area of the failure from the disaggregation of horsts, which protrude further above the avalanche surface with time of emplacement. The medial horsts are separated by broad lock-filled basins (grabens) and also display stratigraphic back-tilting.

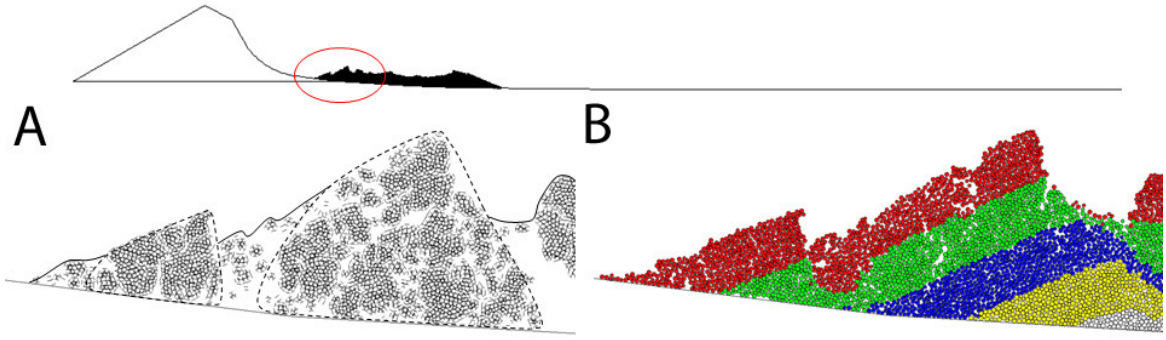

Figure 75 – Toreva structures developed in the most proximal area of the DEM model at 80 s. (A) Triangular torevas showing bonds only; (B) Particle assembly showing back-tilted and normally offset stratigraphy. Original cone height is 1,000 m; scale of A and B 1 cm ≈ 75 m.

As a result of decreased surface stresses (Chapter 7), bonded blocks of material remain on the surface of the deposit, which generally become smaller with emplacement time and distance (Figure 76; Figure 73H2). These features qualitatively appear to be more numerous towards the distal end of the resultant deposit (Figure 73H2). A general rounding of these blocks also occurs as particles which protrude from newly disaggregated

blocks are sheared away. Bonds in the lower sections of the latter stage avalanche and the resulting deposit are generally broken though they remain intact at some points beneath the toreva/horst structures. As observed in the unbonded avalanche simulations described in Chapter 7, stratigraphic relationships are generally retained though individual layers are stretched and thinned considerably.

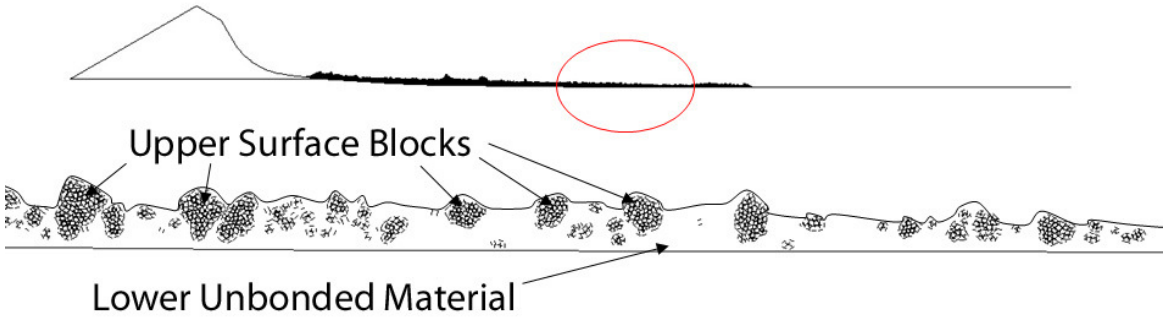

Figure 76 – Rounded blocks of bonded material (black) on the surface of the VDA simulation deposit and lower unbonded material (white). Original cone height is 1,000 m; scale of lower figure 1 cm ≈ 50 m.

8.3.2.2. Runout space variations

It is clear from discussions in Chapters 3, 4 and 5 that the character of the basin in which a VDA is deposited may influence its emplacement behaviour and the characteristics of the resultant deposit. Thus, real world behaviour may depart significantly from the purely extensional scenario discussed above. Potential influences include variations in the material properties of the basal surface material and any topographic barriers or irregularities the avalanche may encounter. These situation have been considered here by introducing a number of different scenarios to the runout space: gaps of increased/decreased friction, increasing friction 'ramps', topographic barriers of varying geometry and sinusoidal topography intended to mimic simple irregular topography. In each case, the bonded assemblage properties employed above were again used. The proximal location of each runout space variation occurs at a point after the horst and graben mechanism identified above has begun to develop within the failure mass.

8.3.2.2.1. Runout surface property influences

The behaviour of an avalanche encountering a basal substrate of either low or high frictional properties was modelled here by altering the value of μ_w at various distances along the runout space. Both 0.5 km and 1.0 km long walls of μ_w values of 0.0 and 0.7

were examined. The μ_w value of 0.7 represents the limiting value of friction as μ_p also equals 0.7. μ_w retained its original value both proximally and distally from the wall with the altered μ_w value, creating a friction 'gap'. 0.5 km walls with the altered μ_w values were placed at 1.0, 1.5, 2.0, 2.5, 3.0, 3.5 and 4.0 km from the original slope toe; 1.0 km walls were placed at 1.0, 2.0, 3.0, 4.0 and 5.0 km. The friction gaps might mimic encounters with material such as weak lacustrine sediments or hard rock surfaces.

In the case of 0.5 km decreasing gap wall friction (μ_w = 0.0), runout distance significantly increases due to the presence of the frictionless material but remains generally consistent with the original value of 5.9 km as gap wall friction is increased (μ_w = 0.7; Figure 77A). The slight decrease and increase in the linear regression trendlines of the low and high friction gap plots, respectively, suggests a decrease in the influence of the gap wall as it moves distally. In other words, basal surfaces with influential properties closer to the failure source may have more of an effect on emplacement behaviour than those located further away. Similar observations are made for both the 0.5 km and 1.0 km gap wall cases though the effects are amplified for the 1.0 km case as decreased/increased friction affects avalanche behaviour over a greater distance (Figure 77B).

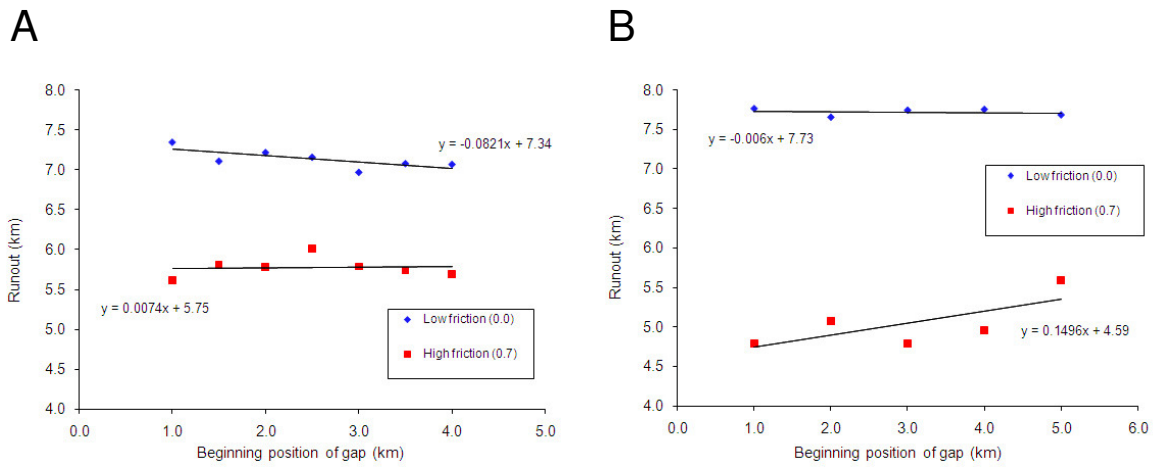

Figure 77 – Relationship between simulation avalanche runout and the location of the high and low friction gaps. (A) 0.5 km gap walls; (B) 1.0 km gap walls. Note that the runout distance of the exclusively extensional scenario avalanche described in Section 8.3.2.1 was 5.9 km.

In terms of avalanche structure the friction gaps were highly influential in all cases. When μ_w was low, the avalanche body was spread thinly on top of and distally from the gap wall. The thinnest deposit depth corresponded to the junction between the original and low μ_w value walls as the avalanche came to rest proximally from this point and stretched away distally. Deposit thickness decreased when gap wall length was increased from 0.5 km to

1.0 km. As more motion occurred between particles due to increased thinning, bonds are broken to a greater degree on top of and distally from the gap wall; only small-scale surface blocks are retained. Larger concentrations of distal surface blocks were observed as the gap wall was progressively moved from 1.0 km to 5.0 km, confirming the idea that gap walls located closer the failure source are more influential in affecting emplacement behaviour. Stratigraphic relationships are generally retained throughout the resulting deposit. Deposit morphology and structure on the proximal side of the gap wall is generally unaffected as normally offset faults, horst and surface blocks remain. Gap walls with increased friction affect emplacement behaviour significantly as the failure tends to pile-up and deposit on top of the gap wall. Bonds are generally broken as the avalanche encounters the gap wall due to frictional coupling effects and possibly increased particle rolling (i.e., differential movement between particles). A folding-over of stratigraphies is observed within the pile, similar to that observed in Section 7.6.1, though compressive forces or material yield strength is not great enough to generate any reverse offset fault structures. The deposit proximal to the high friction gap wall is again generally unaffected and extensional structures remain dominant. Distally from the gap wall pile-up a tapering wedge of particles with few surface blocks defines the remainder of the deposit. Again, the influence of the high friction gap walls decreases as it is moved distally.

A ramp of increasing friction was also used to observe the effects of varying runout surface material properties, which might loosely mimic a more gradual encounter with a basal surface of varying material properties, such as lacustrine sediments in the emplacement basin. In this case μ_w was incrementally increased from its original value of 0.1 to the limiting value of 0.7 over a series of six 0.25 km long wall segments and held constant at 0.7 thereafter. Simulations were conducted with the beginning of the friction ramp at 1.0, 2.0, 3.0 and 4.0 km from the original slope toe. Though decreased on the whole by the addition of higher runout surface friction, runout distance increases linearly with increasing distance of the beginning of the friction ramp (Figure 78). Deformation of the landslide body was generally similar to that observed when the high friction gap wall was considered though material pile-up and layer deformation are not as extreme as the encounter with high friction material was not as abrupt (i.e., deformation evolved gradually). The morphology and structure of the proximal section of the deposit were generally not affected in that extensional structures similar to those discussed in Section 8.3.2.1 were retained at deposition.

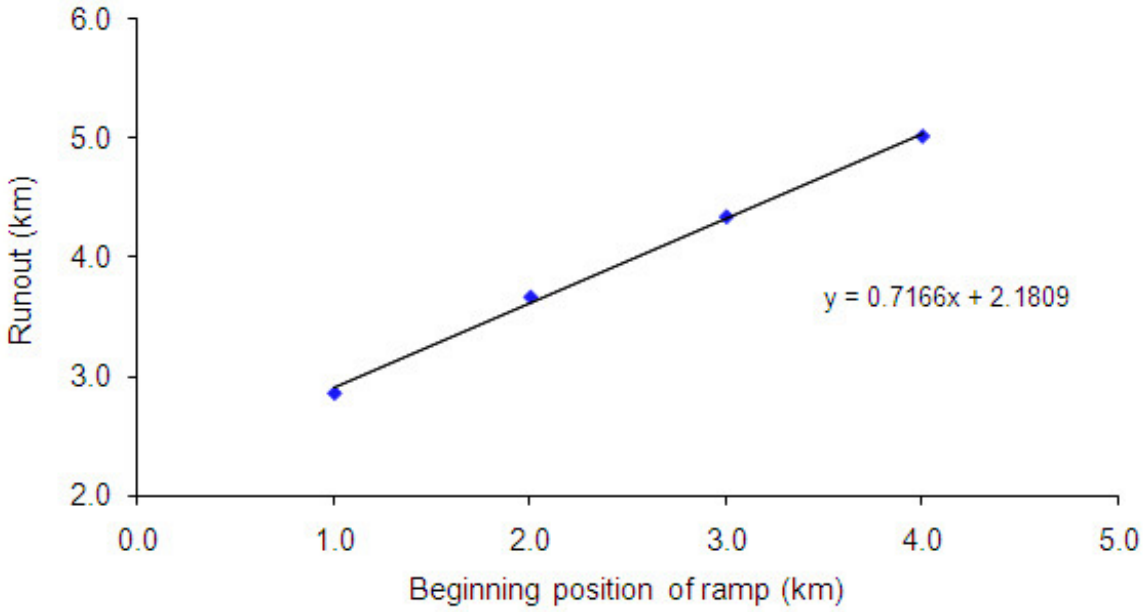

Figure 78 – Increase in avalanche runout distance with increasing distal position of the friction ramp. Runout of the avalanche was 5.9 km when the friction ramp was not included (pure extension, Section 8.3.2.1).

8.3.2.2.2. Topographic barrier influence

A number of simple topographic barrier scenarios were introduced to the runout space to observe the effects similar structures might have on emplacement behaviour and deposit morphology. Barrier walls inclined at 45°, 25° and an angle mirroring the downslope of the emplacement basin (to create a symmetric basin, maximum 7°) were first considered. The location of the junction of the barrier wall and the original runout surface was considered at distances of 2.0, 3.0, 4.0 and 5.0 km from the original slope toe (12 total simulations). Material properties were again held constant to those employed in Section 8.3.2.1 and μ_w was held at 0.1.

The avalanches' encounter with the 45° wall at 2.0 km is characterized by compression of the individual stratigraphies and associated thickening of the distal mass of the avalanche body. Adjacent to the barrier some blocks are present, represented by particles that remain bonded, though the majority of bonds have been broken. No clear reverse offset fault structures are observable, as might be expected. The majority of the proximal section of the deposit retains its extensional character as discussed in Section 8.3.2.1. Similar observations are made as the location of the wall is progressively increased to 5.0 km though the distal compressional effects are gradually reduced as initial avalanche momentum is lost. Qualitatively, the percentage of the avalanche which is affected by the

barrier is minimal as compared to portion of the avalanche which retains its extensional character; the size of the affected area also decreases with increasing barrier distance. The vertical distance the avalanche travels up the barrier is seen to diminish significantly as the barrier is moved further away from the failure source (Figure 79). The fact that the overall heights obtained by the avalanche are greater when encountering the 25° barrier than when encountering the mirror slope is a reflection of the higher elevations of the 25° slope; horizontal runout distances are decreased as they are a function of horizontal barrier location. The avalanche likely does not reach greater heights upon encountering the 45° barrier because of the abrupt loss in energy upon encountering the steeper slope.

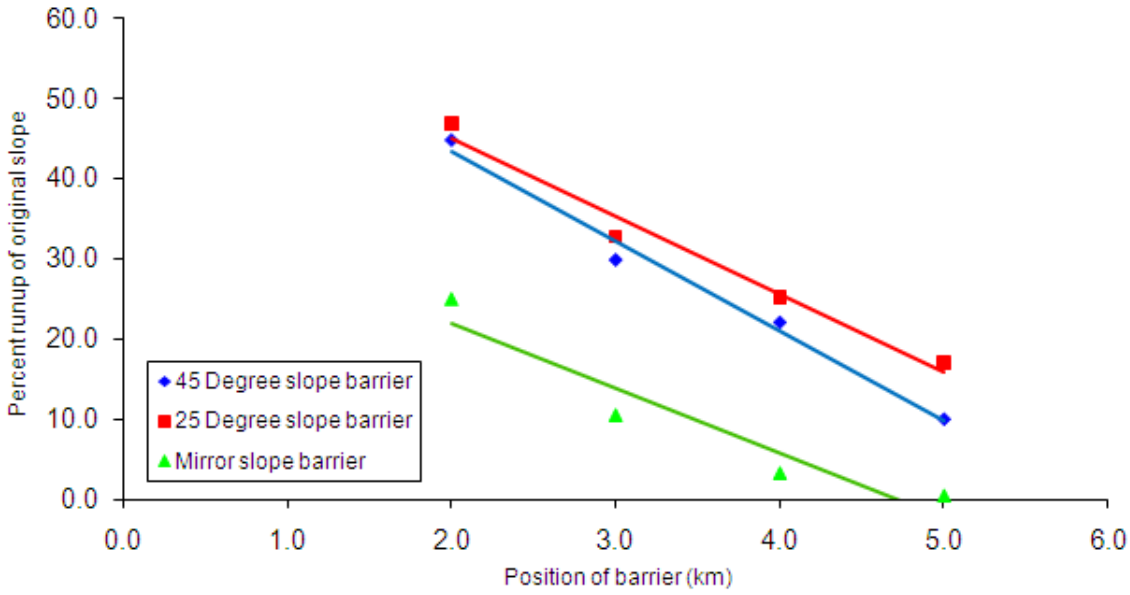

Figure 79 – Vertical distance in which the avalanche has travelled up the slope of the barrier, measured here by percentage of the initial failure slope height (800 m, which includes the vertical height of the initial slope and the vertical distance between the bottom of the initial slope and the lowest point of the runout basin).

Deformation of the avalanche body and associated stratigraphies is reduced as barrier slope angle is reduced to 25° and the mirror angle. Extensional morphology remains dominant throughout the majority of the failure body, particularly as the barrier is moved further away from the failure source. However, when the 25° barrier at a distance of 1.0 km is observed closely, a possible series of thrust stacks can be identified (Figure 80). These features are not observed in other simulations, however. As the barriers are moved further distally no significant deformation associated with possible compressional stress regimes is observed.

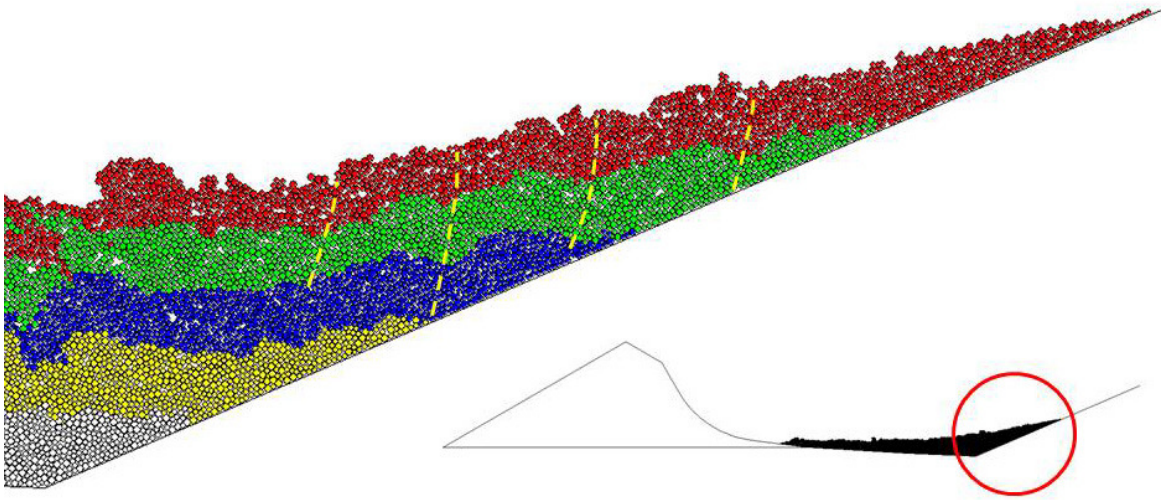

Figure 80 – Likely series of thrust fault structures (yellow dashed lines) observed in the distal section of simulation avalanche due to the encounter with the 25° barrier wall at 1.0 km (from the original slope toe). Notice slightly curved surface expressions which define the location of each thrust; similar surficial structures are observed in natural deposits as discussed in Chapter 5. Original cone height is 1,000 m; scale of zoom 1 cm ≈ 60 m.

Topographic influence was also considered by the addition of sinusoidal patterns to the runout surface (Figure 81). This approach is meant to consider generic irregular topography; the sinusoidal pattern loosely depicts hummocky or ridge-type topography, perhaps representing something similar to the morphology of a previously deposited VDA. The influence of a number of varying geometries was tested; specific dimensions were generally arbitrary but reasonably scaled (Table 18). As above, material properties were constant and identical to those presented in Section 8.3.2.1.

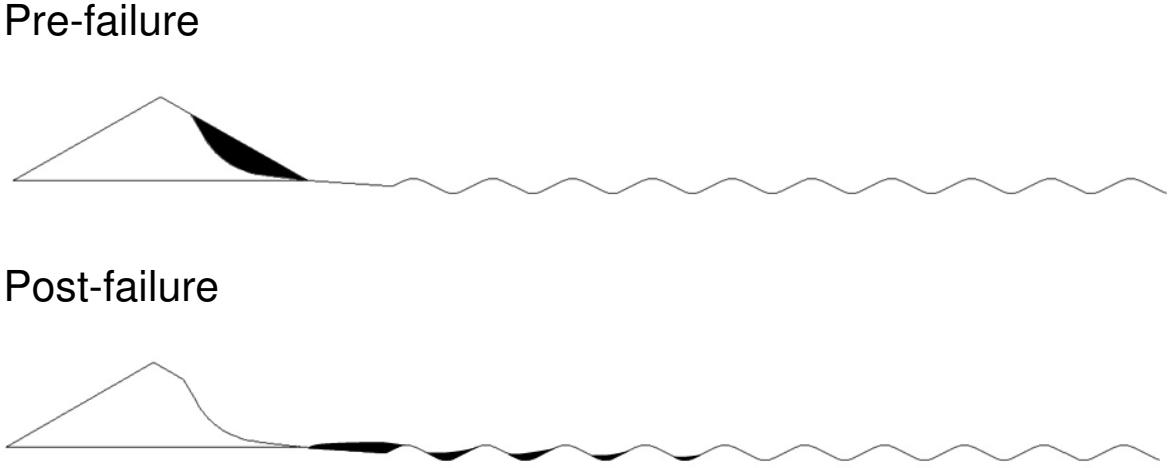

Figure 81 – Sinusoidal runout space pattern showing both a pre- and post-failure scenario where the failure material piled up into the proximal topographic basins. In this case wave patterns have a wavelength, λ, of 940 m and an amplitude, A, of 170 m. Full cone height is 1,000 m.

Table 18 – Sinusoidal wave topography scenarios considered.

Amplitude, A (m)	Wavelength, λ (m)	First motion
170.0	940.0	Up
170.0	940.0	Down
170.0	1880.0	Up
170.0	1880.0	Down
85.0	940.0	Up
85.0	940.0	Down
85.0	1880.0	Up
85.0	1880.0	Down

In total, variations in deposit feature evolution from case to case were minor and avalanche body deformation was generally consistent with extensional scenario discussed in Section 8.3.2.1. The most significant observation made during this exercise was the fact that extensional structures and morphology were generally retained even though irregular topography was encountered. Extensional structures consistent with those discussed in Section 8.3.2.1 (e.g., Figures 73 and 75), such as toreva/horst blocks and normally offset faults, were always retained in the proximal section of the failure (before the first instance of runout basin topography) and subsequent deposit as this section did not encounter topography itself. These structures were maintained in cases where the avalanche encountered subtle topography (low amplitude, high wavelength). In the cases where the failure met with more abrupt features (high amplitude, low wavelength), the majority of

structures/bonds were destroyed as the failure possessed enough energy to 'launch' over the topographic highs and become airborne to be deposited primarily on the opposite side of the adjacent basin. In these cases, however, stratigraphic relationships were still generally retained. The most significant differences between the simulations conducted here were distances travelled by each failure; failures which encountered steeper, more compact topographies (high amplitude, low wavelength) did not travel as those which encountered shallow, extended features (low amplitude, high wavelength). In most cases the avalanche did not extend past the fourth basin (sinusoidal low), where only a small fraction of particles were deposited.

8.4. Discussion

8.4.1. General Behaviour

The main observation concerning the behaviour of the bonded avalanche simulations in a purely extensional scenario is the development and evolution of the horst and graben model and the confirmation that this mechanism may work to create many of the characteristic deposit features observed (Voight *et al.*, 1981, 1983, 2002; Siebert, 1984; Glicken, 1991, 1998; Abele, 1997; Ponomareva, *et al.*, 1998; Belousov *et al.*, 1999; van Wyk de Vries *et al.*, 2001; Kelfoun *et al.*, 2008; Shea *et al.*, 2008). While this idea has been generally accepted for some time, and is indeed included in the general emplacement model discussed in Section 4.3.1, the DEM simulations allow better constraints on the timing and influence of this mechanism. Based on distal and proximal displacement and velocity of the avalanche body, emplacement of the simulated avalanche can be divided into two main periods (refer to Figure 82):

Frictional sliding (0-45 s) – The proximal and distal sections of the avalanche are moving at similar velocities though the distal section is accelerating at a slightly faster rate than the proximal section. This action works to extend the failure body but only to a small degree. Avalanche behaviour is characterized by frictional block sliding of mostly bonded material, brittle fracture of intact blocks and early stage fault propagation. Faulting which defines horst and graben morphology has for the most part initiated but has not developed to a significant degree. This period begins upon failure initiation and ends as the whole of the failure is beyond the initial failure scarp and in the runout area.

Extension (45-245 s) – The velocity of the proximal section of avalanche peaks sharply and begins a rapid decline but the distal section continues to accelerate, though at a decreasing rate. Deposition therefore progresses from proximal to distal, stretching the avalanche. Distal velocity plateaus and eventually decreases until deposition. The morphology of proximal toreva structures is defined and develops as the distal portion of the failure continues to extend, though in general toreva deposition occurs early in this stage. The majority of avalanche body extension occurs during this period, which is characterized mainly by disaggregation of the lower layers of the graben basins and minor but progressive block disaggregation. Faults which define the horst and graben system propagate from the upper surface downwards and progressively widen to incorporate adjacent areas. While this action is modelled here by interparticle bond breakage, in reality this may involve widening deformation or fault zones within mostly matrix material. Frictional sliding of bonded block material progressively becomes less prevalent. It is during this stage that a dynamic, fine-grained basal mobility layer might be most likely to progressively develop.

A

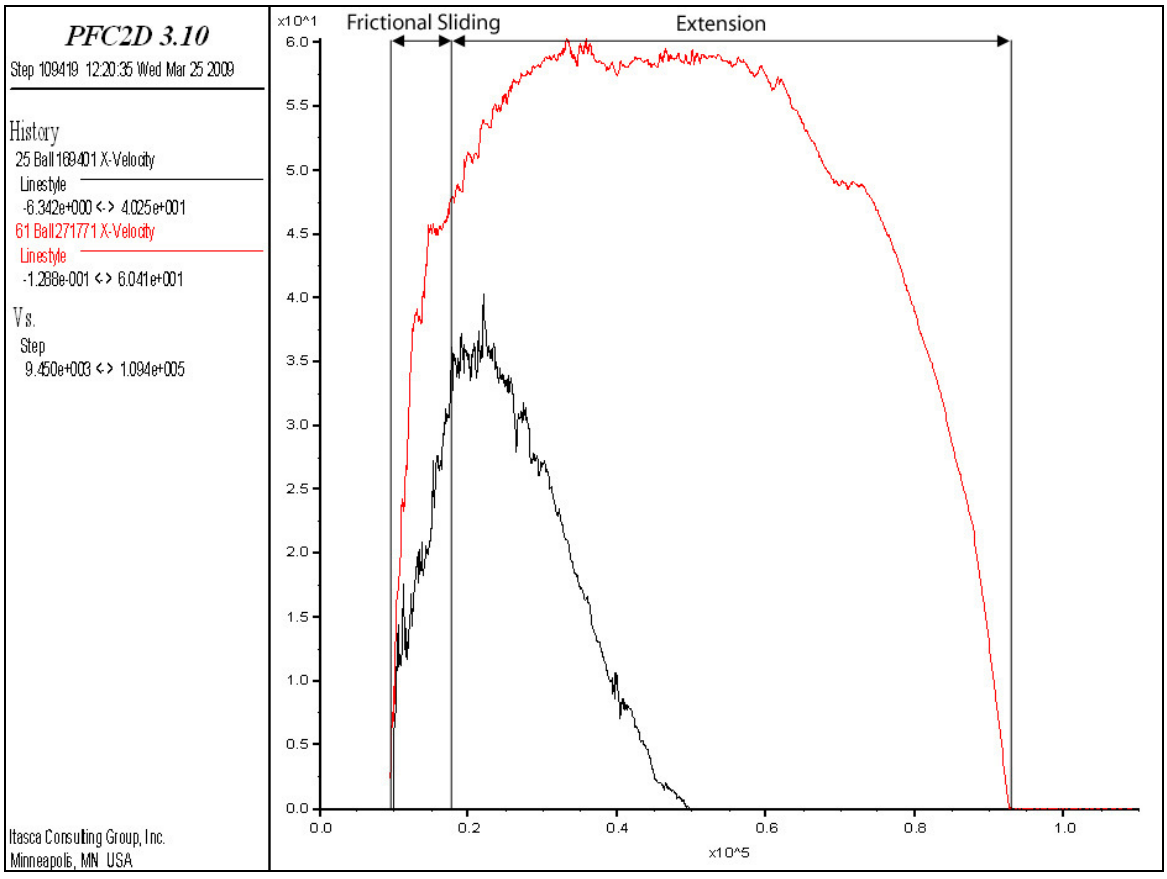

(Figure 82 continued on following page)

B

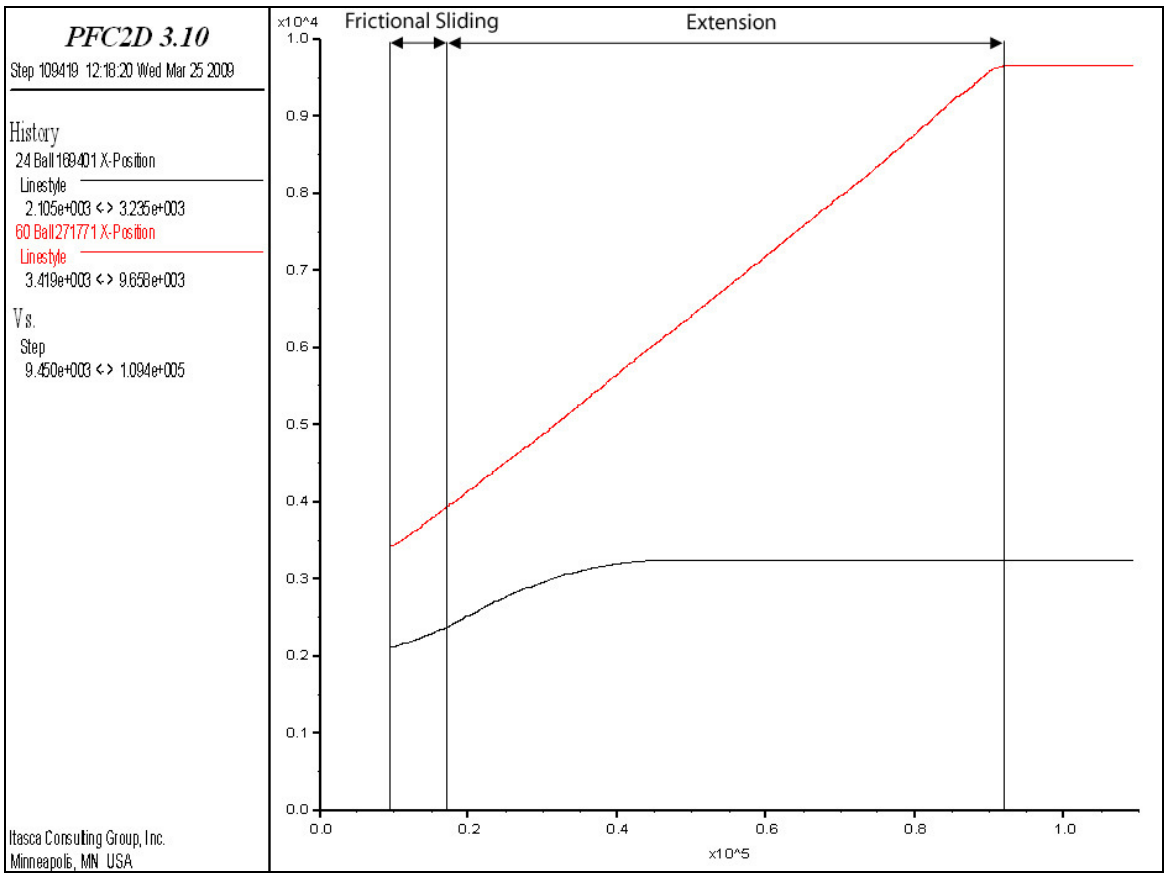

Figure 82 – Horizontal velocity (A) and displacement (B) of the avalanche head (black curve) and toe (red curve) from failure initiation to deposition. Ordinate units in m/s and m for velocity and displacement, respectively. Notice that model cycle number, rather than time, is plotted on the abscissa. Plot generated by *PFC*^{2D}.

Simulated avalanche behaviour is therefore consistent with the general emplacement model and VDA behaviour observed through digital orthophoto analysis (Sections 4.3 and 5.4, respectively), confirming both validity of the DEM model and the accuracy of the hypothesized behaviour. In the DEM simulation, the period of frictional sliding is brief in comparison with that dominated by extension, less than 20% of the total emplacement time. This figure would vary based upon failure surface and runout surface geometry and may be significantly less in nature. Additionally, the horizontal distance covered by the proximal section of the failure (i.e., toreva blocks) equals approximately 20% of the total deposit length ((1386 m/7292 m)*100 = 19%). This figure agrees with the emplacement behaviour zone characterized by frictional block sliding (Zone A) as discussed in Section 5.4, which covers the proximal 20%, on average, of the VDA deposits analysed. It can therefore be suggested that a process similar to that observed in the DEM simulations may be occurring during VDA emplacement and frictional block sliding is the main emplacement behaviour for the initial 20% of failure, in both space and time. Zone B

extensional behaviour, characterized by increased but progressive disaggregation of the initial failure mass and deposition of continuously smaller blocks, begins with the deposition of the toreva blocks in the DEM simulations at approximately 50 s. This zone represents the period of the most intense elongation of the avalanche body and begins only as the horst and graben structures develop and faults propagate through the full depth of the failure. This can be considered the beginning of avalanche 'flow' (Siebe *et al*., 1992). In a reality, this would represent a period of progressive matrix material formation, represented here by increased bond breakage to develop completely unbonded areas. Zone C progressive depositional behaviour discussed in Chapter 5 is represented in the extensional DEM simulation by the most distal portions of the particulate deposit which slowed due to momentum loss and increased basal friction influence. Surface blocks are generally smaller in dimension in this distal zone, which is small in proportion to the area represented by Zone B behaviour, a relationship also suggested in the orthophoto interpretations presented in Chapter 5. Matrix mobility associated with Zone C behaviour is difficult to simulate with the current DEM approach as individual particles are rigid (refer to discussion in Section 7.7).

The behaviour of the fault zones specifically has not been considered in detail here though this topic is thoroughly discussed by Morgan (1999), Morgan and Boettcher (1999) and Morgan (2004). Morgan and Boettcher (1999) highlight the effects of interparticle frictional coupling and resultant particle rolling on fault zone widening; a mechanism that is likely at play here. This mechanism also works to reduce the shear strength of the fault or fault zone. Restricting particle rolling may result in fault behaviour approaching real world values (Morgan, 2004). This approach was not investigated in detail here but provides a topic for future research. However, as in Chapter 7, a single bonded emplacement simulation was conducted where particle rolling was completely restricted in order to observe the effects of this mechanism on emplacement behaviour. Behaviour in this case was again markedly different from cases where rolling was uninhibited and unrealistic in the manner particle packing developed. Stress concentration did, however, result in fault propagation through emerging bond breakage though it was dissimilar from the horst and graben model discussed thus far. Completely restricting particle rolling therefore appears to be unrealistic, as established in Chapter 7; the true effects of this phenomenon remain a topic for future research.

Fault motion in the horst and graben scenario is exclusively normal. Top-down development of the initial faults is consistent with the hypotheses of Voight *et al*. (1983).

A listric geometry similar to that described qualitatively by Voight *et al.* (1983), Glicken (1991, 1998) and Wadge *et al.* (1995) is also observed. Faults coalesce and shallow to form broad graben basins separated by high-standing horst ridges with a steep-sided triangular geometry. Resulting morphology is thus remarkably similar to that of the Mount Shasta VDA deposit where a series of flow-perpendicular ridge systems are present throughout the proximal and medial areas of the deposit, separating closed basins of lower relief (Figures 13 and 14; Crandell *et al.* [1984], Crandell [1989]). Similar to this DEM simulation, the ridges are largest in the medial area of the deposit and display steep-sided triangular morphology. In the DEM model, this morphology is the result of the development of initial upper surface tensile fractures which evolve into large-scale normal faulting spreading away from the centre of the avalanche body as it extends. The similarities between the Mount Shasta and DEM simulation deposit morphologies may suggest similar emplacement behaviour for each case. Of the well-preserved deposits still present on the Earth's surface, the Mount Shasta VDA may indeed have possessed a behaviour most similar to the extensional two-dimensional case modelled here as it was confined along its axis length by parallel topographic highs, inhibiting lateral spreading but not to a significant degree as to considerably affect emplacement behaviour. Furthermore, it does not appear to have been significantly channelled or redirected.

8.4.2. Morphologic features

As the normal faults which define the graben basins join together, bonds along basal surface are broken to develop a reversely graded appearance throughout the full depth of the deposit. Reverse grading has been described at a number of VDA deposits (Schneider and Fisher, 1998; Belousov *et al.*, 1999; Takarada *et al.*, 1999; Reubi and Hernandez, 2000; Bernard *et al.*, 2008; Shea *et al.*, 2008) and in other DEM simulations (Tommasi *et al.*, 2005; Campbell *et al.*, 1995) and is consistent with a granular flow model shearing throughout its depth. The observations made here show that, though the *act* of reverse grading may not specifically be occurring, fault evolution downwards into the graben basins, and subsequent shallowing of those faults with emplacement distance may work to create a reverse grading appearance within a deposit. Similar mechanisms may be at work in natural scenarios. While overburden and runout surface interaction likely influence the development of the unbonded lower layer to some degree, fault evolution appears to be the primary mechanism for the formation of this layer in the DEM simulations and may suggest a degree of structural influence in the development of basal shearing layers in nature.

Arguably the most remarkable aspect of the DEM simulations is the development of the triangular, steep-sided, proximal structures; a morphology and position comparable to that of observed toreva blocks observed in natural VDA deposits (Figures 5 and 18, for instance). In the case of the DEM simulations, toreva morphology results from the initial shape of the failure mass and normal fault evolution in an extensional regime. Back-tilting is common to both natural cases and the simulated deposits. In the DEM simulations, the back-tilted appearance is a product of a high original position within the pre-failure slope where the blocks have slid into place along the listric failure surface relatively undisturbed. A similar mechanism has been suggested by Crandell *et al.* (1984), Crandell (1989), Wadge *et al.* (1995) and van Wyk de Vries *et al.* (2001). The basal area of the torevas is fractured only to a minor extent as they have been emplaced mainly through frictional sliding. These observations suggest a close comparison between toreva formation and the DEM simulations: original position high within the pre-failure slope, horst-type morphology formed through the development of bounding normal faults, and frictional sliding emplacement.

High toreva block position would result in a potential energy higher than the remainder of the avalanche body, though the blocks are deposited in the proximal section of the deposit. This phenomenon, where the toe of the slide travels the greatest distance though it has the least potential energy, was explored by van Wyk de Vries *et al.* (2001) and Shea *et al.* (2008) and explained by the explosive energy of the loaded substrate. A similar scenario, however, is observed in the DEM simulations: material at the toe of the original slope, with the least potential energy, travels the furthest and is found in the distal area of the simulation deposit. This behaviour was also inferred through orthophoto interpretation and may suggest that the relative positions of material in a deposit may be more dependent on their original positions within the edifice slope rather than pre-failure stresses.

Where the horst and graben extensional model may be responsible for the formation of toreva blocks and ridge-type structures, another mechanism of hummock-type feature formation is suggested by the blocks which remain on the surface of the simulated VDA deposit (Figure 73H2). Syn- or post-emplacement break-down of unstable blocks in VDAs may result in the conical hummock form often observed (Siebe *et al.*, 1992; Ponomareva *et al.*, 1998; Belousov *et al.*, 1999). The two hummock-feature types represented in the DEM simulations are similar to those suggested by Glicken (1998) where the toreva blocks represent A-type features and the surface blocks may represent B- and C-type hummocks. It should also be noted that, as discussed in Section 3.3.1., Strom (2006) suggests upper

surface tension as key hummock-forming mechanism, though in that case lower layer spreading was the primary cause of this tension. In this study, however, extension of the initial failure body geometry is the principal cause for upper surface tension. Nonetheless, the DEM simulations confirm that upper surface tension may be highly influential in VDA feature formation, whatever its source. This idea was also suggested by Voight *et al.* (1983).

A decrease in surface block size with distance is generally observed over the length of the simulation deposit. Due to the unrestricted extension of the distal half of the failure in the initial stages of emplacement, bond breakage and faulting occur in this area before taking place in the proximal section. Subsequently, extension is greater in this forward section and deformation has a longer period over which to disaggregate blocks, resulting in smaller blocks surface blocks with distance. This mechanism could also be at work in VDAs, suggesting that smaller block size with distance is a product of the *time* blocks have been subjected to deformation, not necessarily *how far* they have travelled. Distal sections of the avalanche experience extension and deformation earlier, and therefore longer, than proximal sections, resulting in smaller features. Block size decrease with emplacement distance is clearly visible in figures and plots presented in Chapter 5.

The addition of varying runout surface material properties and topographic features has also led to several interesting observations. Gaps of low friction appear to have a more significant influence on increasing avalanche runout than gaps of high friction do on decreasing runout (Figure 77, determined by that fact that the low friction gap trendline is a greater distance from runout value of the avalanche simulation with no variation in runout surface properties, 5.9 km, than the high friction gap trendline). In each case the behaviour of the avalanche, and therefore the character of the resultant deposit, are more affected by runout surface material property changes closer to the failure source rather than far into the runout basin. Additionally, the larger the gaps of varied properties are, the more effect they have on avalanche behaviour (Figure 77B). Encounters with high friction or more competent runout surface material can be regarded as compressional-type scenarios (Zone D) as they are observed here resulting in piling-up and internal fold-over structures. This can also be considered an upward aggradation-type deposition scenario as basal particles come to rest initially through basal frictional coupling. It can be imagined that thrust complexes would likely develop in relatively high strength matrix materials. In any case, it has been observed here that the properties of the basal runout area do have a significant influence on emplacement behaviour.

8.4.3. Effects of runout space variation

The most significant observation made with the addition of topographic barriers to the runout space is perhaps the overall *lack* of influence these structures have on influencing the character of deposit. This suggestion also holds true for the sinusoidal wave topographic simulations. Topography has been recognized as a primary factor in deposit morphology (Section 3.4.2); while topographic barriers do in most cases decrease the distance the simulation avalanche may travel, extensional structures remain dominant throughout the majority of the deposit as only a minor area immediately adjacent to the barrier is typically affected. This can also be observed in the emplacement behaviour zone maps presented in Chapter 5 by the relatively small proportion of Zone D compressional conditions in each map. These observations suggest that compressional stress regimes caused by topographic encounters are not efficiently transferred proximally throughout the moving avalanche mass and confirm the idea that compression influences structure formation only relatively locally, as was suggested in Section 5.4 based on the orthophoto interpretations. The fact that extensional structures predominate in both the avalanche simulations and kinematic maps of real world deposits, even though a particular failure may have encountered topographic variation, further confirms extension as the main emplacement behaviour. Furthermore, the general lack of structural variety observed from one DEM simulation to the next might also suggest that there are few variables which significantly affect deposit character, which mainly results from the general extensional deformation sequence of the failed slope and its material properties.

Clearly recognizable thrust structures are only present in one simulation. This may result from an inability of DEM to develop such features because of its discrete nature. Perhaps this type of structure requires a cohesive or yield strength material. On the other hand, the fact that the thrust stacks were only observed in the one scenario may hint that run-up angle plays a primary role in whether or not thrust faulting may develop. For instance, no such faulting was observed when the barrier angle was steeper or shallower than 25°; steeper angles may result in increased horizontal compression where clear reverse offset fault are not able to develop and shallower angles are still dominated by extensional stress regimes. Further sensitivity analyses on the influence of barrier angle are needed to confirm this hypothesis. An optimum barrier angle range for avalanche run-up is also suggested by Figure 79; if the angle is too steep the avalanche may be stopped abruptly, too shallow and significant compression does not develop in the first instance.

8.4.4. Final thoughts

The effects of initial material properties on emplacement behaviour and deposit products have frequently been mentioned throughout this thesis (Sections 3.4 and 7.6, for instance). In Section 4.2.9, attention was brought to Chile's Lastarria VDA, which was mainly composed of weak pumice fragments and therefore the deposit possesses no irregular topography such as conical hummocks or steep-sided hummock blocks (Naranjo and Francis, 1987). This contrasts with VDA events such as that at Jocotitlan, where the mechanical competence of the failure material has led to extraordinary steep deposit features. An additional example concerning the effects of material properties on emplacement behaviour can be observed at the Socompa VDA, which was comprised of a significant proportion of fine-grained, ductile basin sediments (RIF) and is observed to have significantly reflected off of a topographic high at the northwestern margin of the emplacement basin. Reflection in this manner is likely a direct product of the fluid nature of the ductile basement material involved in this VDA. The fact that significant topographic reflection to this degree is not commonly observed in VDA deposits may suggest that ductile material of this type and proportion are not commonly involved in VDAs, which may be mostly comprised of more competent, brittle source material (e.g., lava blocks). These examples provide first-order insight into the effects of material properties on deposit character. A further example on the effects of initial material properties on emplacement behaviour and deposit character can be drawn by comparing the topography created here in the bonded DEM simulations as opposed to the unbonded simulations discussed in Chapter 7, where no steep or irregular deposit topography was created. The influence of material strength can also be seen in the material calibration exercises discussed in Section 8.3.2, where the strongest bond strengths resulted in an unrealistically rigid failure and the weakest bond strengths resulted in a purely discrete granular material.

In Section 7.7 pseudo-stratigraphic layers of more or less competent material were introduced into the pre-failure mass to observe the effect they might have on emplacement behaviour and deposit morphology. A similar exercise was conducted with the bonded materials by introducing a single stratigraphic layer to the centre of the pre-failure slope and varying the bond strength of this layer up and down by factors of 2-5. The internal stratigraphic layer varied in thickness from 25-100 m. Additionally, alternating 25 m layers with increased and decreased bond strength were introduced. In each of these cases, however, realistic behaviour was generally not observed as competent layers commonly

remained as intact 'rafts' supported by weaker rapidly unbonding material. Though this behaviour may be comparable to real world scenarios to some degree, such as the large-scale raft blocks in the Socompa VDA (Kelfoun *et al.*, 2008), it is unknown how relatable it might be to a general case and therefore was not explored further in this study. This approach does, however, provide an interesting topic for future scrutiny, particularly if the intention were to model a specific collapse scenario or event.

However, the fact that a diverse range of structures such as toreva blocks, a reversely graded appearance and surface blocks have been formed from a pre-failure flank with homogeneous properties suggest that the spatial variation in flank material properties might not be as important in determining deposit features as the general structural evolution within the failing avalanche mass may be. Structural development, in turn, is dependent on stress evolution and subsequent deformation and brittle behaviour of a pre-failure mass with an initially listric geometry (i.e., the general deformation sequence discussed in previous chapters). A field example of this scenario might be regarded as the two flank collapse events of Mombacho as detailed by Shea *et al.* (2008), where differing triggering mechanisms are suggested for each episode though the final deposits possess similar macroscopic structure (Section 4.2.7). This hypothesis may, so some degree, negate deposit feature formation mechanisms such as the 'domain' idea of Clavero *et al.* (2002), where deposit feature morphology is thought to be defined exclusively by pre-failure discontinuities (Sections 4.2.6 and 5.3.5).

Chapter 9 - Conclusions

9.1. Summary

The investigation presented herein has provided valuable insight concerning the geomechanical behaviour of large-scale volcanic debris avalanches. As smaller non-volcanic rockslides are considered to behave in an essentially similar manner, the findings discussed here may also be applicable to those cases (Shea and van Wyk de Vries, 2008). Chapters 2-4 mainly represent literature review summaries, detailing the major features of VDA deposits and hypothesized geomechanical processes occurring during emplacement. Chapter 2 introduced volcanic edifice failure and the many factors that may play a role in initiating such events. The mechanisms by which an avalanche might achieve the long runout distances observed have also been discussed, namely granular and/or plug follow models. These mechanisms remain heavily debated in the literature; simulations conducted here may help future researchers to identify which processes might be most applicable to natural scenarios or those under question. DEM simulations are consistent with granular flow theories; plug-type systems are also observed in the simulations herein by the development of reversely graded appearance in the subsequent deposits. From these observations it can be concluded that one specific model may be insufficient in universally explaining complex VDA behaviour. Indeed, singular modes of emplacement, whether they are granular, plug-type or another type of hypothesized behaviour, are likely only local and/or time-dependent phenomenon (i.e., highly variable both spatially and throughout the duration of emplacement). Chapter 3 recognized the major features that are characteristic of VDA deposits: distinct sedimentary facies, hummocky topography, toreva blocks, closed depressions and steep margins. The morphology and spatial variation of these features have been recognized as key indicators of VDA emplacement behaviour. Furthermore, the major factors that might affect emplacement behaviour and the morphology and distribution of characteristic deposit features have been recognised and discussed: initial material properties, water content and runout space topography.

Chapter 4 introduced the hypothesis that, as initial failure geometries are generally similar and a particular suite of features is common observed in VDA deposits, a universal deformational sequence likely occurs during emplacement that is responsible for the development of commonly observed deposit morphologies. The hypothesized geomechanical behaviour of VDA events worldwide, generally representing the extent of the literature on VDA geomechanics, was then summarized. Specific focus was given to

major processes occurring throughout emplacement evolution and mechanisms which may have formed characteristic deposit features. The common themes from these descriptions were then combined with emplacement theories of previous authors to develop a general emplacement model, which considers the full geomechanical evolution of a VDA from failure initiation to deposition. This model is generally applicable to all cases and is briefly described by early frictional block sliding with associated rock mass fracture and dilation, normal faulting developing into a horst and graben extensional system, progressive deposition of larger block material and development of matrix material though disaggregation and entrainment. In general, emplacement motion can be described as relatively laminar and organized as the initial failure body spreads into a thin sheet from proximal to distal, retaining original stratigraphic relationships. The general model emplacement sequence can also be separated into several stages, each distinguished by the varying deformation and stress regimes an avalanche might experience and time-/space-dependent variations in the proportions of material constituents. Based on the concept that deposit features are products of their geomechanical environments (i.e., kinematic indicators), a general system whereby the various stages of emplacement behaviour might be recognized by the major features observed at deposit scale was introduced. Thus, zones of distinct morphologic character on a deposit's surface might be used to develop insight into the general geomechanical conditions occurring in a certain area of the failure or at a certain time of emplacement. In total, the emplacement behaviour zones represent the complete evolution of a VDA from the instance of failure until deposition.

In Chapter 5, high resolution orthoimagery was analyzed to test the general emplacement model and behaviour zonation system put forward in the Chapter 4. Surface features such as hummocks and torevas were mapped and quantified by determining the length and orientation of their major axes in relation to their location in the deposit. A reduction in feature size with distance has been observed. A transition from flow-perpendicular linear features to conical and/or flow-parallel features was also observed. Based mainly on literature interpretations, structural features such as folds and faults were also mapped on the orthophoto imagery. The main observation from this exercise was the recognition that extensional features such as normal faulting and flow-parallel lineations are prevalent throughout VDA deposits whereas compressional features such as folds and thrust fault complexes are found only near deposit edges and/or where topographic highs are encountered, indicating extension is the dominant emplacement process in all cases. In total, the observations made through the deposit mapping exercise were generally consistent with the general emplacement model and associated emplacement behaviour

zones introduced in Chapter 4. Separation of the deposits into the emplacement behaviour zones allowed for tangible observation of the various stages of VDA emplacement. Furthermore, general consistency between cases was observed, which supports the hypothesis that a common deformational sequence is highly influential in developing characteristic VDA deposit morphology.

Chapter 6 introduced DEM as a numerical tool with which to investigate the hypothesized emplacement behaviours discussed in Chapters 4 and 5 and develop new insight into the evolving geomechanical character of VDAs. Relevant previous studies, the numerical operation of the chosen code (PFC^{2D}), calibration methodology and the general limitations of this approach were summarized in this chapter. In total, the DEM method has been established as a valuable method for the analysis of complex geomechanical systems and therefore suitable for the purposes of this study. Chapter 7 built upon this introduction to DEM by developing an initial VDA simulation model to gain an understanding of both code operation and simple (i.e., unbonded) avalanche emplacement mechanics. A number of quantitative and qualitative observations were successfully recorded. The effects of frictional properties on deposit morphology are evident; boundary friction (μ_w) affects the system to a larger degree than does constituent particulate friction (μ_p). Mechanical analysis of the avalanche system has shown that the initial stages of failure are chaotic in terms of stresses and strains occurring within the failure; a likely period of increased block fragmentation. Velocity, and therefore kinetic energy, is highest as the avalanche approaches the transition to the horizontal runout surface, whereby the failure settles into a generally steady and organized flow as velocity steadily decreases until deposition. The transition to horizontal motion therefore represents a key moment during emplacement as stress fields must readjust to accommodate this change, promoting block/rock mass fragmentation. Based on observations made during field studies of large-scale volcanic debris avalanche deposits, several authors have also concluded that the changing stress regime associated with this transition is influential in promoting block fragmentation (Ui *et al.*, 1986; Shea *et al.*, 2008). Energy measurements have verified several intuitive assumptions and confirmed that avalanche deposition is generated by its encounter with the horizontal runout surface. In addition to early stages of increased and rapidly fluctuating stresses, measurements reveal that stresses are highest in the lower proximal regions of the failure, a region where particle and block fragmentation and deformation may likely occur. The stresses and displacements observed quantify the degree to which the toe and free surface of the failure are relatively unrestricted as compared to lower and interior sections of the avalanche. This is important for two reasons. First, an unhindered toe, or avalanche

front, facilitates stretching and thinning of the avalanche body, allowing it to attain a higher energy and promoting long runout. Secondly, lack of stress at the top of the failure, or in the latter stages of emplacement in general, may help to preserve angular surface or jigsaw fractured blocks often found in large avalanche deposits, therefore explaining their presence (Campbell *et al.*, 1995). Experiments have shown that a degree of strain is created within the avalanche body due to the contradicting effects of the restricting basal surface and the free upper surface. Accordingly, increased deformation has been recognized in this interior region of these simulations through layer deformation analysis. These observations may be the result of an inability of the model particles to fragment under high stresses/strains but may also highlight the importance of constituent material properties on avalanche emplacement characteristics. If model particles were able to replicate weak natural materials in terms fragmentation, for instance, a basal shearing layer may develop which would influence both mobility and deposit features. Also, time-dependent global strain observations indicate the large-scale granular failure may perhaps travel in a pulsing motion as friction is locally and continually overcome. Original stratigraphic relationships are retained upon deposition though individual layers have been drastically thinned and stretched, the top layers more so than those on the bottom. This phenomenon was also observed in DEM experiments of Campbell *et al.* (1995) and is significant as the retention of original stratigraphic relationships is often observed in the deposits of large-scale rock and debris avalanches (Siebert, 1984; Schneider and Fisher, 1998; Clavero *et al.*, 2002; Shea *et al.*, 2008). Thus, the collective motion of the DEM simulation illustrates how large-scale avalanches may spread out in an organized fashion from the base of the failure source. Macroscopic deformation of the avalanche body shifts from left- to right-lateral at a point in the proximal to medial section of the failure where the deposit is thickest. Proximally from this point the granular material appears to 'fall back' on itself while distally the material cascades off the pile, extending the avalanche in a right-lateral sense. This change in behaviour develops as the avalanches encounters the transition to the horizontal runout surface.

While the initial unbonded simulations proved valuable in developing further understanding of avalanche emplacement mechanics, they were limited in their capacity to develop characteristic debris avalanche topography such as hummocks and steep margins. The unbonded simulations also lacked the ability to consider realistic situations such as particle and block fragmentation and effects these processes have on emplacement mechanics and deposit features. As these processes are considered a fundamental aspect of large-scale avalanche emplacement, particle bonding was explored in Chapter 8. Material

calibration exercises were first conducted in order to ensure the bonded particulate assembly behaved in a manner representative of real world materials when subjected to stress. This was done with modification to the GCVM scheme of del Potro and Hürlimann (2008) in an effort to consider the wide range of material properties that may be present in a volcanic slope. A new initial model then had to be created to guarantee the material calibration measures remained sound and realistic initial lithostatic stresses were considered. These efforts resulted in a calibrated model at equilibrium with a realistic initial stress field. When subjected to further body forces (i.e., gravity), cones with the weakest material properties failed in a realistic lateral spreading and retrogressive manner, indicating both a validation of the modelling techniques and constraints on the material properties controlling failure. In order to consider failure emplacement exclusively, however, a listric failure surface was 'carved out' of the initial calibrated cone at equilibrium.

The manner in which emplacement of the bonded avalanche evolves is consistent with the general emplacement model put forward in Section 4.3, thus defining a deformational sequence perhaps common to the majority of large-scale VDA events. Specifically, the DEM model confirms the development of the initial block sliding and horst and graben models and the development of characteristic deposit features from these evolving mechanisms. While these ideas had been hypothesized previously, both in the literature and Chapters 4 and 5, the numerical approach used here has allowed for constraints to be placed on the timing and precise mechanisms of emplacement evolutions and characteristic feature formation. For instance, block sliding is seen to occur for approximately the initial 20% of emplacement, both in terms of emplacement time and distance covered. While fracturing and associated bulking likely occur in real world scenarios, these processes are not apparent in the DEM model due to the circular shape of the constituent particles. However, the manner in which macroscopic stresses develop is similar. During initial block sliding, tension created in the upper free surface through deformation of the listric failure geometry leads to propagation of top-down distal-facing normal faults to accommodate increasing extension. As the failure moves away from a block sliding mechanism to an extending mass characterized by increasing differential movement of constituent particles, normal faults develop into a classic horst and graben system. The triangular horst structures deposit and decrease in dimension progressively with distance, coming to rest mainly in the proximal and medial sections of the deposit. Inter-toreva basins (i.e., grabens) and distal areas are characterized by rounded blocks retained on the deposit surface which have developed due to the lack of stress in this area as bond

breakage (i.e., stress concentrations) tends to propagate downward then along the lower section of the basin. Surface blocks can be regarded as hummock features which may develop a conical form upon post-deposition erosion. It can therefore be suggested that the location and morphology of torevas and hummocks are the product of the propagation of stress concentrations and the subsequent development of discontinuities due to initial failure surface shape and progressive extension of this mass during emplacement. In general, toreva location/morphology is defined by discontinuities which develop relatively early in emplacement. Back-tilted toreva structures in the DEM simulations are consistent with field observations, suggesting the most likely point of origin for these structures is high in the failure slope. According to the DEM model, their emplacement is likely concurrent with the rest of the failure, though relatively likely early during emplacement as deposition progresses from proximal to distal. Where torevas are developed from the propagation of initial normal faults, hummocks in this case form by preservation of surface blocks as faults coalesce in lower basin areas in latter stages. Two separate mechanisms have therefore been defined for toreva and hummock development. Reversely graded deposits over their full depth deposit are consistent with granular flow models (Section 2.4). Therefore, formation of characteristic deposit features through the granular flow simulations considered here indicate this may be the dominant emplacement process, whether or not an associated 'plug' may develop, which is likely more of a local phenomenon (e.g., Glicken [1998]). Additionally, initial stratigraphies are preserved throughout the deposit, though stretched thinly. This and other observations indicate extension is the dominant emplacement process and occurs in an organized and laminar fashion. Simulations have also shown that the character of a deposit is for the most part only locally affected by variations in runout basin topography and extensional behaviour remains dominant throughout the majority of a given VDA, supporting the idea that a common extensional deformational sequence is the most influential control on deposit morphology. Again, this deformation sequence was defined by the general emplacement model and bonded DEM avalanche simulations discussed Sections 4.3 and 8.3, respectively.

In total, there is good agreement between the numerical models and VDAs, indicating the validity of DEM modelling and its ability to capture realistic geomechanical processes. Furthermore, the main objective of this study, to develop further insight into VDA emplacement geomechanics using this innovative numerical modelling technique, has been accomplished. As mentioned in the main introduction to this thesis, an additional objective of this study was to consider the feasibility of DEM, and PFC^{2D} specifically, for modelling

the problem in question: large-scale debris avalanche emplacement geomechanics. The performance of the technique can be judged by its ability to simulate a number of the key elements of emplacement mechanics which have been discussed throughout this paper, including development of the characteristic deposit features outlined in Chapter 3 and the major elements of the general emplacement model detailed in Section 4.3. As indicated by Table 19, DEM has the ability to consider the majority of the important aspects involved in VDA emplacement, including the major factors identified as having significant influence on emplacement behaviour and deposit morphology: material properties, saturation level and topographic interaction (Section 3.4). Each of these factors has been considered in detail here with the exception of saturation level, which provides an interesting topic for future research. Topographic features have in this case been seen to have only a relatively local influence on emplacement evolution and deposit character. Overall, the capability of DEM has for considering the progressive disaggregation of brittle material over long distances, based on evolving stresses throughout the failure body, is its key strength. The influence of factors not necessarily considered here, such as fluid interaction and particle comminution, may be easily incorporated into future studies through user-defined functions. Overlooking these factors in the current study may indicate their relatively minor influence in emplacement mechanics and the development of characteristic deposit features; macroscopic stress evolution and resultant discontinuity propagation appears to be the most important elements. In any case, the simulations discussed herein should be regarded as first-order approximations of real world events; they nonetheless show how it is likely these fundamental mechanisms which are the most influential factors in determining debris avalanche emplacement behaviour and deposit character.

Table 19 – Emplacement elements which DEM does or does not have the ability to simulate. Internal deformation has been captured in the current study in that some deformation of original stratigraphy was observed, though truly dynamic deformation such as clastic dike propagation and fluid interactions were not. Basal shearing layer development in this study was observed to be a structural phenomenon formed though the propagation of faults, not material communition or basin sediment entrainment.

Factors needed to be considered	Ability of DEM to consider factor 'off-the-shelf'	Ability of DEM to consider factor 'with modification	Factors needed to be considered	Ability of DEM to consider factor 'off-the-shelf'	Ability of DEM to consider factor with modification
Empirical runout relationships	Yes		Topographic control	Yes	
Block and matrix facies development	Yes		Stratigraphic layer development and/or retention	Yes	
Hummock develoment	Yes		Block disaggregation	Yes	
Toreva block development	Yes		Fault development	Yes	
Closed depression development	No[a]		Dilation/bulking		Yes[b]
Levees and margins	No[a]		Particle comminution		Yes[c]
Internal deformation structures	No		Basal shearing layer development		Yes[d]
Fluid/gas interaction		Yes	Basin sediment entraiment		Yes

[a]3D issue

[b]Likely possible with a particle cluster model

[c]Can likely be developed with user-written functions

[d]'Fine-grained' basal shearing layers may develop by adding a particle comminution mechanism

9.2. Future work

This study represents a first attempt to investigate the development of structure and characteristic deposit features of VDAs using a numerical model and has been successful in developing new and original insight in these areas. However, the true success of the study may lie in the number of ideas for future work which have developed from it.

In regards to the specific exercises conducted herein, a number of topics beyond the scope of this current project are worth examining further. One such topic is particle rolling and the influence this mechanism has on material calibration, local fault and macroscopic emplacement behaviour. As discussed in Section 6.2, restricting particle rolling results in a

failure envelope more representative of actual laboratory values, and therefore, a more realistically calibrated material. On a fault behaviour scale, Morgan (2004) notes that restricting particle rolling results in fault behaviour more like that observed. When macroscopic avalanche emplacement mechanics are considered, it has been observed here that emplacement evolves in a markedly different fashion if particle rolling is completely restricted (unrealistically in each case). A thorough investigation of this phenomenon is needed in order to fully characterize the influence of particle rolling on macroscopic behaviour. Perhaps sensitivity analyses on the influence of μ_p and μ_w values may be the best way forward. The onset of rolling as a function wall stiffness values may also be an appropriate approach for future research (A. Preh, personal communication, 2009). Particle clustering, which creates irregular shapes, may be an additional approach to future modelling.

Another interesting topic for future research concerns the sinusoidal behaviour of avalanche body strain as recognized in Chapter 7. Strain energy in PFC^{2D} is dependent on particle stiffness values. Therefore, sensitivity analyses on this behaviour may shed light on the true meaning of this phenomenon, including how this mechanism might or might not relate to the emplacement behaviour of natural avalanches (e.g., association with a pulsating form of avalanche motion). Also, as discussed in Section 6.3.5, the behaviour of a bonded particle assembly is dependent on the ratio of bond normal to shear strength as it dictates whether bonds will fail in a brittle or ductile manner (Itasca, 2004c; Preh and Poisel, 2006). In this study, this ratio was held constant at unity for each emplacement simulation discussed. A limited sensitivity analysis was conducted where the bond normal/shear strength ratio was varied from 0.1-10, though no noticeable effects on subsequent avalanche emplacement behaviour were observed. However, in the DEM slope stability analyses of Preh and Poisel (2006), a significant change in emplacement behaviour was observed when this ratio was varied. Further work is therefore necessary to understand the true effects of this ratio on macroscopic behaviour, and in this case, why a noticeable change was not observed. Evaluation of additional forms of energy potentially created by VDAs, such as heat and seismic/acoustic energy may also be interesting topic for future research.

Concerning volcanic collapse scenarios specifically, investigation of the dependency of emplacement mechanics on initial slope size and geometry may be an interesting topic for future research. The initial failure geometry considered here is based on a stereotypical listric failure similar to those observed in nature; overall geometry in this case is similar in

proportion to the first slide block of the retrogressive sequence at Mount St. Helens. Larger collapse scenarios, perhaps developing from a retrogressive sequence, are commonly observed in nature (Siebert, 1984). These scenarios were briefly considered here by running larger collapse models 'carved' from the initial calibrated cone. In these cases, structural evolution and failure mass evolution proceeded in a similar manner to that discussed throughout this thesis, supporting the idea that common structural evolution processes are the key factor in determining emplacement mechanics and subsequent deposit characteristics. As larger failures involve greater numbers of particles, which significantly increases simulation run-time, a full investigation of failure size influence was not conducted here. Considering retrogressive scenarios specifically may be an additional topic for future research.

DEM may also be used to consider more complex issues possibly significant in volcanic collapse scenarios, such as fluid and gas interactions, blast effects, and rigid particle fragmentation. While *PFC* currently possesses a limited fluid coupling model, each of these aspects would require significant modifications to the original code and/or use of user defined functions. Because of the intensive code work required, these aspects were not considered here.

One of the key limitations of this study has been the exclusive use of the two-dimensional DEM code. While this approach allowed for the development of significant insight into avalanche behaviour, it is recognized that avalanche emplacement is a three-dimensional problem. Thus, three-dimensional investigations are a natural next step for avalanche emplacement research, which will allow out-of-plane processes to be considered. Three-dimensional simulations will also allow further speculation on the development of characteristic deposit features such as closed depressions, steep lateral margins and the spatial distribution of block and matrix facies, hummocks and torevas. Furthermore, realistic topography may be considered in more detail in three dimensions, allowing topographic controls on emplacement behaviour to be investigated further (Poisel and Preh [2008], for instance).

This study has demonstrated the ability of DEM for modelling the evolution of slope processes, which can be applied to catastrophic scenarios as done here or general instability determination problems. The methods discussed herein might be considered for specific instability cases in future studies, which is not limited to volcanic or even subaerial/terrestrial environments. For instance, the structure of offshore landslide

complexes, for which an understanding is crucial for the hydrocarbon industry, might be investigated further with minor modifications to the approach discussed herein (Hesthammer and Fossen, 1999; Prather, 2003; Welbon *et al*., 2007; Bull *et al*., 2008). The internal structures of these complexes, often determined through three-dimensional seismic interpretations, are remarkably similar to those created with the DEM model in this study, and therefore, DEM may be a valuable tool with which to interpret both the evolution of these complexes and the factors that control current stability. On a wider scope, it can be suggested that the ability of DEM to simulate large-scale geomechanical processes is not limited to slope processes but may be applied to a number of scenarios, such as structural geology or tectonic problems. In summary, DEM has proven to be a very valuable tool here and can be used to develop insight into any number of geomechanical problems from micro- to macroscopic scales.

References

Abele, G., 1997. Rockslide movement supported by the mobilisation of groundwater-saturated valley floor sediments. *Zeitschrift fur geomorphologie*, 41, 1-20.

Abrams, M., 2000. ASTER: Data products for the high spatial resolution imager on NASA's Terra platform. *International journal of Remote Sensing*, 21, 847-853.

Alloway, B., McComb, P., Neall, V., Vucetich, C., Gibb, J., Sherburn, S., Stirling, M., 2005. Stratigraphy, age, and correlation of voluminous debris-avalanche events from an ancestral Egmont Volcano: implications for coastal plain construction and regional hazard assessment. *Journal of the Royal Society of New Zealand*, 35, 229-267.

Anders, M.H., Aharonov, E., Walsh, J.J., 2000. Stratified granular media beneath large slide blocks: Implications for mode of emplacement. *Geology*, 28, 971-974.

Azzoni, A., de Freitas, M.H., 1995. Experimentally gained parameters, decisive for rock fall analysis. *Rock mechanics and rock engineering*, 28, 111-124.

Bagnold, R.A., 1954. Experiments on a gravity-free dispersion of large solid spheres in a Newtonian fluid under shear. *Proceedings of the Royal Society of London*, *Series A*, *Mathematical and Physical Sciences*, 225, 49-63.

Barla, G., Barla, M., 2001. Investigation and the modelling of the Brevna Glacier rock avalanche on the Mont Blanc range. *Eurorock* 2001, 35-40.

Beget, J. E., Kienle, J., 1992. Cyclic formation of debris avalanches at Mount St. Augustine volcano. *Nature*, 356, 701-704.

Belousov, A., 1996. Deposits from the 30 March 1956 directed blast at Bezymianny volcano, Kamchatka, Russia. *Bulletin of Volcanology*, 57, 649-662.

Belousov, A., Belousova, M., Voight, B., 1999. Multiple edifice failures, debris avalanches and associated eruptions in the Holocene history of Shiveluch volcano, Kamchatka, Russia. *Bulletin of Volcanology*, 61, 324-342.

Bernard, B., van Wyk de Vries, B., Barba, D., Leyrit, H., Robin, C., Alcaraz, S., Samaniego, P., 2008. The Chimborazo sector collapse and debris avalanche: Deposit characteristics as evidence of emplacement mechanisms. *Journal of Volcanology and Geothermal Research*, 176, 36-43.

Boudal, C., Robin, C., 1989. Volcan Popocatepetl: Recent eruptive history and potential hazards and risks in future eruptions. *Volcanic hazards*, *IAVCEI Proceedings in Volcanology*, Berlin and Heidelberg: Springer, 1, 110-128.

Bull, S., Cartwright, J., Huuse, M., 2008. A review of kinematic indicators from mass transport complexes using 3D seismic data. *Marine and Petroleum Geology*, doi:10.1016/j.marpetgeo.2008.09.011.

Calvetti, F., Crosta, G., Tatarella, M., 2000. Numerical simulation of dry granular flows: from the reproduction of small-scale experiments to the prediction of rock avalanches. *Rivista Italiano di Geotechnica*, 21, 21-38.

Campbell, C.S., 1989. Self-lubrication for long runout landslides. *Journal of Geology*, 97, 653-665.

Campbell, C.S., 1990. Rapid granular flows. *Annual Review of Fluid Mechanics*, 22, 57-92.

Campbell, C.S., Cleary, P.W., Hopkins, M., 1995. Large-scale landslide simulations: global deformation, velocities and basal friction. *Journal of Geophysical Research*, 100, 8267-8273.

Capra, L., Macias, J.L., Scott, K.M., Abrams, M., Garduno-Monroy, V.H., 2002. Debris avalanches and debris flows transformed from collapses in the Trans-Mexican Volcanic Belt, Mexico - behavior, and implications for hazard assessment. *Journal of Volcanology and Geothermal Research*, 113, 81-110.

Carrasco-Núñez, G., Díaz-Castellón, R., Siebert, L., Hubbard, B., Sheridan, M.F., Rodríguez, R., 2006. Multiple edifice-collapse events in the Eastern Mexican Volcanic Belt: The role of sloping substrate and implications for hazard assessment. *Journal of Volcanology and Geothermal Research*, 158, 151-176.

CaSIL, 2008, *California Spatial Information Library*. Available from: http://www.atlas.ca.gov/ [accessed November, 2008].

Clavero, J.E., Sparks, R.S.J., Huppert, H.A., 2002. Geological constraints on the emplacement mechanism of the Parinacota debris avalanche, northern Chile. *Bulletin of Volcanology*, 64, 40-54.

Clavero, J.E., Polanco, E., Godoy, E., Aguilar, G., Sparks, R.S.J., van Wyk de Vries, B., Pérez de Arce, C., Matthews, S., 2004. Substrata influence in the transport and emplacement mechanism of the Ollagüe debris avalanche (Northern Chile). *Acta Vulcanologica*, 16, 59-76.

Cleary, P.W., Campbell, C.S., 1993. Self-lubrication for long runout landslides: Examination by computer simulation. *Journal of Geophysical Research*, 98, 21911-21924.

Cleary, P.W., Mériaux, C., Owen, P.J., 2007. Prediction of quasi-static fall of planar granular columns using 2D discrete element modeling. *CD Proceedings of the Fourth International Conference on Discrete Element Methods*, *27-29 August*, *Brisbane*, *Australia*, Minerals Engineering International, 12 pp.

Coduto, D.P., 1999. *Geotechnical engineering: principles and practices*. Upper Saddle River, New Jersey: Prentice Hall.

Collins, G.S., Melosh, H.J., 2003. Acoustic fluidization and the extraordinary mobility of sturzstroms. *Journal of Geophysical Research*, 108, 1-14.

Crandell, 1989. Gigantic debris-avalanche of Pleistocene age from ancestral Mount Shasta volcano, California, and debris avalanche hazard zonation. *Bulletin of the US Geological Survey*, 1861, 32 pp.

Crandell, D.R., Miller, C.D., Glicken, H.X., Christiansen, R.L., Newall, C.G., 1984. Catastrophic debris avalanche from from ancestral Mount Shasta volcano, California. *Geology*, 12, 143-146.

Crosta, G., Calvetti, F., Imposimato, S., Roddeman, D., Frattini, P., Agliardi, F., 2001. *Granular flows and numerical modelling of landslides*. Universita di Milano, available from: http://damocles.irpi.pg.cnr.it/docs/reports/Granular_Flows_Thematic_Report.pdf [Accessed 30 November 2006].

Crosta, G.B., Imposimato, S., Roddeman, D.G., 2003. Numerical modelling of large landslides stability and runout. *Natural Hazards and Earth Systems Sciences*, 3, 523-538.

Cundall, P.A., 1971. A computer model for simulating progressive large scale movements in blocky rock systems. *Proceedings of the Symposium of the International Society of Rock Mechanics*, *Nancy*, *France*, 1, paper no. II-8.

Cundall, P.A., Strack, O.D.L., 1979. A discrete numerical model for granular assemblies. *Geotechnique*, 29, 47-65.

Cundall, P.A., Hart, R., 1992. Numerical modelling of discontinua. *Journal of Engineering Computations*, 9, 101-113.

Dade, W.B., Huppert, H.E., 1998. Long runout rockfall. *Geology*, 26, 803-806.

Davies, T.R.H., 1982. Spreading of rock avalanche debris by mechanical fluidization. *Rock Mechanics*, 15, 9-24.

Davies, T.R.H., McSaveney, M.J., 1999. Runout of dry granular avalanches. *Canadian Geotechnical Journal*, 36, 313-320.

Davies, T.R.H., McSaveney, M.J., 2002. Dynamic simulation of the motion of fragmenting rock avalanches. *Canadian Geotechnical Journal*, 36, 313-320.

Davies, T.R.H., McSaveney, M.J., Beetham, R.D., 2006. Rapid block glides: slide-surface fragmentation in New Zealand's Waikaremoana landslide. *Quarterly Journal of Engineering Geology and Hydrogeology*, 39, 115-129.

Davies, T.R.H., McSaveney, M.J., 2008. The role of rock fragmentation in the motion of large landslides. *Engineering Geology*, doi: 1016/j.enggeo.2008.11.004.

Day, S.J., 1996. Hydrothermal pore-fluid and the stability of porous, permeable volcanoes. *In*: McGuire, W.J., Jones, A.P., Neuberg, J., eds. *Volcano Stability on the Earth and Other Planets, Geological Society Special Publication*, 110, 77-94.

Day, S.J., Carracedo, J.C., Guillou, H., and Gravestock, P., 1999. Recent structural evolution of the Cumbre Vieja volcano, La Palma, Canary Islands: volcanic rift zone reconfiguration as a precursor to volcano flank instability? *Journal of Volcanology and Geothermal Research*, 94, 135-167.

del Potro, R., Hürlimann, M., 2008. Geotechnical classification and characterisation of materials for stability analyses of large volcanic slopes. *Engineering Geology*, 98, 1-17.

Deluzarche, R.B., Dedecker, F., Fry, J.J., 2003. Static and dynamic analysis of stability of rocky slopes via particle methods. *In*: Konietzky, H., ed. *Numerical Modelling in Micromechanics via Particle Methods, Proceedings of the 1st International PFC Symposium, Gelsenkirchen, Germany, 6-8 November 2002*, Lisse: Balkema, p. 125-131.

Drake, T.G., 1990. Structural features in granular flows. *Journal of Geophysical Research*, 59, 8681-8696.

Ellsworth, D., Voight, B., 1996. Evaluation of volcano flank stability triggered by dike intrusion. *In*: McGuire, W.J., Jones, A.P., Neuberg, J., eds. *Volcano Stability on the Earth and Other Planets*, *Geological Society Special Publication*, 110, 45-53.

Endo, K., Sumita, M., Machida, M., Furuichi, M., 1989. The 1984 collapse and debris avalanche deposits of Ontake volcano, central Japan. *In*: Latter, J.H., ed. *Volcanic Hazards, IAVCEI Proceedings in Volcanology*, 1, Berlin Heidelberg: Springer, 210-229.

Erismann, T.H., 1979. Mechanisms of large landslides. *Rock Mechanics and Rock Engineering*, 12, 15-46.

Fahnestock, R.K., 1978. Little Tahoma Peak rockfalls and avalanches, Mount Rainier, Washington, U.S.A. *In*: Voight, B., ed. *Rockslides and Avalanches*, *1*, *Natural Phenomena*, Amsterdam: Elsevier, 181-196.

Francis, P.W., 1994. Large volcanic debris avalanches in the central Andes. *Proceedings of International Conference on Volcano Instability on the Earth and Other Planets*, The Geological Society of London.

Francis, P.W., Gardeweg, M., Ramirez, C.F., Rothery, D.A., 1985. Catastrophic debris avalanche deposit of Socompa volcano, northern Chile. *Geology*, 13, 600-603.

Francis, P.W., Self, S. 1987. Collapsing volcanoes. *Scientific American*, 255, 90-97.

Francis, P.W., Wells, G.L., 1988. Landsat Thematic Mapper observations of debris avalanche deposits in the Central Andes. *Bulletin of Volcanology*, 50, 258-278.

Francis, P., Oppenheimer, C., 2004. *Volcanoes*, Oxford University Press.

Glicken, H.X, 1982. Criteria for identification of large volcanic debris avalanches. *EOS, Transactions of the American Geophysical Union*, 63, 1141.

Glicken, H.X., 1991. Sedimentary architecture for large volcanic debris avalanches. *In*: Smith, G.A., Fisher, R.V., eds. *Sedimentation in Volcanic Settings, SEPM Special Publications*, 45, 99-106.

Glicken, H.X, 1998. Rock slide debris avalanche of May 18, 1980 Mount St. Helens volcano, Washington. *Bulletin of the Geological Society of Japan*, 49, 55-105.

Goguel, J., 1978. Scale-dependent rockslide mechanisms, with emphasis on the role of pore fluid vaporization. *In*: Voight, B., ed. *Rockslides and Avalanches*, *1*, *Natural Phenomena*, Amsterdam: Elsevier, 693-705.

Gonzalez, E., Herreros, M.I., Pastor, M., Quecedo, Fernandez Merodo, J.A., 2003. Discrete an continuum approaches for fast landslide modeling. *In*: Konietzky, H., ed., *Numerical Modeling in Micromechanics via Particle Methods, Proceedings of the 1st International PFC Symposium, Gelsenkirchen, Germany, 6-8 November 2002*, Balkema, Lisse, 307-313.

Gorshkov, G.S., 1959. Gigantic eruption of volcano Bezymianny. *Bulletin of Volcanology*, 20, 77-109.

Gorshkov, G.S., Dubik, J.M., 1970. Gigantic directed blast at Shiveluch (Kamchatka). *Bulletin of Volcanologique*, 34, 262-288.

Habib, P., 1975. Production of gaseous pore pressure during rock slides. *Rock Mechanics*, 7 193-197.

Hakuno, M., Iwashita, K., Uchida, Y., 1989. DEM simulation of cliff collapse and debris flow. *In*: Mustoe, G.G.W., Henrikson, M., Huttelmaier, eds. *Proceedings of the 1st US Conference on Discrete Element Methods*, Golden: C.S.M. Press, 1-12.

Hampton, M.A., Lee, H.J., Locat, J., 1996. Submarine landslides. *Review of Geophysics*, 34**,** 33-59.

Hayashi., J.N. Self, S., 1992. A comparison of pyroclastic flow and debris avalanche mobility. *Journal of Geophysical Research* , 97, 9063-9071.

Heim, A., 1932. Bergsturz und Menschenleben. *Vjschr. d. Naturforsch Ges*. Zürich, 216 pp.

Hesthammer, J., Fossen, H., 1999. Evolution and geometries of gravitational collapse structures with examples from the Statfjord Field, northern North Sea. *Marine and Petroleum Geology*, 16, 259-281.

Hoek, E., 2007. *Practical rock engineering*. Available from: http://www.rocscience.com/hoek/PracticalRockEngineering.asp [accessed 16 March, 2009].

Hoek, E., Kaiser, P.K., Bawden, W.F., 1995. *Support of underground excavations in hard rock*. Rotterdam: Balkema.

Hoek, E., Brown, E.T., 1997. Practical estimates of rock mass strength. *International Journal of Rock Mechanics and Mining Sciences and Geomechanics Abstracts*, 34, 1165-1186.

Hoek, E., Carranza-Torres, C.T., and Corkum, B., 2002. Hoek-Brown failure criterion – 2002 edition. *In*: *Proceedings of the North American Rock Mechanics Society*, *Toronto*, 267-273.

Hsu, K. J., 1975. Catastrophic debris stream (Sturzstroms) generated by rockfalls. *Geological Society of America Bulletin*, 86, 129-140.

Hungr, O., 1995. A model for the runout analysis of rapid flow slides, debris flows and avalanches. *Canadian Geotechnical Journal*, 32, 610-623.

Hungr, O., Evans, S.G., 1997. A dynamic model for landslides with changing mass. *Engineering Geology and the Environment*, 41, 719-722.

Hürlimann, M., Garcia-Piera, J.O., Ledesma, A., 2000. Causes and mobility of large volcanic landslides: application to Tenerife, Canary Islands. *Journal of Volcanology and Geothermal Research*, 103, 121-134.

Hutter, K., Savage, S.B., 1988. Avalanche dynamics: the motion of a finite mass of gravel down a mountain side. *In*: Bonnard, C., ed. *Proceedings of the 5th International Symposium on Landslides, 10-15 July, Lausanne, Switzerland*, Rotterdam: Balkema, 691-697.

Hutter, K., Siegel, M., Savage, S.B., Nohguchi, Y., 1993. Two-dimensional spreading of a granular avalanche down an inclined plane, Part 1. Theory. *Acta Mechanica*, 100, 37-68.

Hutter, K., Koch, T., Pluss, C., Savage, S.B., 1995. The dynamics of avalanches of granular materials from initiation to runout. Part II. Experiments. *Acta Mechanica*, 109, 127-165.

Itasca, 2004a. *Theory and background*. Third Edition (Version 3.1), November, 2004.

Itasca 2004b. *Users Guide*, Third Edition (Version 3.1), November, 2004.

Itasca, 2004c. *FISH in PFC^{2D}*. Third Edition (Version 3.1), November, 2004.

Itasca, 2004d. *Verification problems and examples*. Third Edition (Version 3.1), November, 2004.

Itasca, 2009. *Large Open Pit research model*. Available from: http://www.itascacg.com/research/index.html [Accessed 10 March, 2009].

Iverson, R.M., Costa, J.E., LaHusen, R.G., 1992. Debris-Flow Flume at H.J. Andrews Experimental Forest, Oregon. *United States Geological Survey Open-File Report*, 92-483.

Iverson, R.M., 1997. The physics of debris flow. *Review of Geophysics*, 35, 245-296.

Jaeger, J.C., Cook, N.G.W., 1979. *Fundamentals of rock mechanics*. Chapman and Hall, 3rd ed.

Johnson, B., 1978. The Blackhawk landslide, California, U.S.A. *In*: Voight, B., ed. *Rockslides and Avalanches*, *1*, *Natural Phenomena*, Amsterdam: Elsevier, 71-93.

Kelfoun, K., Druitt, T.H., 2005. Numerical modeling of the emplacement of Socompa rock avalanche, Chile. *Journal of Geophysical Research-Solid Earth*, 110, B12202.1-12202.13, doi:10.1029/2005JB003758.

Kelfoun, K., Druitt, T.H., van Wyk de Vries, B., Guilbaud, M.N., 2008. Topographic reflection of the Socompa debris avalanche, Chile. *Bulletin of Volcanology*, 70, 1169-1187.

Kent, P.E., 1966. The transport mechanism in catastrophic rockfalls. *Journal of Geology*, 74, 79-83.

Kerle, N., van Wyk de Vries, B., 2001. The 1998 debris avalanche at Casita volcano, Nicaragua – investigation of structural deformation as the cause of slope instability using remote sensing. *Journal of Volcanology and Geothermal Research*, 105, 49-63.

Komorowski, J.C., Glicken, H.X., Sheridan, M.F., 1991. Secondary electron imagery of microcracks and hackly fracture surfaces in sand-sized clasts from the 1980 Mount St. Helens debris-avalanche deposit: implications for particle-particle interactions. *Geology*, 19, 261-264.

Kuraoka, S., Makino, T., 2007. Application of DEM for assessment of rock slope stability. *In*: *CD Proceedings of the Fourth International Conference on Discrete Element Methods*, *27-29 August, Brisbane, Australia, Minerals Engineering International*, 8 pp.

Le Friant, A., Boudon, G., Komorowski, J.C., Heinrich, P., Semet, M.P., 2006. Potential flank-collapse of Soufriére volcano, Guadeloupe, Lesser Antilles? Numerical simulation and hazards. *Natural Hazards*, 39, 381-393.

Legros, F., Cantagrel, J.M., Devourd, B., 2000. Pseudotachylyte (Frictionite) at the base of the Arequipa Volcanc Landslide deposit (Peru): Implications for emplacement mechanisms. *Journal of Geology*, 108, 601-611.

Legros, F., 2002. The mobility of long runout landslides. *Engineering Geology*, 63, 301-331.

Legros, F., 2006. Landslide mobility and the role of water. *In*: Evans, S.G., Scarascia Mugnozza, G., Strom, A., Hermanns, R.L., eds. *Landslides From Massive Rock Slope Failure.* Amsterdam: Springer, 233-242.

Lipman, P.W., Mullineaux, D.R. (eds.), 1981. The 1980 Eruptions of Mount St. Helens, Washington. *U.S. Geological Survey Professional Paper*, 1250.

Lopez, D.L., Williams, S.N., 1993. Catastrophic volcanic collapse: relation to hydrothermal processes. *Science*. 260, 1794–1796.

Lorig, L.J., Gibson, W., Alvial, J., Cuevas, J., 1995. Gravity flow simulations with the Particle Flow Code (PFC), *ISRM News Journal*, 3, 18-24.

Lorig, L.J., Watson, A.D., Martin, C.D, 2007. Rockslide runout prediction from distinct element analysis. *In*: *CD Proceedings of the Fourth International Conference on Discrete Element Methods, 27-29 August, Brisbane, Australia, Minerals Engineering International*, 10 pp.

MacSaveney, M.J., 1978. The Sherman glacier rock avalanche. In: Voight, B., ed. *Rockslides and Avalanches*, *1*, *Natural Phenomena*, Amsterdam: Elsevier, 71-96.

McEwan, A.S., 1989. Mobility of large rock avalanches: evidence from Valles Marineris, Mars. *Geology*, 17, 1111-1114.

McEwan, A.S., Malin, M.C., 1989. Dynamics of Mount St. Helens' 1980 pyroclastic flows, rockslide-avalanche, lahars, and blast. *Journal of Volcanology and Geothermal Research*, 37, 205-231.

McGuire, W.J., 1996. Volcano instability: a review of contemporary themes. *In*: McGuire, W.J., Jones, A.P., Nueberg, J., eds. *Volcano Instability on the Earth and Other Planets*, *Geological Society Special Publication*, 110, 1-23.

McGuire, W.J., 2003. Volcano stability and lateral collapse. *Revista*, 1, 33-45.

Melekestev, I.V., 2006. Large modern collapses on the active volcanoes of Kamchatka: causes and mechanisms of formation. *In*: Evans, S.G., Scarascia Mugnozza, G., Strom, A., Hermanns, R.L., eds. *Landslides From Massive Rock Slope Failure*. Amsterdam: Springer, 431-444.

Melosh, H.J., 1979. Acoustic fluidization – a new geologic process? *Journal of Geophysical Research*, 84, 7513-7520.

Melosh, H.J., 1986. The physics of very large landslides. *Acta Mechanica*, 64, 89-99.

Mimura, K., Fujimoto, U., Hyuga, T., Ichikawa, S., Kawachi, S., Taneichi, M., 1971. Natural remnant magnetism of Niraski pyroclastic flow. *Bulletin of the Geological Society of Japan*, 15, 146-147.

Mimura, K., Kano, K., Nakano, S., Hoshizumi, H., 1988. Ontake debris avalanche in 1984 – flow and deposition mechanism inferred from the deposit. *Bulletin of the Geological Society of Japan*, 39, 495-523.

Moore, J.G., Normark, W.R., Holcomb, R.T., 1994. Giant Hawaiian landslides. *Annual Review of Earth and Planetary Sciences*, 22, 119–144.

Morgan, J.K., 1999. Numerical simulations of granular shear zones using the distinct element method 2. Effects of particle size distribution and interparticle friction. *Journal of Geophysical Research*, 104, 2721-2732.

Morgan, J.K. 2004. Particle dynamics simulations of rate- and state-dependent frictional sliding of granular fault gouge. *Pure and Applied Geophysics*, 161, 1877-1891.

Morgan, J.K., Boettcher, M.S., 1999. Numerical simulations of granular shear zones using the distinct element method 2. Effects of particle size distribution and interparticle firction on mechanical behaviour. *Journal of Geophysical Research*, 104, 2721-2732.

Morgan, J.K., McGovern, P.J. 2003. Discrete element simulations of volcanic spreading: implications for the structure of Olypmus Mons. *35th Lunar and Planetary Science Conference*, abstract 2008.

Morgan, J.K., McGovern, P.J., 2005a. Discrete element simulations of gravitational volcanic deformation. 1: Deformation structures and geometries, *Journal of Geophysical Research*, 110, B05403, doi:10.1029/2004JB003253.

Morgan, J.K., McGovern, P.J., 2005b. Discrete element simulations of gravitational volcanic deformation. 2: Mechanical analysis, *Journal of Geophysical Research*, 110, B05403, doi:10.1029/2004JB003252.

Morgan, J.K., 2006. Volcanotectonic interactions between Mauna Loa and Kilauea: Insights from 2-D discrete element simulations. *Journal of Volcanology and Geothermal Research*, 151, 109-131.

NAIP, 2008. *National Agriculture Imagery Program*. Available from: http://165.221.201.14/NAIP.html [accessed November, 2008].

NASA, 2008. *Land Process Distributed Active Archive Center*. Available from: https://lpdaac.usgs.gov/ [accessed March, 2008].

Nakamura, Y., 1978. Mode of volcanic dry avalanche from the 1888 explosive eruption of Bandai volcano. *IAVCEI Symposium of Arc Volcanism*, *Tokyo and Hakone*, 254-255.

Naranjo, J.A., Francis, P.E., 1987. High velocity debris avalanche at Lastarria volcano in the northern Chilean Andes. *Bulletin of Volcanology*, 49, 509-514.

Ord, A., 2003. Modeling of magma ascent. *In*: Konietzky, H., ed. *Numerical Modeling in Micromechanics via Particle Methods, Proceedings of the 1st International PFC Symposium, Gelsenkirchen, Germany, 6-8 November 2002*, Lisse: Balkema, 291-294.

Palmer, B.A., Alloway, B.V., Neall, V.E., 1991. Volcanic-debris avalanche deposits in New Zealand: lithofacies organisation in unconfined, wet-avalanche flows. *In*: Smith, G.A., Fisher, R.V., eds. *Sedimentation in Volcanic Settings*, *SEPM Special Publications*, 99-106.

Preh, A., Poisel, R., Krastanov, J., 2003. Investigation of the failure mechanism of hard, competent rock lying on a soft, incompetent base by PFC^{2D}. *In*: Konietzky, H., ed. *Numerical Modeling in Micromechanics via Particle Methods, Proceedings of the 1st International PFC Symposium, Gelsenkirchen, Germany, 6-8 November 2002*, Lisse: Balkema, 277-281.

Preh, A., Poisel, R., 2006. Models for landslide behaviour with large displacements by the particle Flow Code. *Felsbau*, 25, 31-37.

Poisel, R., Preh, A., 2008. Modifications of $PF3^{2D}$ for rock mass fall modelling. *In*: Hart, R., Detournay, C., Cundall, P., eds. *Continuum and Distinct Element Numerical Modeling in Geo-engineering, Proceedings of the 1st International FLAC/DEM Symposium, 25-27 August, Minneapolis, Minnesota*, 29-38.

Ponomareva, V.V., Pevzner, M.M., Melekestev, I.V., 1998. Large debris avalanches and associated eruptions in the Holocene eruptive history of Shiveluch Volcano, Kamchatka, Russia. *Bulletin of Volcanology*, 59, 490-505.

Ponomareva, V.V., Melekestsev, I.V., Dirksen, O.V., 2006. Sector collapse and large landslides on the Late Pleistocene-Holocene volcanoes in Kamchatcka, Russia. *Journal of Volcanology and Geothermal Research*, 158, 117-138.

Potyondy, D.O., Cundall, P.A., 1999. Modelling of notch formation in the URL mine-by tunnel: Phase IV – enhancements to the PFC model of rock. *Itasca Consulting Group*, *Inc*., *Report to the Atomic Energy of Canada Limited* (*AECL*), Ontario Hydro Nuclear Waste Management Division Report No. 06819-REP-01200-10002-R00.

Potyondy, D.O., Cundall, P.A., 2004. A bonded-particle model for rock. *International Journal of Rock Mechanics and Mining Sciences*, 41, 1329-1364.

Prather, B., 2003. Controls on reservoir distribution, architecture and stratigraphic trapping in slope settings. *Marine and Petroleum Geology*, 20, 529-545.

Pudasaini, S.P., Hutter, K., 2007. *Avalanche dynamics*: *Dynamics of rapid flows of dense granular avalanches*. Amsterdam: Springer.

Reiche, P., 1937. The Toreva block – a distinctive landslide type. *Journal of Geology*, 45, 538-548.

Reid, M.E., Christian, S.B., Brien, D.L., 2000. Gravitational stability of three-dimensional stratovolcano edifices. *Journal of Geophysical Research*, 105, 6043-6056.

Reid, M.E., Sisson, T., Brien, D., 2001. Volcano collapse promoted by hydrothermal alteration and edifice shape, Mount Rainier, Washington. *Geology*, 29, 779-782.

Reubi, O., Hernandez, J., 2000. Volcanic debris avalanche deposits of the upper Marrone valley (Cantal Volcano, France): evidence for contrasted formation and transport mechanisms. *Journal of Volcanology and Geothermal Research*, 102, 271-286.

Richards, J.P., Villeneuve, M., 2001. The Llullaillaco volcano, northwest Argentina: construction by Pleistocene volcanism and destruction by sector collapse. *Journal of Volcanology and Geothermal Research*, 105, 77-105.

Robin, C., Boudal, C., 1987. A gigantic Bezymianny-type event at the beginning of modern Volcan Popocatepetl. *Journal of Volcanology and Geothermal Research*, 31, 115-130.

Rodríguez-Losada, J.A., Hernández-Gutiérrez, L.E., Olalla, C., Perucho, A., Serrano, A., Eff-Darwich, A., 2009. Geomechanical parameters of intact rocks and rock masses from the Canary Islands: Implications on their flank stability. *Journal of Volcanology and Geothermal Research*, 182, 67-75.

Savage, S.B., 1984. The mechanics of rapid granular flows. *Advances in Applied Mechanics*, 24, 289-366.

Savage, S.B., Hutter, K., 1989. The motion of a finite mass of granular material down a rough incline. *Journal of Fluid Mechanics*, 199, 177-215.

Scheidegger, A.E., 1973. On the prediction of the reach and velocity of catastrophic landslides. *Rock Mechanics*, 5, 231-236.

Schöpfer, M.P.J., Abe, S., Childs, C., Walsh, J.J., 2008. The impact of porosity and crack density on the elasticity, strength and friction of cohesive granular materials: Insights from DEM modelling. *International Journal of Rock Mechanics and Mining Sciences*, doi: 10.1016/j.ijrmms.2008.03.009.

Schuster, R.L., Crandell, D.R., 1984. Catastrophic debris avalanches from volcanoes. *IV International Symposium on Landslides Proceedings*, 1, 567-572.

Schneider, J.L., Fisher, R.V., 1998. Transport and emplacement mechanisms of large volcanic debris avalanches: evidence from the northwest sector of Cantal volcano (France). *Journal of Volcanology and Geothermal Research*, 83, 141-165.

Seyferth, M., Henk, A., 2003. Coupling of PFC2D and ANSYS® – concepts to combine the best of two worlds for improved geodynamic models. *In*: Konietzky, H., ed. *Numerical Modeling in Micromechanics via Particle Methods, Proceedings of the 1st International PFC Symposium, Gelsenkirchen, Germany, 6-8 November 2002*, Lisse: Balkema, 283-290.

Shaller, P. J., Smith-Shaller, A., 1996. Review of proposed mechanisms for Sturzstroms (long-runout landslides). *In*: Abott, P. L., Semour, D. C., eds. *Sturzstroms and Detachment Faults*, *Anbza-Borego Desert State Park*, *California*, *South Coast Geological Society*, 185–202.

Shea, T., van Wyk de Vries, B., 2008. Structural analysis and analogue modelling of the kinematics and dynamics of rockslide avalanches. Geosphere, 4, 657-686.

Shea, T., van Wyk de Vries, B., Pilato, M., 2008. Emplacement mechanisms of contrasting debris avalanches at Volcán Mombacho (Nicaragua), provided by structural and facies analysis. *Bulletin of Volcanology*, 70, 899-921.

Shreve, R.L., 1968a. The Blackhawk landslide. *Geological Society of America Special Paper*, 108, 1-47.

Shreve, R.L., 1968b. Leakage and fluidization in air-layer lubricated avalanches. *Geological Society of America Bulletin*, 79, 653-658.

Siebe, C., Komorowski, J.C., Sheridan, M.F., 1992. Morphology and emplacement of an unusual debris-avalanche deposit at Jocotitlan Volcano, Central Mexico. *Bulletin of Volcanology*, 54, 573-589.

Siebert, L., 1984. Large volcanic debris avalanches: characteristics of source areas, deposits and associated eruptions. *Journal of Volcanology and Geothermal Research*, 22, 163-197.

Siebert, L., Glicken, H.X., Ui, T., 1987. Volcanic hazards from Bezymianny- and Bandai-type eruptions. *Bulletin of Volcanology*, 49, 435-459.

Sitharam, T.G., Nimbkar, M.S., 1997. Numerical modelling of the micromechanical behavior of granular media by discrete element method. *Geotechnical Engineering Bulletin*, 6, 261-283.

Sonmez, H., Ulusay, R., 1999. Modification to the geological strength index (GSI) and their applicability to stability of slopes. *International Journal of Rock Mechanics and Mining Sciences*, 36, 743-760.

Sousa, J., Voight, B., 1995. Multiple-pulsed debris avalanche emplacement at Mount St. Helens in 1980: Evidence from numerical continuum flow simulations. *Journal of Volcanology and Geothermal Research*, 66, 227-250.

Staron, L., 2008. Mobility of long-runout rock flows: a discrete numerical investigation. *Geophysical Journal International*, 172, 455-463.

Stevens, N.F., Garbeil, H., Mouginis-Mark, P.J., 2004. NASA EOS Terra ASTER: Volcanic topographic mapping and capability. *Remote Sensing and the Environment*, 90, 405-414.

Straub, S., 1996. Self-organisation in the rapid flow of granular materials: evidence for a major flow mechanism. *International Journal of Earth Sciences (Geol. Rundsch.)*, 85, 85-91.

Strom, A.L., 2006. Morphology and internal structure of rockslides and rock avalanches: grounds and constraints for their modelling. *In*: Evans, S.G., Scarascia Mugnozza, G., Strom, A., Hermanns, R.L., eds. *Landslides From Massive Rock Slope Failure*, Amsterdam: Springer, 305-326.

Takarada, S., Ui, T., Yamamoto, Y., 1999. Depositional features and transportation mechanism of valley-filling Iwasegawa and Kaida debris avalanches, Japan. *Bulletin of Volcanology*, 60, 508-522.

Thompson, N., Watters, R.J., Schiffman, P., 2008. Stability analysis of Hawaiian island flanks using insight gained from strength testing of the HSDP core. *Journal of Volcanology and Geothermal Research*, 171, 163-177.

Tibaldi, A., Bistacchi, A., Pasquarè, F.A., Vezzoli, L., 2006. Extensional tectonics and volcano lateral collapses: insights from Ollagüe volcano (Chile-Bolivia) and analogue modelling. *Terra Nova*, 18, 282-289.

Tommasi, P., Consorti, C., Campedel, P., Ribacchi, R., 2003. Analysis of rock avalanches generated by large planar rock slides by means of numerical methods for discontinua. *Technology Roadmap for Rock Mechanics, Proceedings of the 10th Congress of the ISRM, Johannesburg*, 2, 1235-1240.

Ui, T., 1983. Volcanic dry avalanche deposits – identification and comparison with nonvolcanic stream deposits. *Journal of Volcanology and Geothermal Research*, 18, 135-150.

Ui, T., 1989. Discrimination between debris avalanche and other volcaniclastic deposits. *In*: Latter, J.H., ed. *Volcanic Hazards*, Berlin: Springer, 201-209.

Ui, T., Glicken, H., 1986. Internal structural variations in a debris-avalanche deposit from ancestral Mount Shasta, California, USA. *Bulletin of Volcanology*, 48, 189-194.

Ui, T., Kawachi, S., Neall, V.E., 1986. Fragmentation of debris avalanche material during flowage – evidence from the Pungarehu formation, Mount Egmont, New Zealand. *Journal of Volcanology and Geothermal Research*, 27, 255-264.

Ui, T., Takarada, S., Yoshimoto, M., 2000. Debris avalanches. *In*: Sigurdsson, H., Houghton, B., McNutt, S.R., Rymer, H., Stix, J., eds. *Encyclopaedia of Volcanoes*, Academic Press, 617-626.

USACE, 1999. *Engineering and design*: *settlement analysis*. U.S. Army Corps of Engineers, Engineer Manual 1110-1-1904.

Utili, S., Nova, R., 2008. DEM analysis of bonded granular materials. *International Journal for Numerical and Analytical Methods in Geomechanics*, 32, 1997-2031.

Uttini, A., Apuani, T., Massetti, M., Vezzoli, L., Corazzato, C., 2006. First contribution to debris slope stability analysis of Sciara del Fuoco (Stromboli island, Italy) via particle numerical modeling. *Geophysical Research Abstracts*, 8, 08103.

Uttini, A., Apuani, T., Massetti, M., 2007. The Sciara del Fuoco debris stability (Stromboli volcano, Italy): a distinct element numerical modelling of possible triggering mechanisms. *Geophysical Research Abstracts*, 9, 04319.

Van Gassen, W., Cruden, D.M., 1989. Momentum transfer and the friction in debris of rock slides. *Canadian Geotechnical Journal*, 26, 623-628.

van Wyk de Vries, B., Kerle, N., Petley, D., 2000. Sector collapse forming at Casita volcano, Nicaragua. *Geology*, 28, 167-170.

van Wyk de Vries, B., Self, S., Francis, P.W., Keszthelyi, L., 2001. A gravitational spreading origin for the Socompa debris avalanche. *Journal of Volcanology and Geothermal Research*, 105, 225-247.

Vezzoli, L., Tibaldi, A., Renzulli, A., Menna, M., Flude, S., 2008. Faulting-assisted lateral collapses and influence on shallow magma feeding system at Ollagüe volcano (Central Volcanic Zone, Chile-Bolivia Andes). *Journal of Volcanology and Geothermal Research*, 171, 137-159.

Victor, T., 2003. Numerical simulation of collisional orogeny using the distinct element technique. *In*: Konietzky, H., ed. *Numerical Modeling in Micromechanics via Particle Methods, Proceedings of the 1st International PFC Symposium, Gelsenkirchen, Germany, 6-8 November 2002*, Lisse: Balkema, 295-301.

Vidal, N., Merle, O., 2000. Reactivation of basement faults beneath volcanoes: a new model of flank collapse. *Journal of Volcanology and Geothermal Research*, 99, 9-26.

Voight, B., 2000. Structural stability of andesite volcanoes and lava domes. *Philosophical Transactions of the Royal Science A: Mathematical, Physical, and Engineering Sciences*, 358, 1663-1703.

Voight B., Glicken, H., Janda, R.J., Douglass, P.M., 1981. Catastrophic rockslide avalanche of May 18. *In*: Lipman, P.W., Mullineaux, D.R., eds. *The 1980 Eruption of Mount St. Helens, Washington*, U.S. Geological Survey Professional Paper, 1250, 347-377.

Voight, B., Janda, R.J., Glicken, H.X., Douglass, P.M., 1983. Nature and mechanics of the Mount St. Helens rockslide-avalanche of 18 May 1980. *Geotechnique*, 33, 243-273.

Voight, B., Sousa, J., 1994. Lessons from Ontake-san: A comparative analysis of debris avalanche dynamics. *Engineering Geology*, 38, 261-297.

Voight, B., Elsworth, D., 1997. Failure of volcano slopes. *Geotechnique*, 47, 1-31.

Voight, B., Komorowski, J.C., Norton, G.E., Belousov, A.B., Belousova, M., Boudon, G., Francis, P.W., Franz, W., Heinrich, P., Sparks, R.S.J., Young, S.R., 2002. The 26 December (Boxing Day) 1997 sector collapse and debris avalanche at Soufrière Hills Volcano, Montserrat. *In*: Druitt, T.H., Kokelar, B.P., eds. *The Eruption of Soufriere Hills Volcano, Montserrat, From 1995 to 1999*, Geological Society of London Memoir, 363-407.

Wadge, G., Francis, P.W., Ramirez, C.F., 1995. The Socompa collapse and avalanche event. *Journal of Volcanology and Geothermal Research*, 66, 309-336.

Ward, S.N., Day, S., 2006. Particulate kinematic simulations of debris avalanches: interpretation of deposits and landslide seismic signals of Mount Saint Helens, 1980 May 18. *Geophysical Journal International*, 167, 991-1004.

Ward, S.N., 2009. *List of computer simulations*. Availiable from: http://es.ucsc.edu/~ward/ [accessed March, 2009].

Welbon, A.I.F., Brockbank, P.J., Brundsen, D., Olsen, T.S., 2007. Characterizing and producing from reservoirs in landslides: challenges and opportunities. *Geological Society of London Special Publication*, doi:10.1144/SP292.3.

Appendices

Appendix A – Results of bonded DEM calibration exercises for each material considered. Input particle values for each random number seed resulting in desired macroscopic output values properties are presented. The normalized total is determined by comparing the output of each realization to the mean output values from the 30 realizations, normalizing the differences to the smallest value and summing these values. Therefore, the smallest normalized total value represents the realization most similar to the mean output of the 30 realizations. The realizations are thus ranked vertically from most similar to the mean output value (top) to lease similar (bottom).

Strong material										
Random number seed	Friction coefficient (μ_p)	Unit weight (kg/m^3)	Input E_c, E_{cb} (GPa)	Input k_n/k_s, k_{nb}/k_{sb}	Input σ (MPa)	Input τ (MPa)	Output σ'_{cm} (MPa)	Output E_m (GPa)	Output ν	Normailized total
1	0.84	2500	59.7	5.25	28.5	28.5	31.9	51.1	0.31	0.190
17	↓	↓	52.5	4.70	20.5	20.5	32.0	51.4	0.31	0.287
20			62.7	5.50	28.5	28.5	32.2	50.5	0.31	0.411
14			56.2	5.00	22.5	22.5	32.3	50.6	0.31	0.455
12			58.0	5.40	23.9	23.9	32.2	50.7	0.31	0.495
13			58.0	5.40	23.2	23.2	32.0	50.5	0.31	0.612
28			58.0	5.40	27.0	27.0	32.2	51.2	0.31	0.633
21			65.7	5.80	26.3	26.3	31.8	50.4	0.31	0.715
26			60.0	5.40	25.7	25.7	32.2	51.5	0.31	0.843
27			59.0	5.40	24.0	24.0	32.2	51.4	0.30	0.997
18			63.0	6.40	27.0	27.0	31.6	50.4	0.31	1.011
19			62.7	6.40	23.7	23.7	32.1	50.6	0.30	1.095
11			58.0	4.70	23.3	23.3	32.2	50.8	0.30	1.274
2			59.8	5.25	23.8	23.8	32.1	51.9	0.31	1.288
29			58.0	4.90	25.5	25.5	32.2	51.3	0.30	1.300
4			61.9	6.90	26.0	26.0	32.1	51.3	0.32	1.525
9			63.9	6.85	26.2	26.2	32.1	52.1	0.31	1.559
16			60.0	5.30	25.0	25.0	32.0	50.0	0.30	1.910
25			58.0	5.30	22.2	22.2	32.0	51.2	0.30	2.067
30			67.0	5.30	26.5	26.5	32.2	51.3	0.30	2.136
23			58.0	5.20	22.2	22.2	32.1	51.3	0.30	2.608
24			58.0	4.80	29.0	29.0	31.4	50.8	0.30	2.739
22			52.0	4.70	18.2	18.2	32.0	50.9	0.30	3.104
7			66.8	6.90	25.0	25.0	32.0	51.5	0.30	3.278
15			55.4	5.00	25.2	25.2	32.0	52.0	0.30	3.483
6			67.0	6.90	27.0	27.0	32.1	51.3	0.32	4.238
10			63.9	6.85	30.7	30.7	31.9	51.1	0.33	6.455
3			66.0	6.90	28.5	28.5	32.1	50.4	0.33	11.758
5			67.0	6.90	30.3	30.3	32.0	50.5	0.33	16.495
8			66.5	6.85	23.5	23.5	32.3	51.6	0.34	19.373
		Mean	60.8	5.7	25.3	25.3	32.0	51.1	0.3	
		Standard deviation	4.3	0.8	2.8	2.8	0.2	0.5	0.01	

Mean material (E_m = 15 GPa)										
Random number seed	Friction coefficient (μ_p)	Unit weight (kg/m^3)	Input E_c, E_{cb} (GPa)	Input k_n/k_s, k_{nb}/k_{sb}	Input σ (MPa)	Input τ (MPa)	Output σ'_{cm} (MPa)	Output E_m (GPa)	Output v	Normalized total
19	0.7	1300	9.0	3.0	9.0	9.0	13.0	15.1	0.23	0.002
29	↓	↓	9.2	2.7	9.9	9.9	13.0	15.1	0.23	0.003
29			9.1	2.7	9.2	9.2	13.0	15.1	0.23	0.003
23			9.1	3.0	8.3	8.3	13.1	15.1	0.23	0.005
24			9.0	2.8	10.2	10.2	13.1	15.1	0.23	0.006
4			9.4	2.9	10.0	10.0	13.0	15.0	0.23	0.009
10			8.9	2.6	8.5	8.5	13.0	15.0	0.23	0.009
16			9.1	2.8	10.8	10.8	13.0	15.0	0.23	0.009
22			8.9	3.0	7.9	7.9	13.0	15.0	0.23	0.010
30			9.1	2.7	9.0	9.0	13.0	15.0	0.23	0.010
9			8.9	2.8	10.2	10.2	13.1	15.0	0.23	0.011
2			9.0	2.8	7.8	7.8	13.1	15.1	0.23	0.013
27			9.2	2.7	9.9	9.9	13.0	15.2	0.23	0.017
15			9.1	2.8	10.5	10.5	13.1	15.2	0.23	0.019
1			9.0	2.7	11.3	11.3	13.1	15.1	0.23	0.027
11			8.7	2.7	8.8	8.8	13.2	15.1	0.23	0.033
26			9.2	2.7	10.8	10.8	12.9	15.0	0.23	0.034
12			8.7	2.6	8.8	8.8	13.0	14.9	0.23	0.035
14			9.1	2.6	10.0	10.0	13.1	14.9	0.23	0.037
6			9.0	3.0	9.6	9.6	12.9	15.2	0.23	0.042
20			9.0	3.0	8.3	8.3	13.0	15.3	0.23	0.051
5			9.4	2.9	10.3	10.3	13.2	15.3	0.23	0.081
18			9.0	3.0	9.7	9.7	13.2	15.3	0.23	0.098
2			9.4	2.9	10.1	10.1	13.0	15.1	0.24	0.111
8			9.0	2.8	9.9	9.9	13.0	15.0	0.22	0.433
21			8.9	3.1	9.0	9.0	13.0	15.0	0.22	0.435
17			9.0	2.8	11.0	11.0	13.0	15.1	0.24	0.439
13			8.8	2.6	9.1	9.1	13.0	15.0	0.24	0.445
7			9.0	2.8	9.7	9.7	13.0	15.2	0.24	0.453
25			9.2	2.8	10.5	10.5	13.1	14.9	0.21	1.746
		Mean	9.0	2.8	9.6	9.6	13.0	15.1	0.2	
		Standard deviation	0.2	0.1	0.9	0.9	0.1	0.1	0.01	

Mean material (E_m = 1 GPa)										
Random number seed	Friction coefficient (μ_p)	Unit weight (kg/m^3)	Input E_c, E_{cb} (GPa)	Input k_n/k_s, k_{nb}/k_{sb}	Input σ (MPa)	Input τ (MPa)	Output σ'_{cm} (MPa)	Output E_m (GPa)	Output v	Normalized total
2	0.7	1700	0.90	2.70	9.0	9.0	13.1	1.1	0.23	0.066
5	↓	↓	0.90	3.00	11.2	11.2	13.0	1.0	0.23	0.125
6			0.90	3.10	10.9	10.9	13.0	1.0	0.23	0.255
11			0.89	2.90	8.7	8.7	13.0	1.0	0.23	0.265
14			0.86	3.30	9.7	9.7	13.0	1.0	0.23	0.311
20			0.91	2.70	10.0	10.0	13.0	1.0	0.23	0.325
25			0.92	3.00	8.6	8.6	13.0	1.0	0.23	0.335
29			0.92	2.90	9.2	9.2	13.0	1.0	0.23	0.344
12			0.89	2.80	10.0	10.0	13.1	1.0	0.23	0.351
13			0.89	3.30	10.3	10.3	13.1	1.0	0.23	0.359
26			0.92	3.00	9.0	9.0	13.1	1.0	0.23	0.361
4			0.90	3.00	11.0	11.0	13.2	1.0	0.23	0.378
8			0.90	3.00	9.2	9.2	13.2	1.0	0.23	0.391
3			0.90	3.00	10.5	10.5	13.0	1.0	0.22	0.404
10			0.10	2.90	9.2	9.2	13.0	1.1	0.23	0.448
16			0.91	3.30	10.1	10.1	13.0	1.1	0.23	0.454
17			0.90	3.00	11.3	11.3	13.0	1.1	0.23	0.464
28			0.92	2.90	9.4	9.4	13.0	1.1	0.23	0.474
24			0.91	3.10	8.8	8.8	13.1	1.1	0.23	0.476
9			0.90	2.80	9.0	9.0	12.9	1.1	0.23	0.478
23			0.91	3.10	9.9	9.9	13.2	1.1	0.23	0.482
1			0.90	2.70	8.6	8.6	13.1	1.1	0.23	0.517
10			0.91	2.90	12.0	12.0	13.0	1.0	0.24	0.626
7			0.97	3.10	11.0	11.0	13.0	1.0	0.22	0.686
30			0.92	3.10	9.0	9.0	13.0	1.1	0.24	0.730
27			0.92	2.90	9.0	9.0	12.0	1.0	0.22	1.716
15			0.90	3.30	9.8	9.8	13.2	1.1	0.21	1.810
22			0.91	2.80	10.2	10.2	13.1	0.9	0.23	3.340
21			0.91	2.70	10.2	10.2	13.0	1.2	0.23	3.645
18			0.90	3.00	11.2	11.2	13.1	1.2	0.23	3.652
		Mean	0.9	3.0	9.9	9.9	13.0	1.0	0.2	
		Standard deviation	0.1	0.2	0.9	0.9	0.2	0.1	0.01	

Weak Material										
Random number seed	Friction coefficient (μ_p)	Unit weight (kg/m^3)	Input E_c, E_{cb} (GPa)	Input k_n/k_s, k_{nb}/k_{sb}	Input σ (MPa)	Input τ (MPa)	Output σ'_{cm} (MPa)	Output E_m (GPa)	Output v	Normalized total
4	0.47	1300	0.59	1.30	0.75	0.75	1.1	0.1	0.11	0.00100
10	↓	↓	0.58	1.30	0.87	0.87	1.0	0.1	0.11	0.00154
16			0.58	1.34	0.79	0.79	1.0	0.1	0.12	0.00203
2			0.59	1.30	0.80	0.80	1.1	0.1	0.11	0.00206
27			0.56	1.35	0.77	0.77	1.1	0.1	0.11	0.00259
6			0.58	1.20	0.75	0.75	1.0	0.1	0.11	0.00267
23			0.56	1.31	0.78	0.78	1.0	0.1	0.11	0.00292
24			0.56	1.37	0.75	0.75	1.1	0.1	0.11	0.00326
30			0.56	1.24	0.79	0.79	1.1	0.1	0.11	0.00334
18			0.58	1.39	0.79	0.79	1.0	0.1	0.11	0.00341
15			0.58	1.35	0.80	0.80	1.0	0.1	0.11	0.00352
19			0.58	1.30	0.77	0.77	1.0	0.1	0.11	0.00371
20			0.58	1.34	0.77	0.77	1.1	0.1	0.11	0.00441
1			0.59	1.34	0.75	0.75	1.1	0.1	0.12	0.00449
13			0.58	1.27	0.81	0.81	1.0	0.1	0.11	0.00500
11			0.58	1.30	0.87	0.87	1.1	0.1	0.11	0.00596
28			0.56	1.32	0.77	0.77	1.1	0.1	0.11	0.00647
25			0.56	1.37	0.80	0.80	1.0	0.1	0.11	0.00662
3			0.59	1.28	0.75	0.75	1.0	0.1	0.11	0.00692
29			0.56	1.32	0.77	0.77	1.0	0.1	0.11	0.00765
17			0.58	1.27	0.79	0.79	1.1	0.1	0.11	0.00794
21			0.57	1.28	0.75	0.75	1.1	0.1	0.12	0.00951
22			0.57	1.30	0.73	0.73	1.1	0.1	0.12	0.01005
9			0.58	1.30	0.87	0.87	1.0	0.1	0.11	0.01015
26			0.56	1.35	1.00	1.00	1.0	0.1	0.11	0.01023
5			0.58	1.30	0.75	0.75	1.2	0.1	0.11	0.01040
8			0.58	1.30	0.78	0.78	1.0	0.1	0.11	0.01082
7			0.58	1.36	0.78	0.78	1.0	0.1	0.11	0.01180
12			0.58	1.27	0.81	0.81	1.1	0.1	0.12	0.01264
14			0.58	1.41	0.74	0.74	1.2	0.1	0.12	0.02125
		Mean	0.6	1.3	0.8	0.8	1.1	0.1	0.1	
		Standard deviation	0.01	0.04	0.1	0.1	0.1	0.005	0.004	

Appendix B – Example of the code written to control the bonded assembly avalanche simulations. The following description is divided into sections by the primary function performed, as described at the beginning of each section.

```
new

;==================INITIAL SETTINGS==================

;THIS SECTION RESTORES A LARGE SCALE CALIBRATED BLOCK OF A GIVEN MATERIAL AND SETS INITIAL
CONTROLS

restore F_iniblock.sav

set disk on

set gravity 0.0 -9.8

set max_balls 90000

set damping local 0.0

set damping viscous normal 0.1

set damping viscous shear 0.1

;==================BASE WALLS==================

;THIS SECTION INSTALLS A SERIES OF WALLS ALONG THE BASE OF THE BLOCK TO CREATE A REALISTIC
STRESS FIELD UPON CYCLING

wall id 101 nodes 0.0 0.0 341.41 0.0 kn 1.74e8 ks 1.74e8 fric 0.0
wall id 102 nodes 341.41 0.0 677.82 0.0 kn 1.74e8 ks 1.74e8 fric 0.0
wall id 103 nodes 677.82 0.0 1014.23 0.0 kn 1.74e8 ks 1.74e8 fric 0.0
wall id 104 nodes 1014.23 0.0 1350.64 0.0 kn 1.74e8 ks 1.74e8 fric 0.0
wall id 105 nodes 1350.64 0.0 1687.05 0.0 kn 1.74e8 ks 1.74e8 fric 0.0
wall id 106 nodes 1687.05 0.0 1787.05 0.0 kn 1.74e8 ks 1.74e8 fric 0.0
wall id 107 nodes 1787.05 0.0 2123.46 0.0 kn 1.74e8 ks 1.74e8 fric 0.0
wall id 108 nodes 2123.46 0.0 2459.87 0.0 kn 1.74e8 ks 1.74e8 fric 0.0
wall id 109 nodes 2459.87 0.0 2796.28 0.0 kn 1.74e8 ks 1.74e8 fric 0.0
wall id 110 nodes 2796.28 0.0 3132.69 0.0 kn 1.74e8 ks 1.74e8 fric 0.0
wall id 111 nodes 3132.69 0.0 3469.1 0.0 kn 1.74e8 ks 1.74e8 fric 0.0
wall id 112 nodes 3469.1 0.0 3474.1 0.0 kn 1.74e8 ks 1.74e8 fric 0.0

;==================HISTORY AND MONITORING==================

;THIS SECTION ASSIGNS ANY DESIRED MONITORING AND/OR DIAGNOSTICS

history id 1 diagnostic mcf ; MEAN COMPRESSIVE FORCE
history id 2 diagnostic muf ; MEAN UNBALANCED FORCE
history id 3 wall yforce id=106 ; VERTICAL FORCE ON BASAL WALL
history id 4 ball xp id=344 ; LEFT TOE BALL OF CONE, X-DISPLACEMENT
history id 5 ball yp id=139911 ; SUMMIT BALL OF CONE, Y-DISPLACEMENT
history id 6 ball xp id=271659 ; RIGHT TOE BALL OF CONE, X-DISPLACEMENT

measure id 1 x 1737.05 y 50.0 rad 50.0 ; BASAL MEASUREMENT CIRCLE

history id 15 measure s22 id=1 ; VERTICAL STRESS IN MEASURMENT CIRCLE

history id=16 energy body
history id=17 energy bond
history id=18 energy boundary
history id=19 energy frictional
history id=20 energy kinetic
history id=21 energy strain

;==================INCREASE BOND STRENGTH==================

;THIS SECTION INCREASES BOND STRENGTH TO 500 MPA WHILE THE CONE IS CREATED TO ENSURE NO
;DEFORMATION OCCURS DURING THIS PROCESS

def increase_bond_str
  _pbonds = 1
  cp = contact_head
  loop while cp # null
    if _pbonds = 1 then
      if md_pbond = 1 then
        pb_nstrength(cp) = pb_nstrength(cp) * 263 ; SET CONE TO 500 MPa
```

```
        pb_sstrength(cp) = pb_sstrength(cp) * 263 ; SET CONE TO 500 MPa
      end_if
    end_if
    cp = c_next(cp)
  end_loop
end

increase_bond_str

;==================INCREASE BOND STRENGTH==================

;THIS SECTION SEQUENTIALLY REMOVES PARTICLES ABOVE THE CONE TO PRODUCE THE DESIRED
GEOMETRY, CYCLING EACH TIME A SECTION IS REMOVED TO ALLOW THE SYSTEM TO COME TO EQUILIBRIUM

cycle 10000

group negative range x 0.0 5000.0 y -500.0 0.0
del bal range group negative

group one range line origin 3122.69 1000.0 dip 30.0 above
group two range line origin 351.41 1000.0 dip 150.0 below
del bal range group one
del bal range group two
cycle 10000

group three range line origin 2776.28 1000.0 dip 30.0 above
group four range line origin 697.82 1000.0 dip 150.0 below
del bal range group three
del bal range group four
cycle 10000

group five range line origin 2429.87 1000.0 dip 30.0 above
group six range line origin 1044.23 1000.0 dip 150.0 below
del bal range group five
del bal range group six
cycle 10000

group seven range line origin 2083.46 1000.0 dip 30.0 above
group eight range line origin 1390.64 1000.0 dip 150.0 below
del bal range group seven
del bal range group eight
cycle 10000

group nine range line origin 1737.05 1000.0 dip 30.0 above
group ten range line origin 1737.05 1000.0 dip 150.0 below
del bal range group nine
del bal range group ten
cycle 10000

;==================REDUCE BOND STRENGTH==================

;THIS SECTION DECREASES BOND STRENGTH FROM 500 MPA TO ORIGINAL VALUES

def decrease_bond_str
  _pbonds = 1
  cp = contact_head
  loop while cp # null
    if _pbonds = 1 then
      if md_pbond = 1 then
        pb_nstrength(cp) = pb_nstrength(cp) / 263
        pb_sstrength(cp) = pb_sstrength(cp) / 263
      end_if
    end_if
    cp = c_next(cp)
  end_loop
end

decrease_bond_str

save F_cone_30.sav ; SAVES FILE OF INITIAL CONE

;=========================================================

;THE FOLLOWING SECTION DEFINES THE FAILURE SURFACE GEOMETRY, DELETES ALL PARTICLES NOT
INVOLVED IN THE FAILURE AND INSERTS PARTICLES ALONG THE BASAL WALL TO CREATE A SMOOTH BASAL
SURFACE.  THIS PROCEDURE WAS DEVELOPED WITH THE MARTIN SCHOPFER OF THE FAULT ANALYIS GROUP
AT UNIVERSITY COLLEGE, DUBLIN

;=========================================================

;FUNCTION TO DETERMINE IF THERE IS OVERLAP IN NEWLY CREATED PARTICLES
```

```
def check_overlap
  check = 0
  section
  bp = ball_head
  loop while bp # null
    dist = sqrt( (b_x(bp)-xnew)^2 + (b_y(bp)-ynew)^2 )
    if b_rad(bp) + rnew > dist*1.001
      check = 1
      exit section
    end_if
  bp = b_next(bp)
  end_loop
  end_section
end

;=========================================================

;FUNCTIONS TO AQUIRE ARRAY TABLES (TEXT FILE) FOR WALL POSITIONS, WHOSE POINTS ARE DEFINED
;IN CAD

def xy_arrays
  array xpos(1000)
  array ypos(1000)
end
xy_arrays

def get_pos
  status = open('Xpos_small.txt',0,1)
  status = read(xpos,(1000))
  status = close
  status = open('Ypos_small.txt',0,1)
  status = read(ypos,(1000))
  status = close
end
get_pos

;=========================================================

;FUNCTION TO OBTAIN NUMBER OF WALLS FROM ARRAYS

def get_nw
  section
  nw = 0
  loop while 1 # 0
  nw = nw+1
  if float(xpos(nw)) = 0
    nw=nw-2
    exit section
  end_if
  end_loop
  end_section
end
get_nw

;=========================================================

;FUNCTION TO CREATE WALLS WITH ENPOINTS DEFINED BY ARRAYS

def make_walls
  loop i(1,nw)
  _x1 = float(xpos(i))
  _x2 = float(xpos(i+1))
  _y1 = float(ypos(i))
  _y2 = float(ypos(i+1))
  _wid = i+5
    command
      wall id=_wid nodes _x1 _y1 _x2 _y2
    end_command
  end_loop
end
make_walls

;=========================================================

;FUNCTION TO FIND APPROPRIATE DISTANCE FROM NEW WALLS TO DELETE PARTICLES SO THAT NO
;PARTICLES ARE IN CONTACT WITH THESE WALLS

def get_rmax
  rmax = -1.0
  rmin = 10000.0
  bp = ball_head
  loop while bp # null
```

```
    if b_rad(bp) > rmax
      rmax = b_rad(bp)
    end_if
    if b_rad(bp) < rmin
      rmin = b_rad(bp)
    end_if
  bp = b_next(bp)
  end_loop
end
get_rmax

;=========================================================

;FUNCTION TO DELETE PARTICLES NOT INCLUDED IN FAILURE

def remove_balls
  loop i(1,nw)
  _x1 = float(xpos(i))
  _x2 = float(xpos(i+1))
  _y1 = float(ypos(i))
  _y2 = float(ypos(i+1))
  _d = -atan((_y1 - _y2)/(_x1 - _x2))*180/pi
  _a = (90-_d)*pi/180
  _xp = _x1 + rmax*cos(_a)
  _yp = _y1 + rmax*sin(_a)
  command
    delete ball range line origin _xp _yp dip _d below
  end_command
  end_loop
end
remove_balls

;=========================================================

; FUNCTION TO LOCATE PARTICLES CLOSEST TO WALL/CORNER

def get_nearest_ball
  mindist1 = 1e9
  mindist2 = 1e9
  bp = ball_head
  loop while bp # null
  dist = sqrt( (b_x(bp)-_xC)^2 + (b_y(bp)-_yC)^2  ) - b_rad(bp)

;GET NEAREST PARTICLE
  if dist < mindist1
    mindist1 = dist
    bp_nearest1 = bp
  end_if

;GET 2ND NEAREST PARTICLE
  if dist > mindist1
    if dist < mindist2
      mindist2 = dist
      bp_nearest2 = bp
    end_if
  end_if

  bp = b_next(bp)
  end_loop
end

;=========================================================

;FUNCTION THAT RETURNS MAXIMUM ID OF EXISTING PARTICLES, NECESSARY FOR CREATION OF
ADDITIONAL PARTICLES
def _max_id
  _max_id_temp = 0
  bp = ball_head
  loop while bp # null
    if b_id(bp) > _max_id_temp
      _max_id_temp = b_id(bp)
    end_if
  bp = b_next(bp)
  end_loop
  _max_id = _max_id_temp
end

;=========================================================

;FUNCTION TO INSTALL A PARTICLES AT WALL INTERSECTIONS

def put_balls_in_corners
```

```
  loop i(2,nw)
  _xC = float(xpos(i))
  _yC = float(ypos(i))
  _xL = float(xpos(i-1))
  _yL = float(ypos(i-1))
  _xR = float(xpos(i+1))
  _yR = float(ypos(i+1))
  a1 = (_yC-_yL)/(_xC-_xL)
  a2 = (_yR-_yC)/(_xR-_xC)
  b1 = _yC-a1*_xC
  b2 = _yC-a2*_xC
  get_nearest_ball
  x1 = b_x(bp_nearest1)
  y1 = b_y(bp_nearest1)
  r1 = b_rad(bp_nearest1)
  DD = (a1-a2) ; COMMON DENOMINATOR

;COEF. OF LIN EQNS
  Ax =  -(-(1.0+a1^2)^(0.5)*(1.0+a2^2)^(0.5)+1.0+a1^2)/(1.0+a1^2)^(0.5)/DD

  Bx = -((1.0+a1^2)^(0.5)*b1-(1.0+a1^2)^(0.5)*b2)/(1.0+a1^2)^(0.5)/DD
  Ay = -(-a1*(1.0+a2^2)^(0.5)*(1.0+a1^2)^(0.5)+a2+a2*a1^2)/(1.0+a1^2)^(0.5)/DD
  By = -(-a1*(1.0+a1^2)^(0.5)*b2+(1.0+a1^2)^(0.5)*b1*a2)/(1.0+a1^2)^(0.5)/DD

  mq = (Ay^2+Ax^2-1.0) ; COEFFICIENTS OF QUADRATIC EQUATION (mx^2 + nx + o = 0)
  nq = (2.0*(Bx-x1)*Ax+2.0*(By-y1)*Ay-2.0*r1)
  oq = (Bx-x1)^2-r1^2+(By-y1)^2

  rnew = (-nq-sqrt(nq^2-4.0*mq*oq))/(2.0*mq) ; SOLVE QUADRATIC EQUATION, GIVES r
  xnew = Ax*rnew+Bx ; CALCULATE x AND y USING r
  ynew = Ay*rnew+By

;CHECK WHETHER INSERTED BALL IS WITHIN DEFINED SIZE RANGE

  check_overlap
  if check = 0
  if rnew >= rmin ; rmin ALWAYS KEPT AS IS
  id_new = _max_id+1
    command
      ball x xnew y ynew rad rnew id=id_new
    end_command
  bp_new = find_ball(id_new)
  _install_bonds_new_balls
  end_if
  end_if
  end_loop
end

;============================================================

;FUNCTION TO INSTALL PARTICLES ALONG WALLS

def put_balls_along_walls
  dz = rmax/2.0
  loop i(1,nw)
  _x1 = float(xpos(i))
  _x2 = float(xpos(i+1))
  _y1 = float(ypos(i))
  _y2 = float(ypos(i+1))
  _d = atan((_y2 - _y1)/(_x2 - _x1))
  section
  count = 0.0
  loop while 1 # 0
  count = count + 1.0
  _xn = _x1 + dz*count*cos(_d)
  _yn = _y1 + dz*count*sin(_d)
    if _xn > _x2
      exit section
    end_if
  a = (_y2 - _y1)/(_x2 - _x1)
  b = _y1-a*_x1
  _xC = _xn
  _yC = _yn
  get_nearest_ball
  x1 = b_x(bp_nearest1)
  y1 = b_y(bp_nearest1)
  r1 = b_rad(bp_nearest1)
  x2 = b_x(bp_nearest2)
  y2 = b_y(bp_nearest2)
  r2 = b_rad(bp_nearest2)

  DD = (x1+y1*a-x2-y2*a) ; COMMON DENOMINATOR
```

```
;COEF. OF LIN EQNS
  Ax = -0.5*(2.0*y1*(1.0+a^2)^(0.5)+2.0*r1-2.0*y2*(1.0+a^2)^(0.5)-2.0*r2)/DD

  Bx = -0.5*(-x1^2+2.0*y1*b-y1^2+r1^2+x2^2-2.0*y2*b+y2^2-r2^2)/DD
  Ay = -0.5*(2.0*a*r1-2.0*a*r2-2.0*(1.0+a^2)^(0.5)*x1+2*(1.0+a^2)^(0.5)*x2)/DD
  By = -0.5*(-a*x1^2-a*y1^2+a*r1^2+a*x2^2+a*y2^2-a*r2^2-2.0*b*x1+2.0*b*x2)/DD

  mq = (Ay^2+Ax^2-1.0) ; COEFFICIENTS OF QUADRATIC EQUATION (mx^2 + nx + o = 0)
  nq = (2.0*(Bx-x1)*Ax+2.0*(By-y1)*Ay-2.0*r1);
  oq = (Bx-x1)^2-r1^2+(By-y1)^2;

  rnew = (-nq-sqrt(nq^2-4.0*mq*oq))/(2.0*mq) ; SOLVE QUADRATIC EQUATION, GIVES r
  xnew = Ax*rnew+Bx ; CALCULATE x AND y USING r
  ynew = Ay*rnew+By

  check_overlap

;CHECK WHETHER INSERTED BALL IS WITHIN DEFINED SIZE RANGE

  if check = 0
  if rnew >= rmin/1.0 ; CHANGING THIS CHANGES MIN SIZE OF BALLS INTRODUCED
  ;if rnew <= rmax
  id_new = _max_id+1
    command
       ball x xnew y ynew rad rnew id=id_new
    end_command
   bp_new = find_ball(id_new)
   _install_bonds_new_balls
   ;end_if
   end_if
   end_if
  end_loop
  end_section
  end_loop
end

;=========================================================

;ITERATION OF ABOVE INSTALLATION FUNCTIONS TO INSTALL BALLS IN GAPS POTENTIALLY MISSED EACH
PASS

def iterate
 loop j(1,3) ; 2ND TERM INCREASES FOR INCREASED ITERATIONS, 3 ITERATIONS OK WITH rmin/1.0
   put_balls_along_walls
 end_loop
end

;=========================================================

;THIS SECTION SETS THE BOND PROPERTIES AT THE NEW CONTACTS BASED ON THE PROPERTIES OF THE
;EXISTING BONDS

;NORMAL STRENGTH AND ITS STANDARD DEVIATION
  set pb_sn_mean  = 1e6
  set pb_sn_sdev = 0.2e6 ; CANNOT = 0

;SHEAR STRENGTH AND ITS STANDARD DEVIATION
  set pb_ss_mean = 1e6
  set pb_ss_sdev = 0.2e6 ; CANNOT = 0

;RADIUS MULTIPLIER
  set pb_radmult = 1.0

;BOND YOUNG'S MODULUS
  set pb_Ec = 1e9 ;pb_Ec = (kn/2) IN PFC2D

;=========================================================

;FUNCTION THAT OBTAINS STRENGTH VALUES FROM NORMAL DISTRIBUTION OF EXISTING BONDS

def val_normdist
  loop while 1 # 0
  val = mean + stddev * grand
    if val > mean - stddev
    if val < mean + stddev
      val_normdist = val
      exit
    end_if
    end_if
  end_loop
end
```

```
;OBTAIN STRENGTH VALUES FROM NORMAL DISTRIBUTION
def _assign_pb_props
  mean = pb_sn_mean
  stddev = pb_sn_sdev
  _nstr = val_normdist

  mean = pb_ss_mean
  stddev = pb_ss_sdev
  _sstr = val_normdist

;ASSIGN BOND STRENGTH
  pb_nstrength(pbp) = _nstr
  pb_sstrength(pbp) = _sstr

;ASSIGN BOND RADIUS
  pb_rad(pbp) = pb_radmult
;CALCULATE STIFFNESS USING MODULUS STIFFNESS RELATION
  _radsum = b_rad(c_ball1(cp)) + b_rad(c_ball2(cp))
  _kn = pb_Ec/_radsum
  _ks = _kn/2.5 ;DENOMINATOR=PARTICLE STIFFNESS RATIO

  pb_kn(pbp) = _kn
  pb_ks(pbp) = _ks
end

;FUNCTION TO CYCLE THROUGH NEWLY CREATED PARTICLES AND INSTALL BONDS
def _install_bonds_new_balls
  bp_new = find_ball(id_new)
  cp = b_clist(bp_new)
  loop while cp # null
    if c_ball1(cp) = bp_new
      bp_other = c_ball2(cp)
    else
      bp_other = c_ball1(cp)
    end_if
    if pointer_type(bp_other) = 100
      pbp = c_installpb(cp)
      _assign_pb_props ; FUNCTION THAT ASSIGNS BOND PROPERTIES
    end_if
    if c_ball1(cp) = bp_new
      cp = c_b1clist(cp)
    else
      cp = c_b2clist(cp)
    end_if
    end_loop
end

;=========================================================

;THIS SECTION CALLS THE ABOVE FUNCTIONS TO INSERT NEW BALLS, BONDS ARE CREATED AS PARTICLES
;CREATED

_max_id ; GET CURRENT MAXIMUM BALL ID
put_balls_in_corners ; PUT PARTICLES INTO CORNERS
iterate ; PUT PARTICLES ALONG WALLS, REITERATES n TIMES

;==================DELETE WALLS=================

;THIS SECTION DELETES WALLS ORIGINALLY AT THE BASE OF THE CONE WHICH ARE NOW NOT NEEDED AND
;INSTALLS THE RUNOUT WALL, THE ENDPOINTS OF WHICH ARE DEFINED IN CAD

delete wal 101
delete wal 102
delete wal 103
delete wal 104
delete wal 105
delete wal 106
delete wal 107
delete wal 108
delete wal 109
delete wal 110
delete wal 111
delete wal 112

;RUNOUT WALL
wall id 113 nodes 3469.1 0.0 &
4415.95 -56.59 5062.8 -84.89 &
6356.5 -99.04 7200.2 -106.11 &
8943.9 -109.65 10237.6 -111.51 &
13769.1 -111.51
```

```
;==================STRATIGRAPHY==================

;THIS SECTION DEFINES THE NUMBER, ANGLE AND THICKNESS OF ANY STRATIGRAPHIC LAYERS WHICH MAY
;BE ADDED TO THE PRE-FAILURE EDIFICE/SLOPE

;NUMBER OF LAYERS (3 OF 5O M THICKNESS IN THIS CASE)
def layers
  nb_layer = 3
  xtable(1,1) = 50.0
  xtable(1,2) = 50.0
  xtable(1,3) = 50.0
end

def find_X
  bp = ball_head
  X0 = 0.0
  loop while bp # null
    X0 = max(b_x(bp)+b_rad(bp),X0)
    bp = b_next(bp)
  end_loop
end

def find_Y
  bp = ball_head
  Y0   = 1e20
  Ymax = 0.0
  loop while bp # null
    Y0   = min(b_y(bp)-b_rad(bp),Y0)
    Ymax = max(b_y(bp)+b_rad(bp),Ymax)
  bp = b_next(bp)
  end_loop
end
def strat_mod

;FIND THE COORDINATES OF LINE OF SYMMETRY
  X_sym = X0 - (Y0-Ymax)/tan(_angle*degrad)
  Y_sym = Ymax

;DELETE BALLS ABOVE FIRST LINE PASSING FROM (X0,Y0) AND CREATES EDIFICE SYMMETRY
  norm_I = -1.0*tan(_angle*degrad)
  norm_J =  1.0
    command
      delete ball range line normal (norm_I,norm_J) origin (X0,Y0) above
    end_command

  _angle_reverse = -1.0*_angle
  norm_I = -1.0*tan(_angle_reverse*degrad)
  norm_J =  1.0
    command
      delete ball range line normal (norm_I,norm_J) origin (X_sym,Y_sym) above
    end_command

;CREATE LAYERS
  X_inf = X0
  Y_inf = Y0
  X_inf_left = X_sym
  Y_inf_left = Y_sym
  loop _layer(1,nb_layer)
    ;RIGHT SIDE
    X_sup  = X_inf
    Y_sup  = Y_inf
    X_inf  = X_sup
    Y_inf  = Y_sup - xtable(1,_layer)/cos(_angle*degrad)
    norm_I = -1.0*tan(_angle*degrad)
    norm_J =  1.0
      command
        prop color @_layer range line normal (norm_I,norm_J) origin (X_sup,Y_sup) below &
        line normal (norm_I,norm_J) origin (X_inf,Y_inf) above &
         line normal (1,0) origin (1737.05,Y_sym) above
      end_command

    ; FOR THE LEFT SIDE
    X_sup_left  = X_inf_left
    Y_sup_left  = Y_inf_left
    X_inf_left  = X_sup_left
    Y_inf_left  = Y_sup_left - xtable(1,_layer)/cos(_angle_reverse*degrad)
    norm_I = -1.0*tan(_angle_reverse*degrad)
    norm_J =  1.0
      command
        prop color @_layer range line normal (norm_I,norm_J) origin (X_sup_left,Y_sup_left)
below    line normal (norm_I,norm_J) origin (X_inf_left,Y_inf_left) above line normal (1,0)
         origin (1737.05,Y_sym) below
```

```
      end_command
  end_loop
end

;ANGLE FOR THE LAYERS (IN DEGREES)
set _angle = -30.0

;COORDINATES FOR THE FIRST LAYER
set X0 = 3469.1
set Y0 = 0.0

;CALL DEFINED FUNCTIONS
find_X
find_Y
layers
strat_mod

;==================PLOTTING==================

;THIS SECTION PLOTS ANY DEFINED ENTITIES ON THE SCREEN

plot ball white red yellow
plot add wall black
plot add axes white
plot set title 'Volcanic edifice collapse'
plot set caption off
plot show

;==================SAVING CURRENT MODEL==================

;THIS SECTION SAVES THE PRE-FAILURE SLOPE AND INITIATE AND SLOPE FAILURE IS INDUCED BY
;MODEL CYCLING.  IN ORDER TO OBSERVE THE EVOLUTION EMPLACEMENT, MODELS ARE SAVED
;INCREMENTALLY

save F_prefailure.sav

cycle 50000

save F_50.sav

cycle 50000

save F_100.sav

return
```